ACOUSTIC TRANSDUCTION – MATERIALS AND DEVICES

Period 31 July 1996 to 31 December 1997

Annual Report

VOLUME VI

OFFICE OF NAVAL RESEARCH
Contract No: N00014-96-1-1173

APPROVED FOR PUBLIC RELEASE –
DISTRIBUTION UNLIMITED

Kenji Uchino

PENNSTATE

1855

THE MATERIALS RESEARCH LABORATORY
UNIVERSITY PARK, PA

19980910 006

REPORT DOCUMENTATION PAGE

Form Approved
OMB No. 0704-0188

1. AGENCY USE ONLY *(Leave blank)*

2. REPORT DATE
05/01/98

3. REPORT TYPE AND DATES COVERED
ANNUAL REPORT 07/31/96-12/31/97

4. TITLE AND SUBTITLE
ACOUSTIC TRANSDUCTION -- MATERIALS AND DEVICES

5. FUNDING NUMBERS
ONR CONTRACT NO:
N00014-96-1-1173

6. AUTHOR(S)
KENJI UCHINO

7. PERFORMING ORGANIZATION NAME(S) AND ADDRESS(ES)
Materials Research Laboratory
The Pennsylvania State University
University Park, PA 16802

8. PERFORMING ORGANIZATION REPORT NUMBER

9. SPONSORING/MONITORING AGENCY NAME(S) AND ADDRESS(ES)

Office of Naval Research
ONR 321SS
Ballston Centre Tower One
800 N Quincy Street
Arlington, VA 22217-5660

Office of Naval Research
Regional Office Chicago
536 S Clark Str., Rm 208
Chicago IL 60605-1588

10. SPONSORING/MONITORING AGENCY REPORT NUMBER

11. SUPPLEMENTARY NOTES

12a. DISTRIBUTION / AVAILABILITY STATEMENT

12b. DISTRIBUTION CODE

13. ABSTRACT *(Maximum 200 words)*

SEE FOLLOW PAGE

14. SUBJECT TERMS

15. NUMBER OF PAGES

16. PRICE CODE

17. SECURITY CLASSIFICATION OF REPORT

18. SECURITY CLASSIFICATION OF THIS PAGE

19. SECURITY CLASSIFICATION OF ABSTRACT

20. LIMITATION OF ABSTRACT

GENERAL INSTRUCTIONS FOR COMPLETING SF 298

The Report Documentation Page (RDP) is used in announcing and cataloging reports. It is important that this information be consistent with the rest of the report, particularly the cover and title page. Instructions for filling in each block of the form follow. It is important to ***stay within the lines*** to meet ***optical scanning requirements***.

Block 1. Agency Use Only *(Leave blank)*.

Block 2. Report Date. Full publication date including day, month, and year, if available (e.g. 1 Jan 88). Must cite at least the year.

Block 3. Type of Report and Dates Covered. State whether report is interim, final, etc. If applicable, enter inclusive report dates (e.g. 10 Jun 87 - 30 Jun 88).

Block 4. Title and Subtitle. A title is taken from the part of the report that provides the most meaningful and complete information. When a report is prepared in more than one volume, repeat the primary title, add volume number, and include subtitle for the specific volume. On classified documents enter the title classification in parentheses.

Block 5. Funding Numbers. To include contract and grant numbers; may include program element number(s), project number(s), task number(s), and work unit number(s). Use the following labels:

C - Contract
G - Grant
PE - Program Element
PR - Project
TA - Task
WU - Work Unit Accession No

Block 6. Author(s). Name(s) of person(s) responsible for writing the report, performing the research, or credited with the content of the report. If editor or compiler, this should follow the name(s).

Block 7. Performing Organization Name(s) and Address(es). Self-explanatory.

Block 8. Performing Organization Report Number. Enter the unique alphanumeric report number(s) assigned by the organization performing the report.

Block 9. Sponsoring/Monitoring Agency Name(s) and Address(es). Self-explanatory.

Block 10. Sponsoring/Monitoring Agency Report Number. *(If known)*

Block 11. Supplementary Notes. Enter information not included elsewhere such as: Prepared in cooperation with....; Trans. of....; To be published in.... When a report is revised, include a statement whether the new report supersedes or supplements the older report.

Block 12a. Distribution/Availability Statement. Denotes public availability or limitations. Cite any availability to the public. Enter additional limitations or special markings in all capitals (e.g. NOFORN, REL, ITAR).

DOD - See DoDD 5230.24, "Distribution Statements on Technical Documents."
DOE - See authorities.
NASA - See Handbook NHB 2200.2.
NTIS - Leave blank.

Block 12b. Distribution Code.

DOD - Leave blank.
DOE - Enter DOE distribution categories from the Standard Distribution for Unclassified Scientific and Technical Reports.
NASA - Leave blank.
NTIS - Leave blank.

Block 13. Abstract. Include a brief *(Maximum 200 words)* factual summary of the most significant information contained in the report.

Block 14. Subject Terms. Keywords or phrases identifying major subjects in the report.

Block 15. Number of Pages. Enter the total number of pages.

Block 16. Price Code. Enter appropriate price code *(NTIS only)*.

Blocks 17. - 19. Security Classifications. Self-explanatory. Enter U.S. Security Classification in accordance with U.S. Security Regulations (i.e., UNCLASSIFIED). If form contains classified information, stamp classification on the top and bottom of the page.

Block 20. Limitation of Abstract. This block must be completed to assign a limitation to the abstract. Enter either UL (unlimited) or SAR (same as report). An entry in this block is necessary if the abstract is to be limited. If blank, the abstract is assumed to be unlimited.

ABSTRACT

The report documents work carried out over the period 31 July 1996 to 31 December 1997 on a Multi-University Research Initiative (MURI) program under Office of Naval Research (ONR) sponsorship. The program couples transducer materials research in the Materials Research Laboratory (MRL), design and testing studies in the Applied Research Laboratory (ARL) and vibration and flow noise control in the Center for Acoustics and Vibration (CAV) at Penn State.

The overarching project objective is the development of acoustic transduction materials and devices of direct relevance to Navy needs and with application in commercial products. The initial focus of studies is upon high performance sensors and high authority high strain actuators. This objective also carries the need for new materials, new device designs, improved drive and control strategies and a continuing emphasis upon reliability under a wide range of operating conditions.

In *Material Studies*, undoubtedly major breakthroughs have occurred in the ultra-high strain relaxor ferroelectric systems. Earlier reports of unusual piezoelectric activity in single crystal perovskite relaxors have been amply confirmed in the lead zinc niobate : lead titanate, and lead magnesium niobate : lead titanate systems for compositions of rhombohedral symmetry close to the Morphotropic Phase Boundary (MPB) in these solid solutions. Analysis of the unique properties of 001 field poled rhombohedral ferroelectric crystals suggests new intrinsic mechanisms for high strain and carries the first hints of how to move from lead based compositions. A major discovery of comparable importance is a new mode of processing to convert PVDF:TrFE copolymer piezoelectric into a relaxor ferroelectric in which electrostrictive strains of 4% have been demonstrated at high fields. Both single crystal and polymer relaxors appear to offer energy densities almost order of magnitude larger than in earlier polycrystal ceramic actuators.

Transducer Studies have continued to exploit the excellent sensitivity and remarkable versatility of the cymbal type flextensional element. Initial studies of a small cymbal arrays show excellent promise in both send and receive modes, and larger arrays are now under construction for tests at ARL. New studies in constrained layer vibration damping and in flow noise reduction are yielding exciting new results.

In *Actuator Studies*, an important advance in piezoelectric generated noise control now permits wider use of acoustic emission as a reliability diagnostic technique. Joint studies with NRL, Washington have developed a completely new d_{15} driven torsional actuator and the CAV program element has designed an exciting high strain high force inchworm.

Finite element analysis continues to be an important tool for understanding the more complex composite structures and their beam forming capability in water. *Thin and Thick Thin Film Studies* are gearing up to provide the material base for micro-tonpilz arrays. New exploitation of ultra sensitive strain and permittivity measurements is providing the first reliable data of electrostriction in simple solids, and suggesting new modes for separating the polarizability contributors in dielectrics and electrostrictors.

APPENDICES

VOLUME I

GENERAL SUMMARY PAPERS

1. Ito, Y. and K. Uchino, Wiley Encyclopedia of Electrical and Electronics Engineering, J. G. Webster, Edit., (Partial Charge "Piezoelectricity"), John Wiley & Sons (1998). [in press].
2. Newnham, R.E., "Molecular Mechanisms in Smart Materials," MRS Bulletin (May 1997).
3. Swartz, S.L., T.R. Shrout, and T. Takenaka, "Electronic Ceramics R&D in the U.S., Japan, Part I: Patent History," The American Ceramic Society Bulletin **76** (8) (1997).

2.0 MATERIALS STUDIES

2.1 Polycrystal Perovskite Ceramics

4. Alberta, E.F., and A.S. Bhalla, "Piezoelectric Properties of $Pb(InNb)_{1/2}O_3$-$PbTiO_3$ Solid Solution Ceramics," J. Korean Phys. Soc. **32**, S1265-S1267 (February 1998).
5. Alberta, E.F. and A.S. Bhalla, "High Strain and Low Mechanical Quality Factor Piezoelectric $Pb[Sc_{1/2}Nb_{1/2})_{0.575}Ti_{0.425}]O_3$ Ceramics" (1997).
6. Zhang, Q.M. and J. Zhao, "Polarization Responses in Lead Magnesium Niobate Based Relaxor Ferroelectrics," Appl. Phys. Lett. **71** (12, 1649-1651 (1997).
7. Glazounov, A.E., J. Zhao, and Q.M. Zhang, "Effect of Nanopolar Regions on Electrostrictive Coefficients of a Relaxor Ferroelectric," Proceedings Williamsburg Meeting, Williamsburg, Virginia (1998).
8. Zhao, J. A.E. Glazounov, Q.M. Zhang, and B. Toby, "Neutron Diffraction Study of Electrostrictive Coefficients of Prototype Cubic Phase of Relaxor Ferroelectric $PbMg_{1/3}Nb_{2/3}O_3$," Appl. Phys. Lett. **72** (9), 1-3 (1998).
9. Park, S.-E., T.R. Shrout, P. Bridenbaugh, J. Rottenberg, and G.M. Loiacono, "Electric Field Induced Anisotropy in Electrostrictive $Pb(Mg_{1/3}Nb_{2/3})O_3$ - $PbTiO_3$ Crystals," Ferroelectrics (1997).
10. You, H. and Q.M. Zhang, "Diffuse X-Ray Scattering Study of Lead Magnesium Niobate Single Crystals," Phys. Rev. Lett. **79** (20), 3950-3953 (1997).
11. Zhao, J., V. Mueller, and Q.M. Zhang, "The Influence of the External Stress on the Electromechanical Response of Electrostrictive $0.9Pb(Mg_{1/3}Nb_{2/3})O_3$–$0.1PbTiO_3$ in the DC Electrical Field Biased State," J. Mat. Res. (1998).

VOLUME II

12. Yoon, S.-J., A. Joshi, and K. Uchino, "Effect of Additives on the Electromechanical Properties of $Pb(Zr,Ti)O_3$–$Pb(Y_{2/3}W_{1/3})O_3$ Ceramics," J. Am. Ceram. Soc **80** (4), 1035-39 (1997).
13. Hackenberger, W., M.-J. Pan, V. Vedula, P. Pertsch, W. Cao, C. Randall, and T. Shrout, "Effect of Grain Size on Actuator Properties of Piezoelectric Ceramics," Proceedings of the SPIE's 5th International Symposium on Smart Structures and Materials, San Diego, CA (March 1-5, 1998).

14. Mueller, V. and Q.M. Zhang, "Shear Response of Lead Zirconate Titanate Piezoceramics," J. Appl. Phys. (1998).
15. Park, S.-E., M.-J. Pan, K. Markowski, S. Yoshikawa, and L.E. Cross, "Electric Field Induced Phase Transition of Antiferroelectric Lead Lanthanum Zirconate Titanate Stannate Ceramics," J. Appl. Phys. **82** (4), 1798-1803 (1997).
16. Yoshikawa, S., K. Markowski, S.-E. Park, M.-J. Pan, and L.E. Cross, "Antiferroelectric-to-Ferroelectric Phase Switching Lead Lanthanum Zirconate Stannate Titanate (PLZST) Ceramics)," Proceedings of SPIE's 4th Annual Symposium on Smart Structures and Materials, San Diego, CA (March 3-6, 1997).
17. Pan, M.-J., S.-E. Park, K.A. Markowski, W.S. Hackenberger, S. Yoshikawa, and L.E. Cross, "Electric Field Induced Phase Transition in Lead Lanthanum Stannate Zirconate Titanate (PLSnZT) Antiferroelectrics: Tailoring Properties through Compositional Modification" (1997).
18. Pan, M.-J., P. Pertsch, S. Yoshikawa, T.R. Shrout, and V. Vedula, "Electroactive Actuator Materials: Investigations on Stress and Temperature Characteristics," Proceedings of the SPIE's 5th International Symposium on Smart Structures and Materials, San Diego, CA (March 1-5, 1998).
19. Pan, M.-J. and S. Yoshikawa, "Effect of Grain Size on the Electromechanical Properties of Antiferroelectric-to-Ferroelectric Phase Switching PLSnZT Ceramics" (1997).

2.2 *Relaxor Ferroelectric Single Crystal Systems*

20. Service, R.F., "Shape-Changing Crystals Get Shiftier," Science **275**, 1878 (28 March 1997).
21. Shrout, T.R., S.-E. Park, C.A. Randall, J.P. Shepard, L.B. Hackenberger, "Recent Advances in Piezoelectric Materials" (1997).
22. Park, S.-E. and T.R. Shrout, "Ultrahigh Strain and Piezoelectric Behavior in Relaxor Based Ferroelectric Single Crystals," J. Appl. Phys. **82** (4), 1804-1811 (1997).
23. Park, S.-E. and T. R. Shrout, "Characteristics of Relaxor-Based Piezoelectric Single Crystals for Ultrasonic Transducers," IEEE Transactions, Ferroelectrics, and Frequency Control **44** (5), 1140-1147 (1997).
24. Park, S.-E. and T.R. Shrout, "Relaxor Based Ferroelectric Single Crystals for Electro-Mechanical Actuators," Mat. Res. Innov. **1**, 20-25 (1997).
25. Park, S.-E., M.L. Mulvihill, G. Risch, and T.R. Shrout, "The Effect of Growth Conditions on the Dielectric Properties of $Pb(Zn_{1/3}Nb_{2/3})O_3$ Single Crystals," Jpn. J. Appl. Phys. **36**, 1154-1158 (1997).
26. Mulvihill, M.L., L.E. Cross, W. Cao, and K. Uchino, "Domain-Related Phase Transionlike Behavior in Lead Zinc Niobate Relaxor Ferroelectric Single Crystals," J. Am. Ceram. Soc. **80** (6), 1462-68 (1997).
27. Park, S.-E., P.D. Lopath, K.K. Shung, and T.R. Shrout, "Relaxor-Based Single Crystal materials for Ultrasonic Transducer Applications" (1997).
28. Lopath, P.D., S.-E. Park, K.K. Shung, and T.R. Shrout, "$Pb(Zn_{1/3}Nb_{2/3})O_3/PbTiO_3$ Single Crystal Piezoelectrics for Ultrasonic Transducers" (1997).
29. Lopath, P.D., S-E. Park, K.K. Shung, and T.R. Shrout, "Single Crystal $Pb(Zn_{1/3}Nb_{2/3})O_3/PbTiO_3$ (PZN/PT) in Medical Ultrasonic Transducers" (1997).

2.3 New High Strain Polymer Materials

30. Su. J., Q.M. Zhang, C.H. Kim, R.Y. Ting, and R. Capps, "Effect of Transitional Phenomena on the Electric Field Induced Strain–Electrostrictive Response of a Segmented Polyurethane Elastomer" (1997).
31. Su, J., Q.M. Zhang, and R.Y. Ting, "Space-Charge-Enhanced Electromechanical Response in Thin-Film Polyurethane Elastomers," Appl. Phys. Lett **71** (3), 386-388 (1997).

VOLUME III

32, Su, J., Q.M. Zhang, P.-C. Wang, A.G. MacDiarmid, K.J. Wynne, "Preparation and Characterization of an Electrostrictive Polyurethane Elastomer with Conductive Polymer Electrodes," Polymers for Adv. Tech. (1998).
33. Zhang, Q.M., V. Bharti, and X. Zhao, "Giant Electrostriction and Relaxor Ferroelectric Behavior in Electron Irradiated Poly(vinylidene Fluoride-Trifluoroethylene) Copolymer," Science (1998).

3.0 TRANSDUCER STUDIES

3.1 Cymbal : Moonie : BB Composites

34. Newnham, R.E., "Composite Sensors and Actuators" (1997).
35. Steele, B.CH., R.E. Newnham, and A.G. Evans, "Ceramics, Composites, and Intergrowth," Current Opinion in Solid State & Materials Science **2**, 563-565 (1997).
36. Tressler, J.F. S. Alkoy, and R.E. Newnham, "Piezoelectric Sensors and Sensor Materials" (1997).
37. Tressler, J.F., S. Alko, A. Dogan, and R.E. Newnham, "Functional Composites for Sensors, Actuators, and Transducers" (1997).
38. Dogan, A., K. Uchino, R.E. Newnham, "Composite Piezoelectric Transducer with Truncated Conical Endcaps 'Cymbal'," IEEE Transactions on Ultrasonics, Ferroelectrics, and Frequency Control **44** (3), 597-605 (1997).
39. Dogan, A., J.F. Fernandez, K. Uchino, and R.E. Newnham, "The 'Cymbal' Electromechanical Actuator" (1997).
40. Tressler, J.F., W. Cao, K. Uchino, and R.E. Newnham, "Ceramic-Metal Composite Transducers for Underwater Acoustic Applications" (1997).
41. Tressler, J.F. and R.E. Newnham, "Doubly Resonant Cymbal-Type Transducers," IEEE Transactions on Ultrasonics, Ferroelectrics, and Frequency Control **44** (5), 1175-1177 (1997).
42. Tressler, J.F., W. Cao, K. Uchino, and R.E. Newnham, "Finite Element Analysis of The Cymbal-Type Transducer" (1997).
43. Tressler, J.F., W.J. Hughes, W. Cao, K. Uchino, and R.E. Newnham, "Capped Ceramic Underwater Sound Projector" (1997).

VOLUME IV

44. Alkoy, S., P.D. Lopath, R.E. Newnham, A.-C. Hladky-Hennion, and J.K. Cochran, "Focused Spherical Transducers for Ultrasonic Imaging" (1997).
45. Alkoy, S., A. Dogan, A.-C. Hladky, P. Langlet, J.K. Cochran, and R.E. Newnham, "Miniature Piezoelectric Hollow Sphere Transducers (BBs)" (1997).
46. Zipparo, M.J., K.K. Shung, and T.R. Shrout, "Piezoceramics for High-Frequency (20 to 100 MHz) Single-Element Imaging Transducers," IEEE Transactions on Ultrasonics, Ferroelectrics, and Frequency Control **44** (5), 1038-1048 (1997).

3.2 Frequency Agile Transducers

47. Davis, C. and G.A. Lesieutre, "An Actively-Tuned Solid State Piezoelectric Vibration Absorber" (1997).
48. Davis, C.L., G.A. Lesieutre, and J. Dosch, "A Tunable Electrically Shunted Piezoceramic Vibration Absorber" (1997).
49. Lesieutre, G.A. and U. Lee, "A Finite Element for Beams Having Segmented Active Constrained Layers with Frequency-Dependent Viscoelastic Material Properties" (1997).
50. Hebert, C.A. and G.A. Lesieutre, "Rotocraft Blade Lag Damping Using Highly Distributed Tuned Vibration Absorbers," American Institute of Aeronautics and Astronautics (AIAA 98-2001).
51. Lesieutre, G.A. and C.L. Davis, "Can a Coupling Coefficient of a Piezoelectric Device be Higher than Those of its Active Material?," SPIE 4th Annual Symposium on Smart Structures and Materials, San Diego, CA (March 1997).

3.3 3-D Acoustic Intensity Probes

52. Lauchle, G.C., J.R. MacGillivray, and D.C. Swanson, "Active Control of Axial-flow Fan Noise," J. Acoust. Soc. Am 101 (1), 341-349 (1997).
53. McGuinn, R.S., G.C. Lauchle, and D.C. Swanson, "Low Flow-Noise Microphone for Active Noise Control Applications," AIAA Journal **35** (1), 29-34 (1997).
54. McGuinn, R.S., G.C. Lauchle, and D.C. Swanson, "Low Flow-Noise Pressure Measurements Using a "Hot-Mic," AIAA -97-1665-CP.
55. Capone, D.E., and G.C. Lauchle, "Designing a Virtual Sound-Level Meter in LabVIEW," Education/Acoustics, LabVIEW, National Instruments.

VOLUME V

4.0 ACTUATOR STUDIES

4.1 Materials : Designs : Reliability

56. Uchino, K., "Piezoelectric Actuators" (1997).
57. Uchino, K., "Overview: Materials Issues in Design and Performance of Piezoelectric Actuators," SPIE Mtg. (1997).
58. Uchino, K., "Shape Memory Ceramics," Chapter 8 (1997).

59. Aburatani, H., S. Yoshikawa, K. Uchino, and J.W.C. deVries, "A Study of Acoustic Emission in Piezoelectric Multilayer Ceramic Actuator," Jpn. J. Appl. Phys. **37**, 204-209 (1998).
60. Aburatani, H. and K. Uchino, "Acoustic Emission (AE) Measurement in Piezoelectric Ceramics" (1997).
61. Aburatani, H. and K. Uchino, "The Application of Acoustic Emission (AE) Method for Ferroelectric Devices and Materials," 8th US-Japan Seminar (1997).
62. Uchino, K., "Reliability of Ceramic Actuators" (1997).

4.2 Photostrictive Actuators

63. Tonooka, K. P. Poosanaas, and K. Uchino, "Mechanism of the Bulk Photovoltaic Effect in Ferroelectrics," Proceedings of the 5th SPIE Mtg., San Diego, CA (1998).
64. Poosanass, P. A. Dogan, S. Thakoor, and K. Uchino, "Dependence of Photostriction on Sample Thickness and Surface Roughness for PLZT Ceramics," Proceedings of the 1997 IEEE Ultrasonics Symposium, Toronto, Ontario, Canada (October 1997).
65. Poosanaas, P. A. Dogan, A.V. Prasadarao, S. Komarneni, and K. Uchino, "Photostriction of Sol-Gel Processed PLZT Ceramics," J. Electroceramics **1** (1), 105-111 (1997).

VOLUME VI

66. Poosanaas, P., A. Dogan, A.V. Prasadarao, S. Komarneni, and K. Uchino, "Effect of Ceramic Processing Methods on Photostrictive Ceramics," J. Adv. Perf. Mat. (1997).
67. Thakoor, S., P. Poosanaas, J.M. Morookian, A. Yavrovian, L. Lowry, N. Marzwell, J. Nelson, R.R. Neurgaonkar, and K. Uchino, "Optical Microactuation in Piezoceramics" (1997).

4.3 New Torsional Amplifier/Actuators

68. Glazounov, A.E., Q.M. Zhang, and C. Kim, "Piezoelectric Actuator Generating Torsional Displacement from Piezoelectric d_{15} Shear Response," Appl Phys. Lett. (1997).
69. Glazounov, A.E., Q.M. Zhang, and C. Kim, "A New Torsional Actuator Based on Shear Piezoelectric Response," Proceedings of SPIE Smart Materials, San Diego, CA (March 1998).

4.4 High Force Amplifiers and Inchworms

70. Uchino, K., J. Zheng, A. Joshi, S. Yoshikawa, S. Hirose, S. Takahashi, and J.W.C. deVries, "High Power Characterization of Piezoelectric Materials" (1997).
71. Uchino, K., "High Electromechanical Coupling Piezoelectrics - How High Energy Conversion Rate is Possible," Mat. Res. Soc. Symp. Proc. **459**, 3-14 (1997).
72. Park, S.-E., V. Vedula, M.-J. Pan, W.S. Hackenberger, P. Pertsch, and T.R. Shrout, "Relaxor Based Ferroelectric Single Crystals for Electromechanical Actuators," Proceedings of the SPIE's 5th International Symposium on Smart Structures and Materials, San Diego, CA (March 1998).

Actuator Studies–continued

73. Koopmann, G.H. G.A. Lesieutre, B.R. Dershem, W. Chen, and S. Yoshikawa, "Embeddable Induced Strain Actuators Using Framed 3-3 Piezoceramic Stacks: Modeling and Characterization," Proceedings of the SPIE's 4th Annual International Symposium on Smart Structures and Materials, San Diego, CA (March 1997).
74. Driesch, P.L., G.H. Koopmann, J. Dosch, and H. Iwata, "Development of a Surface Intensity Probe for Active Control Applications," IMECE, Dallas, Texas (November 1997).
75. Galante, T., J. Frank, J. Bernard, W. Chen, G.A. Lesieutre, and G.H. Koopmann, "Design, Modeling, and Performance of a High Force Piezoelectric Inchworm Motor" (1997).
76. Galante, T.P., "Design and Fabrication of a High Authority Linear Piezoceramic Actuator: The PSU H3 Inchworm," Master of Science Thesis, The Pennsylvania State University (August 1997).
77. Lesyna, M.W., "Shape Optimization of a Mechanical Amplifier for Use in a Piezoceramic Actuator," Master of Science Thesis, The Pennsylvania State University (May 1998).

VOLUME VII

78, Uchino, K., "Piezoelectric Ultrasonic Motors: Overview," J. Smart Materials and Structures–Special Issue (1997).
79. Uchino, K., "Compact Piezoelectric Ultrasonic Motors," J. Medical Ultrasonics 24 (9), 1191-92 (1997).

5.0 MODELING and CHARACTERIZATION

5.1 Finite Element Methods

80. Qi, W. and W. Cao, "Finite Element Analysis and Experimental Studies on the Thickness Resonance of Piezocomposite Transducer," Ultrasonic Imaging **18**, 1-9 (1996).
81. Qi, W. and W. Cao, "Finite Element Study on Random Design of 2-2 Composite Transducer," SPIE **3037**, 176-180 (1997).
82. Geng, X. and Q.M. Zhang, "Evaluation of Piezocomposites of Ultrasonic Transducer Applications–Influence of the Unit Cell Dimensions and the Properties of Constituents on the Performance of 2-2 Piezocomposites," IEEE Transactions on Ultrasonics, Ferroelectrics, and Frequency Control **44** (4), 857-872 (1997).
83. Zhang, Q. and X. Geng, "Acoustic Properties of the Interface of a Uniform Medium-2-2 Piezocomposite and the Field Distributions in the Composite," Jpn. J. Appl. Phys. **36**, 6853-6861 (1997).
84. Geng, X. and Q.M. Zhang, "Analysis of the Resonance Modes and Losses in 1-3 Composites for Ultrasonic Transducer Applications," IEEE UFFC (1997).

APPENDIX 66

Submitted to Journal of Advanced Performance Materials

EFFECT OF CERAMIC PROCESSING METHODS ON PHOTOSTRICTIVE CERAMICS

Patcharin Poosanaas, A. Dogan *, A. V. Prasadarao **, S. Komarneni, and K. Uchino.

International Center for Actuators and Transducers, Materials Research Laboratory,
The Pennsylvania State University, University Park, PA 16802.
* Ceramic Engineering Department, Anadola University, Eskisehir, Turkiye
** Department of Inorganic & Analytical Chemistry, Andhra University, India

ABSTRACT

Lanthanum-modified lead zirconate titanate (PLZT) ceramics (3/52/48) doped with 0.5 at.% WO_3 were prepared by three different processing methods, coprecipitation, sol-gel and conventional oxide mixing techniques, to investigate the effect of processing route on photovoltaic and photostrictive properties. The piezoelectric constant (d_{33}) was observed to be independent of processing technique. Photovoltaic and photo-induced strain were found to get enhanced with decreasing grain size and increasing relative density. PLZT ceramics prepared by the coprecipitation route possess unique combination of favorable properties namely: high purity, higher degree of homogeneity, uniform distribution of doping, stoichiometric compositions, finer grain size and highest density. This resulted into enhanced photostrictive properties in coprecipitated PLZT ceramics.

INTRODUCTION

Photostriction is the light induced strain in a material, which can also be regarded as the superposition of photovoltaic and inverse-piezoelectric effects [1]. Materials exhibiting photostrictive effect are of interest for their potential usage in new types of actuators such as wireless remote control photo-actuators. The possibility of directly producing strain by light illumination without any electrical lead wire connection makes them very attractive for micro-actuator and micro-sensor applications. These materials are also promising for the photo-acoustic device of the optical communication system, such as photophone [2]. Adaptive space structures which can be controlled by the illumination are possible and intriguing applications.

Lanthanum-modified lead zirconate titanate (PLZT) ceramics are one of the proven photostrictive material. It has been observed that doping WO_3, donor in the B-site, into the PLZT ceramic results in significant enhancement in this property [3-5]. Besides the effect of doping, fabrication and processing methods have been reported to profoundly affect the photovoltaic properties and the strain response. This effect comes through the influence of processing methods on the microstructure, and other physical properties such as density, porosity, chemical composition. Ceramic materials with high density, low porosity, better homogeneity and a good control of stoichiometry are desired for enhanced photovoltaic and photostrictive properties. Investigation of the microstructure and properties of PLZT ceramics fabricated by different routes are of interest for finding the technique with best photostrictive properties.

It has been observed that the conventional solid-state reaction of the metal oxides and carbonates often results in PLZT products with moderate photovoltaic and photostrictive properties due to the compositional and structural inhomogeneities, characteristic of this fabrication route [6, 7]. Coprecipitation and sol-gel techniques are two of the chemical routes which has the inherent advantage in producing high density homogeneous ceramics with a greater control of stoichiometry [8-10]. Therefore, process for preparation of PLZT via chemical routes with suitable non-oxide precursors is attractive. Among various non-oxide routes, the hydroxide coprecipitation method has also been widely used for the preparation of PLZT powders [9-12]. Fine powders prepared by this route are more homogeneous and more reactive than those prepared by conventional oxide mixing process. In addition, the lower processing temperature also minimizes the loss of PbO evaporation.

In order to investigate the influence of processing techniques on photostrictive property, ceramics of PLZT (3/52/48) doped with 0.5 at.% WO_3 were prepared by three different methods, (i) conventional oxide mixing process, (ii) sol-gel technique using lead (II) acetate trihydrate, lanthanum (III) acetylacetonate hydrate, Zr, Ti and W alkoxides, and (iii) hydroxide coprecipitation routes using nitrate and chloride precursors. The photostrictive effect of these materials were characterized and correlated to the fabrication method.

EXPERIMENTAL PROCEDURE

PLZT (3/52/48) ceramic with a composition of 3 at.% La , Zr/Ti ratio of 52/48 and doped with WO_3 was selected due to its proven high photovoltaic effect [3]. PLZT ceramics doped with 0.5 at.% WO_3 were prepared by the conventional oxide mixing process and by the chemical synthesis (sol-gel and coprecipitation) techniques. Figure 1 illustrates a flow chart for the sample preparation by the conventional oxide mixing process. The flow chart for the sample preparation by the sol-gel technique using lead (II) acetate trihydrate, lanthanum (III) acetylacetonate hydrate, Zr, Ti, and W alkoxides, is shown in Fig. 2. The details of these two preparation techniques were reported in an earlier communication [7]. The details of the processing technique for hydroxide coprecipitation is shown in Fig 3. In order to achieve a product with desired stoichiometry and homogeneity, the optimum coprecipitation conditions for metal hydroxide precursors were determined on the basis of solubility limit for aqueous solutions. [11]. The starting reagents were high purity lead nitrate $Pb(NO_3)_2$, lanthanum nitrate $La(NO_3)_3 \cdot 6H_2O$, zirconium oxychloride $ZrOCl_2 \cdot 8H_2O$, and titanium tetrachloride $TiCl_4$. Sodium tungstate $Na_2WO_4 \cdot 2H_2O$ was added for the doping. The precursor site A comprising of $Pb(NO_3)_2$, $La(NO_3)_3 \cdot 6H_2O$, and $Na_2WO_4 \cdot 2H_2O$ was dissolved together in deionized (DI) water to form an aqueous solution. On the other hand precursor site B with $ZrOCl_2 \cdot 8H_2O$ and $TiCl_4$, was also dissolved in DI water. The coprecipitation was achieved in these precursors by adding aqueous NH_4OH solution. In the precursor site

A, aqueous NH_4OH solution was slowly added and stirred to precipitate A-site powders. The solution pH in A and B precursor sites was adjusted and maintained at pH 10 and 5 respectively. The precipitates of A and B sites were then washed with DI water (pH 10 and 5 respectively) to remove the residual , NO_3^-, Na^+, and Cl^- ion. Both A and B site precipitates were filtered, mixed and rinsed thoroughly using reagent alcohol, followed by overnight drying at 80 °C. The dry cake was crushed and ground using porcelain mortar and pestle. In order to evaporate the absorbed water, thermal treatment was given on the as-dried powder. Thermogravimetric, differential thermal analysis (TGA 7, DTA 1700, Perkin Elmer), and X-ray diffraction (Scintag diffractometer, Vax 3100 System) were performed to characterize the precipitated powders. Subsequently, the powder was calcined and sintered.

The comparison of the properties of ceramics derived from the three different method were made. The density of the sintered samples was determined by the Archimedes method while microstructure and grain size of the samples were observed by scanning electron microscopy (ISI DS-130). Dielectric properties of PLZT samples were measured with an impedance analyzer (HP-4274A). Samples for dielectric measurement were polished to about 10 mm in diameter and 1 mm in thickness, then electroded with platinum (Pt) by sputtering. Piezoelectric properties of all the samples were measured by using a Berlincourt d_{33} meter (Channel Products, Inc.) at 100 Hz. Samples for piezoelectric measurement were of the same dimension as for dielectric measurements, except they were poled in silicone oil at 120 °C under a 2 kV/mm electric field for 10 min.

Photovoltaic measurements were done using a high-input-impedance electrometer (Keithley 617), while the photostriction was measured by a displacement sensor (LVDT, Millitron model 1301). Figure 4 shows the experimental setup for these measurements

[7]. These measurements were done by radiating the light perpendicular to the polarization direction. The samples of 5x5x1 mm^3 were cut and polished for these measurements. The 5x1 mm^2 surfaces were silver electroded. Poling was performed by applying 2 kV/mm electric field for 10 min. in silicone oil at 120 °C. A high pressure mercury lamp (Ushio Electric USH-500D) was used as a light source for the measurement. The white radiation was passed through an IR blocking filter and an UV bandpass filter to obtain a beam with a maximum strength around 366 nm and an intensity of 3.25 mW/cm^2, before illuminating the samples (5x5 mm^2 polished surface).

RESULTS AND DISCUSSIONS

Characterization of powder derived from coprecipitation technique

The as-dried powder from coprecipitation technique was examined using TGA-DTA, and X-ray diffractometer. The physico-chemical change of the precipitate with temperature was investigated with a TGA-DTA apparatus, in the temperature range of 50-1050 °C at a heating rate of 10 °C/min under an air atmosphere and by a powder X-ray diffraction with CuK$_\alpha$ radiation. Figure 5 shows TGA and DTA curves for the as-dried precipitate. The initial weight loss in the temperature range of 55-250 °C may be attributed to the liberation of surface absorbed water and/or occluded solvent (water, ethanol), and is accompanied by an endothermic DTA peak. Dehydration of the powder resulted in the endothermic peak observed at about 150 °C. The weight loss at 330-500 °C is due to the decomposition of hydroxyl group. The final weight loss above 600 °C can be attributed to the strongly bonded hydroxyl group.

Figure 6 shows a series of X-ray diffraction patterns of the as-dried powder at different temperatures. Crystallization of the perovskite phases during thermal treatment can be observed. The precipitate was found to be amorphous up to 450 °C for 1h. The crystalline perovskite phase of PLZT appears after 450 °C for 1h. The complete perovskite phase of PLZT was formed at 550 °C for 1 h. Based on these results the calcination temperature was selected to be 550 °C for 1h.

Comparison of ceramics derived from three different processing techniques.

Physical properties of ceramics produced from three different processing methods are listed in Table 1. As can be seen from this table, depending on the processing technique, the samples with the same composition exhibit different results.

Figure 7 shows the relative sintered density of 0.5 at.% WO_3 doped PLZT ceramics prepared through three different methods as a function of sintering temperature after 2 h sintering time. A relative density of 98% was achieved for PLZT oxide samples sintered at 1200 °C. The sintered density saturated and remained constant as the sintering temperature increases to 1300 °C. On the other hand, in the sol-gel PLZT a maximum density of 93% was observed at a sintering temperature of 1250 °C. The sintered density decreased as the sintering temperature was further increased. This was probably due to the evaporation of PbO during sintering. A relative density of 97% was achieved for coprecipitated PLZT ceramics sintered at 1150 °C. However the relative density of coprecipitated ceramics was enhanced to 99% after 4 h of sintering at the same temperature as shown in Fig 8. As evident from Fig. 7, the sol-gel PLZT exhibits lower density as compared to the oxide PLZT at all the sintering temperatures. This lower density was probably due to finer and agglomerated particles. The high density in PLZT oxide samples is due to higher packing density without agglomeration as compared to sol-gel ceramics. Coprecipitated PLZT ceramics possessed the highest density at the lowest sintering temperature among all ceramics due to no agglomeration associated with this route.

Figure 9 shows the SEM micrographs of the sintered ceramics. The average grain size of samples were determined. The average grain sizes for oxide mixing , sol-gel, and coprecipitated samples were 1.87, 1.72, and 1.12 μm, respectively. The grain size was smallest for the coprecipitated ceramics among all the samples. In general average grain size of ceramics prepared by chemical synthesis is smaller as compared to solid state reaction due to more reactive powder obtained through chemical routes which resulted in lower sintering temperature.

The dielectric constants of the ceramics derived from three different processing techniques are shown in Fig 10. There was no difference in the Curie temperature among three samples. PLZT ceramics from sol-gel and coprecipitation techniques exhibited lower dielectric constant compared to the oxide PLZT due to the smaller grain size observed in these ceramics. The piezoelectric constant d_{33} showed a similar tendency for the ceramics prepared by three different methods with the minimum for the coprecipitated sample. However photovoltaic and photostrictive properties vary greatly with the processing techniques. The photo-induced electric field reached more than 1 kV/cm and the photocurrent density was of the order of nA/cm under the illumination intensity of 3.25 mW/cm^2 for 366 nm wavelength. Coprecipitated PLZT ceramic showed the highest in both the photo-induced electric field and strain among all samples, followed by sol-gel PLZT and oxide mixing PLZT, due to the smaller grain size observed in this ceramic. Coprecipitated sample exhibited photocurrent similar to sol-gel PLZT, which are higher than oxide mixing PLZT. Table 1 listed the calculated product values of piezoelectric constant d_{33}, and photo-induced electric field E_{ph}, which are in good agreement with the experimental data.

Difference between samples prepared by solid-state reaction as in oxide mixing process and chemical synthesis routes as in sol-gel and coprecipitated methods arises due to the difference in a couple of factors. Ceramics prepared by solid state reaction have compositional variation and inhomogeneous distribution of impurities whereas the ceramics prepared by chemical synthesis exhibit high purity with good chemical homogeneity in the nanometer scale. Photovoltage increases with decreasing grain size as the photovoltage is effected by the number of grain boundaries [6, 13]. Increasing the number of grains by decreasing the grain size may increase the photovoltage of the samples as observed in coprecipitated and sol-gel ceramics. Enhancement in photo-induced strain for the coprecipitated sample is due to increase in photovoltage, as the piezoelectric constant of the three samples are similar. The coprecipitated ceramics exhibited the highest photovoltage and photo-induced strain, as it possesses favorable combination of smallest grain size and highest relative density. The lower relative density of ceramics prepared by sol-gel route is a major limitation of this technique.

In conclusion, chemically prepared samples has high purity and preferable properties such as higher degree of homogeneity, uniform distribution of doping and stoichiometric compositions. The atomic level interaction and mixing in chemical synthesis resulted in smaller grain size and lower sintering temperature. As a result the ceramics prepared by sol-gel and coprecipitated techniques exhibit better photovoltaic and photostrictive properties as compared to the oxide mixing process.

ACKNOWLEDGMENTS

One of the authors (P. Poosanaas) would like to acknowledge the Royal Thai Government and Dr. Harit Sutabutr from the National Metal and Materials Technology Center (Thailand) for granting MOSTE fellowship.

REFERENCES

1. K. Uchino and M. Aizawa, Jpn. J. Appl. Phys., **24**, 139 (1985).
2. K. Uchino, Innovations Mater. Res., **1(1)**, 11 (1996).
3. S. Y. Chu and K. Uchino, J. Adv. Performance Mater., **1**, 129 (1994).
4. M. Taminura and K. Uchino, Sensors and Materials, **1**, 47 (1988).
5. K. Nonaka, M. Akiyama, A. Takase, T. Baba, K. Yamamoto, and H. Ito, J. Mater. Sci. Lett., **15**, 2096 (1996).
6. T. Sada, M. Inoue, and K. Uchino, J. Ceram. Soc. Jpn. Inter. Ed., **95**, 499 (1987).
7. P. Poosanaas, A. Dogan, A. V. Prasadarao, S. Komarneni, and K. Uchino, J. Electroceramics, **1(1)**, 111 (1997).
8. B. S. Chiou, J. N. Kno, and H. T. Dai, J. Elec. Mater., **19(4)**, 393 (1990).
9. Y. Yoshikawa, K. Tsuzuki, and T. Kobayashi, and A. Takagi, J. Mater. Sci., **23**, 2729 (1988).
10. J. Thomson, Ceram. Bull., **53(5)**, 421 (1974).
11. J. H. Choy, Y. S. Han, and J. T. Kim, J. Mater. Chem., **5(1)**, 65 (1995).
12. M. Murata, K. Wakino, K. Tanaka, and Y. Hamakawa, Mat. Res. Bull., **11**, 323 (1976).
13. P. S. Brody and B. J. Rod, Integrated Ferroelectrics, **2**, 1 (1992).

Figure captions

Fig. 1. Flow diagram of sample preparation by conventional oxide mixing process.

Fig. 2. Flow diagram of sample preparation by sol-gel technique.

2-MOE: 2-methoxyethanol. $Ti(OPr)_4$: Titanium (IV) isopropoxide.

$Zr(OBt)_4$: Zirconium (IV) butoxide. $W(OEt)_6$: Tungsten (VI) ethoxide.

Fig. 3. Flow diagram of sample preparation by coprecipitation technique.

$Pb(NO_3)_2$: Lead nitrate, $La(NO_3)_3 \cdot 6H_2O$: Lanthanum nitrate,

$ZrOCl_2 \cdot 8H_2O$: Zirconium oxychloride, $TiCl_4$: Titanium tetrachloride.

$Na_2WO_4 \cdot 2H_2O$: Sodium tungstate

Fig. 4. Experimental set up for photovoltaic and photostrictive measurement.

Illumination

- High pressure mercury lamp
- Without polarizer
- Filter - IR blocking filter
  - Bandpass filter
- Wavelength - 366 nm
- Intensity - 3.25 mW/cm^2

Fig. 5. TGA-DTA curves for the as-dried precipitate of PLZT.

Fig. 6. X-ray diffraction patterns of PLZT derived from coprecipitation technique.

Fig. 7. Relative density as a function of sintering temperature after 2 h sintering time.

Fig. 8. Relative density of coprecipitated PLZT ceramics as a function of sintering time (at 1150 °C)

Fig. 9. SEM micrographs of 0.5 at.% WO_3 doped PLZT ceramics prepared by (a) conventional oxide mixing process (b) sol-gel technique and (c) coprecipitation technique

Fig. 10. Dielectric constant of 0.5 at.% WO_3 doped PLZT ceramics as a function of temperature at 1 kHz.

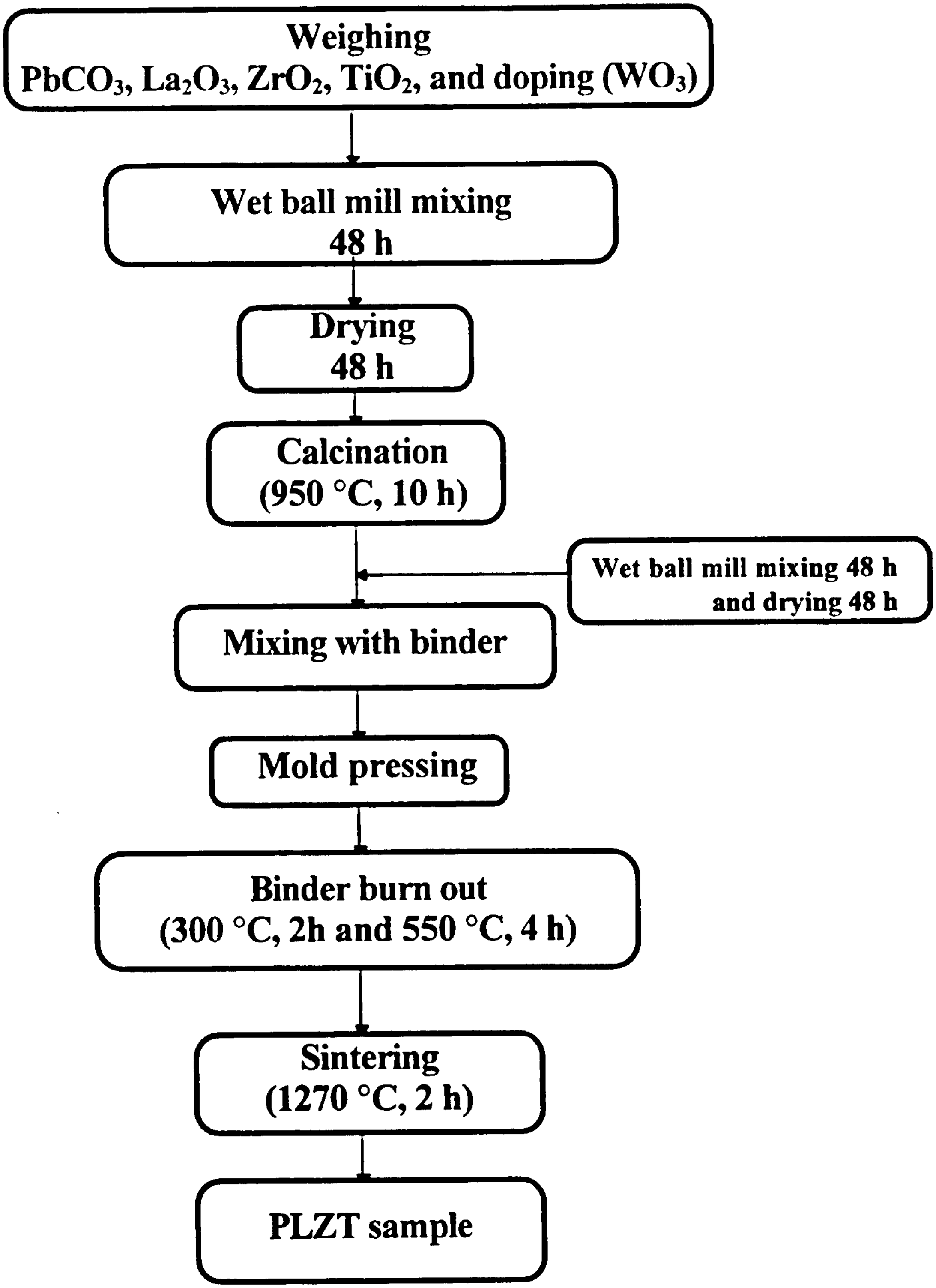
Weighing
$PbCO_3$, La_2O_3, ZrO_2, TiO_2, and doping (WO_3)
Wet ball mill mixing
48 h
Drying
48 h
Calcination
(950 °C, 10 h)
Wet ball mill mixing 48 h
and drying 48 h
Mixing with binder
Mold pressing
Binder burn out
(300 °C, 2h and 550 °C, 4 h)
Sintering
(1270 °C, 2 h)
PLZT sample

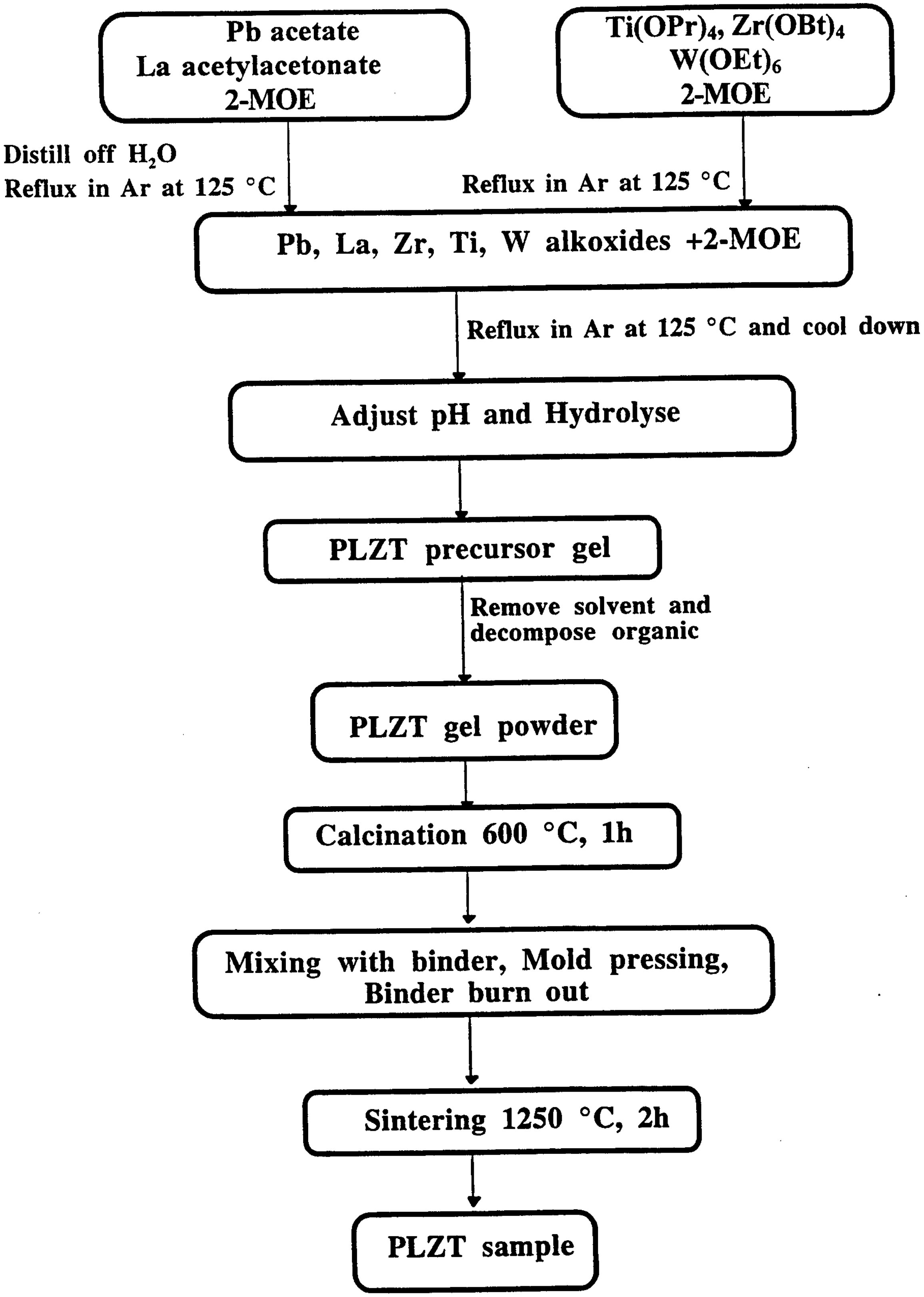
Pb acetate
La acetylacetonate
2-MOE
Ti(OPr)$_4$, Zr(OBt)$_4$
W(OEt)$_6$
2-MOE
Distill off H_2O
Reflux in Ar at 125 °C
Reflux in Ar at 125 °C
Pb, La, Zr, Ti, W alkoxides +2-MOE
Reflux in Ar at 125 °C and cool down
Adjust pH and Hydrolyse
PLZT precursor gel
Remove solvent and decompose organic
PLZT gel powder
Calcination 600 °C, 1h
Mixing with binder, Mold pressing, Binder burn out
Sintering 1250 °C, 2h
PLZT sample

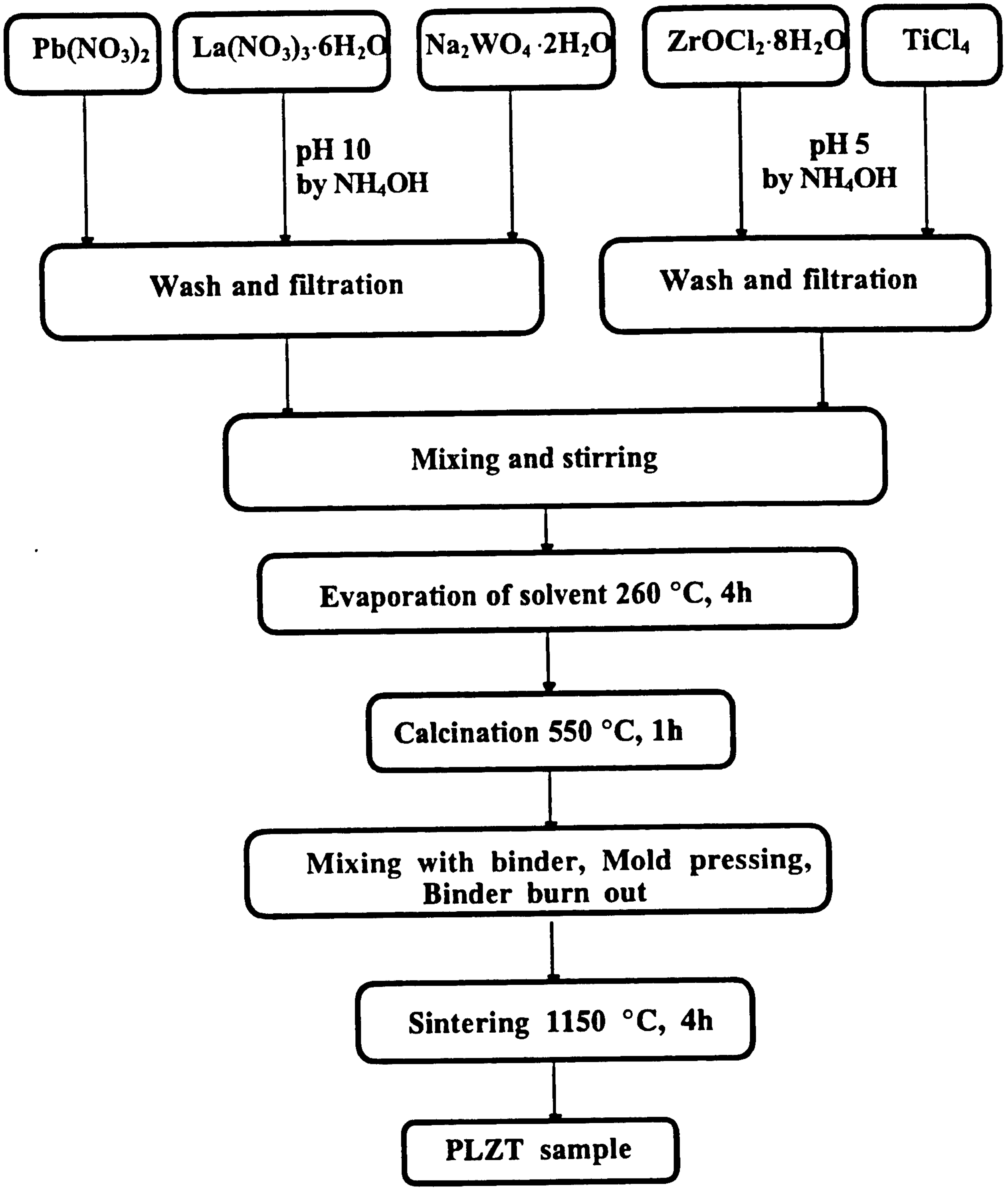
$Pb(NO_3)_2$
$La(NO_3)_3 \cdot 6H_2O$
$Na_2WO_4 \cdot 2H_2O$
$ZrOCl_2 \cdot 8H_2O$
$TiCl_4$
pH 10 by NH_4OH
pH 5 by NH_4OH
Wash and filtration
Wash and filtration
Mixing and stirring
Evaporation of solvent 260 °C, 4h
Calcination 550 °C, 1h
Mixing with binder, Mold pressing, Binder burn out
Sintering 1150 °C, 4h
PLZT sample

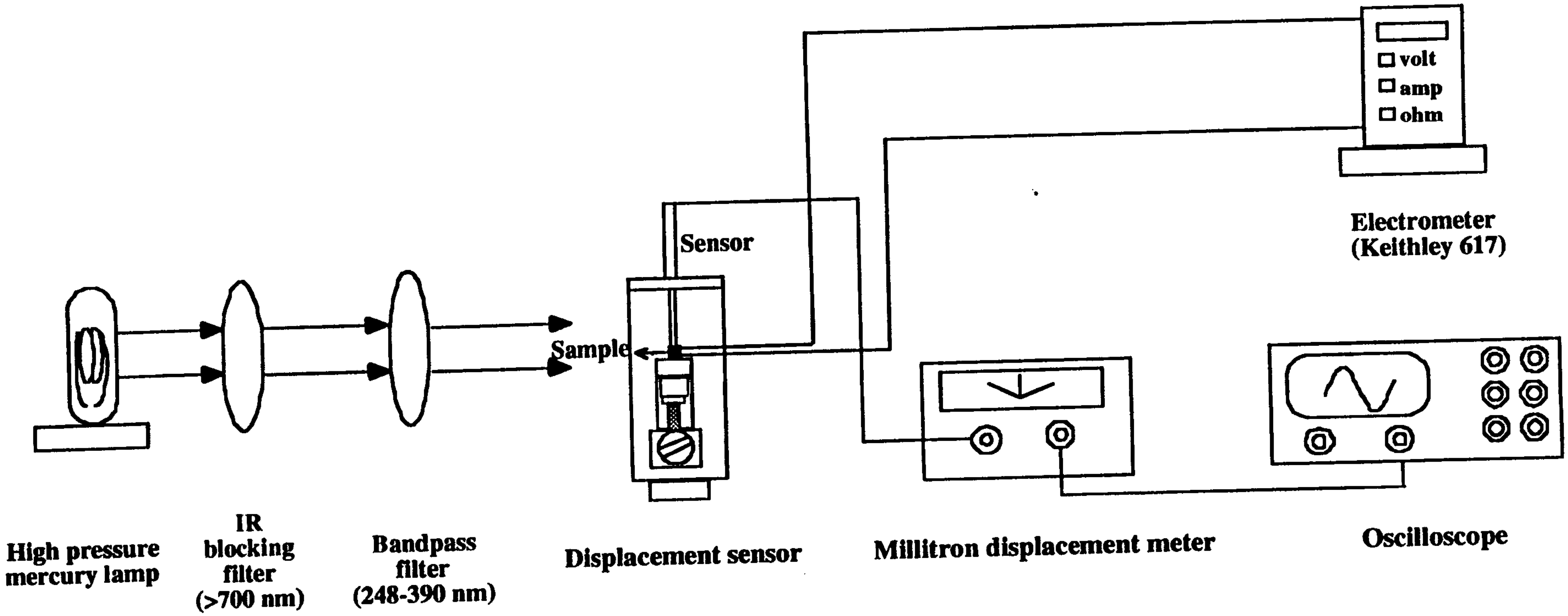
Sensor
Sample
☐ volt
☐ amp
☐ ohm
Electrometer
(Keithley 617)
High pressure
mercury lamp
IR
blocking
filter
(>700 nm)
Bandpass
filter
(248-390 nm)
Displacement sensor
Millitron displacement meter
Oscilloscope

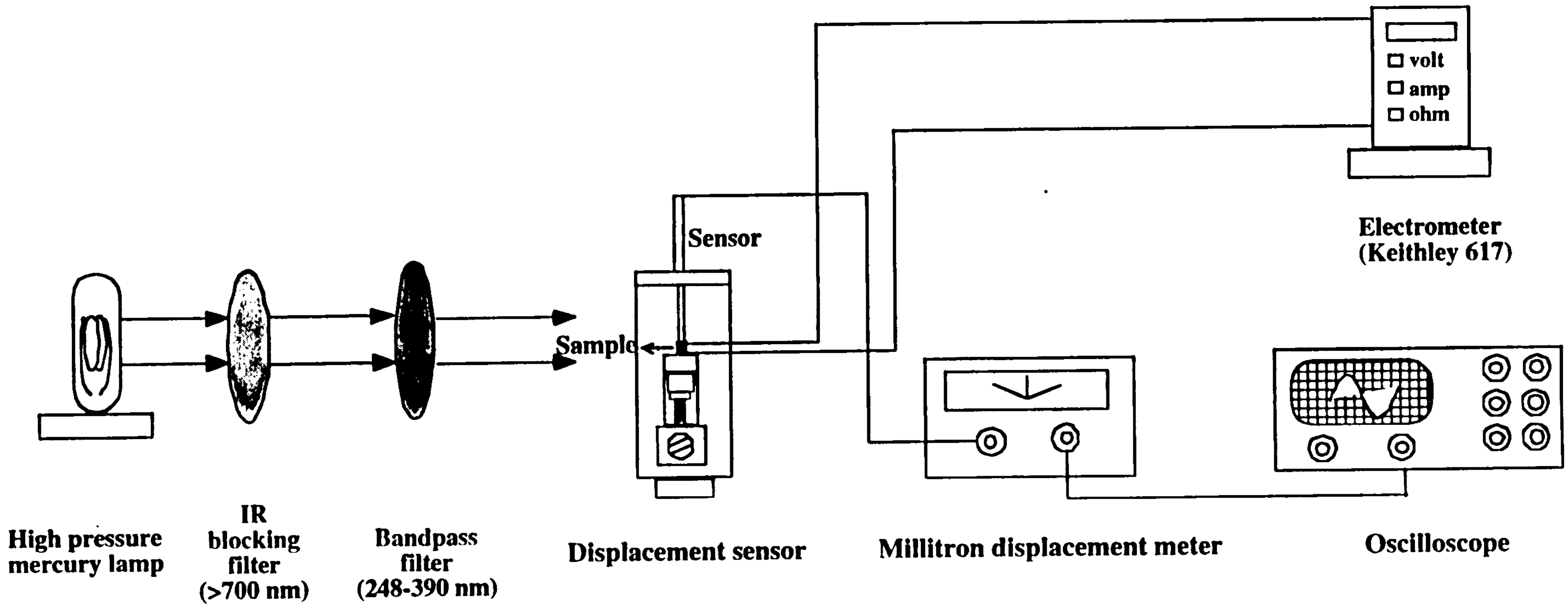
Electrometer
(Keithley 617)
volt
amp
ohm
Sensor
Sample
High pressure mercury lamp
IR blocking filter (>700 nm)
Bandpass filter (248-390 nm)
Displacement sensor
Millitron displacement meter
Oscilloscope

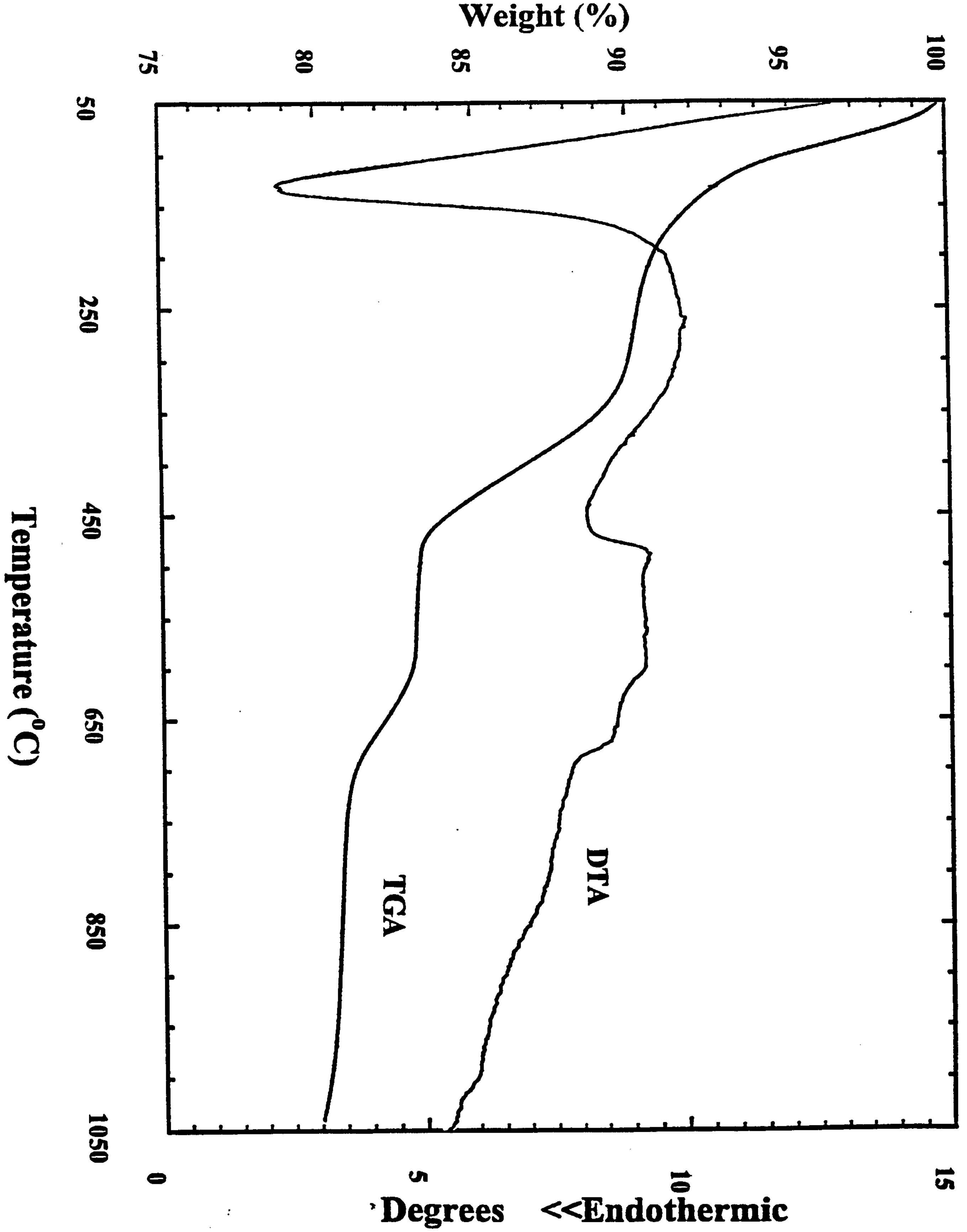
Weight (%)
75
80
85
90
95
100
50
250
450
650
850
1050
Temperature (°C)
0
5
10
15
Degrees <<Endothermic
DTA
TGA

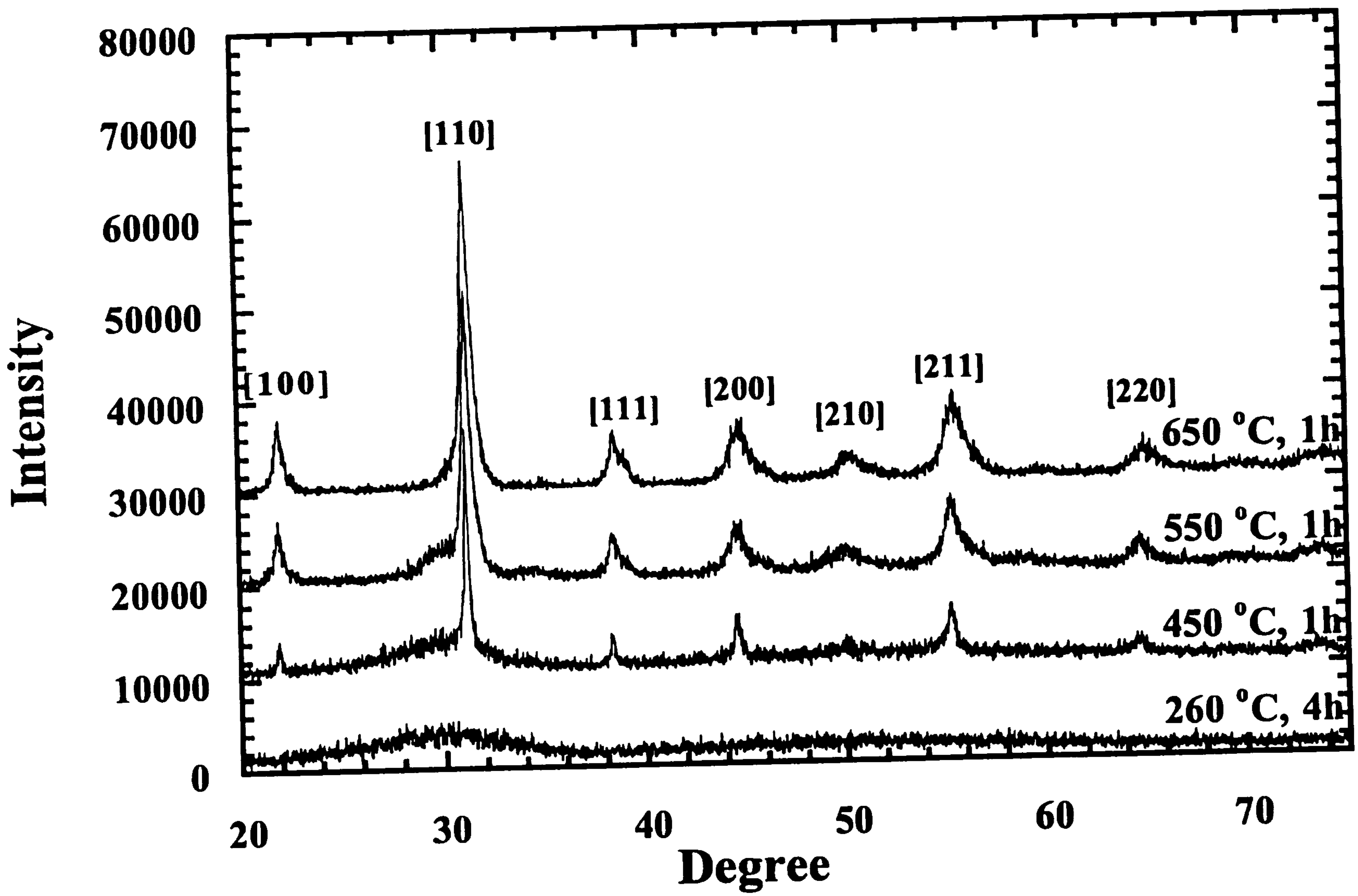

Intensity
80000
70000
60000
50000
40000
30000
20000
10000
0
20
30
40
50
60
70
Degree
[100]
[110]
[111]
[200]
[210]
[211]
[220]
650 °C, 1h
550 °C, 1h
450 °C, 1h
260 °C, 4h

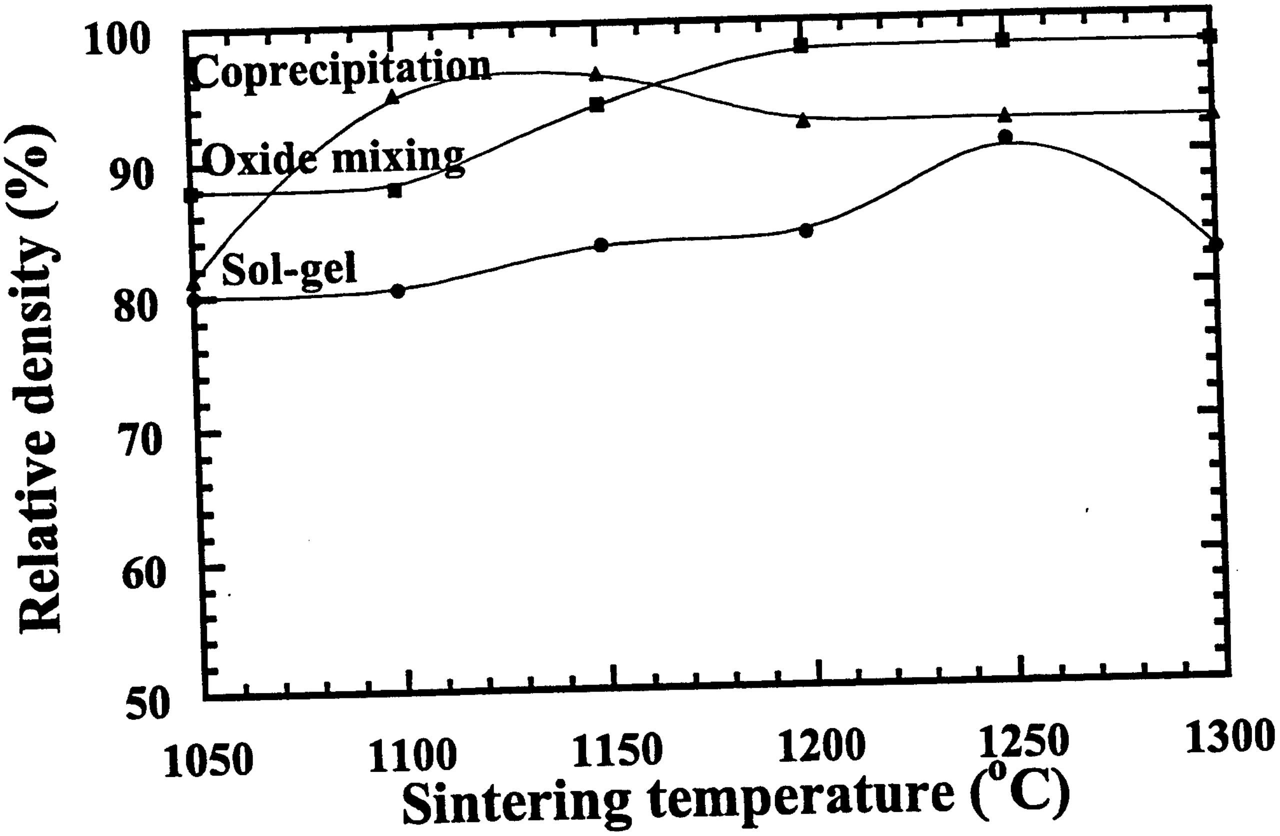
Coprecipitation
Oxide mixing
Sol-gel
Relative density (%)
100
90
80
70
60
50
1050
1100
1150
1200
1250
1300
Sintering temperature (°C)

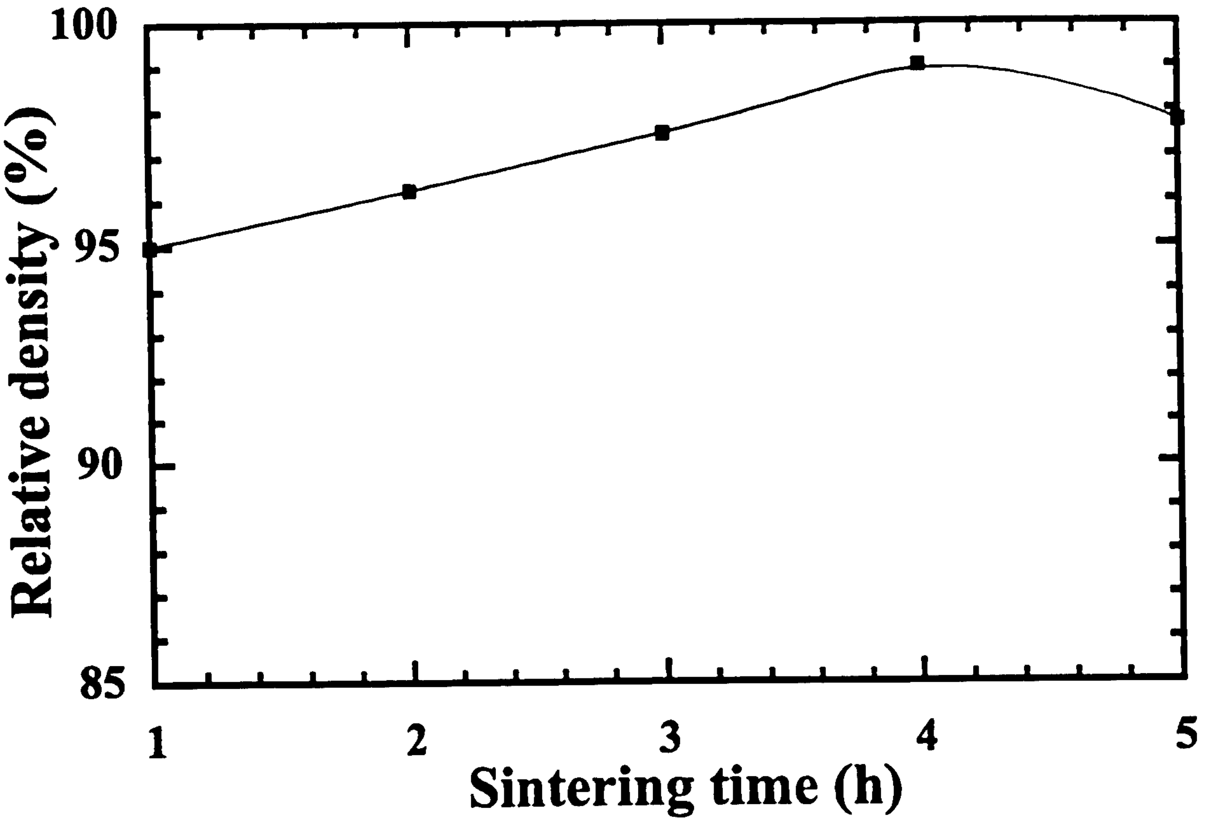

100
95
90
85
Relative density (%)
1
2
3
4
5
Sintering time (h)

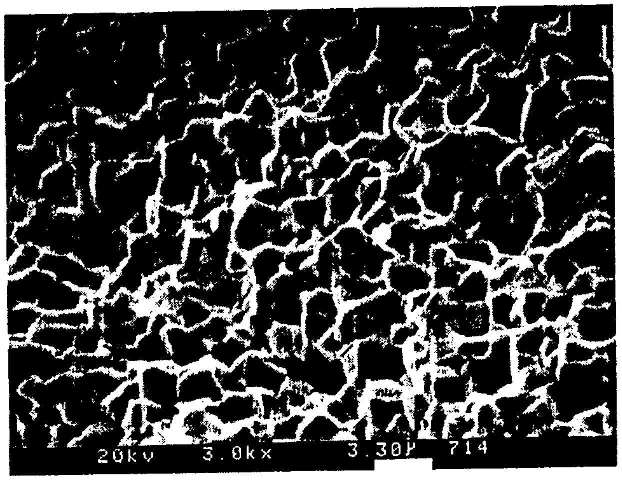
20kv 3.0kx 3.30µ 714

(a)

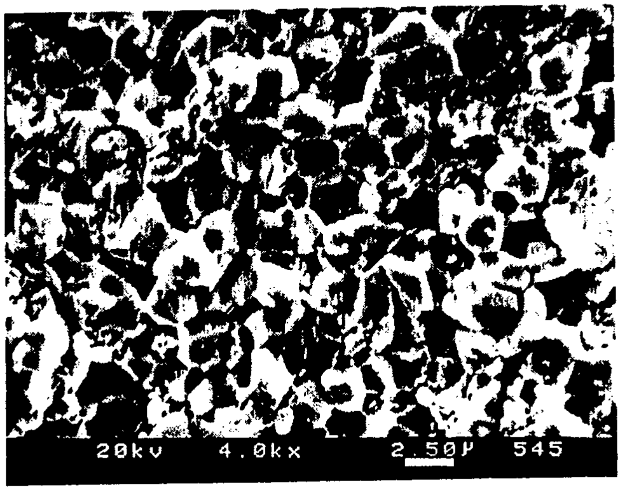
20kv 4.0kx 2.50µ 545

(b)

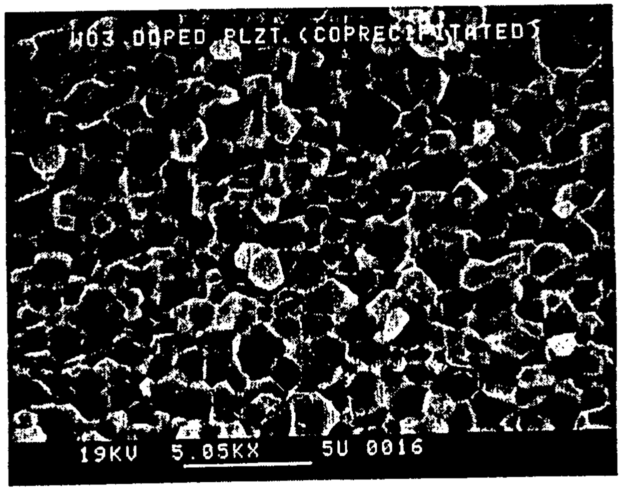
WO3 DOPED PLZT (COPRECIPITATED)
19KV 5.05KX 5U 0016

(c)

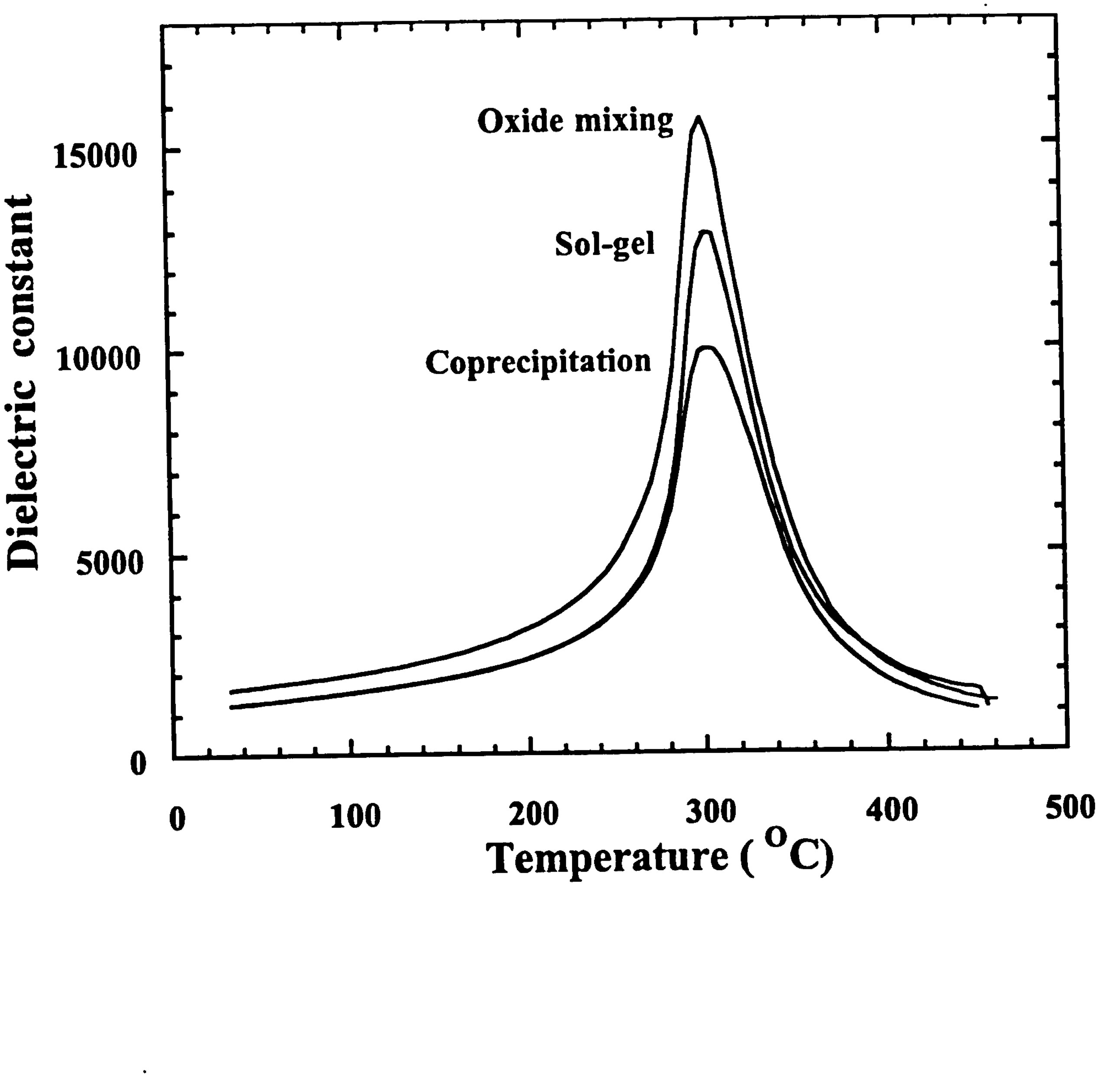
Oxide mixing
Sol-gel
Coprecipitation
Dielectric constant
15000
10000
5000
0
0
100
200
300
400
500
Temperature (^{O}C)

Table 1: Comparison of ceramics derived from three different processing techniques.

Conditions/properties	Conventional Oxide mixing process	Sol-gel technique	Coprecipitation technique
Calcination	950 °C, 10h	600 °C, 1h	550 °C, 1h
Sintering	1270 °C, 2h	1250 °C, 2h	1150 °C, 4h
Maximum relative density (%)	98%	93%	99%
Average grain size (µm)	1.87±0.08	1.72±0.06	1.12±0.05
Piezoelectric constant d_{33} (x 10^{-12} m/V)	320	315	310
Curie temperature (°C)	300	299	299
Maximum dielectric constant	15200±200	12700±100	10000±100
Room temperature dielectric constant	1600±30	1235±20	1220±20
Photovoltage, E_{ph},* (V/cm)	1500	1650	2010
Photocurrent (nA/cm) *	1.7	2.48	2.50
Photoinduced strain * (x 10^{-5})	4.50	4.94	6.10
Calculated (d_{33} x E_{ph})	4.80	5.20	6.23

* For the illumination intensity 3.25 mW/cm^2

APPENDIX 67

OPTICAL MICROACTUATION IN PIEZOCERAMICS

[1]Sarita Thakoor[a], P. Poosanaas[c], J. M. Morookian[a], A. Yavrovian[a], L. Lowry[a],
N. Marzwell[a], J. Nelson[b], R. R. Neurgaonkar[b], and Kenji Uchino[c]

[a]Jet Propulsion Laboratory, California Institute of Technology, PASADENA, CA 91109
[b]Rockwell Science Center, Thousand Oaks, CA 91360
[c]Pennsylvania State University, University Park, PA 16802

ABSTRACT:

Optically/electrically operable flexible film microactuators that can offer upto two orders higher efficiency of photonic to mechanical conversion compared to ceramic actuators are conceptualized. A polarized ceramic wafer of non-centrosymmetric perovskite ferroelectric ABO_3 compounds, such as lead lanthanum zirconate titanate (PLZT), when exposed to an illumination (~350 to 400 nm wavelength) close to the bandgap energy, can generate a large photovoltage (~1.0 kV/mm) across its length, and by the inverse piezoelectric effect cause the piezoceramic wafer to deflect in the direction away from the illumination. The optical actuation effect in piezoceramic wafers is investigated as a function of thickness, composition, and surface roughness. Such flexible microactuators would enable a new generation of micro-electro-mechanical and micro-opto-mechanical systems where the actuation will not be restricted by the clamping effect due to the rigid substrate as in the current silicon based micromachined structures. To deposit the piezoceramic film directly onto a flexible substrate, the substrate must have high temperature stability, high strength (Young's Modulus ~ 4.9×10^{10} N/m^2), a close match of thermal coefficients of expansion with the piezoceramic film, and a tailorable crystal orientation in order to provide a desired template for growth of oriented PLZT.
This paper also presents a comparison of a variety of flexible substrate films and fibers and our recent results on polybenzoxazole (PBO), a polymeric candidate for a flexible high temperature substrate. Variation of the properties of PBO as a function of temperature are also presented.

1. INTRODUCTION

Optically/electrically operable "flexible actuators" that can offer upto two orders higher efficiency of photonic to mechanical conversion are conceptualized[1,2]. A polarized ceramic wafer of non-centrosymmetric perovskite ferroelectric ABO_3 compounds, such as lead lanthanum zirconate titanate (PLZT), when exposed to an illumination (~350 to 400 nm wavelength) close to the bandgap energy, can generate[3] a large photovoltage (~1.0 kV/mm) across its length, and by the *inverse piezoelectric* effect cause the piezoceramic wafer to deflect in the direction away from the illumination. The hypothesis is that if the

---

[1] Further Author Information:
Sarita Thakoor (correspondence): Email: sarita.thakoor @ jpl.nasa.gov; Telephone: (818) 354-0862;
MS 303-308, Jet Propulsion Laboratory, 4800 Oak Grove Drive, Pasadens, CA 91109

absorption of the illumination occurs in at the most ~ tens of microns thick surface layer of the piezoelectric material facing the illumination, the photovoltage generation is expected[3] to be entirely located in this thin top skin layer. Using a film thickness equal to this penetration depth ensures that the entire film is active. In a ceramic typically ~ 200 micron thick, almost 90 % of the bulk is an inactive mass to be bent/deflected. In films, therefore using the analytical treatment for electrically operated bimorphs used by Moulson[4], we expect the deflection to be ~ 500 times larger. This arises because of the 100 times lower thickness and the 5 times higher electrical field strength.

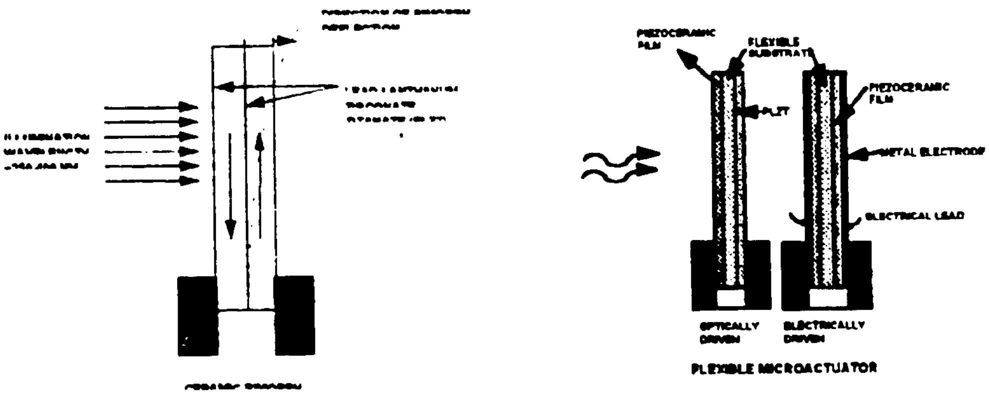

ceramic thickness: 200 micron
(a)

film thickness: 2 micron
(b)

Figure 1

Figure 1a and figure 1b compare a ceramic bimorph and a flexible film bimorph.
The table 1 shows the projected parameters of improvement. The numbers in this table are calculated based on using a 200 micron thick typical ceramic wafer as the current state of the art and a 2 micron thick film as the projected flexible film bimorph. Such a film bimorph activated with 5 V will have~ 25 times higher[1,2,5] energy density than the ceramic bimorph that requires ~ 100 V. In turn, although the net force output from the bimorph will be 20 % of that from the ceramic, the force /volume will be five times higher. Correspondingly, in the case of optical actuation, the film bimorph is projected to deliver force output 2-20 times that of the ceramic due to the enhancement in conversion efficiency (expected value ~ 1% - 10%). This is expected with illumination intensity an order magnitude lower than that currently used for the ceramics. This will result in an enhancement of force per unit power by 20 to 200 times. Obtaining the optical performance enhancement in input photonic power to output mechanical force will provide a substantially enhanced flexible film actuator as indicated. Demonstration of this matrix of improvement will set the foundation for photonic control of mechanical motion and flexible actuators.

TABLE 1: COMPARISON OF BULK PIEZOCERAMIC ACTUATOR WITH PROJECTED PERFORMANCE OF FLEXIBLE FILM ACTUATOR

		Current Status Ceramic Actuator	Projected Improvement Film Actuator
ELECTRICAL ACTUATION PARAMETERS	**Thickness**	**200 microns**	**2 microns: Thickness reduced, material tailored**
	Operating Voltage	**100 V**	**5 V : Operational voltage reduced**
	Energy Density	**1X**	**25 X : Inherent advantage of reduced thickness**
	Deflection	**1X**	**500X enhancement for film actuator**
	Force/Volume	**1X**	**5X enhancement for film actuator**
OPTICAL ACTUATION PARAMETERS	**Optical Power**	**80 mW/cm^2**	**8 mW/ cm^2 : Illumination Intensity**
	Power Ratio	**10X**	**1X**
	Photonic to Mechanical Conversion Efficiency	**0.1%**	**1% - 10% : significant enhancement in overall efficiency**
	Force/Energy	**1X**	**2X to 20X : Multifold enhancement in the film actuator**
	Force/Power	**1X**	**20X to 200X**

2. WIDE APPLICATION DOMAIN

The applications[1,2,6] of the optical actuation effect could be classified into two broad classes:

1. Microactuation &
2. Microsensing

This direct conversion of photonic to mechanical motion will lead to following potential applications:

a. optical shape control of structures

b. a new alternative mechanism for converting solar energy directly into mechanical motion for planetary exploration (for example on Mars where conversion devices that can be operated from the low cryogenic temperature ~ -125°C to + 55°C are required. Piezoceramic based this novel converter will be uniquely suited for such operational cycling with its wide temperature range of operation and excellent cyclability)

c. direct corrective control in adaptive optics/interferometry,

d. optical micropositioning,

e. solar tracking actuator/shutter for self alignment of the spacecraft to the sun for optimal power generation or station keeping using solar sails,
f. optically controlled valves for medical as well as space applications,
g. photophones, that convert flashes of light directly into sound
h. optically controlled microrobots

On the other hand, potential microsensing applications include:

a. a variety of tunable sensors for incident radiation (UV, visible etc.) based on a direct calibration of the deflection as a function of incident radiation intensity, and
b. indirect microsensors based on calibration of the photodeflection in presence of the device "loading" (e.g. change in the deflection when the device is "loaded" with condensing moisture (microhygrometer) or incident interstellar dust (microbalance)).

3. EXPERIMENTAL PROCEDURE:

PLZT (3/52/48) ceramics with 3 at % La and a Zr/Ti ratio of 52/48 and 0.5 at.% WO_3 as dopant were prepared by the conventional oxide mixing process, where $PbCO_3$, La_2O_3, ZrO_2, TiO_2 and dopants (WO_3) were mixed in the proper ratio and ball milled for 48 h. Subsequently, the slurry was dried, calcined at 950°C for 10 h, and sintered at 1270°C for 2 h. The detail of the process has been reported by Poosanaas et al[7].

PLZT samples were cut to the standard size of 4x5 mm^2 with various thickness 50 µm -1 mm. Samples were polished, electroded with silver paste and electrically poled along the length (5 mm) direction in silicone oil at 120°C under a 2 kV/mm for 10 min. Photovoltaic measurements were done by using a high-input-impedance electrometer (Keithley 617) while the photostriction was measured by a displacement sensor (LVDT, Millitron model 1301). A high pressure mercury lamp (Ushio Electric USH-500D) was used as a light source. The lamp radiation was passed through an IR blocking filter and a UV bandpass filter to obtain a monochromatic beam with a maximum strength around 370 nm wavelength. The 4x5 mm^2 polished surface of the sample was illuminated. The experimental set-up for photovoltaic and photostrictive measurements was reported in an earlier paper al[7,8].

Bimorph and unimorph samples are illuminated on either of their faces by ultra-violet light. The samples are clamped at one end. The displacement that results at the far end of the cantilever formed by the body of the sample itself is measured by an optical deflection measurement and/or an eddy current sensor.

The optical deflection measurement is accomplished by affixing to the free end of the sample a thin mirrored glass slide. A He-Ne laser beam is directed onto the mirror at an angle, and a spot from the deflected beam is observed on a grid several meters from the sample. When the sample flexes due to UV radiation, the change in the angle of the sample surface to the He-Ne beam is observed as a displacement of the observed spot (magnified by the large distance arm of the observation grid). This serves as a good visual measure of the displacement, although the accuracy of measurement in terms of deflection and time dynamics measurement is limited to ~ 25 microns and visual discrimination.

The eddy current sensor measurement offers a much higher resolution ~ 2 microns and could allow in conjunction with a fast switch, time dynamics study of the temporal response down to fraction of a microsecond since the contact less electronic measurement does not load the sample mechanically. The sample is prepared by affixing a small square of aluminum foil to the free end of the sample so as to form a suitable target for the eddy current sensor. When the sample flexes due to UV radiation, the foil target is moved toward or away from the eddy current sensor. This displacement causes a change in the inductive field and consequently a change in voltage from the sensor which is recorded by an oscilloscope, allowing fast displacements to be observed and recorded.

4. RESULTS

i. Investigation of flexible substrates:

To deposit the piezoceramic film directly onto a flexible substrate, the substrate must have high temperature stability, high strength (Young's Modulus ~ 4.9×10^{10} N/m^2), a close match of thermal coefficients of expansion with the piezoceramic film, and a tailorable crystal orientation in order to provide a desired template for growth of oriented PZT. Earlier work has shown[9] that ferroelectric PZT could be crystallized at ~ 550°C. Recently[10] polybenzoxazole (PBO) has been validated at JPL to work well up to ~ 550°C and extensively characterized for operation at 460°C. Table 2 & 3 provide a comparison of a variety of substrate films and fibers. PBO stands out as the leading candidate for its high tensile strength, high Young's Modulus, low heat shrinkage and coefficients of thermal expansion and hygroscopic expansion to provide such a high temperature substrate for forming flexible microactuators by this technique. PBO is a conjugated aromatic heterocyclic liquid crystalline polymer (LCP) with a chemical structure as shown in Figure 2.

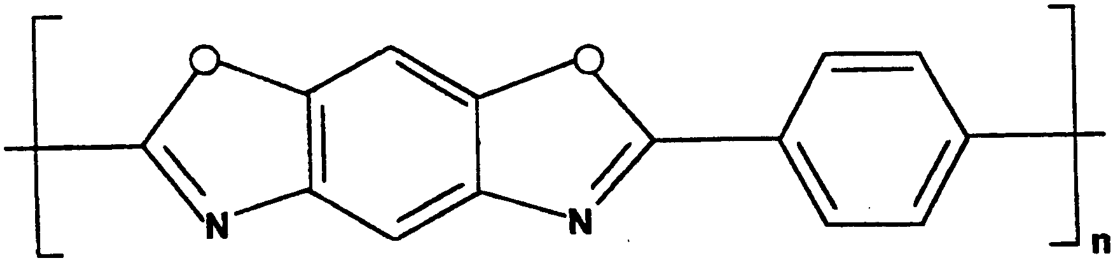

CIS-PBO

Figure 2. Chemical Structure of PBO

PROPERTY	UNIT	KAPTON	ARAMID	PET	PEN	PBO
DENSITY	g/cm³	1.420	1.500	1.395	1.355	1.54
MELTING TEMP	°C	NONE	NONE	263	272	NONE
GLASS TRANSITION TEMP	°C	350	280	68	113	NONE
YOUNG'S MODULUS	kg/mm²	300	1000-2000	500-850	650-1400	4900
TENSILE STRENGTH	kg/mm²	18	50	25	30	56-63
TENSILE ELONGATION	%	70	60	150	95	1-2
LONG-TERM HEAT STABILITY	°C	230	180	120	155	>300
HEAT SHRINKAGE (200°C x % min)	%	0.1	0.1	5-10	1.5	<0.1
COEFFICIENT OF THERMAL EXPANSION	ppm/°C	20	15	15	13	-2
COEFFICIENT OF HYGROSCOPIC EXPANSION	ppm/% RH	20	18	10	10	0.8
MOISTURE ABSORPTION	%	2.9	1.5	0.4	0.4	0.8

Table 2: Comparison of a variety of polymeric films

PROPERTY	PBO	PBO HIGH MODULUS	ARAMID	STEEL	SPECTRA® (HDPE)	CARBON (HI-TENSILE)	GLAS (S-2)
TENSILE STRENGTH (ksi)	820	800	400-500	250	435	500-700	665
TENSILE MODULUS (Msi)	25-30	40-45	10-25	29	25	30-40	12.6
COMPRESSIVE STRENGTH (ksi)	40	65	65	250	10	300-400	>150
ELONGATION, BREAK (%)	3.0	1.5	1.5-4.0	2.0	3.5	1.5-2.0	5.4
DENSITY (g/cc)	1.56	1.56	1.44	7.86	0.97	1.8-1.9	2.4
SPECIFIC TENSILE STRENGTH (ksi)	525	510	280-350	32	450	270-380	280
SPECIFIC TENSILE MODULUS	16	26	7-18	4	26	16-22	5
LIMITING OXYGEN INDEX (LOI: %)	56	56	30		19	50-65	

Table 3: Comparative data for high performance fibers

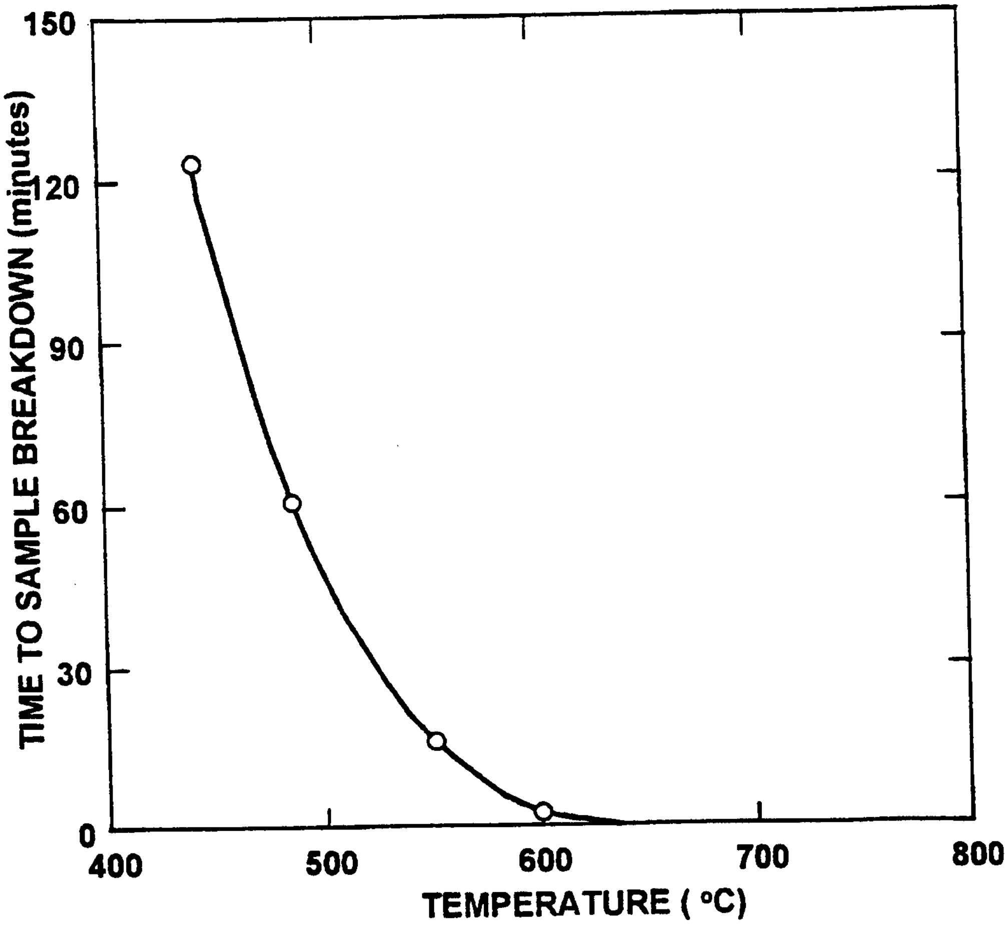

Figure 3: Time to sample breakdown of PBO as a function of temperature

The chemical synthesis of PBO results in a LCP solution that is processed to fiber or film by various techniques. The high strength and superior physical properties of PBO are due to the rod-like nature of the PBO molecule (Figure 3) and the orientation that can be built into the Polymer film. PBO film's self-reinforcing microstructure results in a "molecular fabric" with properties comparable to those of advanced, fiber-reinforced materials, but without the drawbacks of distinct fiber and matrix components. This polymer has no melting point or glass transition temperature.

In conclusion, this comparative analysis suggests that PBO in general is a good candidate for flexible substrates. Figure 3 further shows the dependence of time to PBO sample breakdown as a function of temperature. It is clear, that this substrate is stable for extensive operation at temperatures of 460°C or lower. Therefore, to deposit an active film of PLZT, another challenge needs to be overcome. The crystallization temperature of the piezoceramic film needs to be brought down to about 450°C or the crystallization be obtained by very rapid bursts of high temperatures through rapid laser annealing.

ii. Crystallization Temperature for PZT:

Figure 4 shows the X-ray diffraction patterns of a PZT(52/48) thin film mounted on the hot stage of a Siemens Allis D-500 diffractometer taken progressively at temperatures from

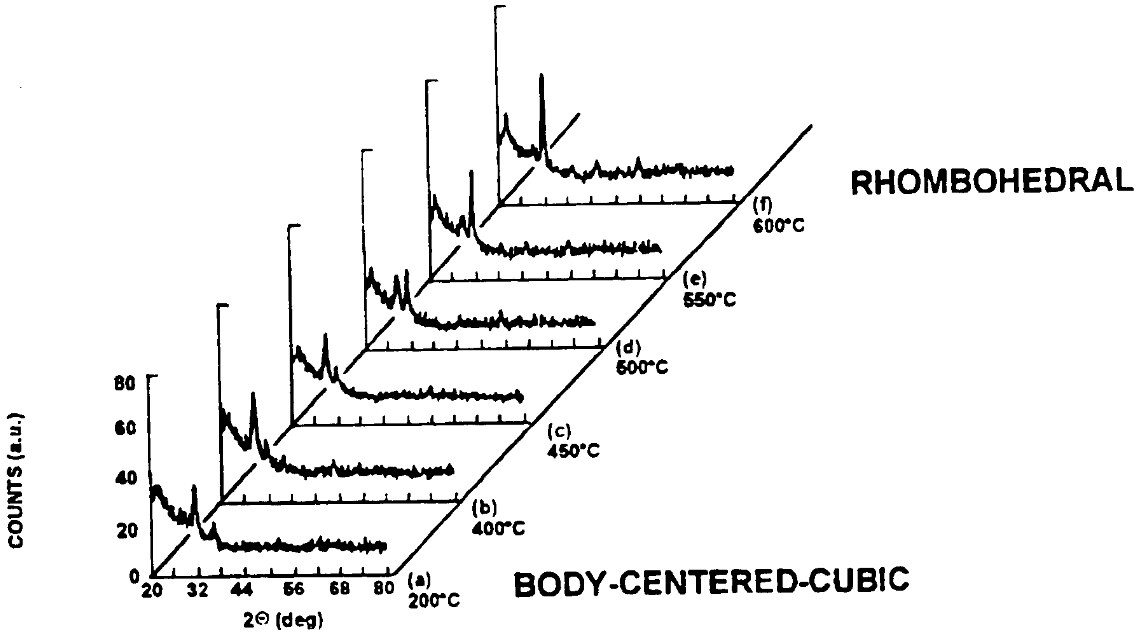

Figure 4: X-Ray Diffraction Patterns From A PZT Film Annealed In Air At Different Temperatures

200°C to 600°C. The x-ray diffraction study was performed in reflection mode using CuKα radiation. As deposited, the film exhibits predominantly the lead structure. In fig. 4, the x-ray pattern at 200°C still predominantly shows all the lead lines. However, at about 400°C the solid state reaction leading to formation of the lead oxides initiates, as is indicated by the appearance of the (111) line. At about 550°C, the reaction completes to give the rhombohedral phase of lead zirconate titanate, as is evident from the comparison in Fig 3. The additional appearance of the (100) line of the rhombohedral phase signifies this transition clearly. Therefore, it is apparent that in-order to deposit the piezoceramic thin films on PBO (which has been demonstrated to operate repeatably at the highest temperature of 460° C), the crystallization temperature of PZT needs to be brought down by another 100 C. Further, for large structures stretched aircraft grade aluminum foils have worked[11] better than coated polymeric films such as mylar. Therefore, keeping in mind the application of shape control in structures, metallic foil of platinum is being used for this work. The technology for depositing piezoceramic thin films on platinum thin films is known and therefore can be more rapidly transitioned to obtain optimized optically actuating thin films on flexible platinum foils.

iii. Optical actuation as function of sample thickness of PLZT Ceramics:

When a sample is illuminated, the incident radiation is absorbed as it penetrates into the crystal lattice. The amount of light intensity reaching at the thickness 'x' of the sample is given as:

$$I(x) = TI_o e^{(-\alpha x)} \quad (1)$$

where I(x) is the light intensity at thickness 'x', I_o is the incident light intensity, T is the transmittance at the sample surface (78%), and α is the absorption coefficient of the sample.

The absorption coefficient (α) was determined by measuring incident and transmitted light intensity, using a digital power meter (Newport model 815), as a function of sample thickness.

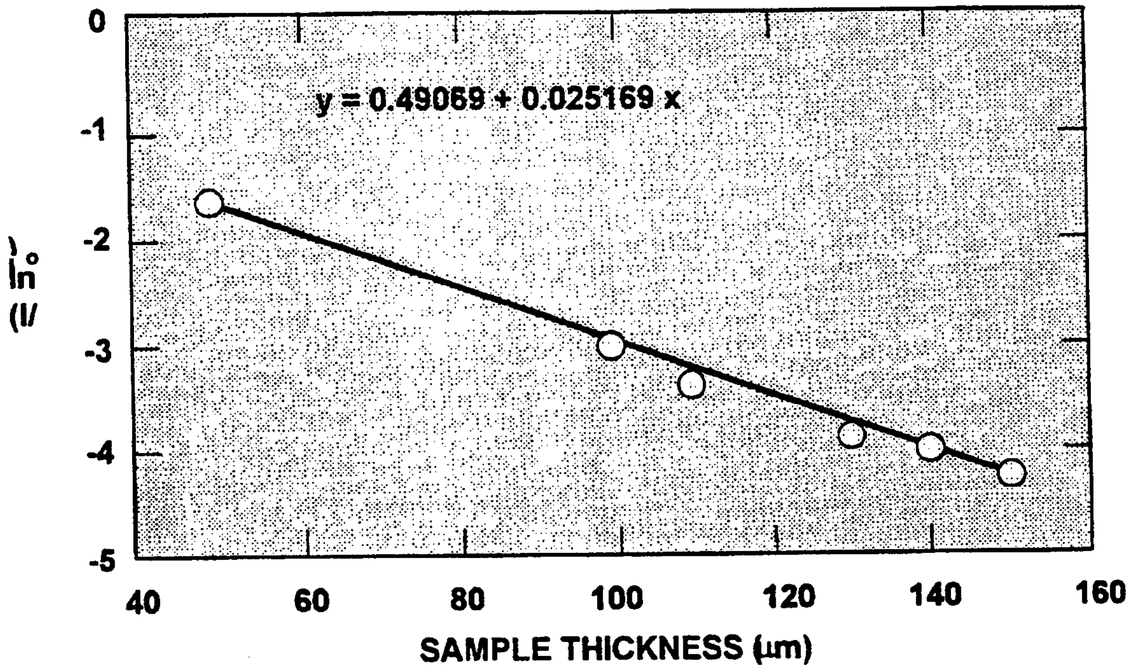

Figure 5: Light intensity as a function of sample thickness

Fig. 5 shows the plot between light intensity as a function of sample thickness. The absorption coefficient, determined from the slope of this plot was found to be 0.0252 μm^{-1}.

In case of thinner sample, there will be substantial intensity 'I' throughout the sample thickness, whereas for thick sample after some distance the intensity 'I' will be very small or negligible. The relationship between light intensity and photocurrent density formulated by Glass[12] given as:

$$J_{ph} = k\alpha I \quad (2)$$

Where J_{ph} is photocurrent density, and k is photovoltaic coefficient. It is apparent from Eq. (2), that the photocurrent will increase with the intensity of radiation, resulting in a higher photocurrent in the thinner samples As is expected, photocurrent increases (Fig. 6) with decrease in the sample thickness

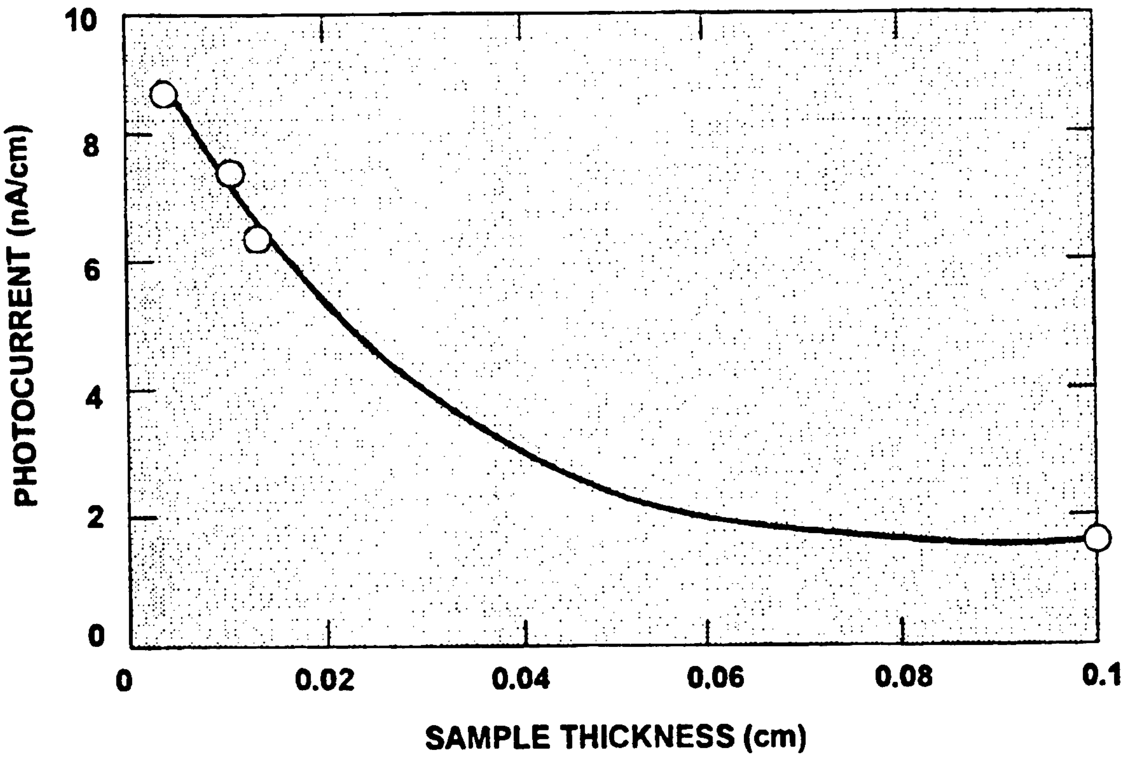

Figure 6: Photocurrent as a function of sample thickness

The relationship between sample thickness and photovoltaic response has been illustrated in Fig. 7. In this model, the absorption coefficient is assumed to be independent of light intensity and the photocurrent density is taken to be proportional to light intensity. The sample is assumed to comprise of thin slices along the thickness direction of the sample. A circuit diagram representing these layers is also shown in the same figure.

The photocurrent flowing through one of the layer of thickness 'dx', located at a distance of 'x' from the sample surface, can be obtained by combining Eq. (1) and (2):

$$di_o = wk\alpha TI_o e^{(-\alpha x)}dx \qquad (3)$$

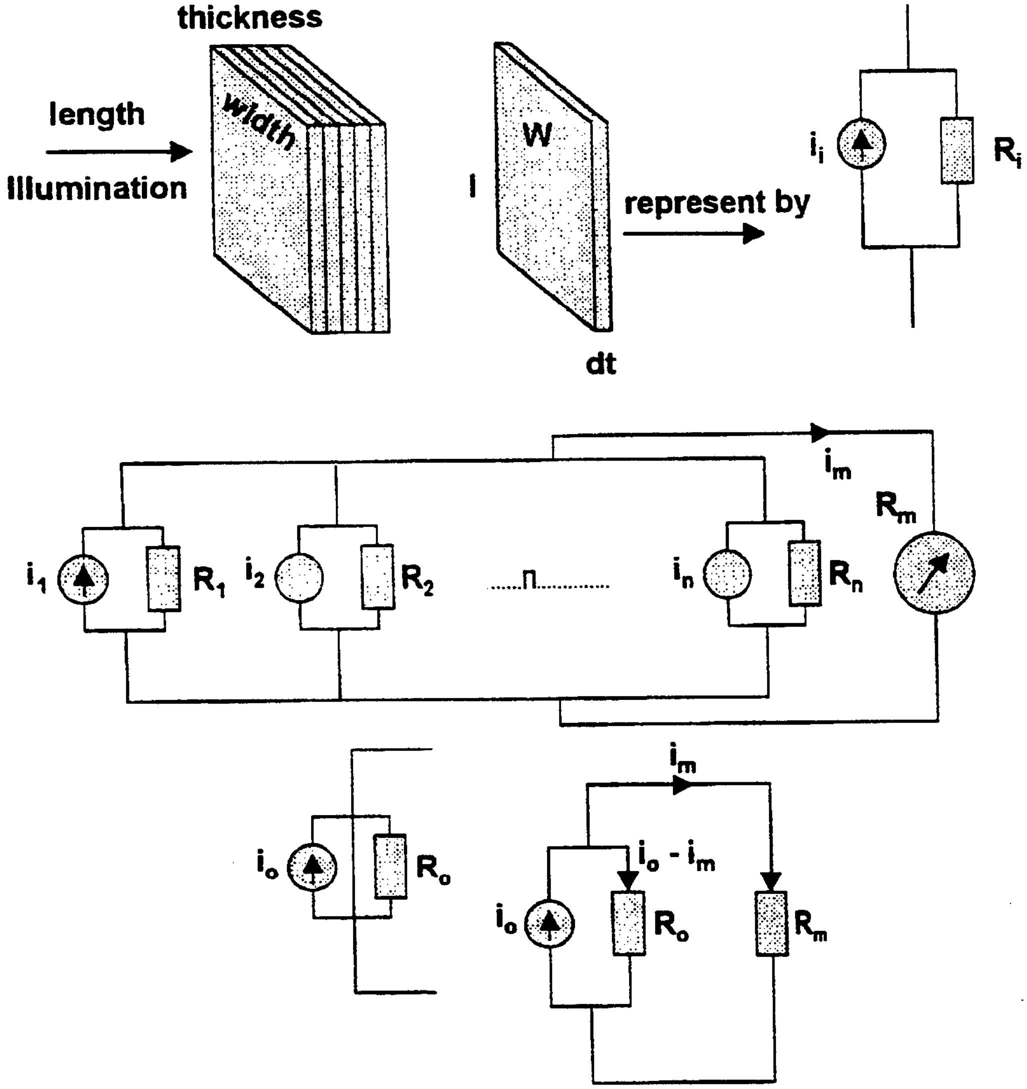

Figure 7: A proposed model for dependence of photocurrent on sample thickness

where di_n is the photocurrent in this layer and w is the sample width. The total photocurrent i_o passing through the sample can be obtained by integrating Eq. (3), over the sample thickness:

$$i_o = \int_0^t wk\alpha TI_o e^{(-\alpha x)} dx = wkTI_o\left(1 - e^{(-\alpha t)}\right) \tag{4}$$

The conductivity of this layer ($\sigma(x)$) can be expressed as a sum of dark conductivity (σ_d) and photoconductivity (σ_{ph}), given as:

$$\sigma(x) = \left(\sigma_d + \sigma_{ph} TI_o e^{(-\alpha x)}\right) \tag{5}$$

The total sample conductance (G_o) (i.e inverse of resistance) can be obtained by integrating Eq. (5), over the sample thickness

$$G_o = \frac{1}{R_o} = \int_0^t \frac{w\,\sigma(x)dx}{L} = \frac{w}{L}\left[\sigma_d t + \frac{\sigma_{ph} T I_o\left(1 - e^{(-\alpha t)}\right)}{\alpha}\right] \tag{6}$$

where L is the electrode gap (length of the sample). In order to measure the photocurrent an external load of resistance R_m was used. The sample and external load are correlated as following:

$$R_o(i_o - i_m) = R_m i_m \tag{7}$$

where i_m is the measured photocurrent and R_m is the external load (Keithley 617) resistance. The Eq. (4), (6) and (7) can be rearranged as:

$$i_m = \frac{wkTI_o\left(1 - e^{(-\alpha t)}\right)}{1 + R_m w\left(\frac{\sigma_d t}{L} + \frac{\sigma_{ph} TIo\left(1 - e^{(-\alpha t)}\right)}{\alpha L}\right)} \tag{8}$$

Fig. 8 shows the plot between i_m (normalized with k) and sample thickness calculated for the external resistance, R_m = 200 TΩ

As is evident from this figure, with increasing sample thickness, i_m increases, reaches a maxima, and subsequently it decreases with the sample thickness. The optimum thickness (for the current set of samples) which yield maximum photocurrent is found at 33 μm which is about the penetration depth of light. It must be noted that the samples used in this study are thicker than this optimum thickness. It is also reflected in results shown in Fig. 6, where the photocurrent is found to increase with decrease in sample thickness.

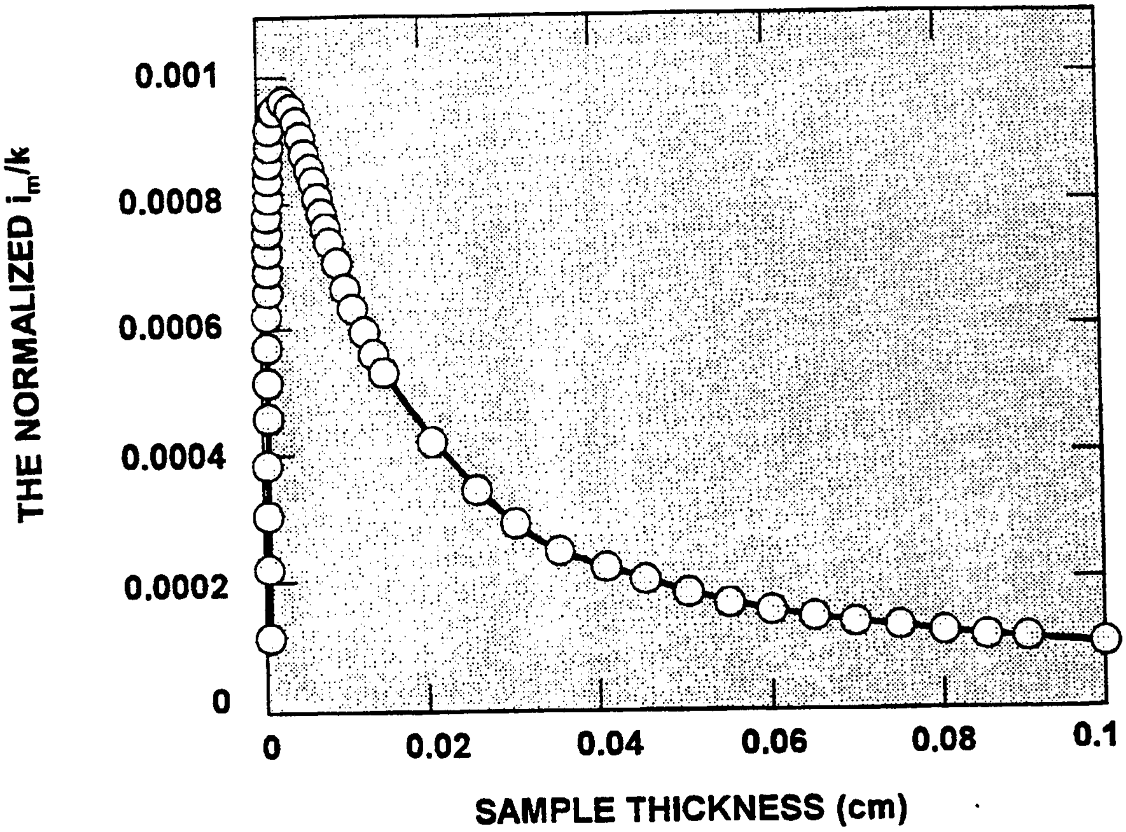

Figure 8: The normalized i_m/k as a function of sample thickness

The results on thickness dependence in the PZT5H composition are summarized in the following table:

Table 4: Thickness Dependence Of Optical Actuation In PZT5H Composition

	THICKNESS microns	RESPONSE mV	DEFLECTION microns	RATIO $D_{ti} / D_{t1=380}$
EXPERIMENTAL DATA				
t_1	380	85	21	1
t_2	200	350	88	4
t_3	165	512	128	6
PROJECTED t_4	33	–	–	20

The results provide confirmation of the analysis summarized in Table 1, and further confirm the projection that optimum film thickness for optical actuation is~ 33 micron with the deflection projected to be ~ 20 times higher than current state of the art wafer of PZT 5H composition at 200 micron thickness

iv. Optical actuation as function of Surface Roughness for PLZT ceramics:

In order to observe the surface roughness effect, PLZT ceramics (3/52/48) with different surface roughness were prepared by using SiC powder of different grit size followed by final finishing with diamond paste The surface roughness was measured by a profilometer (Tencor, Alpha-step 200). The average surface roughness was determined using the graphical center line method Fig. 9 exhibits the photostriction of undoped PLZT as a function of surface roughness

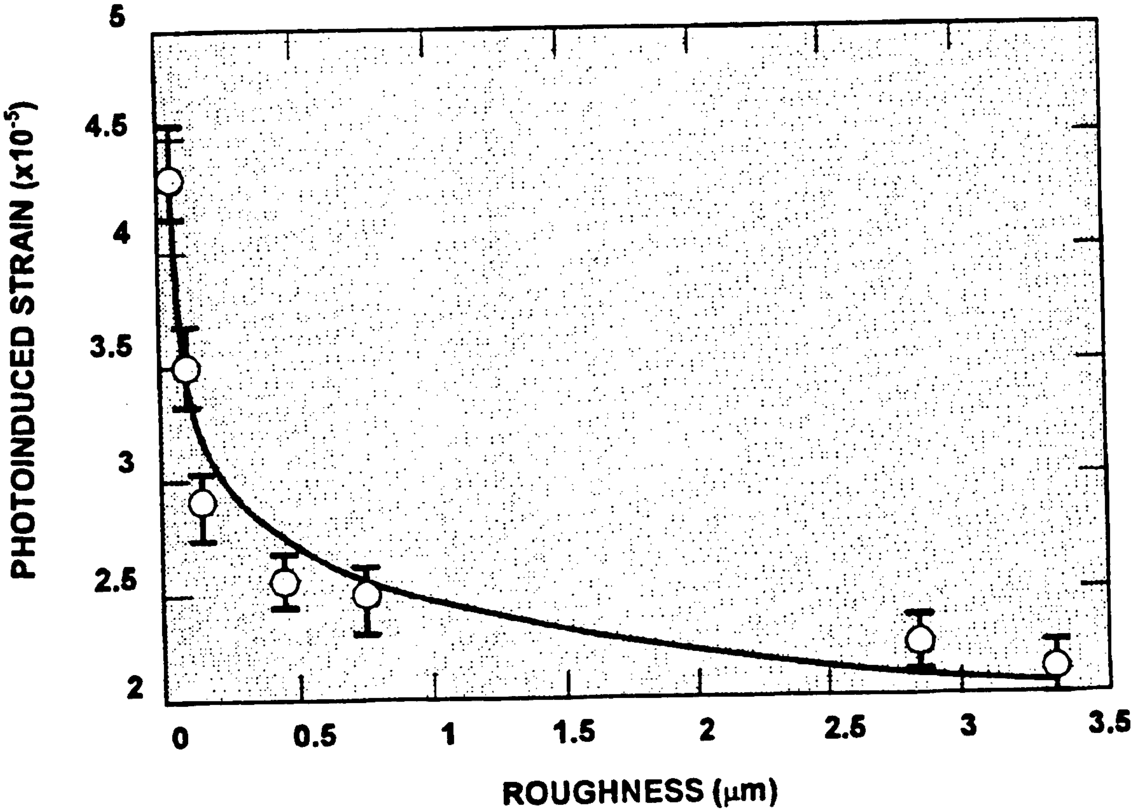

Figure 9: Photoinduced strain as a function of surface roughness

As is evident from this figure, photoinduced strain increases exponentially with the decrease in surface roughness. With increasing surface roughness, the penetration depth of the illumination decreases. This result also reiterates that photostriction is a surface effect and surface preparation is of extreme importance in the fabrication of high efficiency photostrictive materials.

5. CONCLUSIONS

This work has shown that optical actuation in piezoceramics is indeed a viable option. It will be of particular interest where the actuation control is desired to be contact-less and or remote. The actuation properties of piezoceramics depend sensitively on its composition, structure, thermal history, and surface smoothness/roughness; which offers a broad set of parmeters for optimization of the material and thereby its characteristics. The results provide confirmation of the analysis summarized in Table 1, and further confirm the projection that optimum film thickness for optical actuation is~ 33 micron with the deflection projected to be ~ 20 times higher than current state of the art wafer of PZT 5H composition at 200 micron thickness. Further, choice of suitable flexible substrates is of utmost importance and of course application dependent.

6. ACKNOWLEDGEMENTS

We would like to thank Prof. Eric Cross from Penn State, and Prof. Gene Haertling from Clemson Univ for stimulating discussions regarding actuation. At JPL, we would like to thank Anil Thakoor for providing useful suggestions on this manuscript. The work described in this paper was performed by the Jet Propulsion Laboratory, California Institute of Technology, and was sponsored by the Advanced Concepts Office of National Aeronautics and Space Administration (NASA), and the JPL Director's Research and Development Fund.

7. REFERENCES

1. S.Thakoor, J. A. Cutts, "Flexible Microactuators for Advanced Mobility" New technology report, JPL,.August 1996 NPO # 20019/9651; "Smart Materials for Tiny Robotic Rovers", Science News, 150, p 359 (1996).
2. S. Thakoor, J. M. Morookian, and J. A. Cutts, "Role of Piezoceramic Microactuation for Advanced Mobility", Proceedings of the Tenth IEEE International Symposium on Applications of Ferroelectrics Transactions, Vol 1, pp 205-211, (IEEE Catalog # 96CH35948).
3. V. M. Fridkin and B. N. Popov, Sov. Phys. Usp. **21,** (1978); M. E. Lines and A. M. Glass, Principles and Applications of Ferroelectrics and Related Materials (Clarendon, Oxford, 1977), Chaps., 5,12, and 16; K. Uchino, Y. Miyazawa, and S. Nomura, Jap. J. of Appl. Phy., Vol 22, 102, Dec 1983; " Capturing Sound Light and Strength with New Materials", Meeting Briefs, Science, **266,** Dec 1994.
4. A. J. Moulson & J. M. Herbert, Electroceramics, chapman & Hall Publishers, 298 (1992).

5. A. F. Flynn et al., Journal of Microelectromechanical Systems, **1**, 44, (1992); A. F. Flynn, Ph. D Thesis, MIT(June. 1995); R Gerson and T. C. Marshall, J. of App. Phy., **30**, 1650 (1959).
6. S. Thakoor and A. Stoica: "Biomorphic Explorers" New Technology Report, February 1997, NPO# 20142/9778, K. Uchino, J. Rob. Mech., 1, 124 (1989); T. Fukuda, S. Hattori, F. Arai, H. Matsuura, T. Hiramatsu, Y. Ikeda, A. Maekawa, Rob. Automation, **2**, 618, (1993); K. Uchino, "New Applicaitons of Photostriction," *Innovations in Materials Research*, Vol. 1, No. 1, pp. 11-22, 1996.
7. P. Poosanaas, A. Dogan, A.V. Prasada Rao, K. Komarneni and K. Uchino, "Photostriction of Sol-Gel Processed PLZT Ceramics," *J. Electroceramics*, Vol. 1, No. 1, pp. 105-111, 1997.
8. S. Thakoor, and J. Maserjian, "Photoresponse Probe of the space charge distribution in Ferroelectric PZT thin film memory capacitors" J. Vac. Sci. &Tech A, **12** , 295, Mar/April(1994); S. Thakoor, "High Speed, Optoelectronic Response from the Edges of lead Zirconate Titanate Thin Film Capacitors", Appl. Phy. Lett. **63**(23), 3233, 1993
9. S. Thakoor, US patent # 5196101, March 23, 1993.
10. A. Yavrovian, S. P. S. Yen, G. Plett and N. Weissman; High temperature Materials for Venus Balloon Envelopes. Proc. 11th AIAA Lighter than air system technology Conference held May 16-18 1995, Clear water Florida.
11. N. Marzwell, Internal communication, April 1997.
12. M. Glass, D von der Linde. D. H. Auston. and T. J. Negran, "Excited State Polarization, Bulk Photovoltaic Effect and the Photorefractive Effect in Electrically Polarized Media," *Electronic Materials*, Vol. 4, No. 5, pp. 915-943, 1975.

New Torsional Amplifier/Actuators

APPENDIX 68

Appl. Phys. Lett. (submitted 1997).

Piezoelectric actuator generating torsional displacement from piezoelectric d_{15} shear response

A. E. Glazounov and Q. M. Zhang,

Materials Research Laboratory, The Pennsylvania State University, University Park, PA 16802

and Ch. Kim

Naval Research Laboratory, Washington DC 20375

Abstract:

A torsional actuator generating angular displacement from the piezoelectric shear strain was developed. The actuator is a tube consisting of even number of the segments poled along the length, which are adhesively bonded together, and the joints act as electrodes to apply the driving voltage. The experimental data measured on the prototype actuator: (i) prove the proposed concept of the torsional actuator, (ii) show that the actuator functions well under the torque load, and (iii) demonstrate that it has superior characteristics compared to previously reported designs of torsional actuators.

PACS: 77.65.-j, 77.84.-s, 07.07.Mp

Piezoelectric ceramic materials, such as lead zirconate titanate (PZT) are now widely used in solid-state actuators and sensors which were designed for many applications, such as precision positioning, noise and vibration sensing and cancellation, linear motors, and many others.[1,2] Since in many of those applications the torsional displacement is required, many works have recently been devoted to the development of actuators capable of generating a large angular displacement with a large torque output[3-6] from the piezoelectric strain.

In this Letter, we report on a novel type of torsional actuator in which shear piezoelectric effect is used to generate the angular displacement. We, first, present the design of the actuator and describe its operation principle, and, second, demonstrate the experimentally measured characteristics of the prototype actuator. The data obtained shows that this prototype has superior characteristics (angular displacement and torque output developed) compared to the previous designs of torsional actuators reported in the literature.[4,5] In addition, one of the obvious advantages of the present design of the actuator is its simplicity: the piezoelectric shear strain is transformed directly into the angular displacement, whereas in the previous designs,[3,5,6] the conversion mechanism was rather complicated which thus required a sophisticated actuator design. Also, in most piezoelectric materials the shear piezoelectric coefficient, d_{15}, has the highest value among piezoelectric coefficients, which is another advantage of using shear piezoelectric effect here.

Design principle A schematic drawing of the developed torsional actuator is shown in Fig.1. The actuator is a tube consisting of even number of piezoelectric ceramic segments which are adhesively bonded together. The segments are poled along the length, whereas the electric field E is applied perpendicular to the direction of the spontaneous polarization, P_s, in order to induce the piezoelectric shear strain. The tube is assembled in such a way that the neighboring segments have the polarization direction opposite to each other, and are electrically connected in parallel. This geometry provides the unidirectional shear deformation of all the segments under an applied field. Due to the cylindrical symmetry of the actuator, the shear strain, $\alpha = d_{15} \cdot E$, induced in each segment is directly transformed into the angular displacement β of the top of the tube with respect to its bottom, Fig.1, which is equal to:

$$\beta = \frac{L}{R_{out}} \cdot d_{15} \cdot E \quad , \qquad (1)$$

where L is the length of the tube and R_{out} is its outer radius. This equation shows that even though the shear strain, α, is usually quite small in the piezoelectric materials, a large torsional displacement β can be achieved by using a tubular structure with a large ratio of L/R_{out}. Using elastic properties of tube-shaped samples,[7] the torque, T_{dev}, developed by the actuator can be found as:

$$T_{dev} = \frac{\pi\left(R_{out}^4 - R_{in}^4\right)}{2 S_{44} R_{out}} \cdot d_{15} \cdot E \quad , \qquad (2)$$

where S_{44} is the shear elastic compliance of the material and R_{in} is the inner radius of the tube. Equation (2) shows that the torque T_{dev} is independent of the length of the tube, even though the angular displacement β increases linearly with L.

A prototype torsional actuator was fabricated from the commercial piezoelectric ceramic tube of composition PZT-5A.[8] The tube was first cut into 8 segments, which then were poled along the length using a continuous poling technique.[9] Finally, the segments were bonded together using a conductive epoxy according to the design shown in Fig.1. The prototype actuator had the following dimensions: $R_{in} = 0.96$ cm, $R_{out} = 1.27$ cm, and $L = 6.35$ cm, so that the aspect ratio in Eq.(1) was equal to $L/R_{out} = 5$.

Characterization of prototype actuator To characterize the developed torsional actuator, we measured the torsional angle β produced by the applied electric field in the following experiments: (a) β as a function of amplitude, E_m, and frequency, f, of the ac driving field, $\beta(f,E_m)$, and (b) β induced by the dc electric field as a function of the external static torque, $\beta(E,T)$. In both experiments, β was measured using a MTI-2000 fotonic sensor, by putting a mirror on the top of the actuator and measuring the distance change, Δl, between the mirror and the optical fiber probe of the MTI-2000. Afterwards, the value of Δl was converted into the torsional angle, β. The effect of the static torque on the actuator performance was studied using a special home made set-up which was developed in our laboratory.

First of all, we verified the concept of the proposed torsional actuator. In order to do that, we used the experimentally measured data for $\beta(f,E_m)$ to derive the piezoelectric coefficient d_{15} of PZT-5A ceramics using Eq.(1), where E_m was substituted for E, and compared the obtained d_{15} values with those measured directly from the PZT-5A ceramic[8] samples of cubic shape. Figure 2 illustrates this comparison for the data measured at f = 10 Hz. As one can see, within the whole range of the ac field investigated, the values of the d_{15} derived from the actuator (closed circles) are nearly the same as those measured on the cubic ceramic sample (plus signs). The small, less than 5%, difference could be attributed to the difference in the aging states (for the ceramic segments in the actuator, the period of aging was about 100 times longer than that of the ceramic sample), and a possible loss of torsional angle due to the bonding of the segments in the tube. Therefore, the result presented in Fig.2 proves the concept of the proposed torsional actuator, Eq.(1), that is, to use the shear piezoelectric effect, d_{15}, and the amplification, L/R_{out}, to generate the angular displacement, β. For the data shown in Fig.2 for the tube, the torsional angle corresponding to the ac field amplitude $E_m = 2$ kV/cm, is equal to $\beta \approx 0.07°$, which is larger than the values reported earlier for other models of the torsional actuator (see below).

The frequency dependence of the torsional angle was measured within the frequency range 3 - 600 Hz for high electric fields, $E_m \leq 2$ kV/cm. Only a minor decrease in β, equal to 3% per decade, with increasing frequency was observed. For low electric fields, $E_m = 0.05$ kV/cm, the frequency dependence of β was measured over broad frequency range from 100 Hz to 20 kHz. The result is presented in Fig.3, where the torsional angle normalized over the ac field amplitude is plotted as a function of f. A series of the peaks is seen in this plot, and a detailed study,[10] showed that these peaks correspond to resonance frequencies of the actuator, which are defined from the minimum electrical impedance of the tube. Using the actuator dimensions, it was concluded that the lowest resonance, f_r, is the fundamental shear resonance along the length L of the actuator, i.e., along the axis of the tube. At the resonance, $f_r \approx 6$ kHz, the angular displacement of the actuator is approximately 20 times larger than that at frequencies below 1 kHz, cf. Fig.3. Such an amplification of the torsional angle at f_r is very important for the application of the torsional actuator in the piezoelectric motors, where the actuators usually operate in the resonance mode.

We also investigated the effect of the torque load on the actuator performance. In this experiment, (b), a static torque T was first applied to the actuator, thus producing its initial twisting, β_0. Afterwards, a dc field was turned on, and the polarity of the field was such that the field induced a twisting of the actuator in the direction opposite to β_0. The plot in Fig.4 shows the field dependence of the torsional angle at different torque loads. It is clear that the torque load does not change significantly the response of the actuator to the applied field, since the initial twisting β_0, can be completely nullified by the appropriate choice of the magnitude of the electric field, and the slope of $\beta(E)$ curve does not show marked change with increasing T, cf. Fig.4.

Comparison with other existing actuator designs In order to further evaluate the merits of the proposed torsional actuator, we compare the performance of this new design with that of other torsional actuators published earlier,[3-6] when the data are available for the comparison. For example, for similar magnitude of the driving field, $E = 2$ kV/cm, the largest value of the torsional angle β produced by the tube-shaped actuator studied in Ref.[4] was equal to 0.007°, which is an order of magnitude smaller than the value reported in this Letter. In another work, Satanobu *et al.*[5] studied the ultrasonic motor which could generate the torsional motion. For similar actuator dimensions ($R_{out} \approx 1.5$ cm), the torque developed by the motor at the resonance frequency was approximately equal to 1 N·m under an ac driving field of $E_m \approx 1$ kV/cm. For the actuator developed here, the data in Fig.4 show that the torque developed under the field $E = 1$ kV/cm, is equal to 2.8 N·m,[11] which is about 3 times larger than the value reported in Ref.[5]. In addition, it should be pointed out that the elastic compliance of PZT ceramics measured under a dynamic torque is about two times smaller than that measured under the static torque.[10] Therefore, due to the smaller value of S_{44} in Eq.(2), a much higher torque output will be expected for this actuator at higher frequencies.

In conclusion, we have developed a novel type of the piezoelectric torsional actuator and experimentally studied the characteristics of its prototype. The data obtained: (i) prove the proposed concept of the torsional actuator, (ii) show that the actuator functions well under the torque load, and (iii) demonstrate that the actuator has superior characteristics (the angular displacement and the torque output developed) compared to previously reported designs of the torsional actuator.

The authors wish to thank Mr. S. Gross (MRL) for his help in designing the torque load set-up, and DARPA for the financial support of this work.

References:

1. K. Uchino, Bull. Amer. Ceram. Soc. **65**, 647 (1986).
2. L. E. Cross, Ceramic Trans. **68**, 15 (1996).
3. A. Yabuki, M. Aoyagi, Y. Tomikawa, and T. Takano, Jpn. J. Appl. Phys. **33**, 5365 (1994).
4. Y. Fuda and T. Yoshida, Ferroelectrics **160**, 323 (1994).
5. J. Satonobu, N. Torii, K. Nakamura, and S. Ueha, Jpn. J. Appl. Phys. **35**, 5038 (1996).
6. M. Aoyagi, S. Tsuchiya, and Y. Tomikawa, Jpn. J. Appl. Phys. **36**, 6106 (1997).
7. P. Ch. Chou and N. J. Pagano, "Elasticity: tensor, dyadic, and engineering approaches", 115 - 144 (Dover Publications, New York, 1992).
8. Piezoelectric ceramics of PZT-5A composition was purchased from "EDO Inc.", Utah, USA.
9. C. Kim, T. Jessen, V. Degiorgi, C. Wu, M. Kahn, D. Lewis III, Q. M. Zhang, and V. Mueller, Abstracts of the IMF-9, The 9th International Meeting on Ferroelectricity, August 1997, Seoul, Korea.
10. A. E. Glazounov, Q. M. Zhang, and Ch. Kim, to be published.
11. As one can see from Fig.4, at $E \approx 1$ kV/cm, the curve $\beta(E,T)$ measured at $T = 2.8$ N·m intersects the dotted line corresponding to $\beta = 0$, which implies that the absolute value of the torque, T_{dev}, developed by the actuator is equal to the external static torque, T.

Figure captions

Figure 1. The proposed torsional actuator is a tube consisting of even number of the segments of piezoelectric ceramics which are poled along the length and bonded together using a conductive epoxy. Neighboring segments have the spontaneous polarization, P_s, direction opposite to each other, as shown with arrows on the left. The electric field, E, is applied perpendicular to P_s, in order to induce the piezoelectric shear strain, α, and has opposite directions in neighboring segments (as shown with arrows on the right). Therefore, depending upon the polarity of applied voltage, the top of the tube will twist on angle β either clockwise or anticlockwise with respect to its bottom.

Figure 2. Piezoelectric coefficient d_{15} as a function of the amplitude of the ac driving field measured at f = 10 Hz. Closed circles correspond to the data calculated from the torsional angle of the actuator using Eq.(1). Plus signs show the data measured directly from the cubic ceramic sample of the same composition, PZT-5A.

Figure 3. Frequency dependence of the torsional angle normalized over the amplitude of the ac driving field for $E_m = 0.05$ kV/cm.

Figure 4. Torsional angle is plotted as a function of applied dc field and external static torque, T.

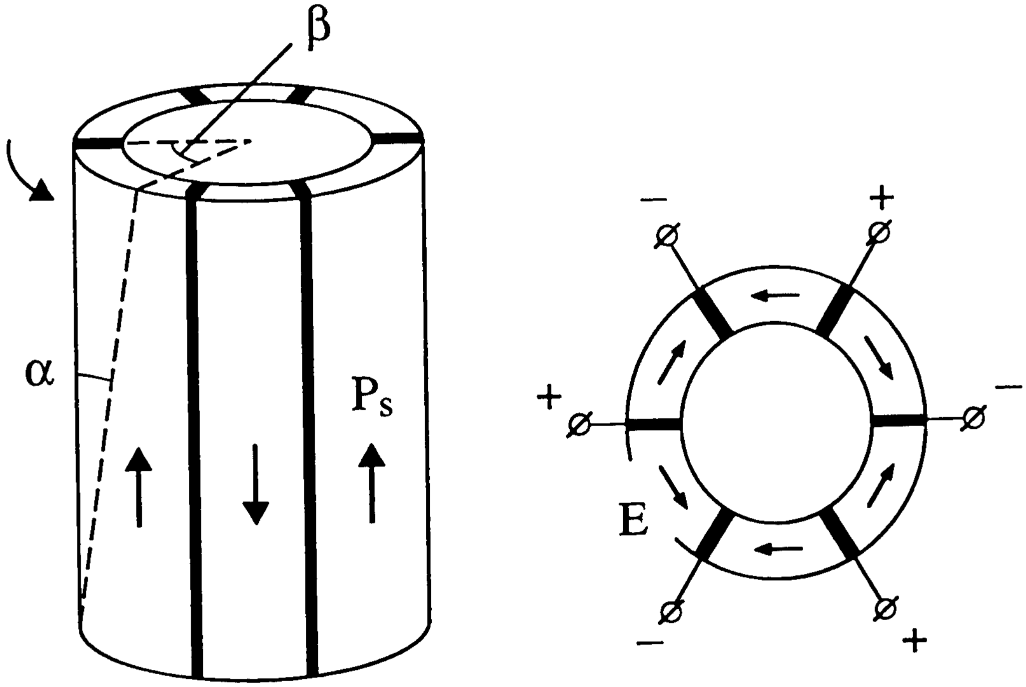

Figure 1

Paper: “Piezoelectric actuator generating torsional displacement from piezoelectric d_{15} shear response”

by: A. E. Glazounov, Q. M. Zhang, and Ch. Kim

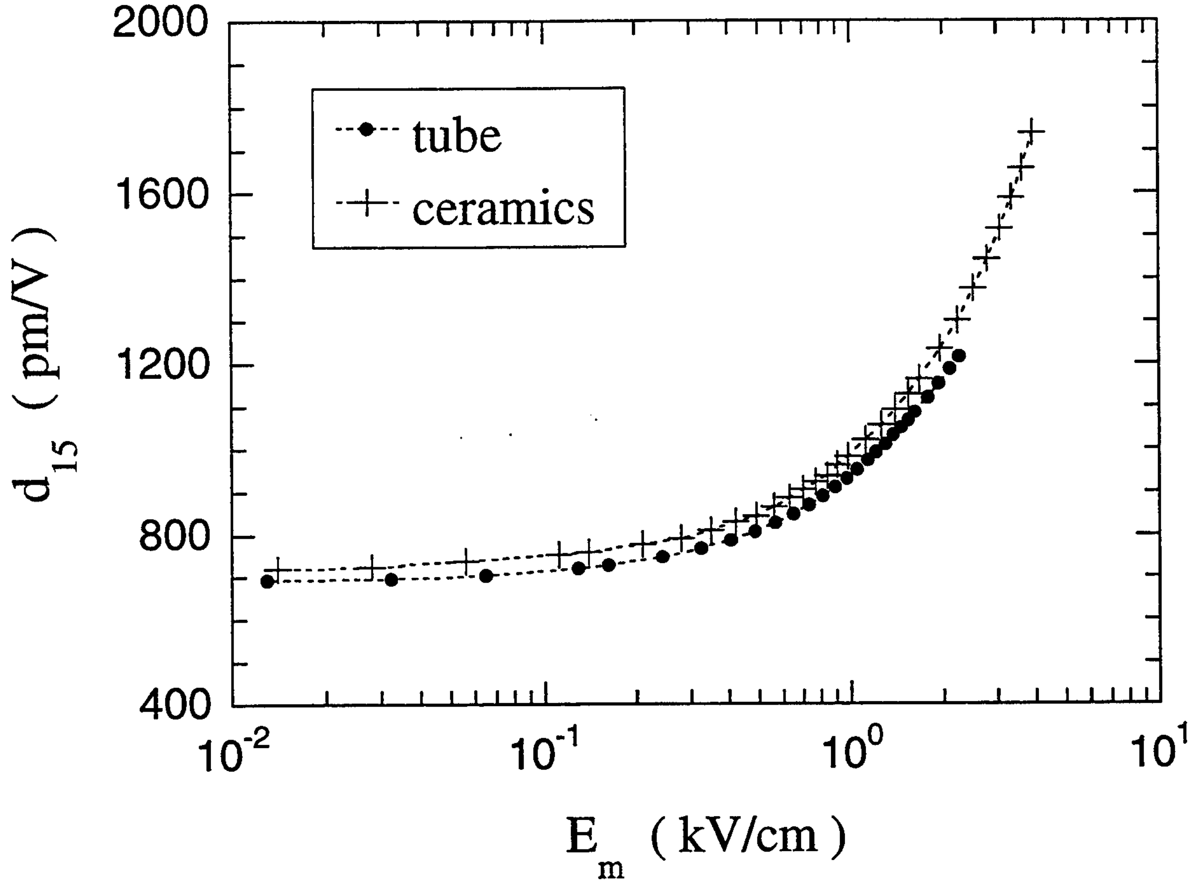

Figure 2

Paper: "Piezoelectric actuator generating torsional displacement from piezoelectric d_{15} shear response"

by: A. E. Glazounov, Q. M. Zhang, and Ch. Kim

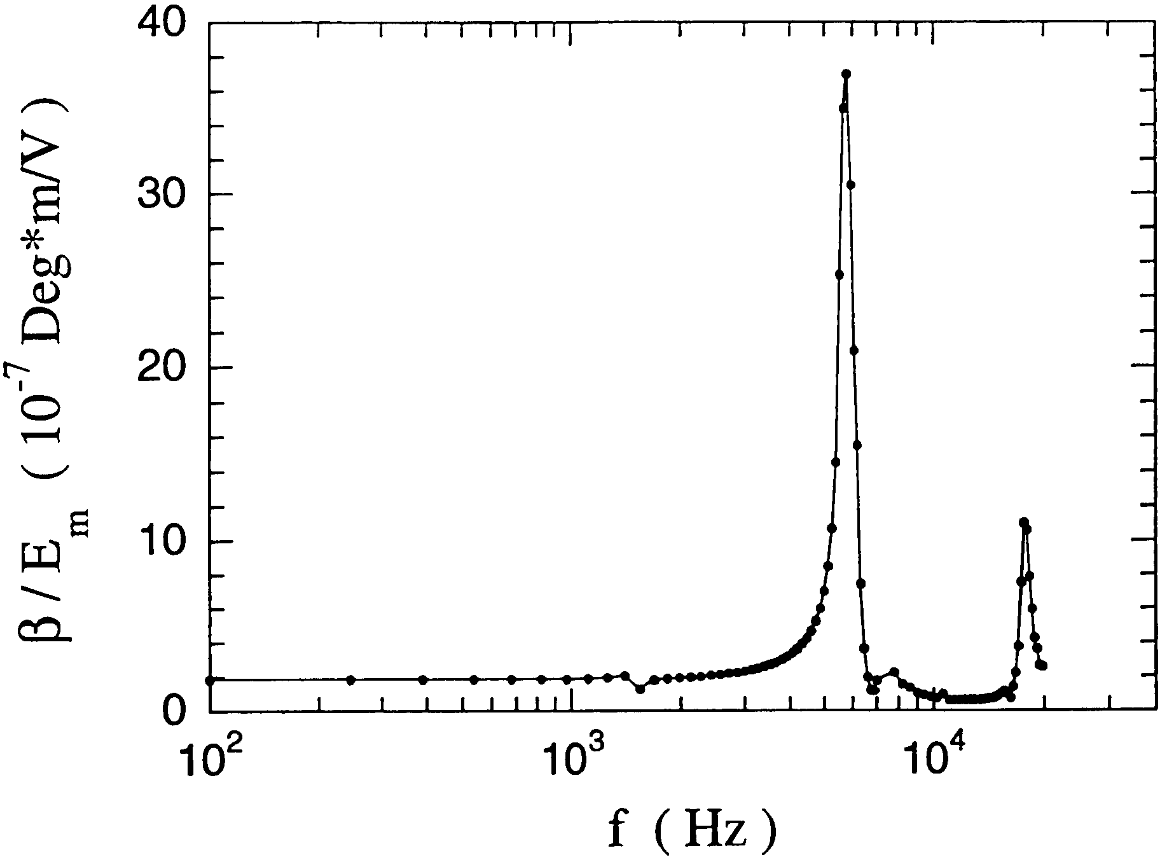

Figure 3

Paper: "Piezoelectric actuator generating torsional displacement from piezoelectric d_{15} shear response"

by: A. E. Glazounov, Q. M. Zhang, and Ch. Kim

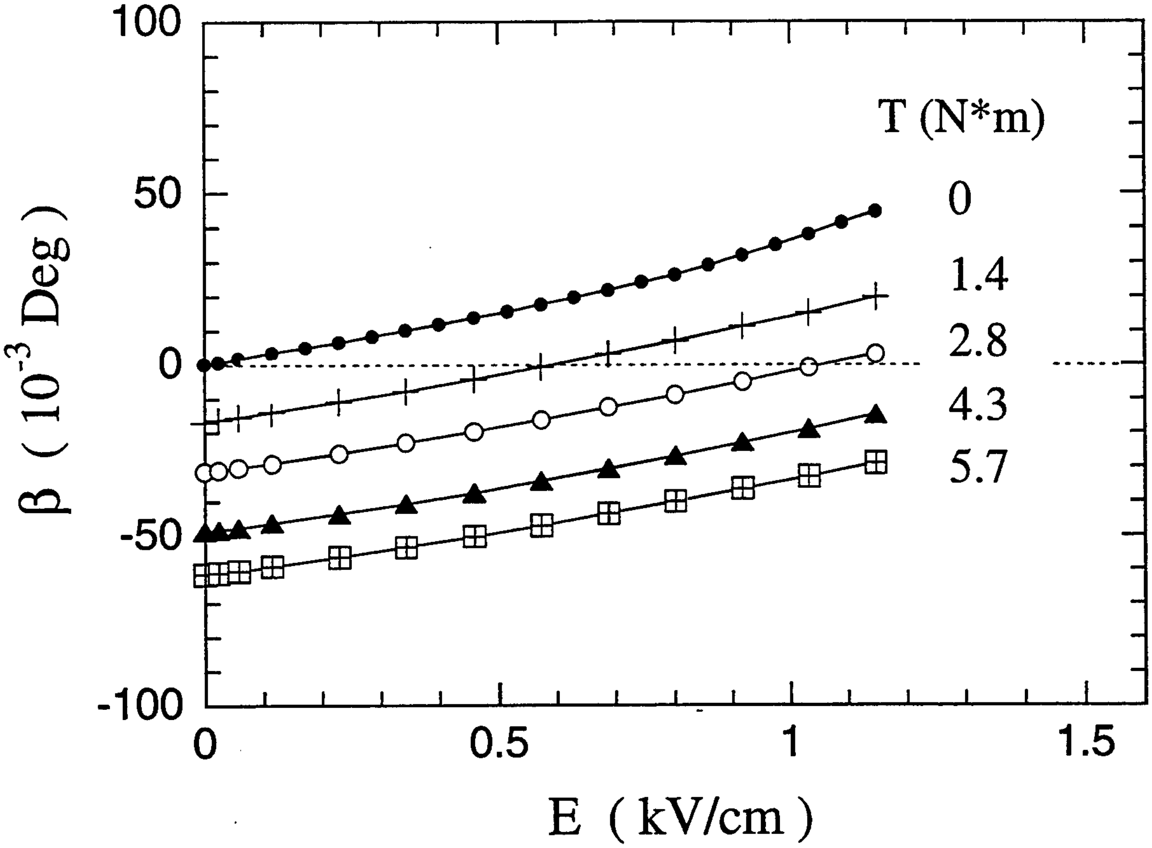

Figure 4

Paper: "Piezoelectric actuator generating torsional displacement from piezoelectric d_{15} shear response"

by: A. E. Glazounov, Q. M. Zhang, and Ch. Kim

APPENDIX 69

Proc. SPIE Smart Materials (1998).

A new torsional actuator based on shear piezoelectric response

A. E. Glazounov,[a] Q. M. Zhang,[a] and Ch. Kim[b]

[a] Materials Research Laboratory, The Pennsylvania State University, University Park, PA 16802
[b] Naval Research Laboratory, Washington DC 20375

ABSTRACT

A torsional actuator generating angular displacement from the piezoelectric shear strain was developed. The actuator is a tube consisting of an even number of the segments poled along the length, which are adhesively bonded together, and the joints act as electrodes to apply the driving voltage. The experimental data measured on the prototype actuator: (i) prove the proposed concept of the torsional actuator, (ii) show that the actuator functions well under the torque load, and (iii) demonstrate that it has superior characteristics compared to previously reported designs of torsional actuators. In addition, one of the obvious advantages of the present design of the actuator is its simplicity: the piezoelectric shear strain is transformed directly into the angular displacement, whereas in the previously reported actuators, the conversion mechanism into the torsional motion was rather complicated which thus required a sophisticated design of the whole system.

Keywords: torsional actuator, shear strain, piezoelectric ceramics, nonlinearity

1. INTRODUCTION

Piezoelectric ceramic materials, such as lead zirconate titanate (PZT) are now widely used in solid-state actuators and sensors which were designed for numerous applications, such as precision positioning, noise and vibration sensing and cancellation, linear motors, and many others.[1,2] In many of those applications, the torsional displacement is required, for example, in robotics to achieve the micropositioning,[3,4] in CD drivers,[5] in helicopters to control the trailing edge flaps of rotor blades,[6] and in many others. To meet this demands, many works have recently been devoted to the development of actuators capable of generating a large angular displacement with a large torque output[3-7] from the piezoelectric strain.

In this paper, we report on a novel type of torsional actuator in which shear piezoelectric effect (when the external electric field is applied perpendicular to the polar axis) is used to generate the angular displacement. We, first, present the design of the actuator and describe its operation principle, and, second, demonstrate the experimentally measured characteristics of the prototype actuator. The data obtained shows that this prototype has superior characteristics (angular displacement and torque output developed) compared to the previous designs of torsional actuators. In addition, one of the obvious advantages of the present design of the actuator is its simplicity: the piezoelectric shear strain is transformed directly into the angular displacement, whereas in the previously reported actuators, the conversion mechanism into the torsional motion was rather complicated which thus required a sophisticated design of the whole system.[3,5-7] Also, in most piezoelectric materials the shear piezoelectric coefficient, d_{15}, has the highest value among piezoelectric coefficients, which is another advantage of using shear piezoelectric effect here.

We also report the data on nonlinear shear piezoelectric response of PZT ceramics. It is shown that this response is controlled by the domain wall motion. The release of the domain walls from the pinning centers by the electric field leads to the increase in the piezoelectric shear coefficient, d_{15}, of PZT ceramics with increasing amplitude of the driving field. This feature is very important for the application of PZT in the proposed torsional actuator, since the higher the d_{15}, the larger will be the values of the torsional angle and the torque output of the actuator.

2. ACTUATOR DESIGN

An idea of the torsional actuator proposed in this paper is to use the shear piezoelectric effect, when the external electric field is applied perpendicular to the direction of the spontaneous polarization, P_s, Fig.1(a), in order to produce the angular displacement. A schematic view of the actuator is shown in Fig.1(b). The actuator is a tube consisting of even number of piezoelectric ceramic segments which are adhesively bonded together using a conductive epoxy, which acts as electrodes to apply the driving field, E. The segments are poled along the length, P_s. The tube is assembled in such a way that the neighboring segments have the polarization direction opposite to each other, and are electrically connected in parallel. This geometry provides the unidirectional shear deformation of all the segments under the applied field. Due to the cylindrical symmetry of the actuator, the shear strain, $S_5 = d_{15} \cdot E$, induced in each segment is directly transformed into the angular displacement β of the top of the tube with respect to its bottom, Fig.1(b), which is equal to:

$$\beta = \frac{L}{R_{out}} \cdot d_{15} \cdot E \quad , \tag{1}$$

where L is the length of the tube and R_{out} is its outer radius. This equation shows that even though the shear strain is usually quite small in the piezoelectric materials, a large torsional displacement β can be achieved by using a tubular structure with a large ratio of L/R_{out}. Using elastic properties of tube-shaped samples,[8] the torque, T_{dev}, developed by the actuator can be found as:

$$T_{dev} = \frac{\pi\left(R_{out}^4 - R_{in}^4\right)}{2 s_{44} R_{out}} \cdot d_{15} \cdot E \quad , \tag{2}$$

where s_{44} is the shear elastic compliance of the material and R_{in} is the inner radius of the tube. Equation (2) shows that the torque T_{dev} is independent of the length of the tube, even though the angular displacement β increases linearly with L, Eq.(1).

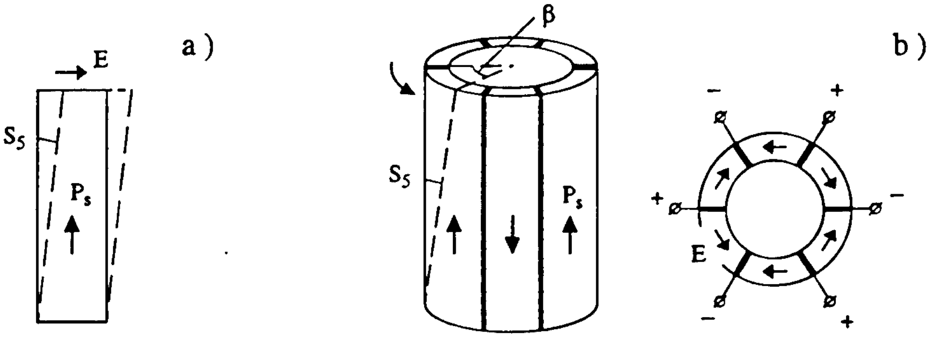

Figure 1. (a) In piezoelectric shear effect, electric field, E, is applied perpendicular to the direction of the spontaneous polarization, P_s, thus producing the shear strain, $S_5 = d_{15} \cdot E$, in the sample. Solid and dashed lines show the sample before and after deformation, respectively. (b) The proposed torsional actuator is a tube consisting of an even number of the segments of piezoelectric ceramics which are poled along the length and bonded together using a conductive epoxy. Neighboring segments have the polarization direction opposite to each other, as shown with arrows on the left. The electric field, E, is applied perpendicular to P_s, and has opposite directions in neighboring segments (as shown with arrows on the right). Therefore, depending upon the polarity of applied voltage, the top of the tube will twist on angle β either clockwise or counterclockwise with respect to its bottom.

3. EXPERIMENTAL

A prototype torsional actuator was fabricated from the commercial piezoelectric ceramic tube of composition PZT-5A.[9] The tube was first cut into 8 segments, which then were poled along the length using a continuous poling technique.[10] Finally, the segments were bonded together using a conductive epoxy according to the design shown in Fig.1. The prototype actuator had the following dimensions: R_{in} = 0.96 cm, R_{out} = 1.27 cm, and L = 6.35 cm, so that the aspect ratio in Eq.(1) was equal to L/R_{out} = 5.

To characterize the developed torsional actuator, we measured the torsional angle β produced by the applied electric field in the following experiments: (i) β as a function of amplitude, E_m, and frequency, f, of the ac driving field, $\beta(f,E_m)$, (ii) β induced by the dc electric field as a function of the external static torque, β(E,T), and (iii) β induced by the ac electric field as a function of the external static torque, $\beta(E_m,T)$. In all the experiments, β was measured using a MTI-2000 fotonic sensor, by attaching a small mirror on the top of the actuator and measuring the distance change, Δl, between the mirror and the optical fiber probe of the MTI-2000. Afterwards, the value of Δl was converted into the torsional angle, β.

The effect of the torque load on the actuator performance, (ii) and (iii), was studied using a special home made set-up which was developed in our laboratory, Fig.2. Although, there are commercial torque load test machines available, they are not suitable for the torque load test of torsional actuators. The main reason is that these machines are mainly designed to test the properties of the metals, and therefore deal with the magnitudes of the torque and twisting angle which are much larger than those expected for the piezoelectric actuators. Additionally, the commercial machines are very expensive, which does not justify their purchase and the following modification to meet the requirements of experiments with actuators. In the developed set-up, Fig.2, the actuator was tightly clamped with its bottom to the base of the set-up, and its top could twist under the applied torque. The external torque was produced by applying the force to the lever using springs with different elastic constants, as shown in the top part of Fig.2.

In the experiment with load-free conditions, (i), the actuator was tightly clamped with its bottom to the optical table, whereas its top was free to move thus producing the torsional displacement, β, Fig.1(b).

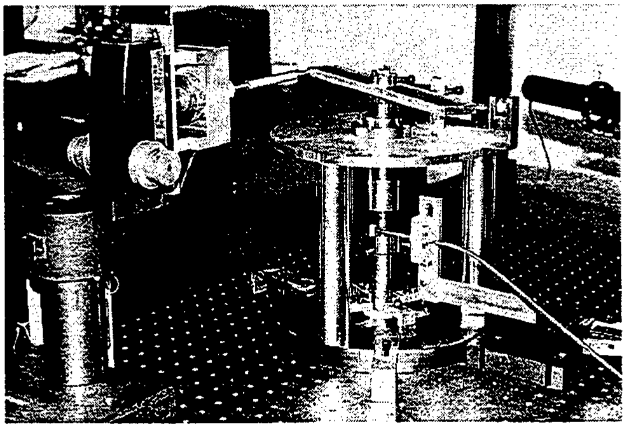

Figure 2. A photograph of the set-up used for the study of the effect of external static torque, T, on the response of the torsional actuator, β(E,T).

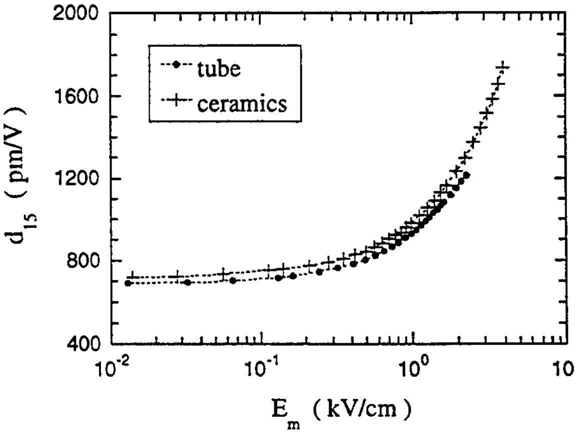

Figure 3. Piezoelectric coefficient d_{15} as a function of the amplitude of the ac driving field measured at f = 10 Hz. Closed circles correspond to the data calculated from the torsional angle of the actuator using Eq.(1). Plus signs show the data measured directly from the cubic ceramic sample of the same composition, PZT-5A.

4. CHARACTERISTICS OF PROTOTYPE ACTUATOR

4.1. Proof of the concept of the proposed torsional actuator

First of all, we verified the concept of the proposed torsional actuator. In order to do that, we used the experimentally measured data for $\beta(f,E_m)$ to derive the piezoelectric coefficient d_{15} of PZT-5A ceramics using Eq.(1), where E_m was substituted for E, and compared the obtained d_{15} values with those measured directly from the PZT-5A ceramic[9] samples of cubic shape. Figure 3 illustrates this comparison for the data measured at f = 10 Hz. As one can see, within the whole range of the ac field investigated, the values of the d_{15} derived from the actuator (closed circles) are nearly the same as those measured on the cubic ceramic sample (plus signs). The small, less than 5%, difference could be attributed to the difference in the aging states of ceramics in segments and cubic samples (for the ceramic segments in the actuator, the period of aging was about 100 times longer than that of the ceramic sample), and a possible loss of torsional angle due to the bonding of the segments in the tube. Therefore, the result presented in Fig.3 proves the concept of the proposed torsional actuator, Eq.(1), that is, to use the shear piezoelectric effect, d_{15}, and the amplification, L/R_{out}, to generate the angular displacement, β. For the data shown in Fig.3 for the tube, the torsional angle corresponding to the ac field amplitude E_m = 2 kV/cm, is equal to $\beta \approx 0.07°$, which is larger than the values reported earlier for other models of the torsional actuator (see below).

4.2. Frequency dependence of torsional angle

The frequency dependence of the torsional angle was measured within the frequency range 3 - 600 Hz for high electric fields, $E_m \leq 2$ kV/cm. Only a minor decrease in β, equal to 3% per decade, with increasing frequency was observed.

For small electric fields, E_m = 50 V/cm, the frequency dependence of β was measured over a broad frequency range from 100 Hz to 20 kHz. The data obtained is presented in Fig.4(a), where the torsional angle normalized over the ac field amplitude is plotted as a function of frequency. For the experiment where the bottom of the actuator is clamped and the top is free, two peaks are seen in the plot which is shown with the dotted line. In order to verify the origin of these peaks, we also measured electric impedance, Z(f), of the actuator, and additionally studied β(f) and Z(f) in the experiment, where both ends of the tube (top and bottom) were mechanically free (the actuator was standing freely on the sheet of a foam). This study showed that the peaks in β(f), Fig.4(a), correspond to resonance frequencies of the actuator, which are defined from the minimum electrical impedance of the tube, Fig.4(b). Using the actuator dimensions, it was concluded that the lowest resonance, f_r, is the fundamental shear resonance along the length L of the actuator, i.e., along the axis of the tube. Mechanical clamping of the bottom of the tube reduces the resonance frequency from 12 kHz down to 6 kHz, as can be seen in Figs.4(a) and 4(b).

As one can see from Fig.4(a), when the bottom of the actuator is clamped, the angular displacement of the actuator measured at the resonance, $f_r \approx 6$ kHz, is approximately 20 times larger than that corresponding to frequencies below 1 kHz. Such amplification of the torsional angle at f_r is very important for possible application of the torsional actuator in the piezoelectric motors, where the actuators usually operate in the resonance mode. In the motor, the tube shown in Fig.1(b) must be combined with the piezoelectric disk poled along its thickness in order to make the stator of the motor. While the torsional vibrations of the tube will provide the driving force to the rotor of the motor, the longitudinal vibrations of the ceramic disk will control the normal force between the rotor and the stator which is necessary to transmit the torsional vibration.

4.3. Effect of torque load on prototype actuator performance

We investigated the effect of the torque load on the static (ii) and dynamic (iii) response of the prototype actuator. In the experiment (ii), a static torque, T, was first applied to the actuator, thus producing its initial twisting, β_0. Afterwards, a dc field was turned on, and the polarity of the field was such that the field induced a twisting of the actuator in the direction opposite to β_0. Figure 5 presents the results of this experiment. In Fig.5(a), the field dependence of β is plotted at different torque loads. The same data are replotted in Fig.5(b) in the form of the load curves, where the measured torsional angle is shown as a function of the torque at different levels of the dc field. The results presented in Fig.5 clearly demonstrates that the torque load almost does not change the response of the actuator to the dc field, because the initial twisting β_0, can be completely nullified by the appropriate choice of the magnitude of the electric field, and because the slope of β(E) curve, which gives the shear piezoelectric coefficient, $d_{15}(E)$, Eq.(1), does not show marked change with increasing T, cf. Fig.5(a).

In the experiment with the effect of external static torque on the dynamic response of the prototype actuator, the ac driving field of 10 Hz was applied to the actuator and the torsional angle was measured as a function of the ac field amplitude and the torque load. Figure 6 shows the plot of the ac field dependence of piezoelectric coefficient d_{15} derived from the data on $\beta(E_m)$ using Eq.(1). Similar to the static response, the external torque does not affect significantly the actuator response to the ac field. Application of the torque results only in a small, less that 10%, change in d_{15} from its value measured under load-free condition, T = 0 N·m. With the further increase in the value of T, the d_{15} remains nearly constant, Fig.6.

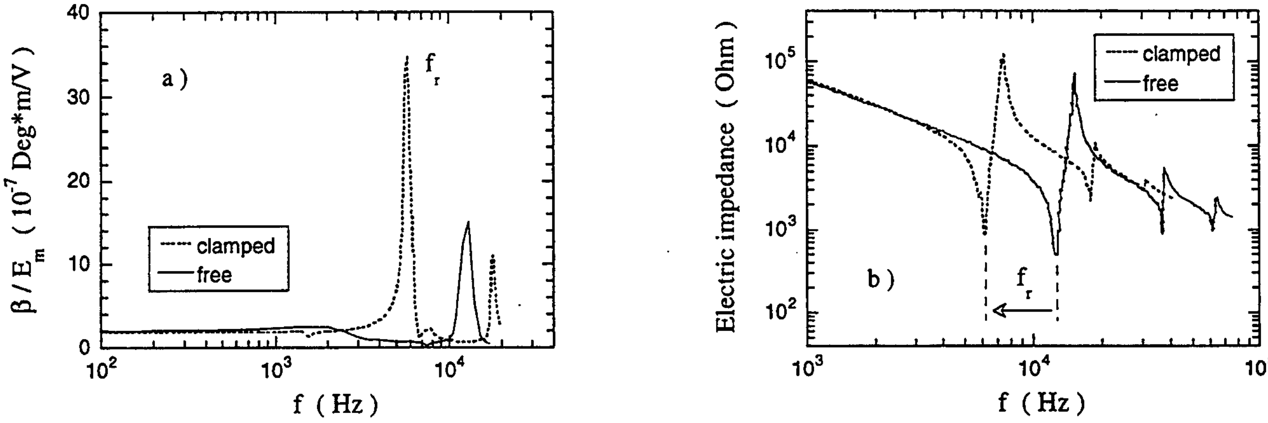

Figure 4. Frequency dependence (a) of the torsional angle normalized over the amplitude of the ac driving field for E_m = 50 V/cm, and (b) of the electrical impedance of the torsional actuator. In both plots, the dotted line corresponds to the experiment where the bottom of the tube was clamped to the optical table, whereas the solid line shows the data measured on the tube with both top and the bottom free. The position of the fundamental shear resonance along the length of the tube is denoted as f_r.

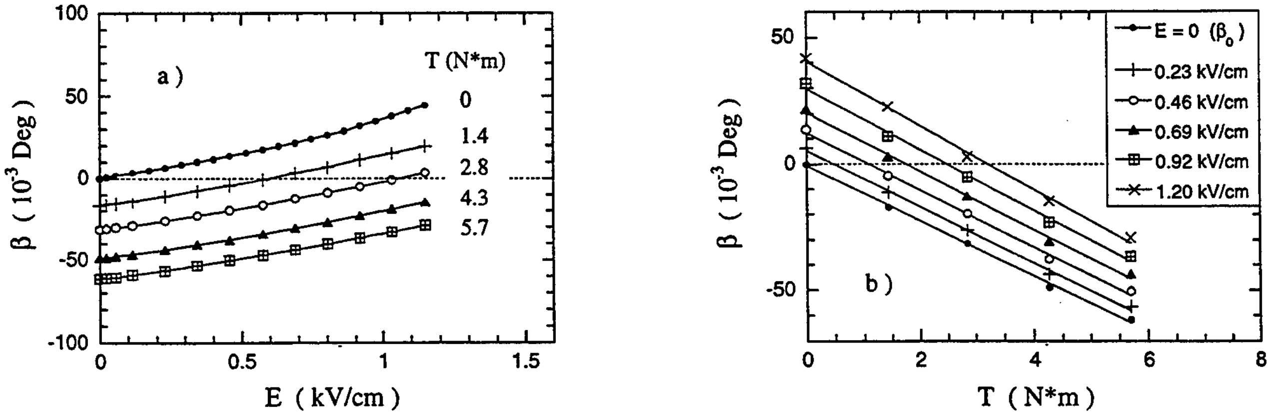

Figure 5. (a) Torsional angle of the prototype actuator is plotted as a function of applied dc field at different external static torque, T. (b) Load curves for the torsional angle are plotted at different levels of applied dc field. Symbols shows experimentally measured values of the torsional angle, and the solid lines correspond to the fit of β(T) to the linear function.

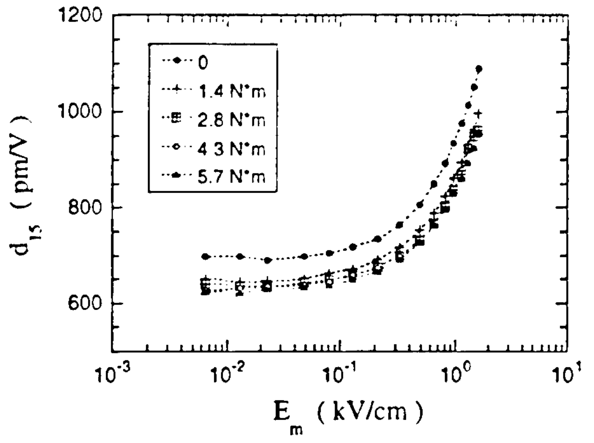

Figure 6. The effect of the static torque on the dynamic response of the torsional actuator. The plot shows the values of the piezoelectric coefficient d_{15} calculated from the data on the torsional angle and plotted as a function of the amplitude of the ac driving field. The frequency of the field is 10 Hz. The values of applied torque are given in the legend.

4.4. Comparison with other torsional actuator designs

In order to further evaluate the merits of the proposed torsional actuator, we compare the performance of the new design with that of other torsional actuators published earlier in the literature,[3-7] when the data are available for the comparison.

For example, for similar magnitude of the driving field, E = 2 kV/cm, the largest value of the torsional angle β produced by the tube-shaped actuator (also having the similar dimensions, L and R_{out}) studied in Ref.[4] was equal to 0.007°, which is an order of magnitude smaller than the value reported in this paper. In another work, the ultrasonic motor which could generate the torsional motion was studied.[3] For similar actuator dimensions ($R_{out} \approx 1.5$ cm), the torque developed by the motor at the resonance frequency was approximately equal to 1 N·m under an ac driving field of $E_m \approx 1$ kV/cm. At the same time, for the actuator developed in the present work, Fig.5(a) shows that the torque developed under the field E = 1 kV/cm, is equal to 2.8 N·m,[11] which is about 3 times larger than the value reported in Ref.[3]. In addition, it should be pointed out that the elastic compliance of PZT ceramics measured under a dynamic torque is about two times smaller than that measured under the static torque.[12] Therefore, due to the smaller value of s_{44} in Eq.(2), a much higher torque output will be expected for this actuator at higher frequencies.

Another possible design of the torsional actuator is to use the piezoelectric bimorph and to convert the displacement of its tip due to its bending under the driving electric field into the torsional motion using the system of levers. Recently, this design of the actuator was discussed in the context of its application to control the trailing edge flaps of rotor blades in helicopters.[6,13] The advantage of the present design of the torsional actuator, Fig.1(b), over that based on the bimorph becomes clear from the following argument. In the bimorph system, the produced torsional angle depends upon the displacement of the tip of the bimorph, η. Since η changes with the length, l_b, of the bimorph, as:[14] $\eta \propto l_b^2$, the longer the bimorph, the larger should be the torsional angle β. However, the increase in l_b will result simultaneously in the decrease of the force, F, developed by the bimorph, since the force is inversely proportional to the length of the bimorph:[14] $F \propto l_b^{-1}$. At the same time, the tube-shaped actuator, Fig.1(b), is free of this drawback. According to Eq.(2), the torque developed by the actuator is independent of the length, L, of the tube. Therefore, by increasing L, one can achieve larger torsional angle, Eq.(1): $\beta \propto L/R_{out}$, without drop in the torque output.

In order to meet the requirements of every particular application, further improvement of the characteristics (torsional angle and/or torque developed) of the proposed torsional actuator, can be achieved as follows. The increase in the magnitude of induced shear strain, $S_5 = d_{15}(E) \cdot E$, will result in the increase of both β and T_{dev}, as predicted by Eqs.(1) and (2). This implies the use of larger values of driving electric field[15] and the development the new piezoelectric materials with higher values of shear piezoelectric coefficient, $d_{15}(E)$ (see Section 5 of this paper). From the engineering point of view, the increase in the torque output of the actuator, Eq.(2), can be achieved by using the tube with a larger outer radius, R_{out}, (which gives an increase proportional to R^3_{out}) and with a smaller ratio R_{in}/R_{out}.

One alternative to the tube-shaped actuator, Fig.1(b), is a conical actuator which is schematically drawn in Fig.7. The advantage of this configuration is that the radius of the end 1 can be made much larger than that of the end 2. If end 1 is fixed at a support and end 2 generates the twisting, this design is quite desirable. For conical geometry, the length, L, of the ceramic segments becomes longer than that in the tubular structure, Fig.1(b), and the effective outer radius of the actuator, R_{out}, becomes smaller, since now it is the radius of the actuator at the end 2. The combined effect will be the increase in the amplification factor, L/R_{out}, in Eq.(1), and, therefore, in the produced torsional angle.

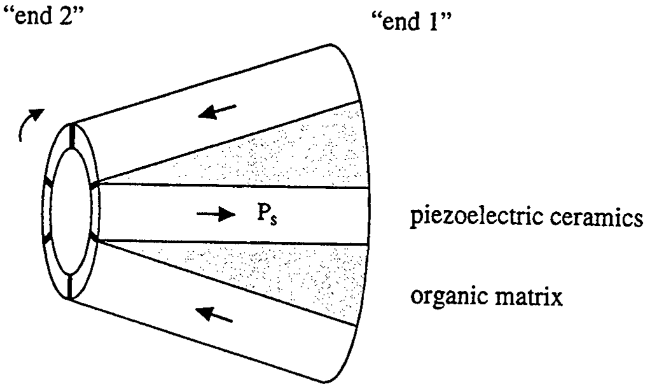

Figure 7. Schematic drawing of the torsional actuator fabricated in the form of the cone. It is expected, that in the real application, the end 1 is fixed at a support, while the torsional displacement is produced at the end 2.

5. NONLINEAR PIEZOELECTRIC EFFECT

In transducer applications, the piezoelectric ceramics is often subjected to high electric fields where the electric field dependence of induced strain is strongly nonlinear.[2] The example of the nonlinear behavior can be seen in Fig.3, where the piezoelectric shear coefficient, d_{15}, of PZT-5A exhibits a pronounced increase in magnitude with increasing ac field. It is believed that the nonlinearity of the piezoelectric response of PZT ceramics is dominated by the irreversible displacement of domain walls[17,18] which separate regions of the material with different orientation of spontaneous polarization, P_s. The domain wall motion may be affected by many factors, including the crystal structure and microstructure of ceramics, the presence of impurities, dopants, defects, and a local variation in the composition of ceramics.[2,17] In this context, the experimental study of electric field dependence of piezoelectric response of PZT should help in the understanding of the role of each of the above factors on nonlinear behavior of the material. In its turn, this should give a clue for the material development for practical applications. For the torsional actuator based on the shear piezoelectric effect, which is proposed in this paper, Fig.1(b), the characteristic which needs to be optimized is the highest value of the piezoelectric coefficient, $d_{15}(E)$, as a function of the driving field. The higher the d_{15}, the larger will be the values of the torsional angle and the torque output, according to Eqs.(1) and (2).

Figure 8 summarizes the results of the study of nonlinear shear piezoelectric response of PZT-5A.[9] In addition to the shear strain, S_5, we also measured the polarization, P_1, induced in the direction of the applied field, i.e., perpendicular to the polar axis, P_s. Both S_5 and P_1 were determined from the measurement of the first harmonics of corresponding signal, i.e., at the frequency f of applied electric field. Using the polarization data, we calculated the dielectric permittivity of the material, using the following relationship: $\varepsilon_1 = P_1 / (\varepsilon_0 \cdot E_m)$, where $\varepsilon_0 = 8.854 \cdot 10^{-12}$ F/m. Figure 8(a) shows the ac field dependence of ε_1 and d_{15} of PZT-5A, measured at 10 Hz. As one can see, both $\varepsilon_1(E_m)$ and $d_{15}(E_m)$ can be well described by the linear function, as shown with the solid lines. This result gives the clear evidence that the nonlinear polarization and strain responses of PZT ceramics are due to the domain wall motion, and not due to the response of the crystal lattice. The reason is that if the nonlinear effect were due to the response of the crystal lattice, it should be described within the Landau-Ginzburg-Devonshire theory of ferroelectrics.[2] Using symmetry arguments for the electric field applied perpendicular to the direction of the spontaneous polarization, this theory predicts the field dependence of the permittivity and piezoelectric coefficient should be described using the following polynomial expansions:[19]

$$\varepsilon_1 = a_0 + a_1 \cdot E_m^2 + a_2 \cdot E_m^4 + \dots \quad , \tag{3}$$

$$d_{15} = b_0 + b_1 \cdot E_m^2 + b_2 \cdot E_m^4 + \dots \quad , \tag{4}$$

where a_k and b_k are the coefficients.

The fact that the data shown in Fig.8(a) are not consistent with Eqs.(3) and (4) let us conclude that the nonlinear polarization and shear piezoelectric response of PZT-5A is controlled by the domain wall motion. Moreover, one can say that the linear function describing $\varepsilon_1(E_m)$ and $d_{15}(E_m)$ corresponds to the nonanalytical behavior of the polarization and strain response of the material to the electric field, in the sense that this function does not conform the symmetry arguments, which predict the material behavior according to Eqs.(3) and (4). The origin of nonanalytical field dependence of the dielectric permittivity and the piezoelectric coefficient is the release of the domain walls from the pinning centers by the electric field, which leads to the increase in both ε_1 and d_{15}. The detailed discussion of nonanalytical field dependence of the piezoelectric properties of PST due to the domain wall motion has recently been presented in Refs.[16,18,19].

In Fig.8(b), we replot the data from Fig.8(a) in the coordinates "piezoelectric shear coefficient versus dielectric permittivity". As one can see, the experimental data (shown with the closed circles) can be well described by the linear function, $d_{15} = g_{15} \cdot \varepsilon_1$, where g_{15} is the coefficient (the fit is shown with the solid line). The linear relationship between d_{15} and ε_1 means that within the studied range of the electric field, $E_m \leq 2$ kV/cm, the same law governs the electric field dependence of the motion of domain walls which contribute to the polarization and strain responses of PZT-5A. Therefore, the domain wall motion can be studied using only one measurement, either strain or polarization.

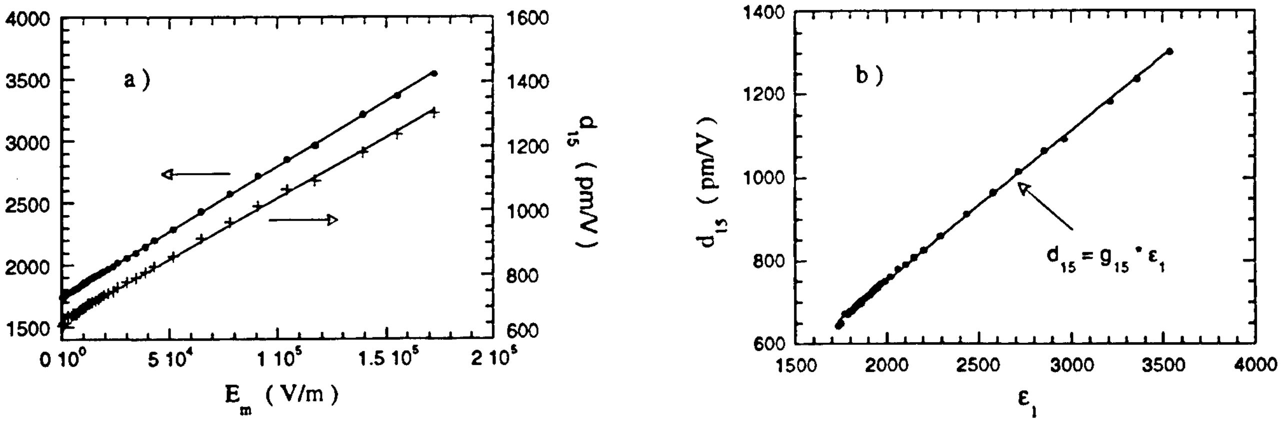

Figure 8. (a) An ac field dependence of shear piezoelectric coefficient, d_{15}, (plus signs) and the dielectric permittivity, ε_1, measured in the direction of applied field (closed circles) of PZT-5A ceramics. Solid lines correspond to the fit of $d_{15}(E_m)$ and $\varepsilon_1(E_m)$ to the linear function. (b) The same data are replotted in the coordinates "d_{15} versus ε_1" and the solid line shows the fit of the data to the linear function, $d_{15} = g_{15} \cdot \varepsilon_1$. In both plots, the data were measured using the frequency of the ac field equal to 10 Hz.

6. SUMMARY

In this work, we have developed a novel type of the piezoelectric torsional actuator and experimentally studied the characteristics of its prototype. The data obtained: (i) prove the proposed concept of the torsional actuator, (ii) show that the actuator functions well under the torque load, and (iii) demonstrate that the actuator has superior characteristics (the angular displacement and the torque output developed) compared to previously reported designs of the torsional actuator.

The study of nonlinear piezoelectric shear response of PZT ceramics demonstrated that the response is controlled by the domain wall motion. The release of the domain walls from the pinning centers by the electric field leads to the increase in the piezoelectric shear coefficient, d_{15}, of PZT ceramics with increasing amplitude of the driving field. This feature is very important for the application of PZT in the proposed torsional actuator, since the higher the d_{15}, the larger will be the values of the torsional angle and the torque output of the torsional actuator. Also, the nonlinear behavior of the piezoelectric coefficient indicates that for this application, the further material development should aim at optimizing the whole characteristic, $d_{15}(E)$, in order to achieve the highest value of the piezoelectric coefficient as a function of the driving field.

ACKNOWLEDGEMENTS

The authors wish to thank Mr. S. Gross (MRL) for his help in designing the torque load set-up, and DARPA for the financial support of this work.

REFERENCES

1. K. Uchino, “Electrostrictive actuators: materials and application,” *Bull. Amer. Ceram. Soc.*, v. 65, pp. 647-652, 1986.
2. L. E. Cross, “Ferroelectric ceramics: materials and application issues,” *Ceramic Trans.*, v. 68, pp. 15-55, 1996.
3. J. Satonobu, N. Torii, K. Nakamura, and S. Ueha, “Construction of megatorque hybrid transducer type ultrasonic motor,” *Jpn. J. Appl. Phys.*, v. 35, pp. 5038-5041, 1996.
4. Y. Fuda and T. Yoshida, “Piezoelectric torsional actuator,” *Ferroelectrics,* v. 160, pp. 323-330, 1994.
5. A. Yabuki, M. Aoyagi, Y. Tomikawa, and T. Takano, “Piezoelectric linear motors for driving head element of CD-ROM,” *Jpn. J. Appl. Phys.*, v. 33, pp. 5365-5369, 1994.
6. I. Chopra, “Status of application of smart structures technology to rotocraft systems,” Presented at the Innovation in rotocraft technology, Royal Aeronautical Society, London, June 1997.
7. M. Aoyagi, S. Tsuchiya, and Y. Tomikawa, “Trial production of an ultrasonic motor using longitudinal and torsional vibrations of a rod vibrator driven by piezoceramic plates inserted in its axial direction,” *Jpn. J. Appl. Phys.*, v. 36, pp. 6106-6109, 1997.
8. P. Ch. Chou and N. J. Pagano, “Elasticity: tensor, dyadic, and engineering approaches”, pp. 115-144, Dover Publications, New York, 1992.
9. Piezoelectric ceramics of PZT-5A composition was purchased from “EDO Inc.”, Utah, USA.
10. C. Kim, T. Jessen, V. Degiorgi, C. Wu, M. Kahn, D. Lewis III, Q. M. Zhang, and V. Mueller, “Composite piezoelectric assemblies for torsional actuators, Presented at IMF-9, The 9th International Meeting on Ferroelectricity, Seoul, Korea, August 1997.
11. As one can see from Fig.5(a), the curve β(E,T) measured at T = 2.8 N·m intersects the dotted line corresponding to $\beta = 0$ at $E \approx 1$ kV/cm which implies that the absolute value of the torque, T_{dev}, developed by the actuator is equal to the external static torque, T.
12. A. E. Glazounov, Q. M. Zhang, and Ch. Kim, to be published.
13. D. K. Samak and I. Chopra, “A feasibility to build a smart rotor: trailing edge flap actuation,” *Proc. of the 1993 SPIE's North American Symposium on Smart Structures and Materials*, Albuquerque, NM, 1993.
14. V. D. Kugel, S. Chadran, and L. E. Cross, “Caterpilar-type piezoelectric d_{33} bimorph transducer,” *Appl. Phys. Lett.*, v. 69, pp. 2021-2023, 1996.
15. The experiments reported in this paper were limited to the use of the driving field of 2 kV/cm, in order to avoid any possible damage to the actuator, e.g. due to the electrical breakdown. However, for the given material composition,

PZT-5A, the limiting field is at least 2 times larger, which is determined by the electrical depoling of the piezoelectric ceramics. A detailed study of this problem is reported in Ref.[16].

16. V. Mueller and Q. M. Zhang, submitted to *J. Appl. Phys.*.
17. Q. M. Zhang, W. Y. Pan, S. J. Jang, and L. E. Cross, "Domain wall excitations and their contributions to the weak-signal response of doped lead zirconate titanate ceramics," *J. Appl. Phys.*, v. 64, pp. 6445-6451, 1988.
18. D. Damjanovic, "Stress and frequency dependence of the direct piezoelectric effect in ferroelectric ceramics," *J. Appl. Phys.*, v. 82, pp. 1788-1797, 1997.
19. V. Mueller and Q. M. Zhang, submitted to *Appl. Phys. Lett.*.

High Force Amplifiers and Inchworms

APPENDIX 70

HIGH POWER CHARACTERIZATION OF PIEZOELECTRIC MATERIALS

Kenji Uchino, Jiehui Zheng, Amod Joshi and Shoko Yoshikawa
International Center for Actuators and Transducers
Materials Research Laboratory, The Pennsylvania State University
University Park, PA 16802, USA;
Seiji Hirose
Yamagata University, Yonezawa-shi 992, Japan;
Sadayuki Takahashi
NEC Corporation, Miyazaki, Kawasaki-shi 216, Japan;
and
J. W. C. de Vries
Ceramic Innovation Center, Philips Components B. V.,
Bredeweg 10, 6042 GG Roermond, The Netherlands

Abstract

Comparisons among three techniques for measuring high-voltage piezoelectric constants were made, which have been developed recently by ourselves: two piezoelectric resonance methods, one with a constant voltage circuit, one with a constant current circuit, and a pulse drive method. The resonance methods generate, in general, heat during the measurement, while the pulse method is not associated with temperature rise. The conventional resonance method with a constant voltage circuit reveals a significant distortion (or a hysteresis) of the resonance frequency spectrum under a high vibration level due to large elastic non-linearity, which prohibits precise determination of the electromechanical coupling parameters. To the contrary, the resonance method with a constant current circuit (i. e. constant velocity) can determine the coupling parameters precisely from a perfectly-symmetrical resoncne spectrum.

INTRODUCTION

High power piezoelectric devices such as piezoelectric actuators, ultrasonic motors and piezoelectric transformers are now being developed intensively [1 - 3]. Here, the piezo-actuators are driven under comparatively high applied voltages. The electromechanical coupling data in the manufacturer's are usually determined under a low applied voltage (1 V) with an impedance analyzer, and sometimes disagree with the high voltage experiments. Figure 1 illustrates the $Pb(Zr,Ti)O_3$ data where parameters such as the mechanical quality factor Q decreases drastically, by 80 %, on increasing drive AC voltage or vibration velocity from 0.05 m/s to 0.5 m/s [4]. The morphotropic phase boundary composition with the lowest Q value at a small vibration velocity exhibits the highest Q value at a high vibration velocity. Thus, low-vibration velocity measurements are not useful to evaluate the high-vibration velocity values, and high power electromechanical coupling parameters must be actually measured under a large vibration level.

This paper describes the comparison among three techniques for measuring high-voltage piezoelectric constants which have been developed recently by ourselves: two piezoelectric resonance methods, one with a constant voltage circuit, one with a constant current circuit, and a pulse drive method. The resonance methods generate heat during the measurement. To the contrary, the pulse method is not associated with temperature rise.

RESONANCE/ANTIRESONANCE METHODS

Piezoelectric transducers have two characteristic electromechanical resonance modes: resonance and antiresonance from an electrical point of view. It is well known that the mechanical vibration level is enhanced at the resonance frequency when driven under a constant voltage. It is worth to note that the piezoelectric transducer can also provide large vibration level even at the antiresonance frequency when it is driven appropriately. For this reason, the resonance and antiresonance are sometimes designated A-type and B-type resonances from a mechanical viewpoint.

(1) Constant Voltage Method

The conventional measurement method is the constant voltage type, which includes impedance analyzers. Figure 2 shows a fundamental circuit for measuring the piezoelectric resonance. L_m, C_m, R_m and C_d are the equivalent motional inductance, capacitance, resistance and damped capacitance of the admittance-type equivalent electric circuit for a piezoelectric resonator. The measurement was carried out using a frequency response analyzer (NF Corporation, 5090) coupled with a high power amplifier (NF Corporation, 4005). A constant voltage measurement provides an admittance curve as a function of frequency, as shown in Fig. 3. From the resonance (maximum) and the antiresonance (minimum) frequencies, the electromechanical coupling parameters are determined [5]. For an example of a rectangular piezo-ceramic plate, the k_{31} value can be calculated as

$$k_{31}^2/(1 - k_{31}^2) = (\pi^2/4)\,(\Delta f / f_r). \quad (\Delta f = f_a - f_r) \qquad (1)$$

However, with increasing applied electric field and vibration velocity, the resonance spectrum peak distorts significantly, sometimes exhibiting large hysteresis of the peak upon rising and falling drive frequency, as shown in Fig. 4 [6]. This distortion causes a serious problem in determining the electromechanical coupling parameters precisely. The distortion originates in elastic nonlinearity, because a very large mechanical vibration is excited at the resonance when a constant voltage method is employed. Figure 5 shows rough estimation of AC voltage dependence of the electromechanical parameters keeping the DC bias at 35 V [7]. H and S in the figure denote "hard" and "soft" piezoelectrics, respectively.

(2) Constant Current Method

Around the electromechanical resonance frequency, the vibration amplitude is proportional not to the voltage, but to the current, as shown in Fig. 6 [8]. Therefore, to determine the electromechanical coupling parameters precisely, an admittance curve should be taken under a constant current condition, i. e. under a constant vibration amplitude [9]. Figure 7 shows an automatic measurement circuit with a differential circuit to maintain a constant current. As demonstrated in Fig. 8, a constant current measurement provides a completely symmetrical admittance peak spectrum without a hysteresis or a jump phenomenon up to a high vibration velocity level [6]. Using a profile fitting technique to the resonance spectrum, we can determine the necessary components, i. e. inductance, capacitance, resistance of the admittance-type equivalent electric circuit for a piezoelectric resonator. On the other hand, to determine the electromechanical coupling parameters at the antiresonance, a constant voltage condition should be employed.

Figure 9 shows example data of mechanical quality factors, Q_A, Q_B and the temperature rise for the resonance and the antiresonance modes for a rectangular-shape PZT resonator plotted as a function of vibration velocity [9]. Note that an effective vibration velocity is a material's constant independent of the sample size, and was defined as $\sqrt{2} \cdot \pi f \cdot u_m$, where f is the resonance or antiresonance frequency and u_m is the maximum vibration amplitude of the the piezoelectric device. It is important that the mechanical quality factor decreases drastically above a certain critical vibration velocity (0.1 m/s), where a drastic temperature rise starts. We have suggested that the heat generation is mainly attributed to a P - E hysteresis loss rather than the mechanical loss. Note also that Q_B is higher than Q_A over the entire vibration velocity range, and that the temperature rise of the sample is less for the B-type resonance (antiresonance) than for the A-type resonance. This indicates that the antiresonance mode is superior to the conventional resonance mode, particularly for high power applications.

PULSE DRIVE METHOD

An alternative method to measure high voltage piezoelectric characteristics is the pulse drive method. By applying a step electric field to a piezoelectric sample, the transient vibration corresponding to the desired mode (extentional, bending etc.) is measured (see Fig. 10). The resonance period, saturated displacement and damping constant are obtained experimentally, from which the elastic compliance, piezoelectric constant, mechanical quality factor and electromechanical coupling factor can be calculated. This time-domain measurement should be equivalent to the above mentioned frequency-domain resonance measurement through the Fourier transformation.

An example procedure to determine the electromechanical parameters is described for a multilayer piezo-actuator. Knowing the permittivity ε, density ρ and size (length) L of the sample independently of the pulse drive experiment, the piezoelectric constant d_{33} can be determined at first from the saturated displacement D_s:

$$D_s = d_{33} E_3 L. \tag{2}$$

Second, from the resonance period T_0 or the resonance frequency f_r (= $1/T_0$), elastic compliance s_{33}^E can be calculated:

$$f_r = 1/\,2L(\rho s_{33}^E)^{1/2}. \tag{3}$$

Then, the electromechanical coupling factor k_{33} is obtained from

$$k_{33} = d_{33} / (\varepsilon_{33}^X s_{33}^E)^{1/2}. \quad (4)$$

Finally, the mechanical quality factor Q_m is calculated from the damping constant t:

$$Q_m = (1/2)\omega_0 t. \quad (\omega_0 = 2\pi/T_0) \quad (5)$$

Although the experimental accuracy is not high, the simple setup is attractive especially for its low cost. Moreover, unlike the resonance/antiresonance methods, this technique requires only one voltage pulse, and thus does not generate heat. The detailed theoretical background of this technique was described in our previous paper [10].

Figure 11 shows the applied field dependence of the electromechanical parameters in a multimorph actuator, the structure of which is also inserted in the figure. A significant increase with increasing the electric field was found in the piezoelectric constant d_{31} and electromechanical coupling factor k_{31}, while a decrease was observed in the quality factor Q_m.

Finally, high power characteristics of a soft piezoelectric PZT-based ceramic sample measured by the constant current and pulse drive methods were compared in Fig. 12. Here, an equivalent vibration velocity for the pulse drive method was estimated by

$$v = (u_{p\text{-}p} / 2\sqrt{2})\,(2\pi f_r), \quad (6)$$

where $u_{p\text{-}p}$ is twice the maximum vibration amplitude of ringing. Although the absolute values were slightly different, similar tendency with changing vibration velocity, i. e. a drastic decrease in Q_m and an insensitive change in the elastic compliance s_{11}^E, was obtained for both the measuring methods.

CONCLUSIONS

This paper demonstrated significant changes in electromechanical parameters such as piezoelectric constants and mechanical quality factors with increasing applied electric field or vibration velocity, thus concluded that high power electromechanical coupling parameters must be actually measured under a large vibration level.

Comparisons among three techniques for measuring high-voltage piezoelectric constants were made, which have been developed recently by ourselves: two piezoelectric resonance methods, one with a constant voltage circuit, one with a constant current circuit, and a pulse drive method. The resonance methods generate, in general, heat during the measurement, while the pulse method is not associated with temperature rise. The conventional resonance method with a constant voltage circuit reveals a significant distortion (or a hysteresis) of the resonance frequency spectrum under a high vibration level, which prohibits precise determination of the electromechanical coupling parameters. To the contrary, the resonance method with a constant current circuit can determine the coupling parameters precisely from a perfectly-symmetrical resoncne spectrum.

Merits (+) and demerits (-) of these measurement techniques for high power piezoelectic characteristics are summarized:

(1) Resonance/antiresonance method	- Heat generation
a) Constant voltage method	- Distortion of the resonance spectrum - Vibration velocity change

b) Constant current method	+ Symmetric resonance spectrum
	+ Constant velocity measurement
(2) Pulse drive method	+ No heat generation
	- Low accuracy

ACKNOWLEDGEMENT

This work was partially supported by the Office of Naval Research through Contract No. N00014-92-J-1510.

REFERENCES

[1] K. Uchino, "Ceramic Actuators: Principles and Applications," Mater. Res. Soc. Bull., **18**, 42-48 (1993).

[2] K. Uchino, "Piezoelectric Actuators/Ultrasonic Motors - Their Developments and Markets," Proc. 9th Int'l Symp. Appl. Ferroelectrics, p.319-324 (1995).

[3] S. Kawashima, O. Ohnishi, H. Hakamata, S. Tagami, A. Fukuoka, T. Inoue and S. Hirose, "Third Order Longitudinal Mode Piezoelectric Ceramic Transformer and Its Application to High-Voltage Power Inverter," Proc. IEEE Int'l Ultrasonic Symp. '94, France (Nov., 1994).

[4] S. Takahashi and S. Hirose, "Vibration-Level Characteristics for Iron-Doped Lead-Zirconate-Titanate Ceramic," Jpn. J. Appl. Phys. **32**, 2422-2425 (1993).

[5] "IRE Standards on Piezoelectric Crystals: Determination of the Elastic, Peizoelectric, and Dielectric Constants - The Electromechanical Coupling Factor," Proc. IRE **46**, 764-778 (1958).

[6] S. Takahashi, S. Hirose and K. Uchino, "High-Power Piezoelectric Ceramics for Actuator Usage," Technical Rep. of Inst. Electron. Inf. Commun. Eng., Jpn., US95-23, EMD95-19, CPM95-31, p.23-30 (1995).

[7] K. Uchino, H. Negishi and T. Hirose, "Drive Voltage Dependence of Electromechanical Resonance in PLZT Piezoelectric Ceramics," Jpn. J. Appl. Phys. **28**, Suppl. 28-2, 47-49 (1989).

[8] S. Hirose and H. Shimizu, "Simple Method of Measuring Vibration Displacement Parallel to Surface by Optical-Fiber Displacement Sensor Detecting the Amount of Reflected Light," J. Acoustic Soc. Jpn. **47**, 35-39 (1991).

[9] S. Hirose, S. Takahashi, K. Uchino, M. Aoyagi and Y. Tomikawa, "Measuring Methods for High-Power Characteristics of Piezoelectric Materials," Proc. Mater. for Smart Systems, Mater. Res. Soc. Vol.**360**, p.15-20 (1995).

[10] K. Uchino, *Piezoelectric Actuators and Ultrasonic Motors*, Kluwer Academic Publishers, MA, p.180-200.

FIGURE CAPTIONS

Fig. 1 Mechanical Q versus basic composition x at effective vibration velocity $v_0 = 0.05$ m/s and 0.5 m/s for $Pb(Zr_xTi_{1-x})O_3$ + 2.1 at% Fe ceramics.

Fig. 2 Conventional constant voltage measurement circuit.

Fig. 3 Admittance curve as a function of frequency measured around the resonance and antiresonance modes under a constant voltage condition.

Fig. 4 Resonance curves for various vibration velocity measured by the constant voltage method.

Fig. 5 AC voltage dependence of the electromechanical parameters for a fixed DC bias of 35 V. H and S denote hard and soft piezoelectrics, respectively.

Fig. 6 Displacement versus motional current at the resonance frequency.

Fig. 7 Automatic measurement system with constant driving current.

Fig. 8 Resonance curves measured by the constant current method.

Fig. 9 Vibration velocity dependence of the quality factor and the temperature rise for both A- (resonance) and B- (antiresonance) type resonances of a rectangular PZT resonator.

Fig.10 Pulse drive technique for measuring the electromechanical parameters.

Fig.11 Applied electric field dependence of the electromechanical parameters in a multimorph piezoelectric actuator measured by the pulse drive method.

Fig.12 Comparison of high power characteristics in a soft piezoelectric PZT-based ceramic sample measured by the constant current and pulse drive methods.

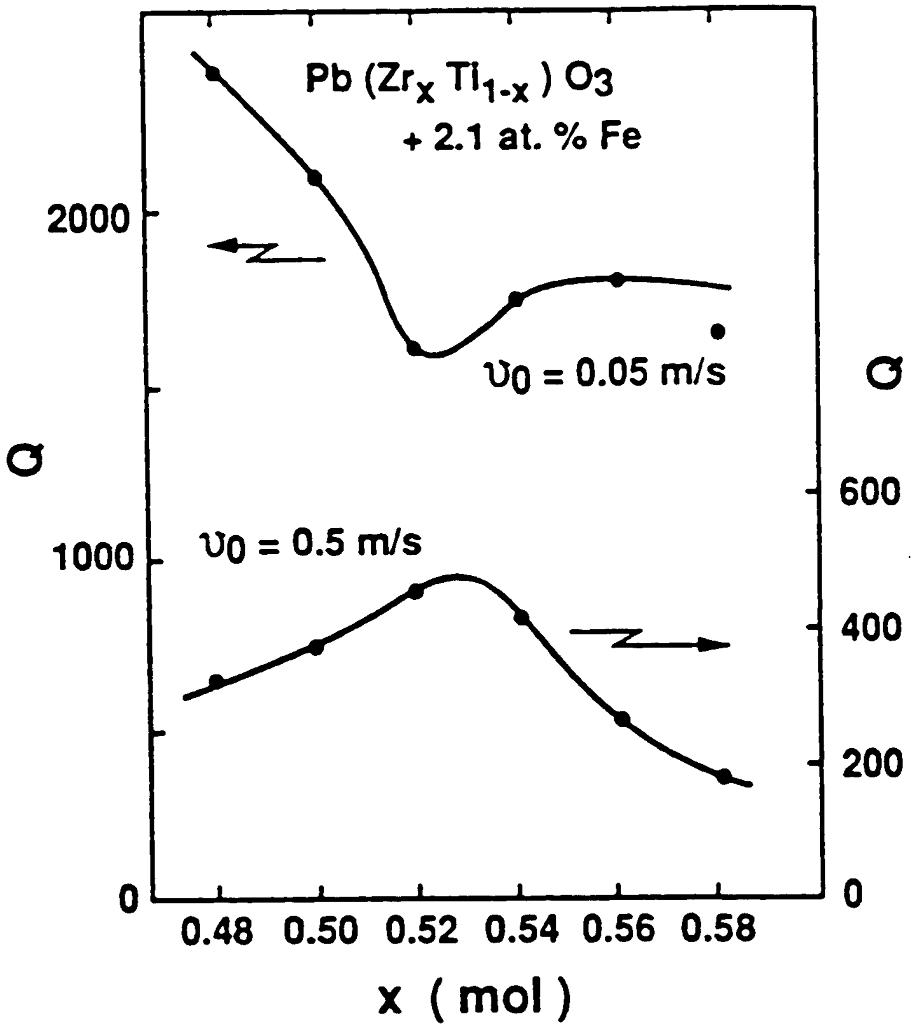
Pb (Zr$_x$ Ti$_{1-x}$) O$_3$
+ 2.1 at. % Fe
2000
1000
0
Q
υ_0 = 0.05 m/s
υ_0 = 0.5 m/s
Q
600
400
200
0
0.48
0.50
0.52
0.54
0.56
0.58
x (mol)

Fig. 1

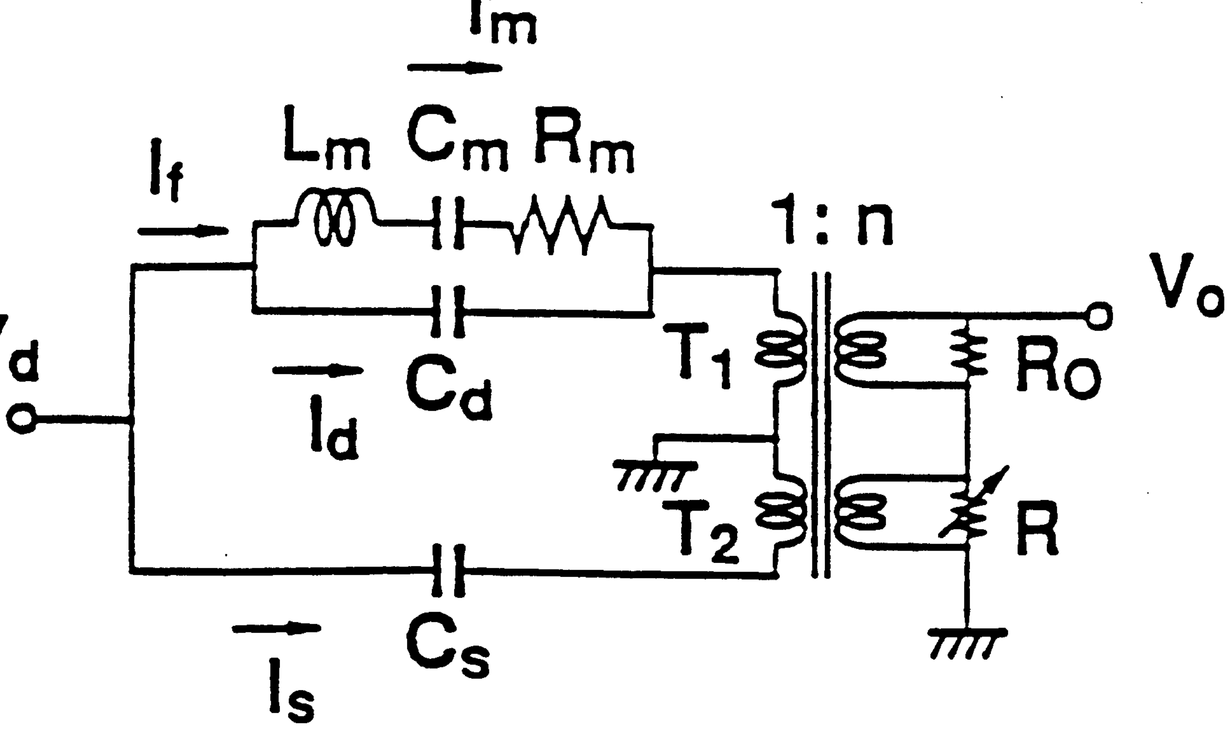

Fig. 2

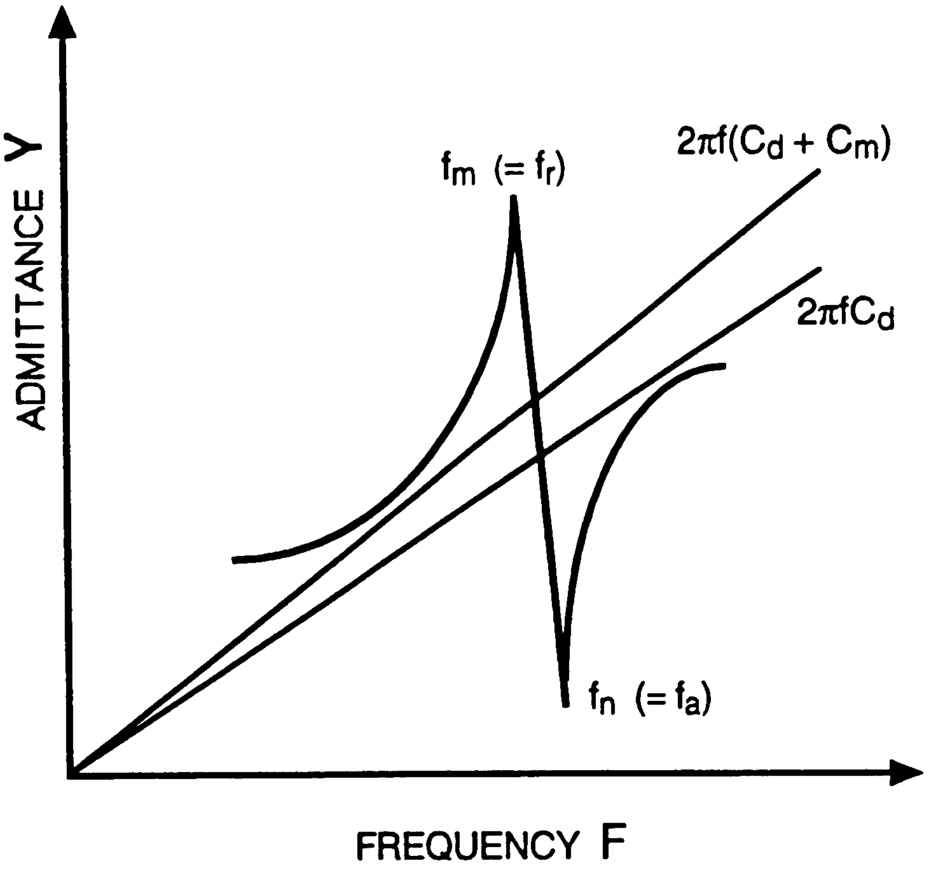

Fig. 3

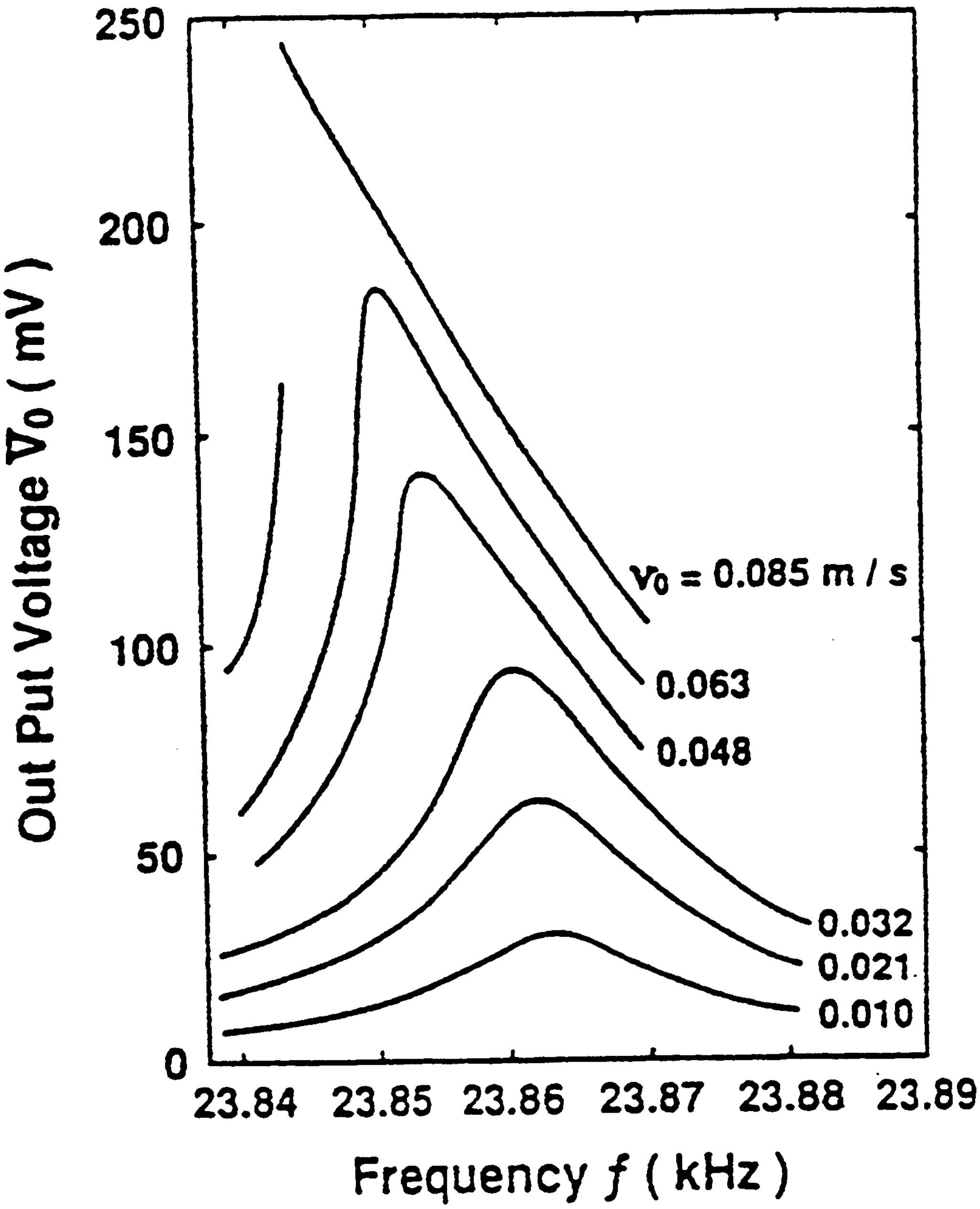

250
200
150
100
50
0
Out Put Voltage V_0 (mV)
V_0 = 0.085 m / s
0.063
0.048
0.032
0.021
0.010
23.84
23.85
23.86
23.87
23.88
23.89
Frequency f (kHz)

Fig. 4

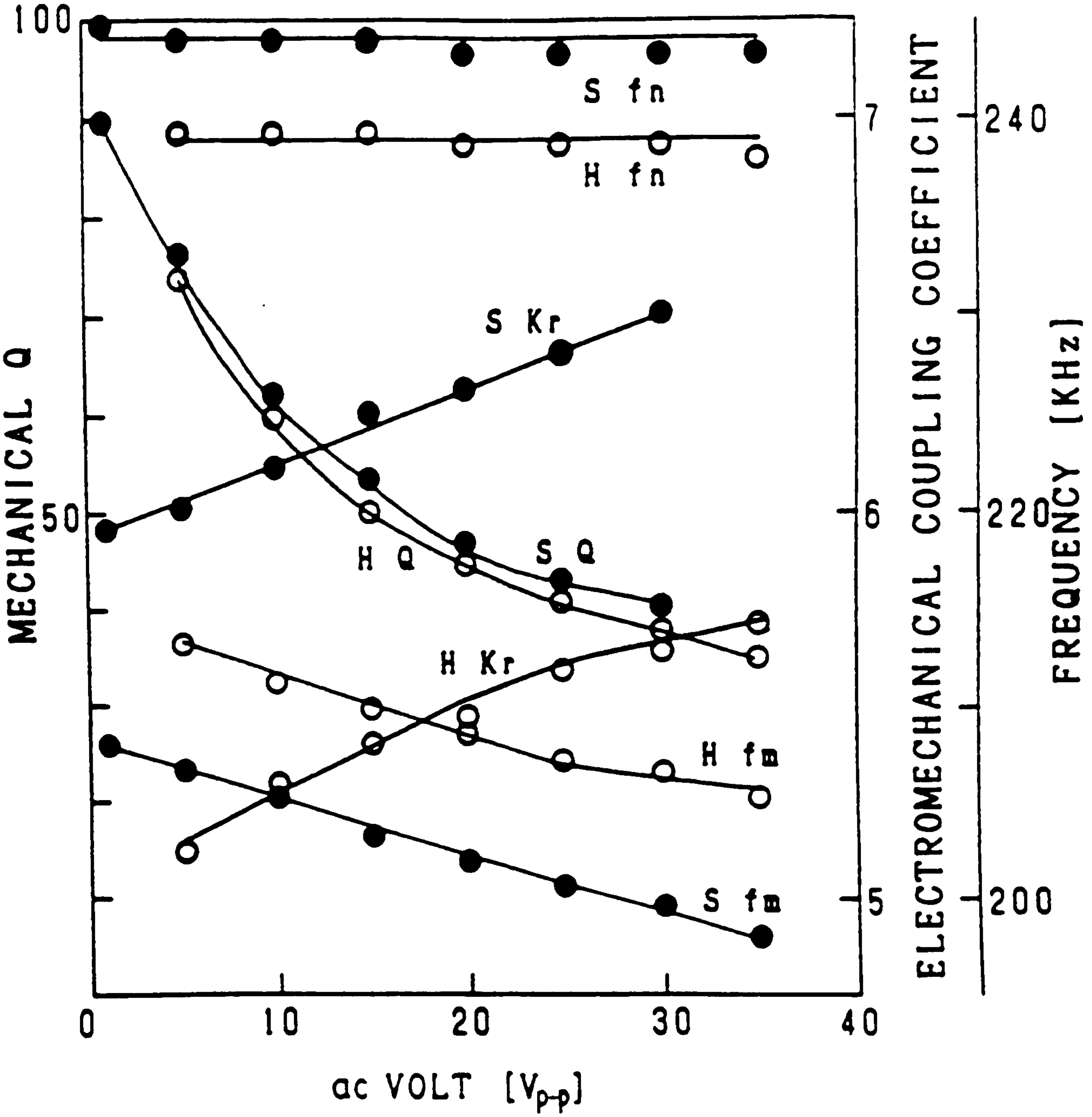

MECHANICAL Q
100
50
ELECTROMECHANICAL COUPLING COEFFICIENT
7
6
5
FREQUENCY [KHz]
240
220
200
S fn
H fn
S Kr
H Q
S Q
H Kr
H fm
S fm
0
10
20
30
40
ac VOLT [$V_{p\text{-}p}$]

Fig. 5

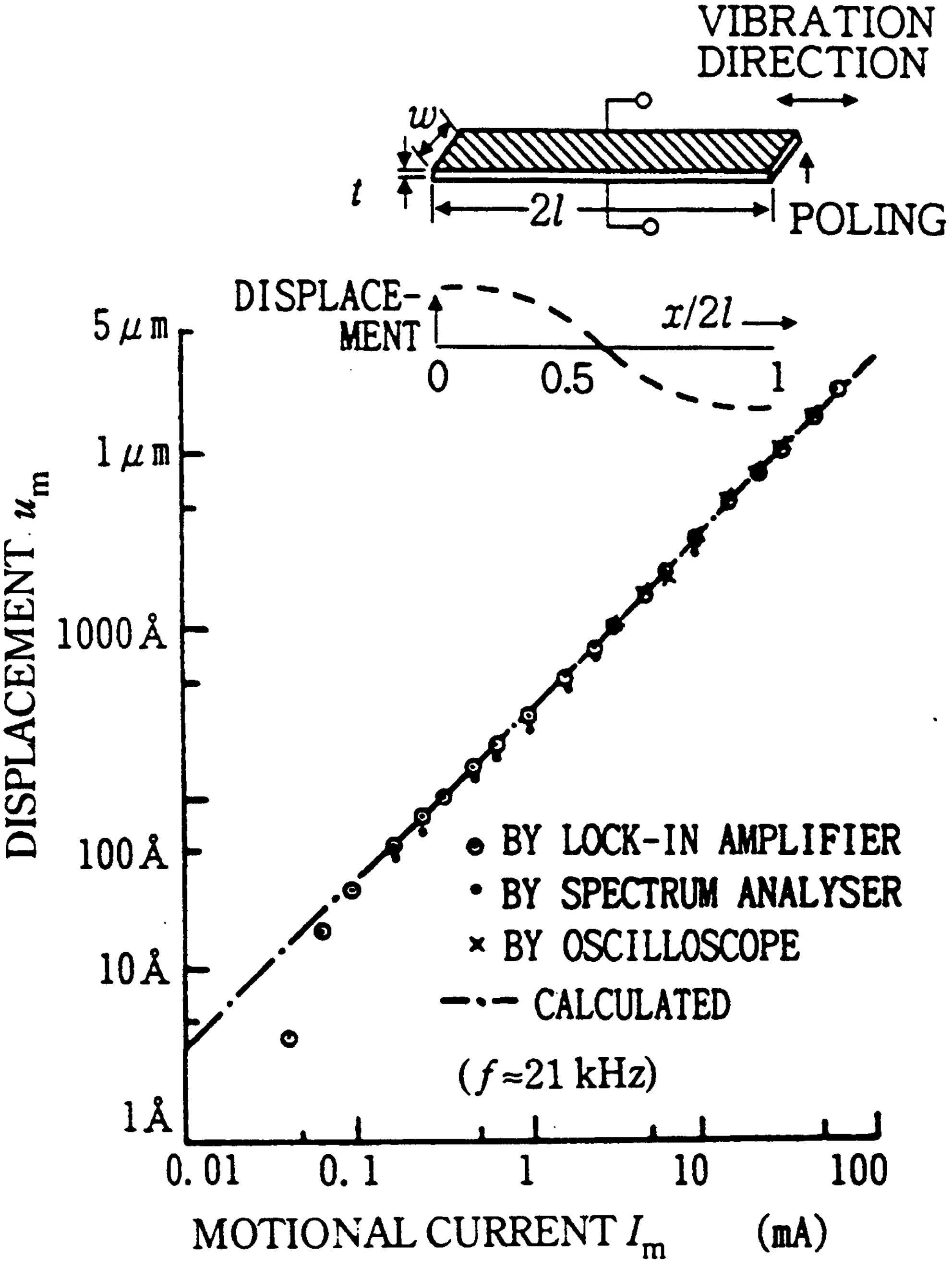
VIBRATION DIRECTION
w
t
2l
POLING
DISPLACEMENT
x/2l
0
0.5
1
5 μm
1 μm
1000 Å
100 Å
10 Å
1 Å
DISPLACEMENT u_m
BY LOCK-IN AMPLIFIER
BY SPECTRUM ANALYSER
BY OSCILLOSCOPE
CALCULATED
(f ≈ 21 kHz)
0.01
0.1
1
10
100
MOTIONAL CURRENT I_m (mA)

Fig. 6

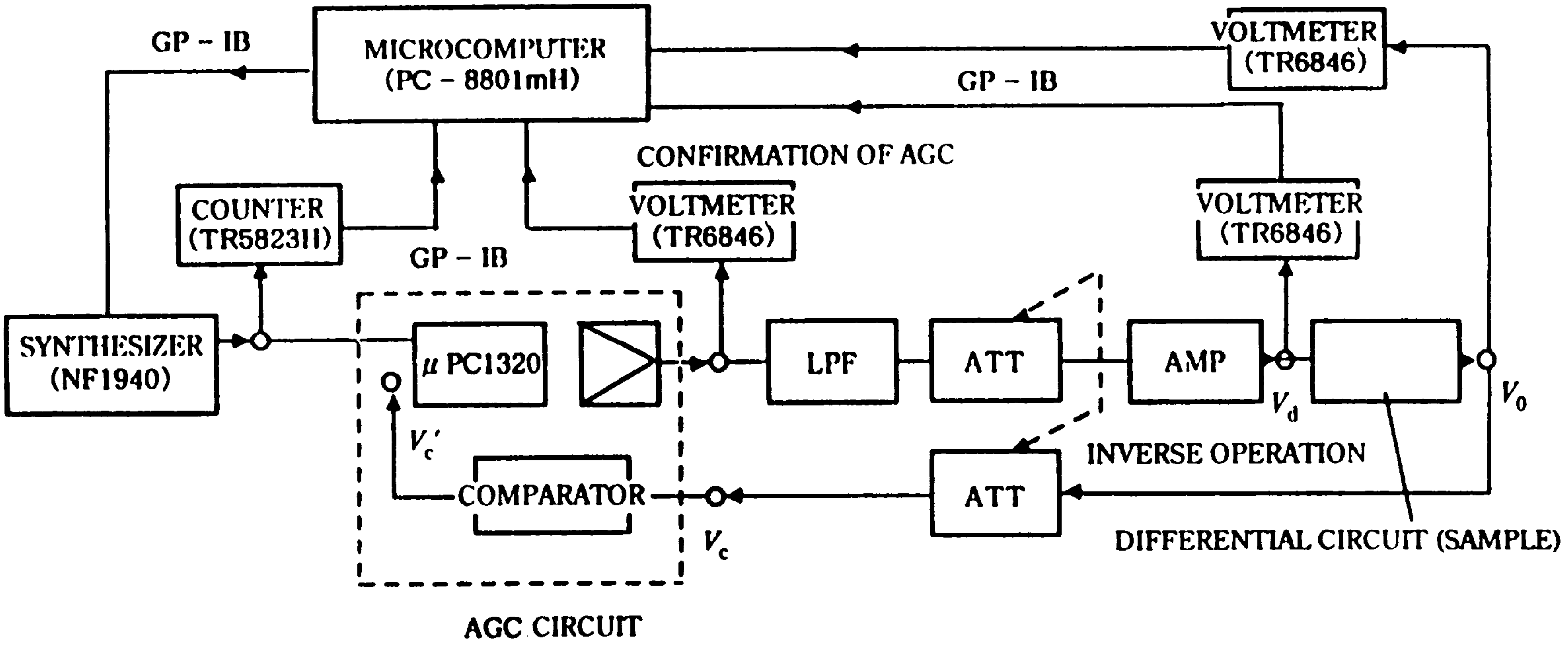
GP - IB
MICROCOMPUTER (PC - 8801mH)
VOLTMETER (TR6846)
GP - IB
CONFIRMATION OF AGC
COUNTER (TR5823H)
GP - IB
VOLTMETER (TR6846)
VOLTMETER (TR6846)
SYNTHESIZER (NF1940)
μ PC1320
LPF
ATT
AMP
V_d
V_0
V_c'
INVERSE OPERATION
COMPARATOR
ATT
V_c
DIFFERENTIAL CIRCUIT (SAMPLE)
AGC CIRCUIT

Fig. 7

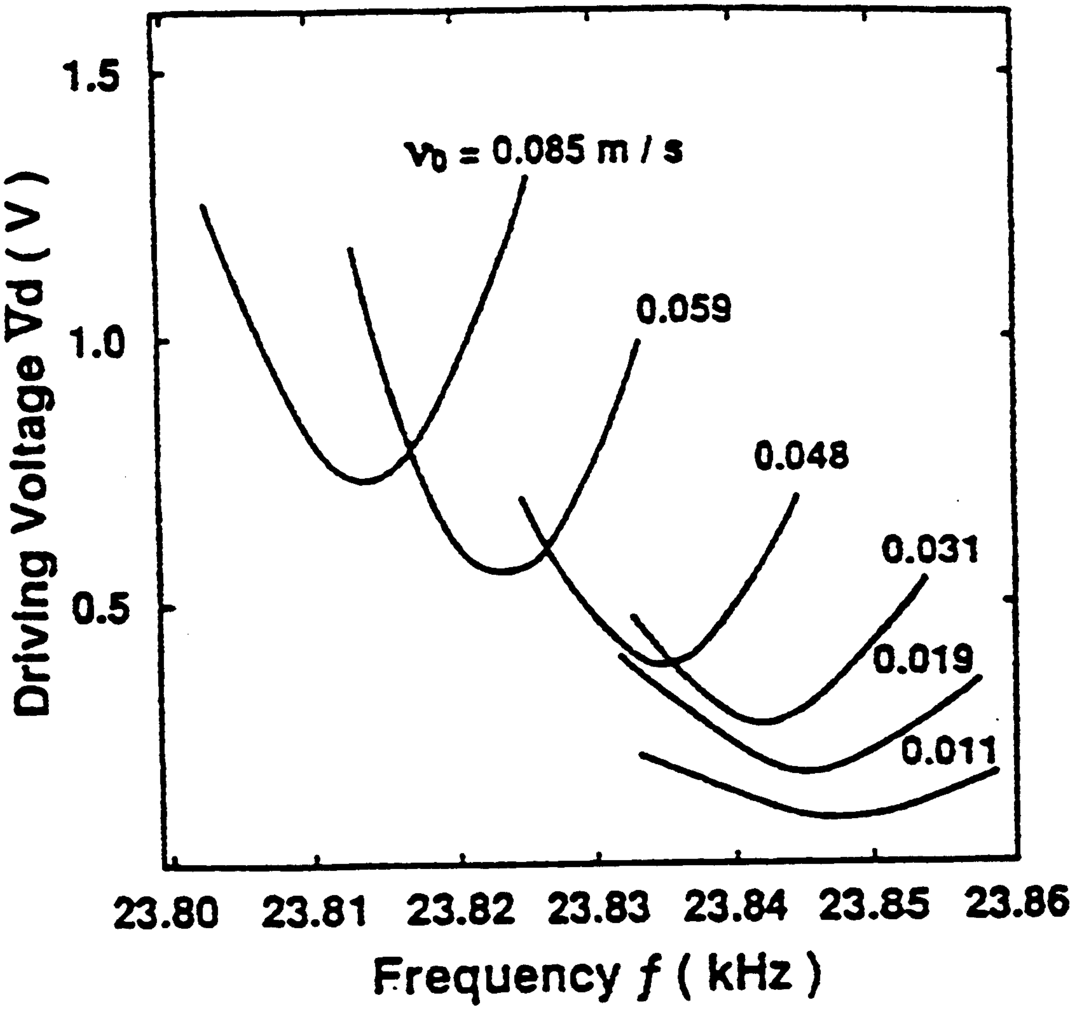
1.5
1.0
0.5
Driving Voltage Vd (V)
V_0 = 0.085 m / s
0.059
0.048
0.031
0.019
0.011
23.80
23.81
23.82
23.83
23.84
23.85
23.86
Frequency f (kHz)

Fig. 8

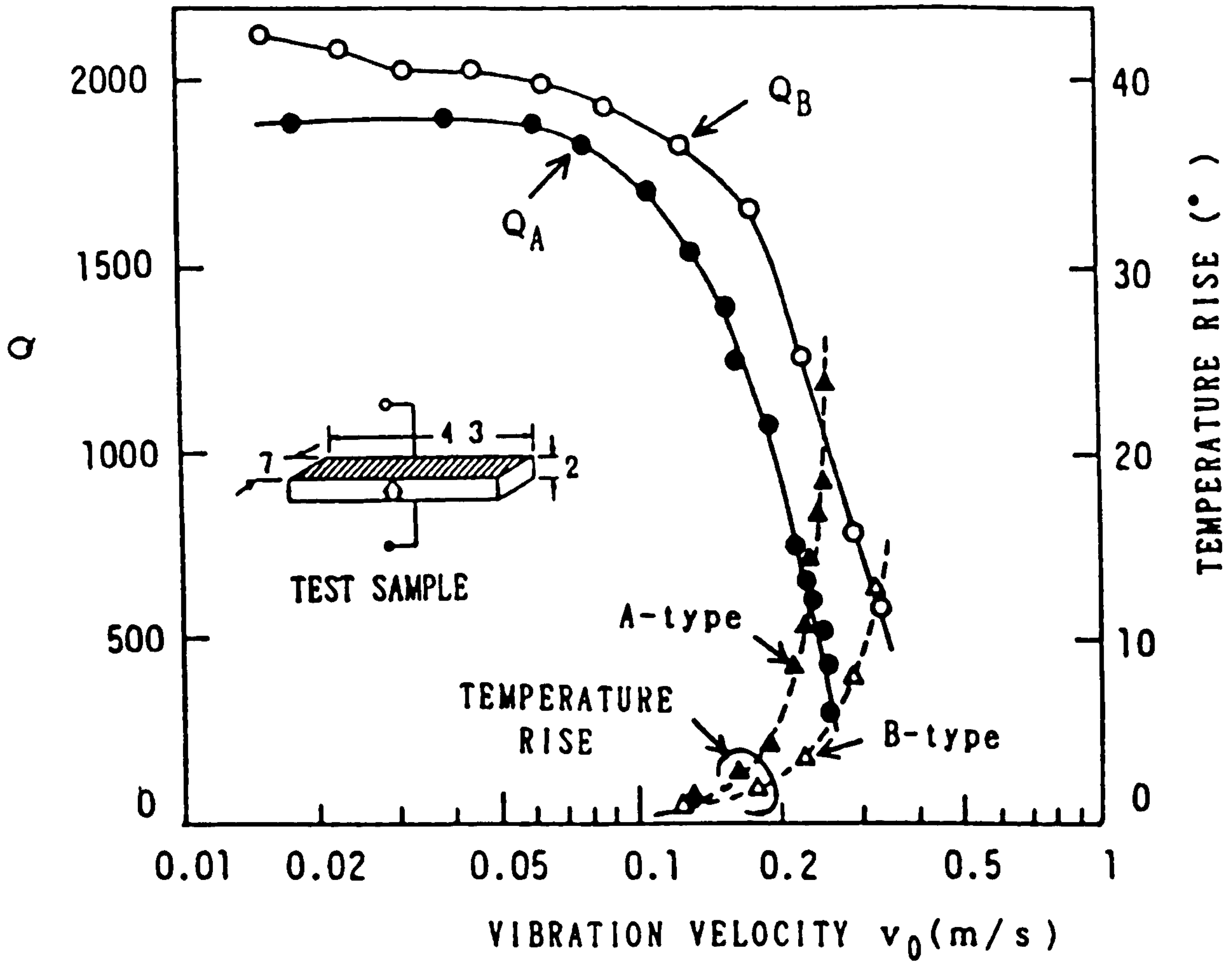
2000
1500
1000
500
0
Q
40
30
20
10
0
TEMPERATURE RISE (°)
Q_B
Q_A
4 3
1
2
7
TEST SAMPLE
A-type
B-type
TEMPERATURE RISE
0.01
0.02
0.05
0.1
0.2
0.5
1
VIBRATION VELOCITY v_0(m/s)

Fig. 9

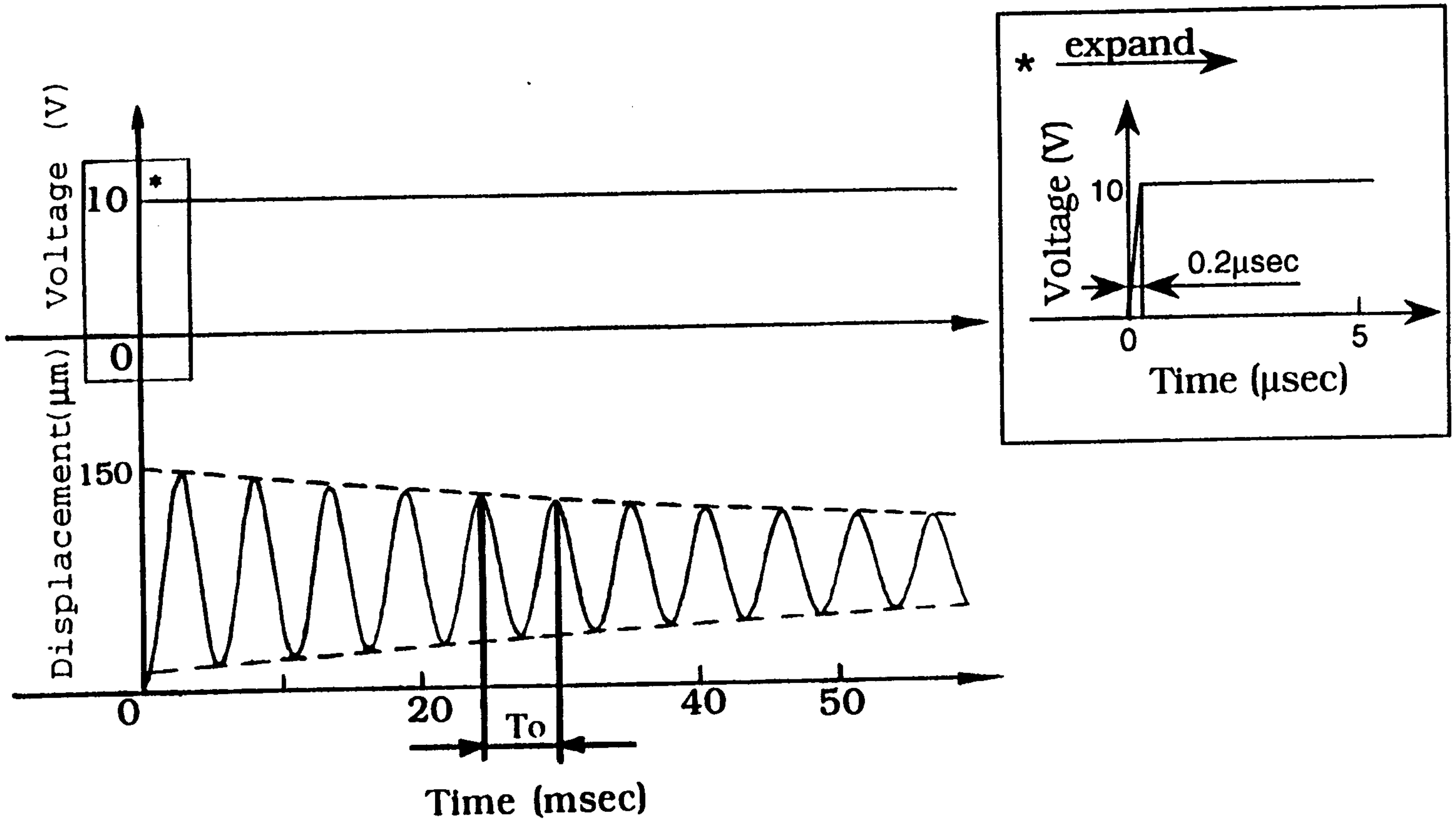
Voltage (V)
10
*
0
Displacement(µm)
150
0
20
40
50
To
Time (msec)
* expand
Voltage (V)
10
0.2µsec
0
5
Time (µsec)

Fig. 10

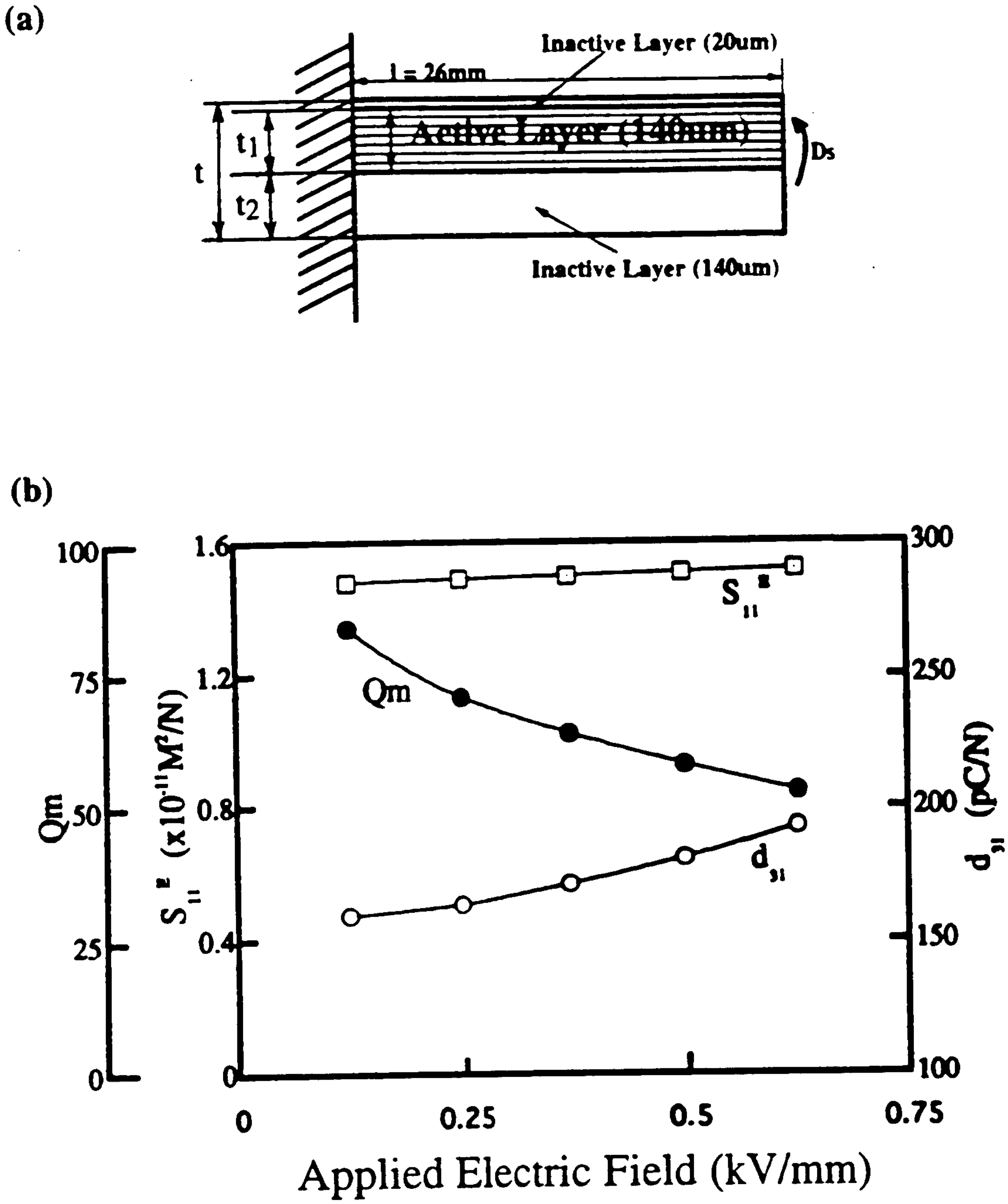

(a)
Inactive Layer (20um)
l = 26mm
Active Layer (140um)
t1
t
t2
Ds
Inactive Layer (140um)
(b)
Qm
100
75
50
25
0
S_{11}^{E} (x10^{-11}M^2/N)
1.6
1.2
0.8
0.4
0
S_{11}^{E}
Qm
d_{31}
d_{31} (pC/N)
300
250
200
150
100
0
0.25
0.5
0.75
Applied Electric Field (kV/mm)

Fig. 11

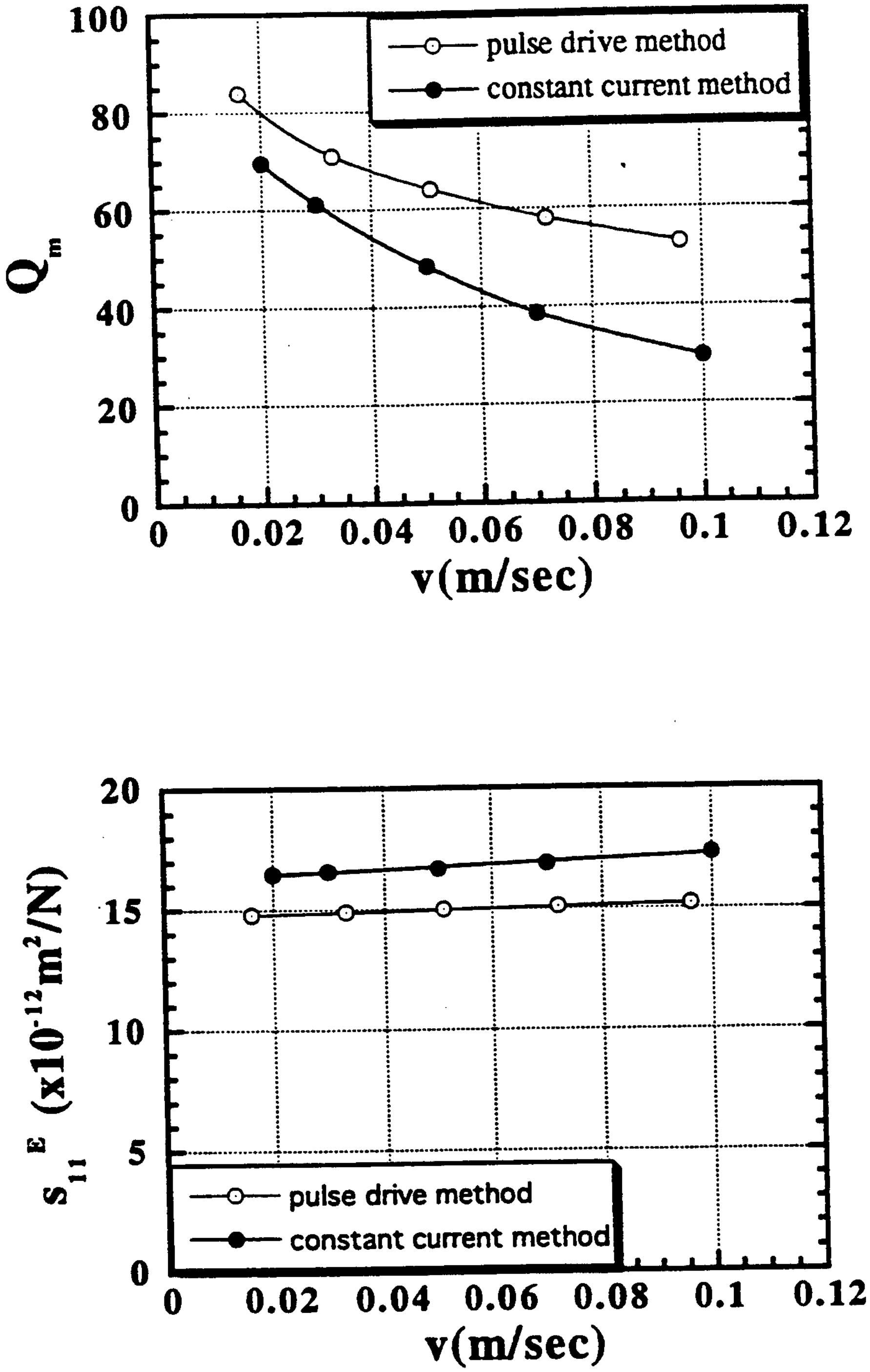
100
80
60
40
20
0
Q_m
pulse drive method
constant current method
0
0.02
0.04
0.06
0.08
0.1
0.12
v(m/sec)
20
15
10
5
0
s_{11}^{E} $(\times 10^{-12} m^2/N)$
pulse drive method
constant current method
0
0.02
0.04
0.06
0.08
0.1
0.12
v(m/sec)

Fig. 12

APPENDIX 71

HIGH ELECTROMECHANICAL COUPLING PIEZOELECTRICS - HOW HIGH ENERGY CONVERSION RATE IS POSSIBLE

KENJI UCHINO
International Center for Actuators and Transducers, Materials Research Laboratory
The Pennsylvania State University, University Park, PA 16802

ABSTRACT

A new category of piezoelectric ceramics with very high electromechanical coupling was discovered in a lead zinc niobate:lead titanate solid solution in a single crystal form. The maximum coupling factor k_{33} reaches 95%, which corresponds to the energy conversion rate twice as high as the conventional lead zirconate titanate ceramics. This paper reviews the previous studies on superior piezoelectricity in relaxor ferroelectric: lead titanate solid solutions and on the possible mechanisms of this high electromechanical coupling.

KEY WORDS: electromechanical coupling, piezoelectric, relaxor ferroelectric, domain motion

INTRODUCTION

Lead zirconate-titanate (PZT) ceramics are well known piezoelectrics widely used in many transducers. Their applications include gas igniters, force/acceleration sensors, microphones, buzzers, speakers, surface acoustic wave filters, piezoelectric transformers, actuators, ultrasonic motors, ultrasonic underwater transducers, and acoustic scanners [1,2]. Particularly in recent medical acoustic imaging, higher electromechanical coupling materials are eagerly required to improve the image resolution. Under these circumstances, relaxor ferroelectric: lead titanate solid solution systems with superior electromechanical coupling factors to the conventional PZT have been refocused, which were initially discovered in a lead zinc niobate:lead titanate system by the author's group in 1981 [3].

This paper reviews the previous studies on superior piezoelectricity in relaxor ferroelectric: lead titanate solid solutions, then on peculiar domain motions in these materials, finally possible mechanisms are considered for this extremely high electromechanical coupling.

ELECTROMECHANICAL COUPLING FACTORS

The terminologies, electromechanical coupling factor and efficiency are sometimes confused. Let us consider them at first. The electromechanical coupling factor k is defined as

$$k^2 = (\text{Stored mechanical energy / Input electrical energy}) \quad (1)$$

or

$$= (\text{Stored electrical energy / Input mechanical energy}). \quad (2)$$

When an electric field E is applied to a piezoelectric actuator, since the input electrical energy is $(1/2)\,\varepsilon_0\varepsilon\, E^2$ per unit volume and the stored mechanical energy per unit volume under zero external stress is given by $(1/2)\,x^2 / s = (1/2)\,(d\,E)^2 / s$, k^2 can be calculated as

$$\begin{aligned} k^2 &= [(1/2)\,(d\,E)^2 / s] \,/\, [(1/2)\,\varepsilon_0\varepsilon\, E^2] \\ &= d^2 / \varepsilon_0\varepsilon \cdot s. \end{aligned} \quad (3)$$

On the other hand, the efficiency η is defined as

$$\eta = (\text{Output mechanical energy}) / (\text{Consumed electrical energy}) \quad (4)$$

or

$$= (\text{Output electrical energy}) / (\text{Consumed mechanical energy}). \quad (5)$$

In a work cycle (e. g. an electric field cycle), the input electrical energy is transformed partially into mechanical energy and the remaining is stored as electrical energy (electrostatic energy like a capacitor) in an actuator. Then, this ineffective energy can be returned to the power source, leading to near 100 % efficiency, if the loss is small. Typical values of dielectric loss in PZT are about 1 - 3 %.

The electromechanical coupling factor is different according to the sample geometry. Figure 1 shows two sample geometries corresponding to k_{33} and k_{31}, which we will discuss later. In some particular applications such as Non-Destructive Testing, large piezoelectric anisotropy, i. e. a large value of the ratio k_{33}/k_{31}, is required to improve the image quality in addition to a large value of k_{33} itself. However, the empirical rule suggests that these two requirements are contradictory to each other. In Figure 2 we plotted the k_{33} versus k_{31} relation for various perovskite oxide piezoelectric polycrystal and single crystal samples such as $Pb(Zr,Ti)O_3$, $PbTiO_3$, $Pb(Zn_{1/3}Nb_{2/3})O_3$ and $Pb(Mg_{1/3}Nb_{2/3})O_3$ based compositions [4]. It is obvious from this convex tendency that the piezoelectricity becomes isotropic (i. e. the k_{33}/k_{31} ratio approaches to 1) with increasing the electromechanical coupling factor (i. e. the k_{33} value).

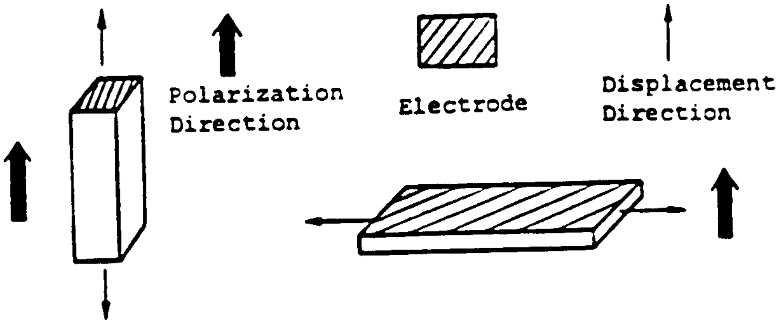

(a) k_{33} (b) k_{31}

Fig.1 Typical vibration modes of piezoelectric devices.

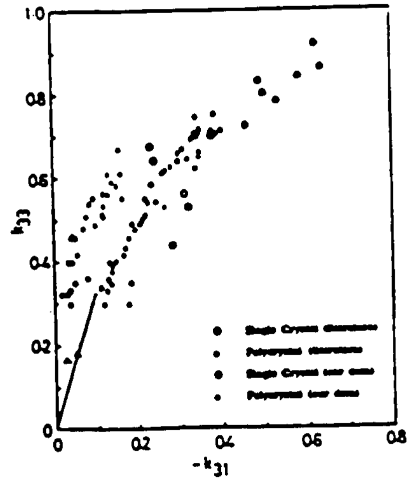

Fig.2 Relation between k_{33} and k_{31} for various perovskite oxide piezoelectrics.

HIGH ELECTROMECHANICAL COUPLING MATERIALS

Morphotropic Phase Boundary Composition

Conventionally, $Pb(Zr,Ti)O_3$ (PZT), $PbTiO_3$ (PT) and PZT based ternary ceramics with a small amount of a relaxor ferroelectric have been utilized for piezoelectric applications. Figure 3 shows the composition dependence of permittivity and electromechanical coupling factor k_p in the PZT system. It is notable that the morphotropic phase boundary (MPB) composition between the rhombohedral and tetragonal phases exhibits the maximum enhancement in dielectric and piezoelectric properties: this is explained in terms of a phenomenological theory [5]. The physical properties of a perovskite solid solution between A and B, (1-x) A - x B, can be estimated through the Gibbs elastic energy of a solid solution, if we suppose a linear combination of the Gibbs elastic energy of each component:

$$\begin{aligned} G_1(P,X,T) = &(1/2)[(1-x)\alpha_A + x\alpha_B]\,P^2 + (1/4)[(1-x)\beta_A + x\beta_B]\,P^4 \\ &+ (1/6)[(1-x)\gamma_A + x\gamma_B]\,P^6 \\ &- (1/2)[(1-x)s_A + xs_B]\,X^2 - [(1-x)Q_A + xQ_B]\,P^2\,X, \end{aligned} \qquad (6)$$

where $\alpha_A = (T - T_{0,A}) / \varepsilon_0 C_A$ and $\alpha_B = (T - T_{0,B}) / \varepsilon_0 C_B$.

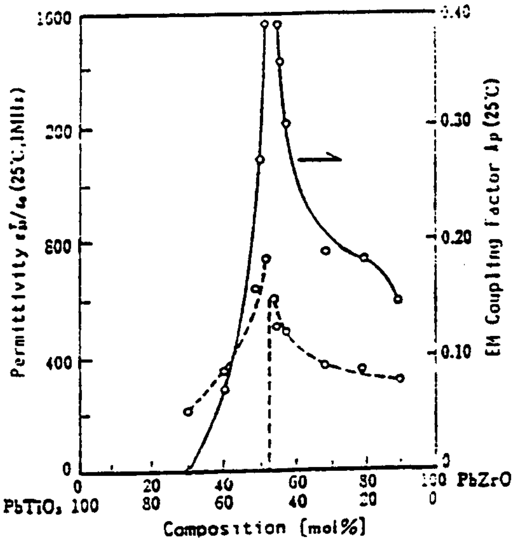

Fig.3 Composition dependence of permittivity and electromechanical coupling factor k_p in the PZT system.

The solution provides reasonable first-order estimates of the Curie temperature, spontaneous polarization and strain, as well as the enhancement of the permittivity, piezoelectric constant and electromechanical coupling at the MPB composition.

Note that in virgin samples of piezoelectric ceramics, the polarizations of grains (micro single crystals making up a polycrystalline sample) are randomly oriented (or domains are oriented randomly even in each grain, if the grain size is large enough for a multi-domain state) so as to cancel the net polarization in total. In a similar fashion, the net strain is negligibly small under an external electric field. Hence, before use, it is necessary to apply a relatively large electric field (> 3 kV/mm) to align the polarization direction of each grain as much as possible. Such a treatment is called electric poling.

Relaxor Ferroelectric Based Composition

On the other hand, relaxor ferroelectrics such as $Pb(Mg_{1/3}Nb_{2/3})O_3$:$PbTiO_3$ compositions have been focused due to their giant electrostriction [6]. Few work has been conducted on piezoelectric properties at the MPB region before the trial by the author's group.

We focused on single crystals of $(1-x)Pb(Zn_{1/3}Nb_{2/3})O_3$- $xPbTiO_3$ (PZN-PT) which are relatively easily grown by a flux method over the whole composition range, compared with the case in the $Pb(Zr,Ti)O_3$ (PZT) system. This system exhibits a drastic change from a diffuse phase transition to a sharp transition with an increase of the PT content, x, correlating to the existence of a morphotropic phase boundary from a rhombohedral to a tetragonal phase around $x = 0.1$ [7]. Figure 4 shows the phase diagram of this system near the MPB region.

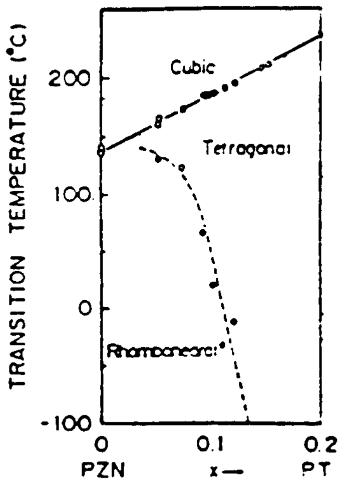

Fig.4 Phase diagram of $(1-x)Pb(Zn_{1/3}Nb_{2/3})O_3$- $xPbTiO_3$ (PZN-PT).

The most intriguing piezoelectric characteristics have been found in the MPB compositions with $0.05< x <0.143$, which exhibit two multiple phase transitions, changing the crystal symmetry from rhombohedral to tetragonal, then to cubic during heating [3]. Figure 5 shows the composition dependence of the pyroelectric coefficient $\lambda_3{}^T$, piezoelectric constants d_{ij}, electromechanial coupling factors k_{ij}, elastic compliances $s_{ij}{}^E$ and dielectric constant $\varepsilon_3{}^T$ measured at room temperature [3]. The superscript * is for the crystal with the rhombohedral symmetry at room temperature poled along the pseudocubic [001] direction. Figure 6 shows the temperature dependence of electromechanical coupling factors k_{33} and k_{31} measured with bar-shaped specimens of 0.91PZN-0.09PT [8]. Special notations have been introduced to describe the elastic and electromechanical constants for a sample poled in a certain direction. The $s^E{}_{[001]//}$ or $s^E{}_{[111]//}$ are defined from the resonance frequency of a bar sample elongated and poled in the pseudocubic [001] or [111] axes, respectively. The [001] and [111] axes are the principle axes of the tetragonal and rhombohedral phases and also the poling directions for each sample. The coupling coefficients $k_{[001]//}$ and $k_{[111]//}$ are consequently calculated from the resonance and antiresonance frequencies of the same sample. All the electromechanical components show a very large kink anomaly at the rhombohedral-tetragonal transition temperature, and a rapid decrease in k or an increase in d and s^E on approaching the Cuie point. These components vanish just above the Curie point.

Table I summarizes the elastic, piezoelectric, electromechanical and dielectric constants and the spontaneous polarization of 0.91PZN-0.09PT for the rhombohedral and tetragonal phases. It is important that the sample electrically poled along the pseudocubic [001] axis (not the principal axis in the rhombohedral phase!) reveals a very large piezoelectric constant $d_{[001]//} = 1.5\text{x}10^{-9}$

C/N and a high electromechanical coupling factor $k_{[001]//} = 0.92$ at room temperature, both of which are much larger than $d_{[111]//}$ and $k_{[111]//}$, respectively. Also these are the highest values among all perovskite piezoelectric materials reported so far. It was found that such a high electromechanical coupling factor could not be explained consistently in terms of a mono-domain single crystal model without considering the complicated domain dynamical motion.

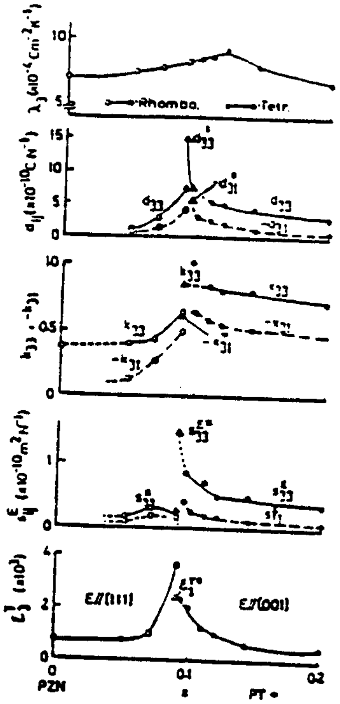

Fig.5 Composition dependence of the pyroelectric coefficient λ_3^T, piezoelectric constants d_{ij}, electromechanial coupling factors k_{ij}, elastic compliances s_{ij}^E and dielectric constant ε_3^T measured at room temperature.

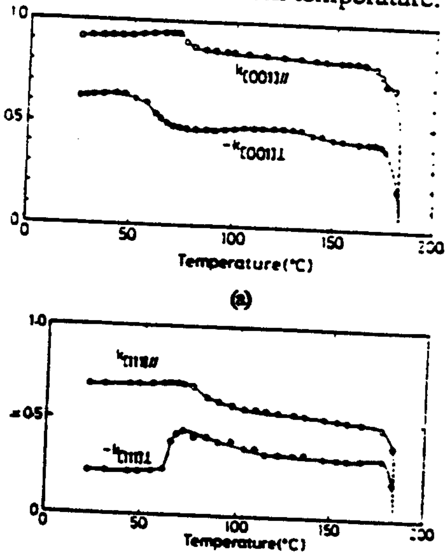

(b)

Fig.6 Temperature dependence of electromechanical coupling factors k_{33} and k_{31} measured with bar-shaped specimens of 0.91PZN-0.09PT.

Table I Elastic, piezoelectric, electromechanical and dielectric constants and the spontaneous polarization of 0.91PZN-0.09PT for the rhombohedral and tetragonal phases.

	Rhomb. phase	Tet. phase	Unit
Temp.	25	130	°C
$s^E_{[111]\perp}$	18	15.5	
$s^E_{[111]//}$	13.6	10.3	
$s^E_{[001]\perp}$	36.9	17.7	
$s^E_{[001]//}$	143	56	$(\mathrm{TPa})^{-1}$
$s^D_{[111]\perp}$	17.1	13.9	
$s^D_{[111]//}$	7.6	7.3	
$s^D_{[001]\perp}$	22.6	13.6	
$s^D_{[001]//}$	21.8	17.6	
$-d_{[111]\perp}$	194	352	
$d_{[111]//}$	625	450	pC/N
$-d_{[001]\perp}$	493	266	
$d_{[001]//}$	1570	795	
$-k_{[111]\perp}$	0.23	0.32	
$k_{[111]//}$	0.68	0.53	—
$-k_{[001]\perp}$	0.62	0.48	
$k_{[001]//}$	0.92	0.83	
$\epsilon^T_{[111]//}$	4100	8200	
$\epsilon^T_{[001]//}$	2200	1880	—
$\epsilon^S_{[111]//}$	2200	—	
$\epsilon^S_{[001]//}$	295	570	
P_s	0.52	0.30	$\mathrm{C/m^2}$

Recently, two groups of Yamashita (Toshiba) and Shrout (Penn State) reconfirmed the author's original work, and extended the investigation to a wide range of relaxor ferroelectrics such as $Pb(Mg_{1/3}Nb_{2/3})O_3$-PT, $Pb(Sc_{1/2}Ta_{1/2})O_3$-PT and $Pb(Sc_{1/2}Nb_{1/2})O_3$-PT. Large electromechanical coupling factors k_p, k_{33} and piezoelectric constant d_{33} of these binary systems are listed in Table II.

Table II Large electromechanical coupling factors k_p, k_{33} and piezoelectric constant d_{33} of relaxor ferroelectric binary systems.

MATERIAL	FEATURE	k_p (%)	k_{33} (%)	d_{33} (pC/N)	REFERENCE
PZT 53/47	Polycrystal	52	67	220	[9]
		67	76	400	[10]
PZN:PT 91/9	Single crystal		92	1500	[8]
PMN:PT 67/33	Polycrystal	63	73	690	[11]
	Single crystal			1500	[12]
PST:PT 55/45	Polycrystal	61	73	655	[13]
PSN:PT 58/42	Polycrystal	71	77	450	[14]

Measurements on electric field-induced polarization and strain were carried out on a pure PZN single crystal by Shrout et al [15]. The polarization and strain curves are plotted for the <111> (the spontaneous polarization direction!) and <100> orientations in Fig. 7. Even though the [100] plate sample showed the "ideal" P vs. E or strain vs. E behaviors of a mono-domain crystal, notice that the absolute value of P is much larger in the [111] plate sample; this indicates again the spontaneous polarization along the <111> axis. He also reported the poling direction-dependent electromechanical coupling factors in PZN: k[001]// = 0.85 was much larger than k[111]// = 0.38, in a similar fashion to 0.91PZN-0.09PT. These results also suggest the importance of the domain contribution to dielectric and piezoelectic properties.

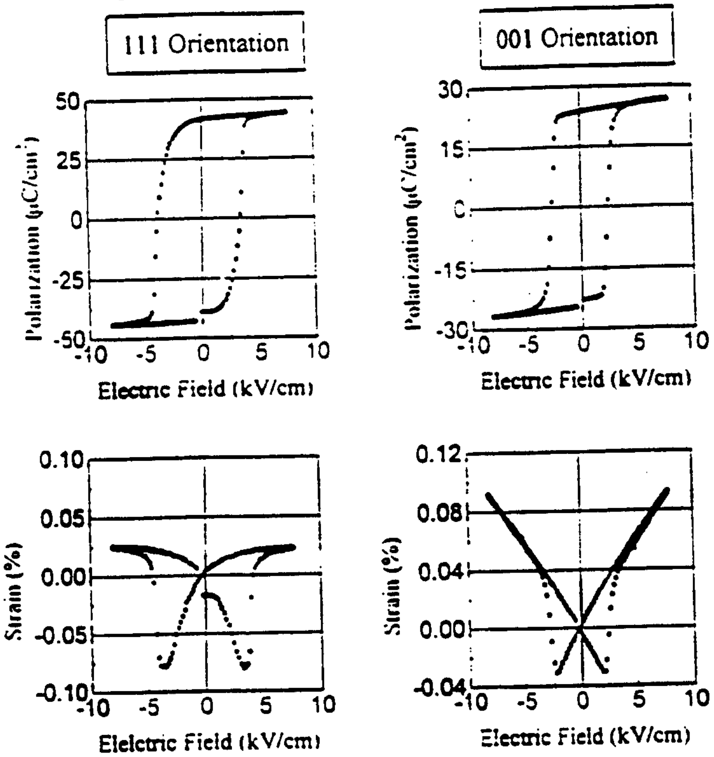

Fig.7 Polarization and strain curves plotted for the <111> and <100> orientations in pure PZN.

DOMAIN MOTION IN RELAXOR FERROELECTRICS

Historical Background of Domain-Controlled Piezoelectric Transducers

Historically, most of the studies on ferroelectric single crystals and polycrystalline materials have aimed to simulate the mono-domain state, desiring to derive the better characteristics from the specimens; ceramics as well as single crystals were poled electrically and/or mechanically to reorient the domains along one direction. Researches on controlling domains intentionally can be found in electrooptic devices and ferroelectric memory devices in particular. However, the intentional domain control has not been utilized or applied occasionally in the actuator and transducer areas. Recent requirements for the higher performance transducers encourages the investigation on the possibility of domain-related effect usage.

Developments in high resolution CCD optical microscope systems and in single crystal growth techniques are also accelerating these domain-controlled piezoelectric devices. A high resolution CCD (Charge Coupled Device) camera was attached to a Nikon Transmission Petrographic Microscope which was connected to a monitor and VCR (illustrated in Fig.8)[16]. The birefringence between the domains permits the observation of the domains with the polarizing light microscope. The microscope system also allows magnifications up to x1300 on the monitor. The temperature-controlled sample stage (Linkam Inc.) in conjunction with the deep focal point of the objective lenses allows an electric field to be safely applied across the sample between -185 and 600°C. The stationary and switching domains can be instantaneously recorded by the VCR and observed on the monitor.

Single crystal growth methods of PZN-PT are described here for example [8]. The powders used were Pb_3O_4, TiO_2, ZnO and Nb_2O_5. Excess ZnO was added in some cases to counteract the evaporation during crystal growth. PbO was used as the flux. The mole ratio of the flux to composition was varied from 1:1 to 3:2. The batch sizes were changed from 75 grams to 500 grams. The raw powders were loaded into a platinum crucible and charged several times at 900°C until the crucible was full. The crucible was then partially sealed with a Pt lid. The sealed Pt crucible was placed in an alumina crucible and sealed once again. The crucibles were placed in a box furnace with a temperature controller. The cooling rate was veried from 0.5 to 3°C/hr down to 900°C. After the temperature reaches 900°C, the furnace was fast cooled at 50°C/hr to room temperature. The single crystals were leached from from the flux with warm 25 vol% nitric acid. Single crystals with a dimension of 1 cm^3 could be obtained.

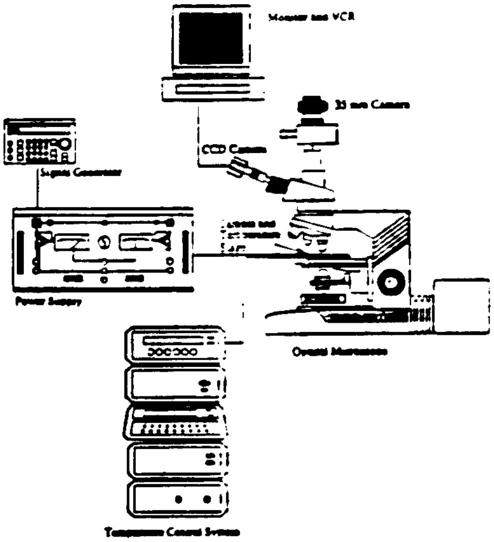

Fig.8 CCD optical microscope system.

Domain Configurations in PZN-PT

Let us review the relation between domain configurations and physical properties in relaxor ferroelectrics. Figure 9 shows the static domain configurations for the samples of x = 0, 0.07 and 0.095 of $(1-x)Pb(Zn_{1/3}Nb_{2/3})O_3$- $xPbTiO_3$ (PZN-PT) [17]. The pure PZN did not exhibit large clear domains in the whole temperature range when it was unpoled (i. e. micro-domains). Rhombohedral domains could be described as having an ambiguous spindle-like morphology. Ambiguity refers to the variation of domain widths and lengths which appear as an interpenetrating structure. With increasing the PT content, this small spindle-like domain was enlarged and the domain wall became sharp. Tetragonal domains appear to have a well defined lamellar morphology, and are either at right angles or antiparallel. Therefore, even though the widths and lengths of the tetragonal domains vary, the divisions between the domains are well defined and no interpenetrating structure is observable. Notice that the morphotropic phase boundary (MPB) composition (x = 0.095) shows the coexistence of both rhombohedral (spindle-like) and tetragonal domains (sharp straight line); the two-phase coexistence can not be found statically in normal ferroelectric materials such as $BaTiO_3$.

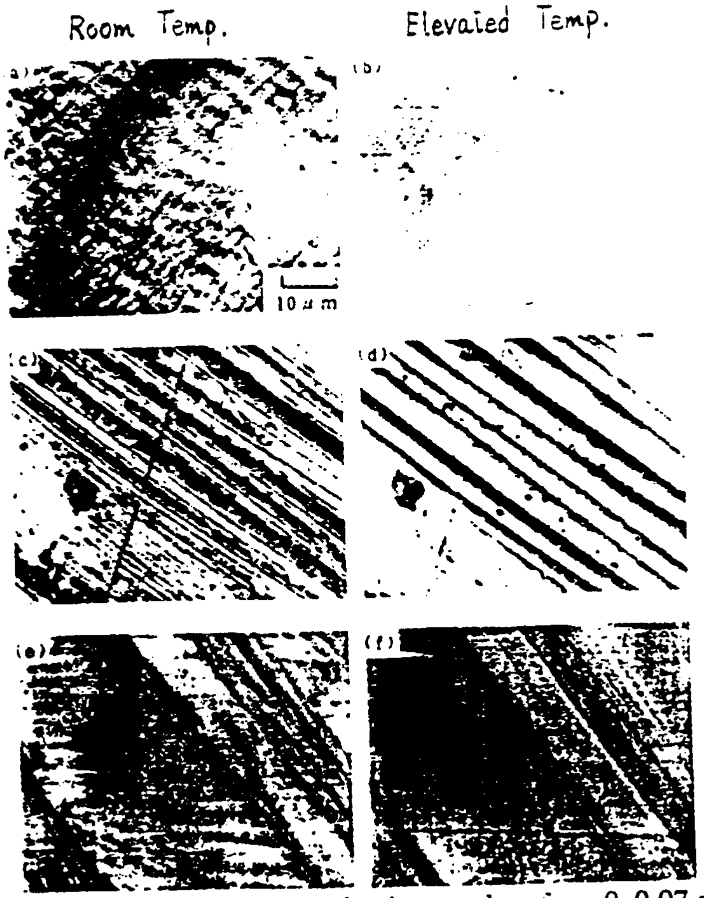

Fig.9 Static domain configurations for the samples of $x = 0$, 0.07 and 0.095 of $(1-x)Pb(Zn_{1/3}Nb_{2/3})O_3$- $xPbTiO_3$ (PZN-PT).

Figures 10 and 11 show the actual domain reversal processes and their schematical illustration under an applied electric field [18]. Sharp 90° domain walls corresponding to the tetragonal symmetry in the sample with $x = 0.2$ moved abruptly and rather independently each other above a coercive field of 1 kV/mm. The situation resembles to the case in normal ferroelectrics. On the contrary, pure PZN ($x = 0.0$) revealed very different domain motion. During electric field cycles, micro- to macro-domain growth occurred, and long narrow spindle-like domains (aspect ratio = 10) were arranged rather perpendicularly to the electric field (18 degree canted). When a field above 0.5 kV/mm was applied, the ambiguous domain walls rippled simultaneously in a certain size region, so that each domain should change synchronously like cooperative phenomena. The domain reversal front (180° domain wall) moved rather slower than in the sample of $x = 0.2$. It is noteworthy that the stripe period of the dark and bright domains (probably corresponding to up and down polarizations) was not changed by the domain reversal, and that each domain area changed under an AC external field with zero net polarization at zero field. Thus, the relaxor crystal is electrically-poled easily when an electric field is applied around the transition temperature, and depoled completely without any remanent polarization. This can explain large apparent secondary non-linear effects in physical properties such as electrostrictive and electrooptic phanomena, without exhibiting any hysteresis.

The relation between the dielectric property and the domain structure was clearly demonstrated in the permittivity measurement of the pure PZN. Figures 12(a) and 12(b) show the permittivity vs. temperature curves taken for the annealed (unpoled) and poled states of the PZN sample[19]. Large dielectric relaxation (frequency dependence of the permittivity) was observed in a wide temperature range below the Curie point for the unpoled state, while the dielectric dispersion was measured only in a narrow temperature range between 100°C and the Curie point for the poled state. Considering that below 100°C the PZN exhibits the micro- to macro-domain growth under a high electric field, we can conclude that the dielectric relaxation is attributed to the micro-domains. Thus, we learned how to control the micro- and macro-domains through temperature change and an external electric field, and how to change the dielectric dispersion, elastic and piezoelectric constants according to these phase transitions.

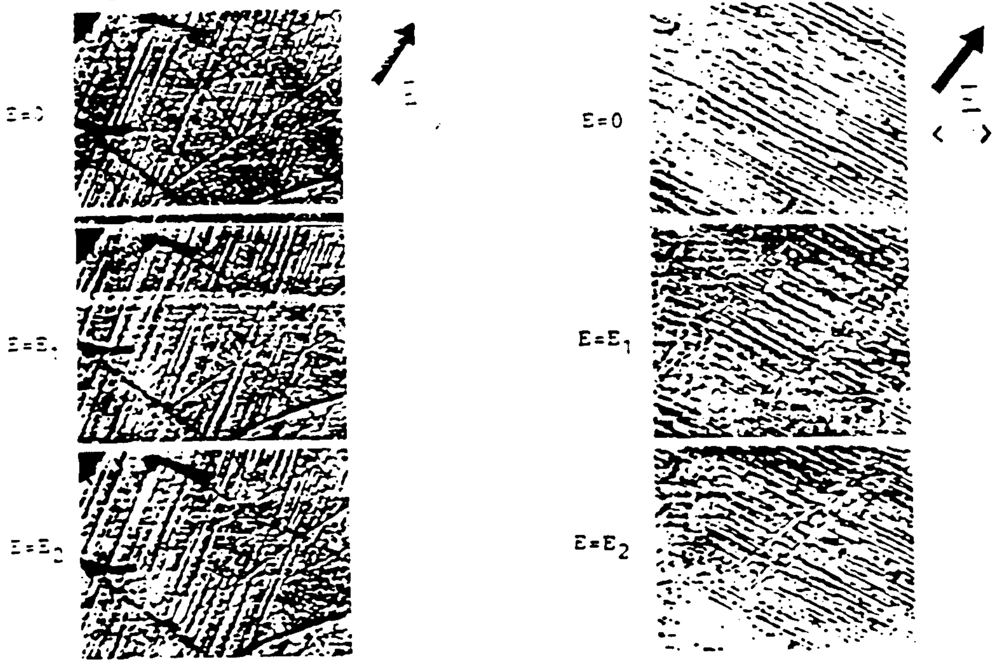

(a) (b)

Fig.10 Actual domain reversal processes under an applied electric field for the samples of $x = 0.2$ (a) and 0 (b) of $(1\text{-}x)Pb(Zn_{1/3}Nb_{2/3})O_3\text{-} xPbTiO_3$.

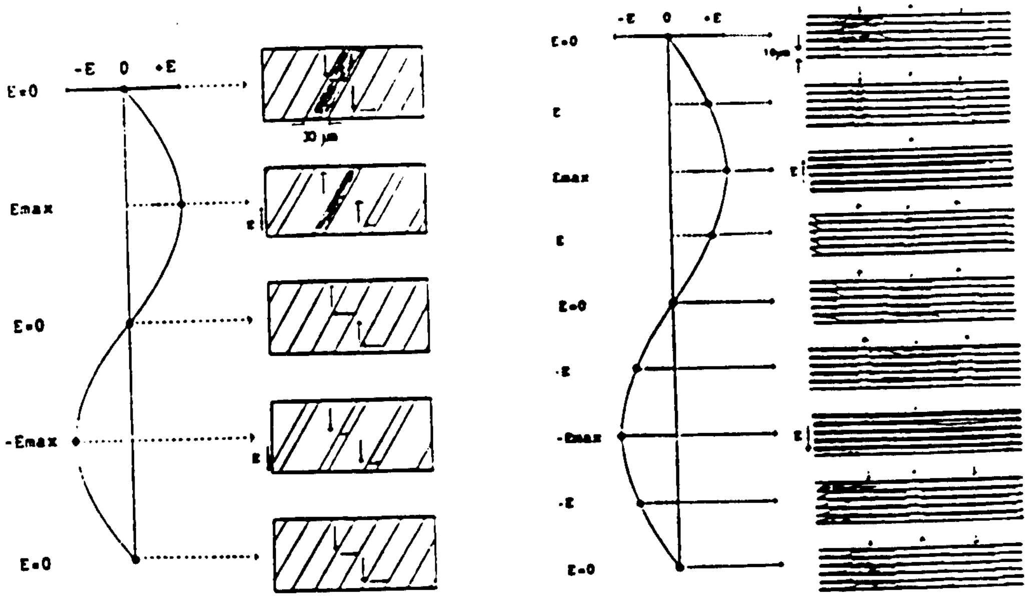

(a) (b)

Fig.11 Schematical illustration of the domain reversal processes under an applied electric field for the samples of $x = 0.2$ (a) and 0 (b) of $(1\text{-}x)Pb(Zn_{1/3}Nb_{2/3})O_3\text{-} xPbTiO_3$.

a.) A depoled 100%PZN single crystal measured on the <111>.

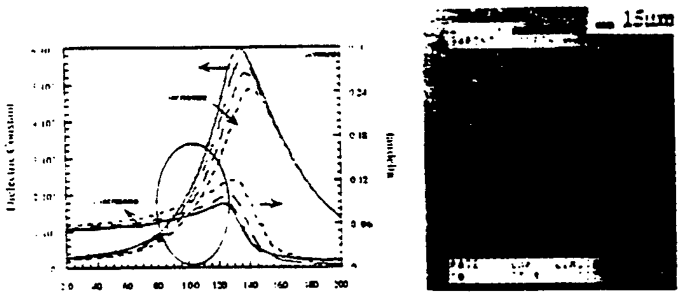

No field, 25°C

b.) A poled 100% PZN single crystal measured on the <111>.

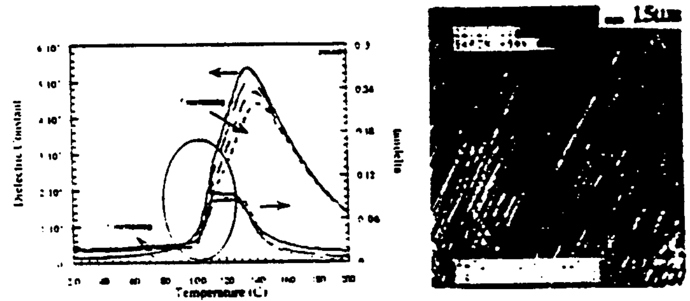

+6.3kV/cm DC, 25°C

Fig.12 Permittivity vs. temperature curves taken for the annealed (unpoled) state (a) and poled state (b) of the PZN sample.

Hierarchical Domain Structures

Figure 13 shows the domain structures observed in a 0.89PZN-0.11PT crystal, which exists on the morphotropic phase boundary. The typical tetragonal stripe domain pattern was observed without an external electric field at room temperature, while the spindle-like rhombohedral domain pattern appeared as overlapped on the stripe pattern, when the electric field was applied along the perovskite pseudo-cubic [111] directions. This domain hierarchy suggests that the morphotropic phase boundary composition may easily change the domain configuration and the crystal symmetry according to the applied electric field direction, much easily than in the normal ferroelectric PZT.

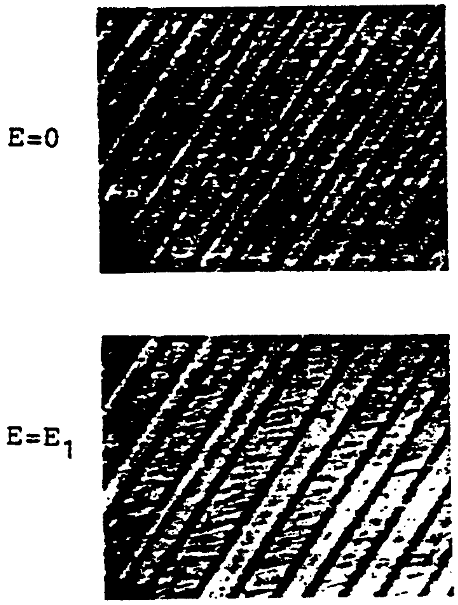

Fig.13 Domain structures observed in an MPB composition crystal 0.89PZN-0.11PT.

Future work will include the dynamic domain observation in the 0.91PZN-0.09PT sample (rhombohedral phase is stable at room temperature) poled along the perovskite [100] axis; this enhances remarkably the electromechanical coupling factor k up to 92 - 95 %. Also the possibility of the different poling direction which enhances the coupling factor more will be explored.

CONCLUSIONS

1. The electromechanical coupling factor k_{33} of more than 90 % can be obtained in the solid solutions between the relaxor and normal ferroelectrics.
2. Promising compositions include: $Pb(Zn_{1/3}Nb_{2/3})O_3$-$PbTiO_3$, $Pb(Mg_{1/3}Nb_{2/3})O_3$-$PbTiO_3$ and $Pb(Sc_{1/2}Nb_{1/2})O_3$-$PbTiO_3$.
3. The highest k in a single crystal form can be obtained when it is electrically-poled along a different axis from the spontaneous polarization direction.

Domain cotrolled single crystals (not in the monodomain state!) may be the key for obtaining the highest electromechanical coupling. The important factors to the domain reconstruction will be realized by changing external electric field, stress and temperature, as well as the sample preparation history.

This work was supported by the Office of Naval Research under Grant No. N00014-91-J-4145.

REFERENCES

1. K. Uchino, Proc. 4th Int'l Conf. on Electronic Ceramics & Appl. Vol.1. p.179, Aachen, Germany, Sept. 5-7 (1994).
2. K. Uchino, Piezoelectric Actuators and Ultrasonic Motors, Kluwer Academic Publ., Boston (1996).
3. J. Kuwata, K. Uchino and S. Nomura, Ferroelectrics 37, 579 (1981).
4. K. H. Hellwege et al.: Landolt - Bornstein, Group III, Vol.11, Springer-Verlag, N.Y. (1979).
5. K. Uchino and S. Nomura, Jpn. J. Appl. Phys. 18, 1493 (1979).
6. K. Uchino, Bull. Amer. Ceram. Soc. 65(4), 647 (1986).
7. S. Nomura, T. Takahashi and Y. Yokomizo, J. Phys. Soc., Jpn. 27, 262 (1969).
8. J. Kuwata, K. Uchino and S. Nomura, Jpn. J. Appl. Phys. 21(9), 1298 (1982).
9. B. Jaffe, R. S. Roth and S. Marzullo, J. Res. Nat'l. Bur. Stand. 55, 239 (1955).
10. H. Igarashi, Mem. Nat'l. Def. Adad. 22, 27 (1982).
11. S. W. Choi, T. R. Shrout, S. J. Jang and A. S. Bhalla, Ferroelectrics 100, 29 (1989).
12. T. R. Shrout, Z. P. Chang, N. Kim and S. Markgraf, Ferroelectrics Lett. 12, 63 (1990).
13. J. F. Wang, J. R. Giniewicz and A. S. Bhalla, Ferroelectics Lett. 16, 113 (1993).
14. Y. Yamashita, Jpn. J. Appl. Phys. 33, 4652 (1994).
15. T. R. Shrout, ONR Transducer Workshop, State College (March. 1996)
16. M. L. Mulvihill, L. E. Cross and K. Uchino, J. Amer. Ceram. Soc. 79, 3345 (1996).
17. K. Kato, K. Suzuki and K. Uchino, J. Jpn. Ceram. Soc. 98(8), 840 (1990).
18. R. Ujiie and K. Uchino, Proc. IEEE Ultrasonic Symp. '90, Hawaii, 2, 725 (1991).
19. M. L. Mulvihill, L. E. Cross and K. Uchino, Proc. 8th Europian Mtg. on Ferroelectrics, Ferroelectrics 186, 325 (1996).

APPENDIX 72

Submitted to the proceedings of the SPIE's 5th International Symposium on Smart Structures
and Materials, March 1-5, 1998, San Diego, CA.

RELAXOR BASED FERROELECTRIC SINGLE CRYSTALS FOR ELECTROMECHANICAL ACTUATORS

Seung-Eek Park, Venkata Vedula, Ming-Jen Pan, Wesley S. Hackenberger*,
Patrick Pertsch** and Thomas R. Shrout

Materials Research Laboratory, The Pennsylvania State University, University Park, PA 16802.
*TRS Ceramics, Inc

ABSTRACT

The piezoelectric properties of relaxor based ferroelectric single crystals, such as $Pb(Zn_{1/3}Nb_{2/3})O_3$ - $PbTiO_3$ (PZN-PT) and $Pb(Mg_{1/3}Nb_{2/3})O_3$ - $PbTiO_3$ (PMN-PT) were investigated for electromechanical actuators. In contrast to polycrystalline materials such as $Pb(Zr,Ti)O_3$ (PZT's), morphotropic phase boundary (MPB) compositions were not essential for high piezoelectric strain. Piezoelectric coefficients (d_{33}'s) > 2500 pC/N and subsequent strain levels up to >0.6% with minimal hysteresis were observed. Crystallographically, high strains are achieved for <001> oriented rhombohedral crystals, though <111> is the polar direction. Ultrahigh strain levels up to 1.7%, an order of magnitude larger than those available from conventional piezoelectric and electrostrictive ceramics could be achieved, being related to an E-field induced phase transformation. Strain vs. E-field behavior under external stress was also much superior to that of conventional piezoelectric ceramics. High electromechanical coupling (k_{33}) > 90% and low dielectric loss <1%, along with large strain make these crystals promising candidates for high performance solid state actuators.

Keywords : Relaxor ferroelectrics, single crystal, actuator, piezoelectrics, hysteresis, prestress.

1. INTRODUCTION

Electromechanical actuators directly transform input electrical energy into mechanical energy. Of the many types of actuator materials including, magnetostrictive, photostrictive, and shape memory alloys, piezoelectric and electrostrictive ceramics are widely used in applications requiring high generative force, high frequency operation, accurate displacement, quick response time, or small device size.[1] Generally, among the material properties determining actuator performance, the electric field (E-field) induced strain is the most important parameter for actuators. This is demonstrated by strain energy density which is a measure of the energy per unit mass an actuator can deliver,

$$e_{max} = 1/\rho \cdot 1/4 \cdot (1/2 \cdot E(s_{max})^2) \qquad (1)$$

where e_{max} is the strain energy density, E is the actuator's elastic modulus, s_{max} is the maximum field induced strain, and ρ is the actuator's density.[1] 1/4 is the appropriate factor for an actuator impedance related to its surroundings. In designing an actuator, the maximum strain energy density should be as high as possible. In electroactive ceramics, density and elastic modulus vary little from material to material, therefore, the level of strain and maximum strain achievable with a reasonable electric field (<50kV/cm) dominates the energy density. The piezoelectric coefficient (d_{ij}), determining the level of induced strain at a given electric field, is the most widely used parameter describing actuator performance. Currently, $Pb(Zr,Ti)O_3$ (PZT) polycrystalline ceramics are used with piezoelectric coefficients (d_{33}) ranging from 200 to 750 pC/N, the later limited by hysteresis. Electrostrictive ceramics such as $Pb(Mg_{1/3}Nb_{2/3})O_3$ offer effective d_{33}'s > 700pC/N, but only over a narrow range of E-field.

** Visiting Scientist from Fraunhofer-Instutute for Applied Optics and Precision Engineering, D-07745 Jena, Germany

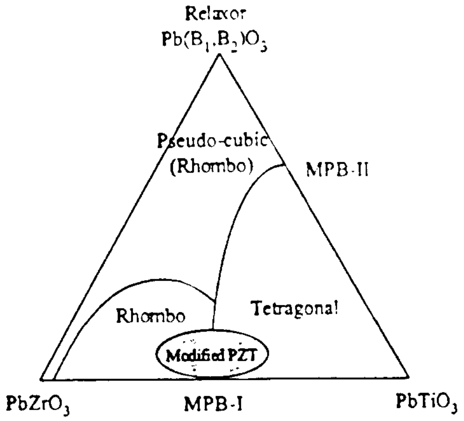

Figure 1 Ternary diagram depicting MPBs in PZT and Relaxor-PT systems for piezoelectric ceramics.

It is the objective of this paper to report ultrahigh piezoelectric coefficients (d_{33}), remarkably high strain levels with low hysteresis, and excellent performance under prestress observed for single crystals of $Pb(Zn_{1/3}Nb_{2/3})O_3$ - $PbTiO_3$ (PZN-PT) and $Pb(Mg_{1/3}Nb_{2/3})O_3$ - $PbTiO_3$ (PMN-PT). Strain behavior as a function of E-field and prestress will be discussed with respect to crystal structure, orientation, and anticipated actuator performance.

2. MORPHOTROPIC PHASE BOUNDARY CERAMICS

$Pb(Zr_{1-x},Ti_x)O_3$ (PZT) ceramics have been the mainstay for high performance actuator applications. Compositionally, PZT ceramics lie near the morphotropic phase boundary (MPB) between the tetragonal and rhombohedral phases as shown in figure 1. MPB compositions exhibit anomalously high dielectric and piezoelectric properties as a result of enhanced polarizability arising from the coupling between two equivalent energy states, i.e. the tetragonal and rhombohedral phases, allowing optimum domain reorientation during the poling process. Alternate MPB systems can be found in Relaxor-$PbTiO_3$, also as shown in figure 1. Lead based relaxor materials are complex perovskites with the general formula $Pb(B_1B_2)O_3$, (B_1=Mg^{2+}, Zn^{2+}, Ni^{2+}, Sc^{3+} ..., B_2=Nb^{5+}, Ta^{5+}, W^{6+} ...). Characteristic of relaxors is a broad and frequency dispersive dielectric maxima[2].

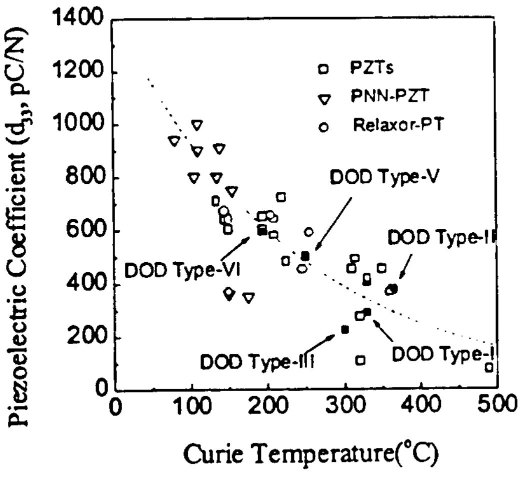

Figure 2 Piezoelectric coefficient d_{33} as a function of transition temperature (Tc) for piezoelectric ceramics, including PZT, modified PZTs, and Relaxor-PT systems.

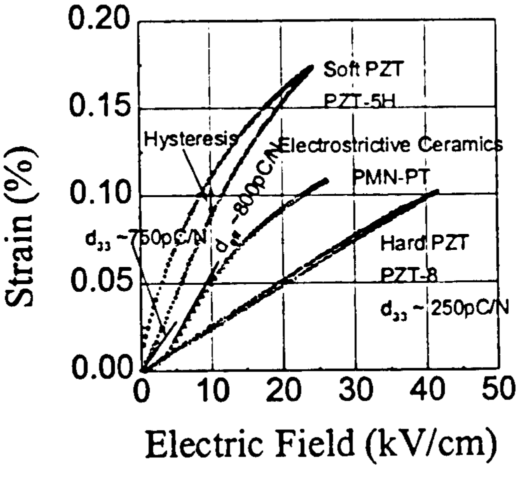

Figure 3. Strain vs. E-field behaviors for various electromechanical ceramics

To achieve a high piezoelectric coefficient, MPB-based ceramics are further engineered by compositionaly adjusting the Curie temperature (T_C) downward relative to room temperature. The effect of transition temperature (T_C) on the piezoelectric properties is clearly evident in figure 2. As shown, the room temperature values of d_{33} are plotted as a function of T_C for a variety of modified PZT ceramics, including Relaxor-PT systems. Enhanced piezoelectric activity of MPB-based ceramics is achieved by compositionaly adjusting Tc downward relative to room temperature resulting in 'soft' piezoelectric ceramics. This enhanced piezoelectric effect, therefore, comes with the expense of more temperature dependent properties, and less polarization stability, i.e. aging and loss of piezoelectric activity. Further details on the relationship between dielectric/piezoelectric properties and Curie temperature (Tc) of piezoelectric ceramics can be found in the article by S.-E. Park et al.[3]

Most importantly, a consequence of increased piezoelectric activity for these "soft" ceramics is large hysteresis in the strain vs. E-field behavior as a result of domain motion. Strain vs. E-field behavior for PZT-5H (Navy type -VI) is shown in figure 3 as an example. Though the piezoelectric coefficient (d_{33}) of PZT-5H ceramics is in the range of ~600 to 700 pC/N[4] (implying ~0.06 to 0.07% strain at 10 kV/cm), strain as high as 0.1% can be observed at 10kV/cm. This enhanced nonlinear strain is the result of domain motion, and therefore, accompanied by significant hysteresis, resulting in poor positioning accuracy. Area within the strain vs. E-field curve or dielectric loss results in significant heat generation during operation. Heat generation combined with a decreased temperature usage range, results in poor temperature stability and limits these ceramics to low frequency applications.

Strain vs. E-field hysteresis can be minimized with the use of the "hard" piezoelectric ceramics. Hard piezoelectric ceramics such as PZT-8 (Navy type III) offer very low hysteresis as shown in figure 3. However, the reduction in hysteresis and loss comes at the expense of d_{33} and subsequent strain level. Typically d_{33} values, for 'hard' PZTs range from ~200 to 300 pC/N.[4] Another category of ceramic materials used in commercial actuators are electrostrictors. Electrostrictive strain is proportional to the square of polarization. A few materials such as PMN and its solid solution with PT exhibit significant electrostrictive strain (> 0.1%) with virtually no hysteresis as shown in figure 3. Effective d_{33} 's > ~800 pC/N calculated directly from the strain vs. E-field curve can be achieved, but only over a very narrow range of E-field. For hard piezoelectric and electrostrictive ceramics, strain level with low hysteresis does not exceed 0.15%. This limitation originates from the material's dielectric breakdown strength and polarization saturation.

In summary, piezoelectric and electrostrictive ceramics offer strain levels up to ~ 0.15%. Soft PZT's, exhibiting piezoelectric coefficients (d_{33}) as high as 750 pC/N, are inherently limited due to hysteresis caused by domain motion. Hysteresis can be minimized with the use of hard piezoelectric ceramics, but d_{33} values of only ~200 - 300 pC/N are available. Even though electrostrictive ceramics offer effective d_{33} 's~ 800 pC/N, maximum strain level is limited by its dielectric breakdown strength and polarization saturation. To achieve E-field induced strain levels > 0.15%, electroactive materials should possess high piezoelectric coefficients (d_{33} >1000pC/N) and high dielectric breakdown strength.

3. SINGLE CRYSTAL PIEZOELECTRICS

Single crystal piezoelectrics such as quartz (SiO_2), lithium niobate ($LiNbO_3$), and the analogue lithium tantalate ($LiTaO_3$) are widely employed in specific applications that include oscillators, surface acoustic wave (SAW) devices, and in optics. In contrast to PZT ceramics, however, these single crystals offer inferior piezoelectric properties, with d_{33} 's< 50 pC/N.

Attempts to grow single crystals of MPB PZTs have been made by numerous researchers, resulting in crystallites too small to allow adequate property measurements.[5-9] In contrast to PZT crystal growth, relaxor-PT materials can be readily grown in single crystal form. This key distinction was first realized by Soviet Researchers[10,11], followed by Nomura and co-workers for PZN-PT system[12,13] and by Shrout for the PMN-PT[14]. In general, most $Pb(B_1,B_2)O_3$-PT crystals can be grown by high temperature solution growth using Pb-based fluxes.[15,16]

Piezoelectric coefficients as high as ~ 1500 pC/N have been reported[13,14] for MPB Relaxor-PT crystals. However, it should be noted that piezoelectric coefficients are generally determined using low field (< 0.1kV/cm) techniques such as the resonance method (IEEE standard).[17] Therefore, direct observation of the strain vs. E-field behavior is essential in order to investigate hysteresis and maximum levels of strain, key experiments to directly confirm actuator performance. In relation to actuators, several questions arise, 1) How do the high d_{33} values determined using low field techniques correlate to direct measurements? As for piezoelectric and electrostrictive ceramics, will the strain level saturate with increased E-field? 2) How much hysteresis accompanies the strain?, 3) Is morphotrophy essential for enhanced piezoelectric properties?, 4) Can E-field induced strain be delivered under external stress? In the following sections, we will attempt to answer many of these questions, reporting piezoelectric properties and direct observation of strain behavior as a function of crystallographic orientation and electric field, and also under prestress for Relaxor-PT single crystals.

4. DIELECTRIC AND PIEZOELECTRIC PROPERTIES OF RELAXOR BASED SINGLE CRYSTALS

In this section, the dielectric and piezoelectric properties of Relaxor-PT systems as a function of crystal composition and orientation are summarized. Commonalties inherent to Relaxor-PT systems have been discussed in reviews by Shrout[18] and Randall[19]. Based on these commonalties, our research was limited to two representative systems, PZN-PT and PMN-PT. Though PMN-PT MPB crystals exhibit piezoelectric properties comparable with PZN-PT, more focus was given to the PZN system owing to its relatively lower PT content for MPB, allowing more uniform crystal growth of these solid solution materials. Experimental procedures are briefly summarized including crystal growth, crystal alignment, dielectric and piezoelectric measurements using direct observation of strain as a function of electric field as well as low field property measurements using the IEEE resonance technique.[17]

CRYSTAL GROWTH, SAMPLE PREPARATION AND PROPERTY MEASUREMENTS

High purity (>99.9%) powders of Pb_3O_4, ZnO, $MgCO_3$, Nb_2O_5 and TiO_2 were used as starting material. Raw powders were weighed with desired molar ratio with excess Pb_3O_4 as a flux. The powders were dry mixed for a desired period of time using a tumbling mill. The mixed powders were loaded into a Platinum crucible, which was placed in an alumina crucible sealed with an alumina lid and alumina cement to minimize PbO volatilization. The crucible and powder were placed in a tube furnace and held at soak temperatures (1100 to 1200°C), followed by slow cooling (1 to 5°C/hr). The crucible was then furnace-cooled to room temperature. Hot HNO_3 is used to separate the crystals out of the rest of the melt. Typically crystal size ranged from 3 to 20 mm. Further details on the flux growth technique of these crystals can be found in ref. 15,16.

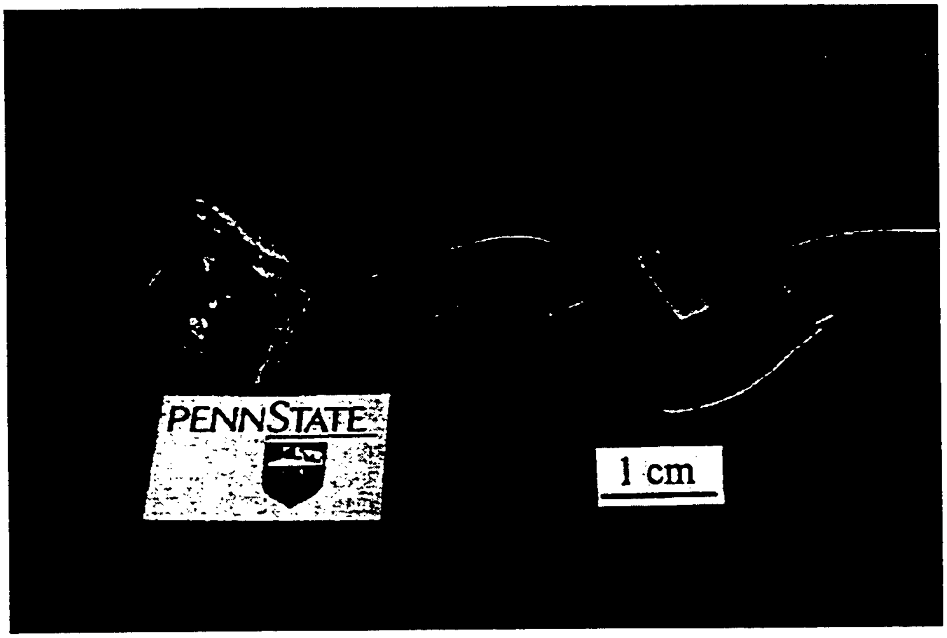

Figure 4. As grown crystal, an aligned sample using the Laue camera, a cut and polished sample, an electroded sample for direct strain observation as well as for low field planar mode resonant sample, and a low field longitudinal mode resonant sample, for PZN-9.5%PT, (from left to right).

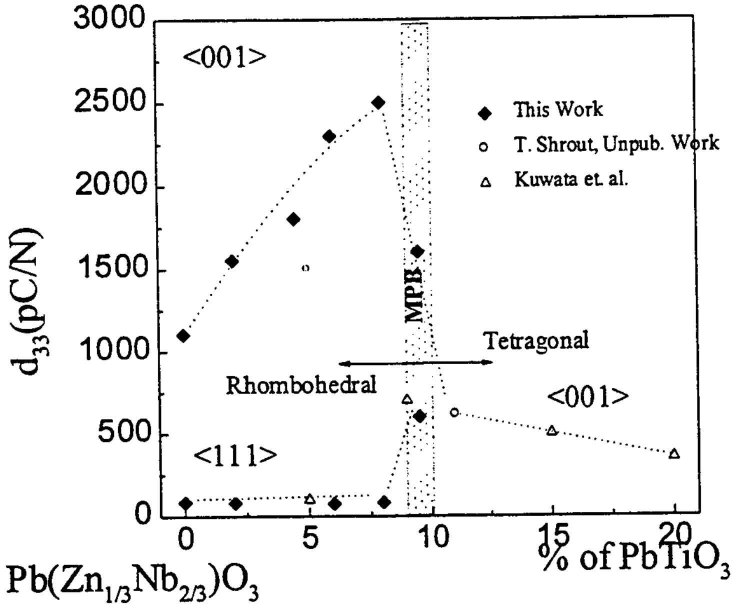

Figure 5 d_{33} as a function of composition and crystallographic orientation in crystals of PZN-PT.

Individual crystals were oriented along their pseudocubic <111> and <001> axis using a Laue back reflection camera. For electrical characterization, samples were prepared by polishing with silicon carbide and alumina polishing powders to achieve flat and parallel surfaces onto which gold electrodes were sputtered. High-field measurements included polarization and strain hysteresis using a modified Sawyer-Tower circuit and linear variable differential transducer (LVDT) driven by a lock-in amplifier (Stanford Research Systems, Model SR830). Plate shape samples with thickness ranging from 0.2 mm to 0.5 mm were used. Electric fields as high as ~140 kV/cm were applied using an amplified unipolar wave form at 0.2 Hz, using a Trek 609C-6 high voltage DC amplifier. During testing the samples were submerged in Fluorinert (FC-40, 3M, St. Paul, MN), an insulating liquid, to prevent arcing. For piezoelectric coefficient(d_{33}) determination, bar shape samples with lengths ranging from 3 mm to 5 mm were tested. Samples were poled either by field cooling (10kV/cm) from temperatures above the dielectric maximum temperature (T_{max}) or by applying 40kV/cm at room temperature. Figure 4 presents, from left to right, a representative of an as grown crystal, an aligned sample using the Laue camera, a cut and polished sample, an electroded sample for direct strain observation as well as for low field planar mode resonant sample, and a low field longitudinal mode resonant sample, for PZN-9.5%PT, respectively.

LOW FIELD MEASUREMENTS

Piezoelectric coefficients as a function of composition and crystal orientation for PZN-PT, calculated based on IEEE standards, are presented in figure 5. As shown, large piezoelectric coefficients (d_{33} ~ 1600 pC/N) were found for PZN-PT with MPB compositions (9.5% PT), as previously reported by Kuwata[11]. PMN-PT crystals with MPB compositions (PMN-35% PT) also exhibited large piezoelectric coefficients (d_{33} ~ 1500 pC/N).[3] It should be noted, however, that all rhombohedral crystals oriented along their psuedocubic <001> direction exhibited large piezoelectric coefficients. As shown in figure 5, d_{33} increased with increased amount of $PbTiO_3$ for <001> oriented rhombohedral crystal. Maximum d_{33} values of ~2500 pC/N were determined with domain engineered rhombohedral crystals[***]. In contrast to PZT's, d_{33} dramatically decreases at MPB to levels ~ 500pC/N for tetragonal composition. Though <111> is the polar direction in rhombohedral crystals, such cuts exhibited low piezoelectric coefficient, believed to be associated with domain instability. Further details

---

[***] Rhombohedral crystals oriented and poled along pseudocubic <001> direction. Crystallographically, polar direction of rhombohedral crystal is pseudocubic <111> direction.

on domain motion and crystal anisotropy are reported in ref 20. Dielectric loss value < 1% and electromechanical coupling constant values (k_{33}) > 90% were reported elsewhere. [3]

5. STRAIN VS. E-FIELD BEHAVIORS FOR RELAXOR BASED SINGLE CRYSTALS

Though high piezoelectric coefficients (d_{33}) were determined, high field measurements are more indicative of actuator performance. The following observations will clearly show the potential of relaxor based ferroelectric single crystals, for applications as actuators.

Strain as a function of electric field for various <001> oriented rhombohedral crystals (pure PZN, PZN-4.5%PT, PZN-8%PT, and PMN-24%PT) are presented in figure 6. Also E-field induced strains of various electromechanical ceramics such as soft PZT (PZT-5H), hard PZT (PZT-8) and electrostrictive ceramics (PMN-PT) are compared. Piezoelectric coefficients (d_{33}) directly calculated from the slope of strain vs. electric field curves confirmed the piezoelectric coefficients determined by the low field resonance method. Strains as high as ~0.6% were observed with low hysteresis for these crystals, significantly larger than that for polycrystalline ceramics. The limitation of achievable strain for polycrystalline ceramics is the result of polarization saturation and subsequent saturation on strain and breakdown strength. However, as shown in figure 6, strain did not saturate with increased E-field for <001> oriented rhombohedral crystals. This remarkable strain vs. E-field behavior with low hysteresis is believed to be related to the engineered domain state.[20] Although crystallographically <111> is the polar direction, low piezoelectric coefficients (d_{33}) < 100 pC/N were determined as shown in figure 5. This inferior piezoelectric activity was found to be related to domain instability after poling. Details on mechanisms are presented in ref. 20.

Saturation of E-field induced strain behavior for <001> oriented rhombohedral crystals was investigated until dielectric breakdown as presented in figure 7. Far from saturation, the strain abruptly increased with strain levels as high as 1.0% being achieved for all crystals tested. Maximum strain levels were determined mainly by sample breakdown voltage. The E-field induced strain behavior observed is believed to be associated with an E-field induced rhombohedral-tetragonal phase transition. This phase transition behavior is more apparent in figure 8 presenting the E-field induced strain behavior of the <001> oriented PZN-8%PT crystal. At ~120kV/cm, the induced strain along with high dielectric breakdown strength resulted in a strain level as high as 1.7%. The piezoelectric coefficient (d_{33}) ~ 480 pC/N calculated directly from the slope of strain vs. E-field in the high field region corresponded to the tetragonal phase (between 40 and 120 kV/cm in figure 8) coincides with a d_{33} value (~500 pC/N) of tetragonal PZN-12%PT crystal. More detail on this phase transformation can be found in ref. 20.

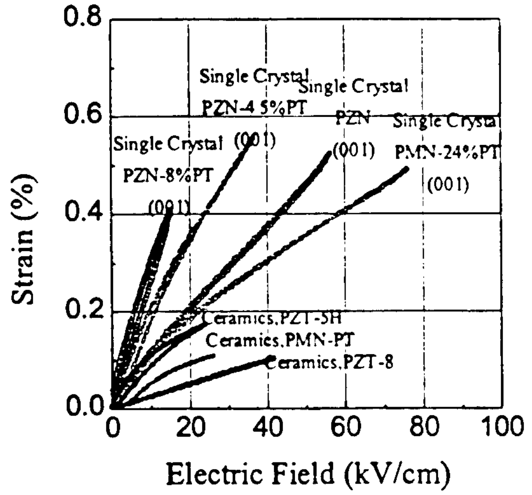

Figure 6 Strain vs. E-field behaviors for crystals of PZN-PT and PMN-PT, and for various electromechanical ceramics.

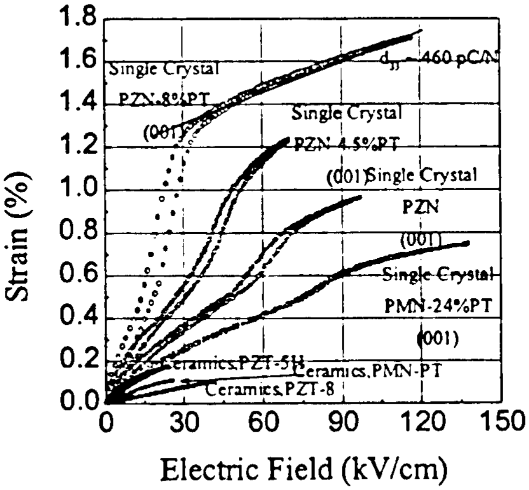

Figure 7 Strain vs. E-field behaviors for crystals of PZN-PT and PMN-PT, and for various electromechanical ceramics till breakdown.

Table 1 Dielectric and Piezoelectric Properties of PZN-4.5%PT Crystals Oriented along <001>.

k_{33}	K	loss	s_{33}^{D} ($10^{-12}m^2/N$)	s_{33}^{E} ($10^{-12}m^2/N$)	d_{33} (pC/N)
0.93	4500	0.012	16.4	111	2000

6. STRAIN BEHAVIOR UNDER APPLIED STRESS

Table 1 presents dielectric and piezoelectric properties of PZN-4.5%PT, measured by low field resonance technique. PZN-4.5%PT was chosen because it is at the center of rhombohedral composition range (0% to 9%PT) for PZN-PT. As can be seen in table 1, longitudinal compliance (s_{33}^{E}) is 111 x 10^{-12} m^2/N (Young's modulus = 9 GPa), significantly lower than piezoelectric ceramics such as PZT-8 (75 GPa). It is important,therefore, to examine the strain behavior of PZN-4.5%PT crystal under various combinations of stress and electric field in order to address the potential of these crystals for actuator applications. The experimental setup for applying stress was presented elsewhere.[21]

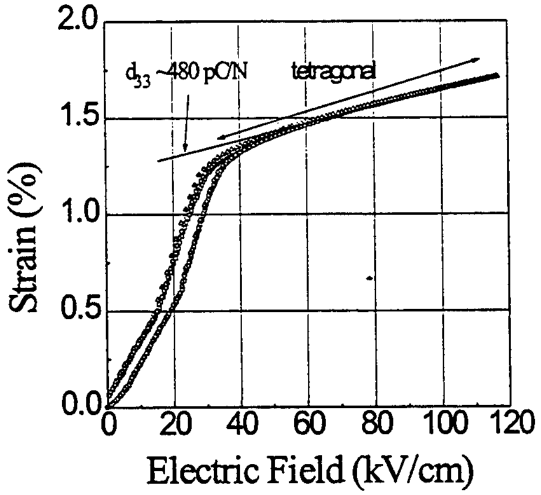

Figure 8 Strain vs. E-field behaviors for <001> oriented PZN-8%PT crystal

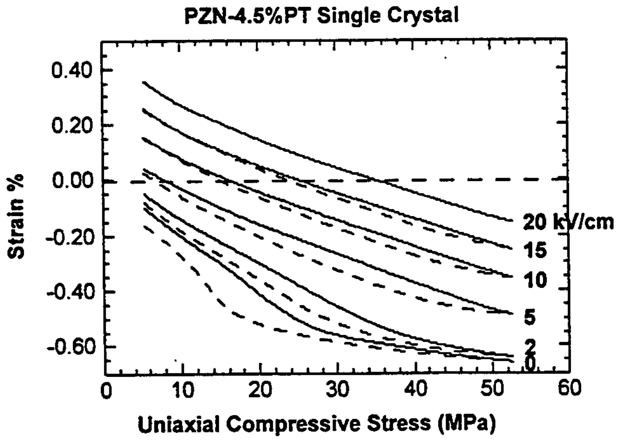

Figure 9 The stress-strain curves of PZN-4.5%PT under different biases. Note the generative stress at 20kV/cm bias is 35 MPa.

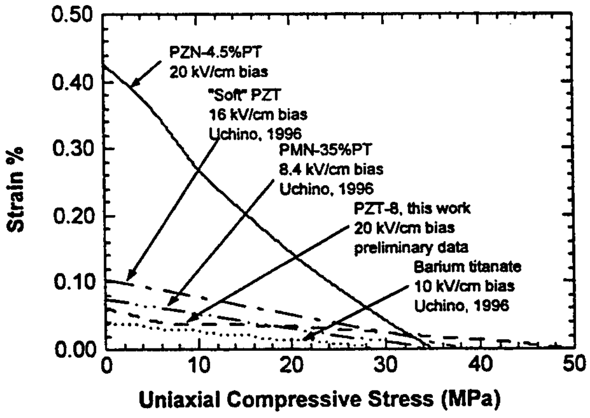

Figure 10 Strain-Stress curves for PZN-PT crystals and various piezoelectric ceramics.

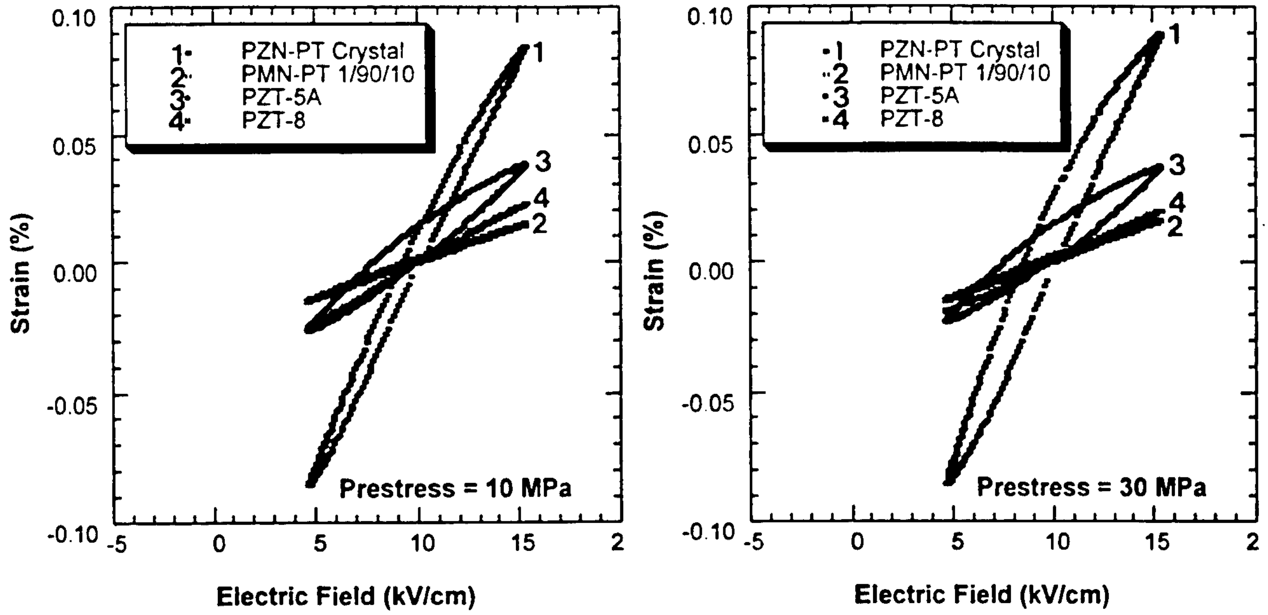

Figure 11 Strain vs. bipolar field (±5 kV/cm) curves under bias (10kV/cm) for PZN-PT crystal, electrostrictive PMN-10%PT ceramics, PZT-5A (Navy type II), and PZT-8 (Navy type 3).

The stress-strain behavior of a PZN-4.5%PT crystal (approximately 4.5x4.5x4 mm) under different biases were shown in Fig. 9. The solid lines are loading curves and the dashed lines are unloading. It was apparent that when there was no bias, the crystal depoled at around 30 MPa, resulting in hysteresis. As bias level increases, increased depoling stress and decreased hysteresis were observed. At 20 kV/cm, the Young's modulus is 11 GPa, which is consistent with the value in table 1. The generative stress, where the generated strain is reduced to zero, is 35 MPa at 20kV/cm.

With such stress-strain curves, comparisons to other actuator materials can be made based on energy density (the area under the curve). Shown in Fig. 10 are the stress-strain curves of PZN-4.5%PT crystal and various ceramics. The energy density of PZN-4.5%PT was determined to be 66400 J/m^3 from the figure, approximately 5 times larger than that can be delivered by PZT-8. Stress-strain curves of various types of piezoelectric ceramics are compared.

Another advantage of relaxor single crystals is demonstrated in Fig. 11 in the form of E-field induced strain under constant pre-stress. For each measurement, a pre-stress was first applied and then a sine wave with ±5 kV/cm amplitude oscillating around the 10 kV/cm bias followed. Note that the 10 kV/cm bias was kept on all samples during measurements to prevent depoling. Although slightly hysteretic, the induced strain in PZN-4.5%PT was several times higher than conventional piezoelectrics ceramics. These results are a strong assurance that relaxor single crystals will out-perform other actuator materials even under external stress.

7. CONCLUSION

Pseudocubic <001> oriented relaxor based rhombohedral crystals such as (1-x) PZN-x PT (x<0.09) and (1-x) PMN- xPT (x<0.35) exhibited actuation levels not available with current piezoelectric ceramics. Ultrahigh piezoelectric coefficients (d_{33}) > ~2200 pC/N and strain levels up to 0.6% with low hysteresis were observed. Ultrahigh strain levels up to 1.7% could be achieved for relaxor based ferroelectric single crystals as a result of E-field induced rhombohedral-tetragonal phase transition. Other relaxor based rhombohedral crystals are expected to exhibit similar strain vs. E-field behavior. Although compliant, PZN-4.5%PT crystal showed excellent performance under applied stress. The strain energy density can be delivered at 20kV/cm is 66400J/m^3 , 5 times higher than hard PZT. Though clearly promising candidates for high performance actuators, further investigations in crystal growth and prestress testing are required for single crystal piezoelectrics to become the next generation material of actuators.

8. ACKNOWLEDGMENT

This research has been supported by Office of Naval Research. Authors would like to thank Hua Lei for her help with the preparation of samples.

9. REFERENCES

1. V. Giurgiutiu, Z. Chaudhry, and C. A. Rogers, "Energy-based Comparison of Solid-State Actuators," Report No. CIMSS 95-101, Virginia Polytechnic Institute and State University, Sept. 1995.
2. L. E. Cross, "Relaxor Ferroelectrics," *Ferroelectrics*, vol. 76, pp. 241-267, 1987.
3. S Seung-Eek Park, and Thomas R. Shrout, "Characteristics of Relaxor-Based Piezoelectric Single Crystals for Ultrasonic Transducers," in press *IEEE Trans. on UFFC*, Vol. 44, No. 5, pp. 1-8, 1997.
4. H. Jaffe and D. A. Berlincourt, "Piezoelectric Transducer Materials," *Proceedings of IEEE*, vol. 53 no. 10, pp. 1372-1386, 1965.
5. S. Fushimi and T. Ikeda, "Phase Equilibrium in the System $PbO-TiO_2-ZrO_2$," *Journal of the American Ceramic Society*, vol. 50, no. 3, pp. 129-132, March 1967.
6. V. A. Kuznetzov, "Crystallization of Titaium, Zirconium and Hafnium Oxies and Some Titanate and Zirconate Compounds under Hydrothermal Conditions," *Journal of Crystal Growth*, vol. 34, pp. 405 - 410, 1968.
7. R. Clarke and R. W. Whatmore, "The Growth and Characterization of $PbZr_xTi_{1-x}O_3$ Single Crystals," *Journal of Crystal Growth*, vol. 33, pp. 29-38, 1976.
8. T. Hatanaka and H. Hasegawa, "Dielectric Properties of $Pb(Zr_xTi_{1-x})O_3$ Single Crystals Including Monoclinic Zirconia," *Japanese Journal of Applied Physics*, vol. 34, pp. 5446-5448, Sept. 1995.
9. K. Yanagisawa, H. Kanai, and Y. Yamashita, "Hydrothermal Crystal Growth of Lanthanum-Modified Lead Zirconate Titanate," *Japanese Journal of Applied Physics*, vol. 34, pp. 536-538 Sept. 1995.
10 V. A. Bokov and I. E. Myl'nikova, *Soviet Physics-Solid State*, Vol. 2, No. 11, pp 2428-2432, 1961
11 G. A. Smolenskii, V. A. Isuov, A. I. Agranovskaya, and S. N. Popov, "Ferroelectric with diffuse Phase Transitions," *Soviet Physics-Solid State*, Vol. 2, No. 11, pp 2584-2594, 1961.
12. J. Kuwata, K. Uchino, and S. Nomura, "Phase Transitions in the $Pb(Zn_{1/3}Nb_{2/3})O_3$ -$PbTiO_3$ System," *Ferroelectrics*, vol. 37, pp. 579-582, 1981.
13 J. Kuwata, K. Uchino, and S. Nomura, "Dielectric and Piezoelectric Properties of $0.91Pb(Zn_{1/3}Nb_{2/3})O_3$ -$0.09PbTiO_3$ Single Crystals," *Japanese Journal of Applied Physics*, vol. 21, no. 9, pp. 1298-1302, Sept. 1982.
14 T. R. Shrout, Z. P. Chang, N. Kim, and S. Markgraf, "Dielectric Behavior of Single Crystals near the $(1-x)Pb(Mg_{1/3}Nb_{2/3})O_3$ - (x) $PbTiO_3$ Morphotropic Phase Boundary," *Ferroelectric Letters*, vol. 12, pp. 63-69, 1990.
15. M. L. Mulvihill, S. -E. Park, G. Risch, Z. Li, K. Uchino, T. R. Shrout, "The Role of Processing Variables in the Flux Growth of Lead Zinc Niobate-Lead Titanate Relaxor Ferroelectric Single Crystals," *Japanese Journal of Applied Physics*, vol. 35, no. 7, pp. 51-57, July 1996.
16. S. -E. Park, M. L. Mulvihill, G. Risch, and T. R. Shrout, "The Effect of Growth Condition on Dielectric Properties of $Pb(Zn_{1/3}Nb_{2/3})O_3$ Crystal," *Japanese Journal of Applied Physics*, Pt. 1, vol. 36, no. 3, March 1997.
17. IEEE Standard on Piezoelectricity, American National Standards Institue, 1976.
18. T. R. Shrout and J. Fielding, Jr. , "Relaxor Ferroelectric Materials," *in Proceedings of the 1990 IEEE Ultrasonics Symposium*, 1990, pp. 711-715.
19. C. A. Randall, A. S. Bhalla, T. R. Shrout, and L. E. Cross, "Classification and Consequences of Complex Lead Perovskite Ferroelectrics with regard to B-site Cation Order," *Journal of Materials Research*, vol. 5, no. 4, pp. 829-834, 1990.
20. S.-E. Park and T. R. Shrout, "Ultrahigh Strain and Piezoelectric Behavior in Relaxor Based Ferroelectric Single Crystals," *Journal of Applied Physics*, Vol 82 [4], 1804 (1997).
21. M.-J. Pan, P. Pertsch, S. Yoshikawa, T.R. Shrout, and V. Vedula, *Proceedings of the SPIE's 5th International Symposium of Smart Structures and Materials*, March 1-5, 1998, San Diego, CA.
22. Kenji Uchino, *Piezolectric Actuators and Ultrasonic Motors*, Kluwer Academic Publications, 1996.

APPENDIX 73

Koopmann, G. H. , Lesieutre, G. A. , Dershem, B. R. , Chen, Weicheng. March 1997
Embeddable Induced Strain Actuators Using Framed 3-3 Piezoceramic
Stacks, Modeling and Characterization, SPIE's 4 the Annual International
Symposium on Smart Structures and Materials, San Diego, CA

Embeddable Induced Strain Actuators Using Framed 3-3 Piezoceramic Stacks : Modeling and Characterization

Gary H. Koopmann, George A. Lesieutre, Brian R. Dershem, Weicheng Chen
Center for Acoustics and Vibration, 157 Hammond Building

Shoko Yoshikawa
151 Materials Research Laboratory

The Pennsylvania State University, University Park, PA 16802

ABSTRACT

In an earlier SPIE paper, we described the development of a strain actuator consisting of a thin, co-fired, multilayered, PZT stack mounted within a titanium frame. The frame concept was designed to facilitate integration of the piezoceramic stack into a composite material during the fabrication process. The frame preloads the stack in compression, protects it during material fabrication and most importantly, provides an efficient shear transfer path to the surrounding host material. Because the piezoceramic stack power requirements are quite high, a special amplifier was also designed to meet the high current and voltage requirements. In this paper we focus on assessing the performance of the framed stack actuator for a variety of loading conditions. The calibration procedure uses a specially designed apparatus which loads the framed stack with a variety of impedances ranging from very compliant to very stiff. The mechanical power generated by the stack is measured directly in terms of the force transmitted to these loads along with their displacement. Electrical power is measured directly in terms of electrical current and voltage and is also computed in terms of the electrical admittance of the stack. Results show that the actuator is most efficient when a nearly matched impedance condition exists between the framed stack and its corresponding load.

1. INTRODUCTION

In this paper, we examine the dynamic performance of the PZT strain actuator that was embedded in an actively controlled, composite structure associated with the SPICES (Synthesis and Processing of Intelligent, Cost Effective Structures) research program sponsored by ARPA (Advanced Research Projects Agency). The actuator performance requirements are similar to those of conventional actuators, e.g., it had to be robust, efficient with adequate force and stroke, lightweight, compatible with the host material and easily embeddable during the fabrication process. The actuator consists of a thin, co-fired, multilayered PZT stack mounted within a frame which preloads the stack in compression and protects it during fabrication of the composite structure. Most importantly, the frame provides a highly efficient shear transfer path to the surrounding host material. For future applications, it is important to know the dynamic response of the 'framed actuator' under a variety of loading conditions, frequency ranges and input voltages. Towards this end, we designed and built a special calibration unit that provides a direct measure of the electro-mechanical efficiency of the framed actuator as a function of input and loading conditions. To link the experimental measurements with existing piezoceramic models, we developed lumped parameter models of the piezoceramic stack, its frame and the impedance of the calibration unit. The paper begins with a short review of the design of the PZT stack and the frame that contains it.

2. DESIGN OF FRAMED ACTUATOR

The actuator design, sketched in Figure 1, consists of a titanium frame (1) in which a PZT ceramic stack (2) is mounted.

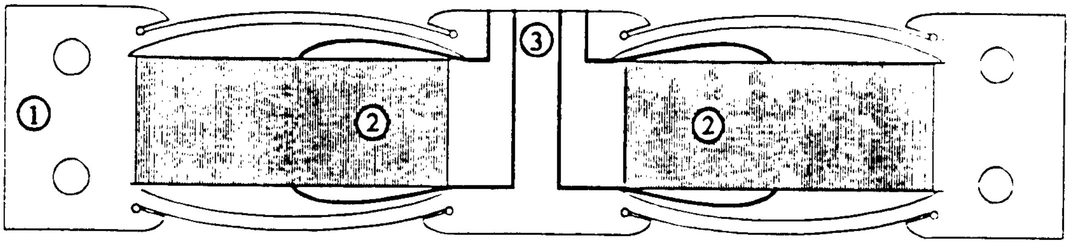

Figure 1. Illustration of the framed double stack actuator (95mm x 18mm x 1mm).

Leads from the stack (3) fit in machined recesses that egress the top edge of the frame. The leads are connected to the center of the ceramic. From a materials compatibility consideration, a primary advantage of the frame design is that it circumvents the problem of bonding a ceramic material directly to host material with different physical properties. Indeed, because the ceramic stack is spring mounted, the bonding stresses between the frame and ceramic are always in a favorable, compressive mode. The frame simply acts to transfer strain from the stack to the surrounding host material. To insure compatibility between the frame and the host material, their material properties are chosen to be as similar as possible. These include thermal expansion coefficients, Young's moduli, and surface chemistry.

The PZT stack, fabricated by Morgan Matroc, Inc., operates using d_{33} coupling coefficient (more than twice that of the d_{31}) at a relatively low voltage. We chose one of the hard PZT family, PZT-4S as our piezoceramic material owing to its higher driving capability, lower loss, and lower displacement hysteresis compared with the softer, commercially available PZT's. The piezoceramic stack consists of two co-fired 93 layer actuators (the active PZT layer thickness is 141 µm). The low field dielectric properties of the actuator are: capacitance (1 kHz, room temp.) 135 ± 7 nF and dielectric loss (1 kHz, room temp.) 7.5 ± 10^{-3}. The internal electrode is platinum so that it can be co-fired with PZT-4S, which requires a high sintering temperature. The external electrode is fired-on silver to accommodate the lead wires, which are attached with solder. The individual stack is coated with a polymer to insure electrical insulation. Selection of a polymer coating is critical, since it has to withstand the high temperatures of the fabrication process and be compliant enough to allow movement between the stack the the adjacent host material. Polymer coatings currently being used are high temperature silicone and polyimide encapsulants.

3. CALIBRATION OF THE FRAMED ACTUATOR

3.1 Lumped parameter modeling

To fully characterize the dynamic performance of the framed piezoceramic stack described above, a calibration unit was developed to measure the force and stroke of the actuator under various loading conditions. The variation in loading is achieved through the use of interchangeable shear mounts that are made with different metallic, composite or elastomeric materials to yield a wide range of load impedance conditions. Under each of these impedance loads, operating curves for actuator force and displacement are established for various drive voltages and frequencies. The load impedances are chosen to simulate the structural impedances of typical host composite and bonding substrate materials used in the fabrication of composite structures. Since an impedance match between the piezoceramic stack and the host material maximizes the load transfer to the structure, simulations provide useful guidelines for composite designers.

The calibrator design, shown in Figure 2, consists of rigid end plates and connecting rods that support the frame for the piezoceramic stack, transducer and shear mounts.

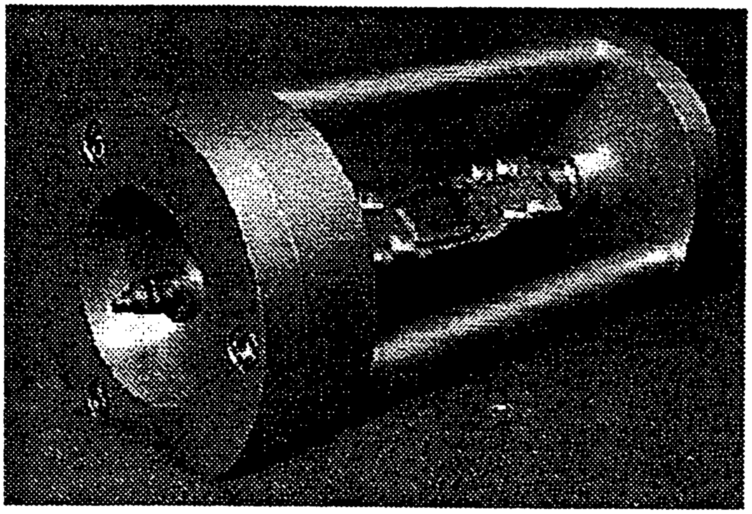

Figure 2. Framed piezoceramic stack calibrator

These elements are combined in terms of a lumped parameter model which allows both a static and dynamic analysis of the framed piezoceramic stack. With this model, the dynamics of both the framed stack and its host material are investigated from impedance matching considerations.

The components shown in Figure 3 include the co-fired, multi-layered piezoceramic stack, stack frame, frame clamps, force transducer and shear mount.

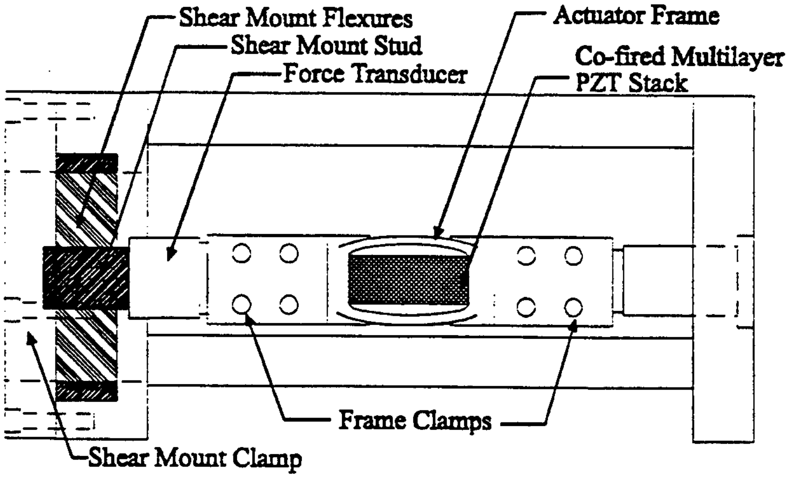

Figure 3. Key components of the framed piezoceramic calibrator

The lumped parameter model includes the mass, stiffness and damping of the shear mount, the mass of the transducer and mounting clamps as well as the mass and stiffness of the stack. This model is idealized as the mass, spring and damper diagram in Figure 4.

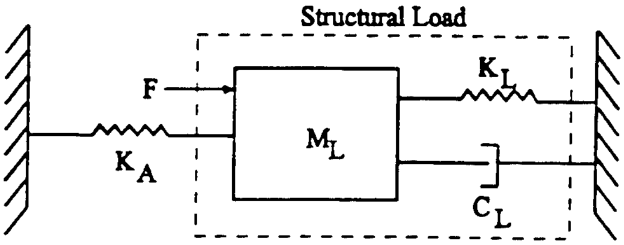

Figure 4. Lumped parameter model of piezoceramic stack and effective load

Note that the frame clamp, force transducer and shear mount stud are assumed to have stiffnesses that are several orders of magnitude higher than the shear flexures and are combined as a single lumped mass. This reduces the system to a single degree of freedom.

In Figure 4, the mass, M_L, includes the mass of the shear mount stud, effective mass of the shear mount flexures, force transducer, frame clamp, and effective mass of the frame. The two springs, K_A and K_L, represent the stiffness of the stack and the load, respectively. The applied force, F, is the actuation force delivered by the piezoceramic stack.

3.1.1 Piezoceramic stack dynamics

The driver consists of a co-fired, multilayered stack of piezoceramic elements (approximately 180) of PZT-4S, poled and driven in the 3-3 mode (z-direction). The constitutive relations for piezoceramics driven in the 3-3 mode relate the electric displacement, D_3, and shear strain, S_3 to the electric field, E_3, and stress, T_3, through the coefficients of permittivity, ε_{33}^T, elastic compliance, s_{33}^E, and piezoelectric coefficient, d_{33}, given in Equation 1.

$$\begin{aligned} D_3 &= \varepsilon_{33}^T E_3 + d_{33} T_3 \\ S_3 &= d_{33} E_3 + s_{33}^E T_3 \end{aligned} \tag{1}$$

From this pair of equations, the relationship between strain and applied electric field, V, can be written as[1,2]

$$\frac{d\zeta}{dz} = -\frac{F_z}{Y_{33}} + \frac{d_{33} V}{L_s} \tag{2}$$

where,

ζ = particle displacement from equilibrium
$d\zeta/dz$ = strain in the z direction
F_z = Force applied in the z direction for a particular z location
Y_{33} = Young's modulus in the 3-3 direction
S_z = Cross sectional area of the piezoceramic element in the x-y plane
L_s = Length of the individual piezoceramic stack element
d_{33} = piezoelectric strain coefficient
V = applied electric field in the 3 direction

The solution for the displacement of the piezoceramic stack is obtained by assuming one-dimensional longitudinal wave motion by

$$\zeta(z) = A\sin(kz) + B\cos(kz), \tag{3}$$

where the wave number $k = \omega / c$ and $c = (Y_{33}/\rho)^{1/2}$, ω is the radial frequency and ρ is the density. By differentiating this equation, the strain in the piezoceramic stack is then

$$\frac{d\zeta}{dz} = kA\cos(kz) - kB\sin(kz). \tag{4}$$

Equating this strain relationship to Equation 2 and applying appropriate boundary conditions for a piezoceramic stack length, L_Z, the constants are obtained for the free displacement and blocked forced output of the actuator. This operation was carried out by Koopmann et al.[3] and is given below for the free displacement, ζ, and blocked force output, F, of the stack at low frequencies as

$$\zeta(L_z) = \frac{d_{33}VL_z}{L_S} \tag{5}$$

$$F = \frac{d_{33}VY_{33}S_z}{L_s}. \tag{6}$$

Having developed these relationships for the piezoceramic stack by itself, next consider the dynamics of the stack when mounted in the frame that transfers the strain to the shear mounts in the calibrator.

3.1.2 Combined framed stack and load dynamics

The quasi-static response of the individual components in the calibrator is determined from the frame stiffness, K_F, piezoceramic stack stiffness, K_A, and flexural stiffness of the shear mount, K_S shown in Figure 5.

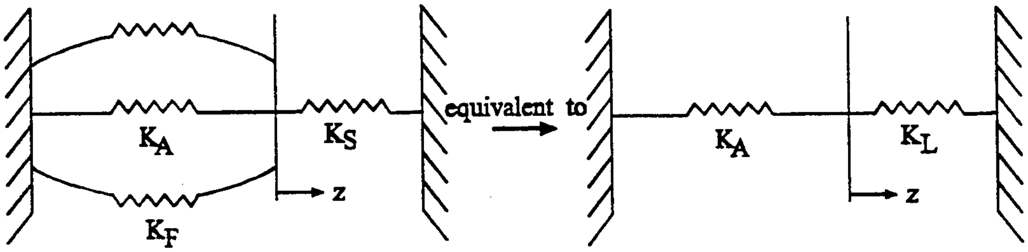

Figure 5. Equivalent parallel spring schematic for frame, stack and shear mount

Although the frame and shear mount stiffness may be treated separately, it is convenient for the experimental measurements discussed later to combine these into a single stiffness, K_L, which is the apparent stiffness that the actuator stack 'sees' in generating a force.

The dynamic interaction between the frame actuator and the shear mount is treated as a single-degree-of-freedom mass, spring and damper system written simply as

$$M_L\ddot{z} + C_L\dot{z} + K_Lz = F\sin(\omega t). \tag{7}$$

The mechanical impedance of the system is the transfer function between the force and velocity and is obtained from Equation 7 by assuming a harmonic response of the system as,

$$\frac{F}{\dot{z}} = Z_L = C_L + \frac{i}{\omega}(M_L\omega^2 - K_L) \tag{8}$$

where M_L is the equivalent mass defined earlier and C_L is the damping in the shear mount flexure. This is the load impedance, Z_L, seen by the piezoceramic stack.

3.1.3 Electro-mechanical impedance model

With the load impedance defined, the constitutive relations for the piezoceramic stack are used to determine the power dissipated by the piezoceramic stack and the shear mount flexure of the calibrator. From this model, the efficiency of the piezoceramic stack is determined by taking the ratio of the mechanical power applied to the load to the electrical power applied to the piezoceramic stack.

An electromechanical model developed by Liang[4] gives an expression for the energy dissipation in a plate driven with a piezoceramic actuator. The same model is applicable to the framed piezoceramic stack in assessing the energy dissipated by mechanical load. The electrical admittance, Y, of the stack is expressed from the transduction equations for a reciprocal transducer[4,5] as

$$Y = \frac{I}{V} = \frac{i\omega n S_z}{L_s}\left(\bar{\varepsilon}^{T}_{33} - \frac{Z_L}{Z_A + Z_L} d_{33}^{2} \bar{Y}^{E}_{33}\right) \tag{9}$$

for the input current, I, and the number of piezoceramic stack layers, n. This electrical admittance fully couples the electro-mechanical response of the piezoceramic stack as a function of frequency, load and stack impedance.

The load impedance, Z_L, can be obtained using the lumped parameters for the spring-mass-damper system in Equation 8. The equivalent piezoceramic stack impedance[6], Z_A, is given by

$$Z_A = \frac{\bar{Y}^{E}_{33} S_z}{i\omega n L_s} \frac{nkL_s}{\tan(nkL_s)}. \tag{10}$$

Based on the electrical admittance, the electrical power dissipated by the stack can be expressed as[7,8]

$$W_d = \frac{V^2}{2}\mathrm{Re}(Y) = \mathrm{Re}(VI^{*}). \tag{11}$$

Here, the voltage given is the peak amplitude of the applied input voltage.

Finally, we can write the efficiency of the framed stack in terms of its dissipated mechanical power delivered to the shear mount, W_{mech}, and input electrical power, W_d, as

$$\eta = \frac{W_{mech}}{W_d}. \tag{12}$$

4.0 EXPERIMENTAL VERIFICATION

To verify the lumped parameter model used for assessing the dynamic behavior of the piezoceramic stack, several steps were taken to verify the mechanical properties of individual components which include the piezoceramic stack, frame and shear mount load. By obtaining the response of each separately and combining them, the total response of the system is obtained.

A good design attempts to minimize the coupling between the 'rigid' parts of the calibration unit and the piezoceramic stack, but in practice this is often difficult to achieve. For example, for the blocked impedance measurement of the actuator, we normally assume that the supporting bars of the calibrator are rigid. However, during a 'blocked' impedance measurement, the displacement of the frame will still have to be accounted for even though it may be very small. Further, it is necessary to account for whatever slip exists between the frame clamps and stack frame as well as between the shear mount and the calibrator shear mount clamp. The measurement techniques to account for these less than ideal conditions will be discussed later.

While the discussion heretofore has focused on a single stack arrangement, the experiments were carried out on a double stack arrangement shown in Figure 1, since in the later stages of the project, this design evolved as an improvement on both reliability and increased authority of the framed stack. The experiments focus on the response of the double stack actuator which includes two piezoceramic elements in a single titanium frame. However, the corresponding lumped parameter model is identical to the one developed in the previous section.

4.1 Measurement of piezoceramic stack mechanical properties

Since the piezoceramic stack includes several layers of platinum electrodes and adhesive layers, it is no longer a monolithic piece of PZT and therefore necessary to determine its Young's modulus when mounted in the frame. An accurate measure of the Young's modulus is obtained from a resonance frequency test, since mass is an easily measured quantity.

The test was performed in two steps. First the stiffness of the actuator frame by itself was determined by adding a known mass to its end mass and tracking the change in the natural frequency of the lowest order mode. The frame is excited along the z-axis in a clamped-free boundary condition with a modal hammer and the in-plane response is measured with a non-contact laser velocimeter.

Next, the framed stack stiffness was calculated using the same technique as above, i.e. progressively adding mass to the frame and tracking the change in frequency. However, in this case, the piezoceramic stack was used to drive the combined frame and stack arrangement in the clamped-free boundary condition. From this test, frame and stack stiffnesses were obtained.

Combining the results of the stiffness measurement with the dimensions for the stack, the short circuit Young's modulus is computed to be 5.8x10 Pa which compares to nominal values for PZT-4S of 6.5x10 Pa. The effect of adhesive layers and electrodes act to reduce the stiffness of the PZT.

GIGA

4.2 Measurement of combined frame and load mechanical properties

The shear mount flexures used in the calibrator are made from epoxy that fills the concentric region between the stainless steel outer ring and center stud shown in Figure 10.

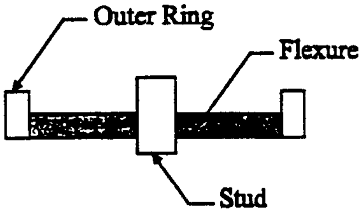

Figure 6. Shear mount used for variation of load impedance

Varying the amount of epoxy allows for the variation of load impedance of the framed piezoceramic stack. By differing the stiffness of the flexures from very compliant (soft) to very stiff (rigid), the stack response is obtained ranging from a zero to a blocked impedance condition.

The load impedance of the frame and shear mount is determined by inserting the shear mount in the calibration fixture with the frame, frame clamps and force transducer without the piezoceramic stack. Using the impact hammer and laser velocimeter focused on the shear mount stud, a direct measure of the frequency response transfer function of velocity to input force or load impedance, Z_L, is obtained. The modal parameters from this test are then obtained using a least squares circle fit on the real and imaginary components of the inverse impedance function. Figure 7 gives the experimental and theoretical impedance based on a choice of modal parameters that minimizes the least squares curve fit error.

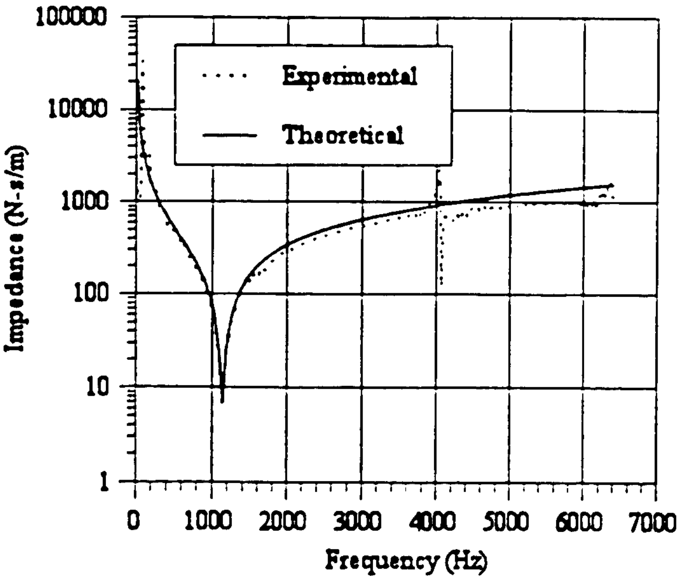

Figure 7. Typical experimental and theoretical effective load impedance

To complete the dynamics of the system, it is necessary to include the mechanical impedance of the piezoceramic stack. To begin, using the equivalent Young's modulus developed previously, the double stack impedance is plotted from Equation 10 in Figure 8.

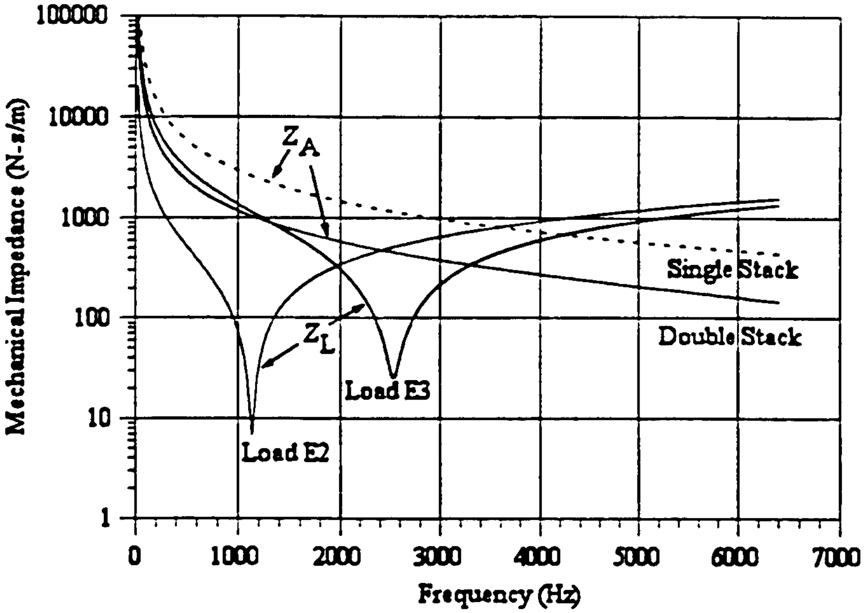

Figure 8. Stack, Z_A and Load, Z_L Mechanical Impedance

The load impedance for two different shear mount flexures and double stack frame combinations are provided to compare with the stack impedance. Note that there is an impedance match between the double stack and the load impedance E3, at frequencies below 1000 Hz.

4.3 Measurement of electro-mechanical admittance

Using the combined load impedance, Z_L, and stack impedance, Z_A, the input electrical admittance can now be determined from Equation 9 using the values for the stack parameters given in Table 1. The electrical admittance is obtained by measuring the transfer function between the input voltage and current. To measure the current, the voltage drop across a 2.36Ω resistor placed in series with the stack gives a direct measure of current. The theoretical and experimental electrical admittance is shown in Figures 9 and 10 for the double stack, in the fixed-free condition (zero impedance) as well as a typical case when the stack drives one of the shear mounts.

Stack Parameter	Value	Comments
stack layers, n	186	twice this number of stack layers for double stack arrangement
cross sectional area, S_z (m^2)	6.66×10^{-6}	active area of stack using electrode dimensions from SEM micrographs
layer width (z-dir), L_s (μm)	141	
permittivity, ε_{33} (F/m)	1.33×10^{-8}	
piezoelectric coefficient, d_{ss} (m/V)	177×10^{-10}	experimentally measured from untreated stack, below nominal values for PZT4-S a result of poor polling
Effective Young's Modulus, Y_{ss} (Pa)	5.8×10^{10}	measured from in-frame stiffness tests at constant electric field

Table 1. Summary of piezoceramic stack parameters

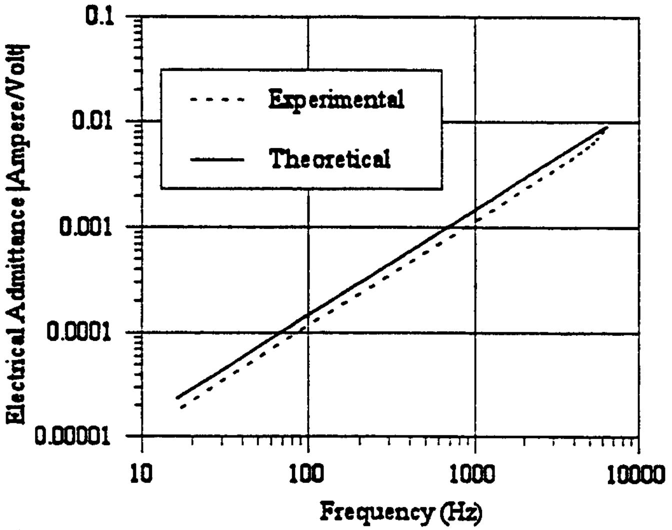

Figure 9. Electrical admittance of the framed piezoceramic stack for a clamped-free boundary condition

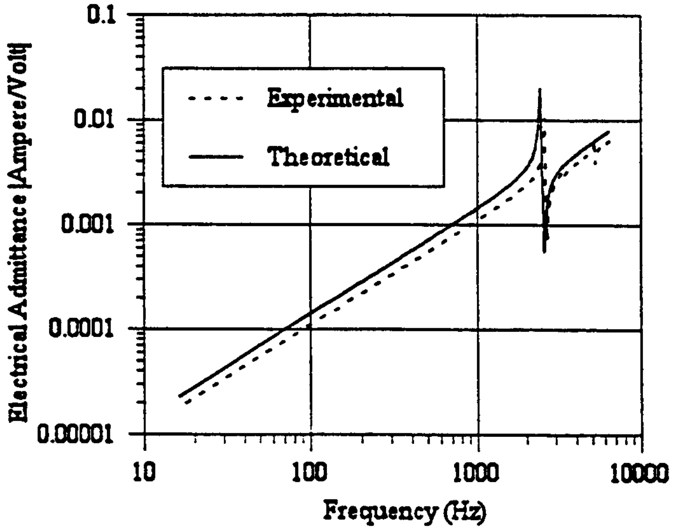

Figure 10. Electrical admittance for the framed piezoceramic stack for a typical load impedance

To compare the power consumption of the piezoceramic stack, the real part of the electrical admittance is computed using Equation 11 and measured via the real part of the cross power spectrum of the input current and voltage.

The mechanical power is also measured in the same manner to determine the work done on the equivalent load. By taking the real part of the cross power spectrum of force transmitted to the load (in this case the force transducer) with the corresponding velocity of the structural load (as measured at the shear mount stud), the output mechanical power is determined. The mechanical power and electrical power is determined for loading conditions ranging from a zero to a fully blocked impedance condition. The experimental setup for these measurement is also shown in Figure 11.

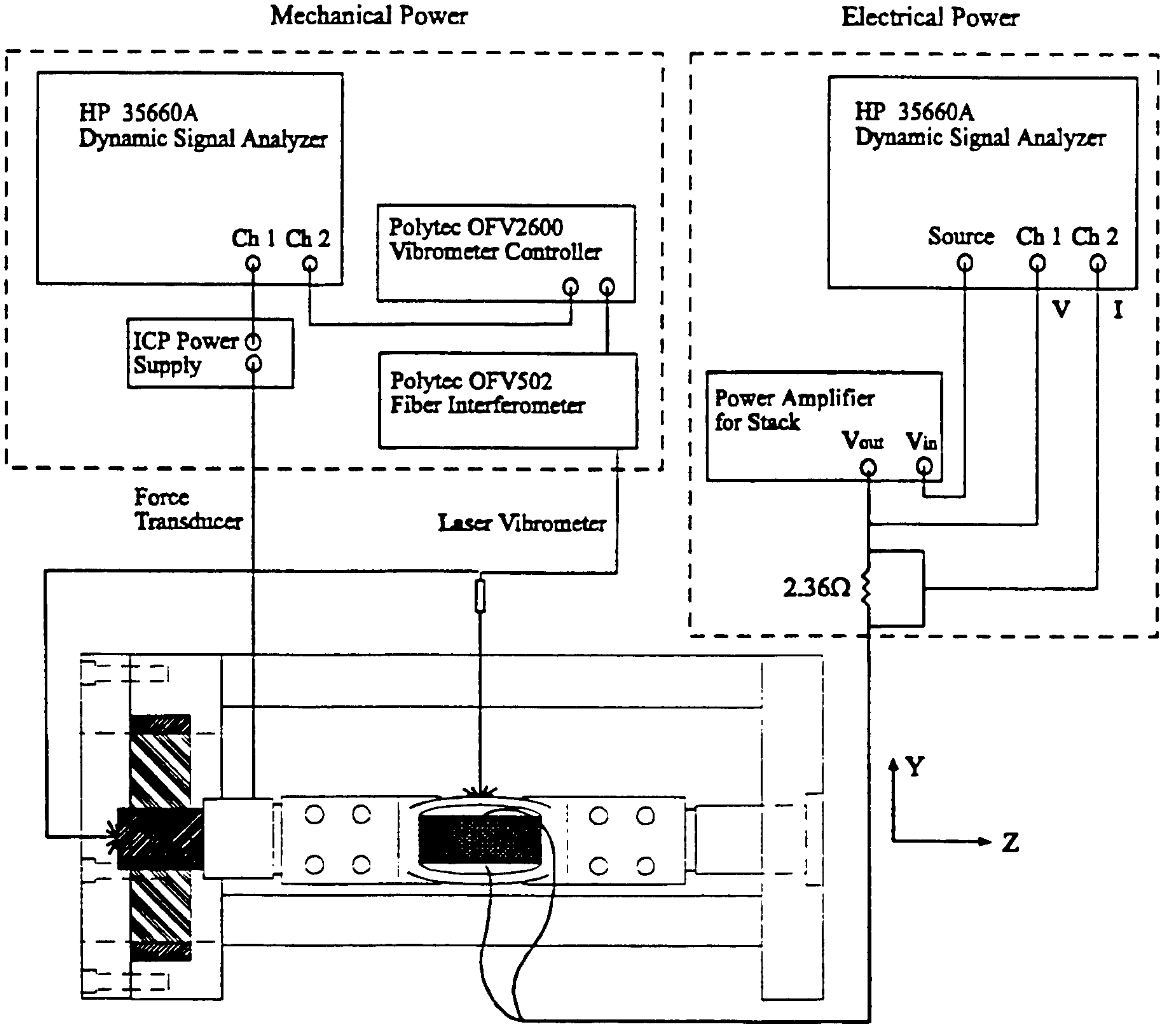

Figure 11. Experimental setup for electrical admittance and efficiency measurements

By taking the ratio of input electrical power to the output mechanical power the actuator efficiency is obtained. The values of efficiency for these different load conditions at a typical drive voltage of 10 V_{rms} are given in Table 2.

Load Impedance	Efficiency (%)
Zero	0
E1	17
E2	9.2
E3	25.1
'Blocked'	4.5

Table 2. Summary of stack efficiency into various impedance loads.

For the quasi-static data shown in Figure 12, to account for the slip between the actuator frame and frame clamps and for the lack of a fully rigid calibration fixture, the true velocity of the load can be measured through the spring arm deflection of the frame. For this approach, it is first necessary to obtain the ratio of framed actuator end displacement (z-direction) to spring arm displacement (y-direction) in a fixed-free condition. This ratio relates frame arm velocity to shear mount stud velocity (see Figure 11).

To further demonstrate the work done on the load as a function of impedance matching, we begin by plotting the output force versus displacement for various load impedances. The corresponding load lines are given in Figure 12 for the stack driven at two different drive voltages under quasi-static conditions (16 Hz).

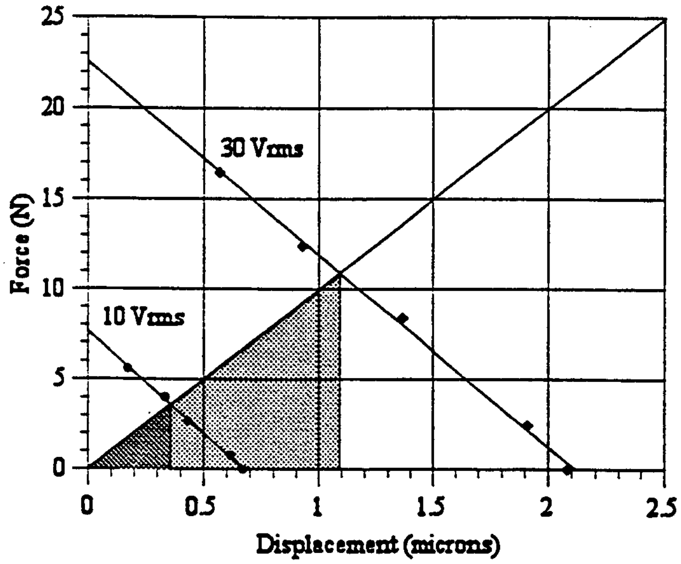

Figure 12. Force and stroke of the double stack actuator under various impedance conditions.

Note that for the matched impedance condition, the work done (shaded area under the curve) on the load is maximum. This is near the E3 load case where the efficiency was highest as shown in Table 2. Also, note that the efficiency is maximum at both input voltages for the same load impedance.

5. Conclusions

A method has been developed for the characterizing the performance of a framed, piezoceramic stack actuator using a specially designed calibration device. The load provided by the calibrator is made from a series of interchangeable shear mounts ranging from very compliant to very stiff. Measurement parameters include transmitted force and displacement, input signal current, voltage and frequency. A lumped parameter model was developed for the combined framed stack and calibrator load impedance. Combining these impedances with the transduction equations for the piezoceramic stack, its electrical admittance was computed as a function of stack and load impedance to provide an expression for the electrical power dissipated. This electro-mechanical model was then validated by measuring the electrical admittance and corresponding dissipated electrical power of the stack.

To compute stack efficiency, the mechanical power was measured via the force and displacement of the framed stack under various load impedances. The ratio of the output mechanical power to the input electrical power gave the stack efficiency as function of load impedance. It was shown that the framed stack efficiency is maximum when the stack and load impedances are closely matched. This same result was evident in the force/displacement relations measured under quasi-static conditions.

6. Acknowledgments

We wish to acknowledge and thank the following organizations for supporting this work under the SPICES project: Advanced Research Projects Agency, Penn State College of Engineering and PCB, Piezotronics, Inc.

7. References

1. D. A. Berlincourt, D. R. Curran and H. Jaffe, "Piezoelectric and piezomagnetic and their function in transducers," *Physical Acoustics*, edited by W. P. Mason, Vol. 1, Part A, pp. 169-270, Academic, NY, 1964.
2. Hueter, T.F. and R.H. Bolt, *Sonics*, Wiley, New York, 1955.
3. Koopmann, et al, 1995,"Design of an Embedded Piezoceramic Actuator for Active Control Applications", *SPIE, Smart Structures and Intelligent Systems. Conference Precedings*, Vol. 2443, pp. 703-713, Feb 27- Mar 3 1995
4. C. Liang, F. P. Sun and C.A. Rogers, "Coupled Electro-Mechanical Analysis of Adaptive Material Systems-Determination of the Actuator Power Consumption and System Energy Transfer", *Journal of Intelligent Material Systems and Structures*, Vol. 5, pp. 12-20, January, 1994.
5. L.E. Kinsler, A. R. Frey, A. B. Coppens, J.V. Sanders, *Fundamentals of Acoustics*, 3rd Ed., pp. 344-363, John Wiley and Sons, New York, 1982.
6. C. Liang, F. P. Sun and C.A. Rogers, "An Impedance Method for Dynamic Analysis of Active Material Systems", *Journal of Vibration and Acoustics. Transactions of the ASME*, Vol. 116, pp. 120-128, January, 1994.
7. E. Flint, C. Liang and C.A. Rogers, "Electromechanical Analysis of Piezoelectric Stack Active Member Power Consumption," *2nd International Conference on Intelligent Materials*, June 5-8, 1994.
8. A. B. Carlson and D.G. Gisser, *Electrical Engineering Concepts and Applications*, 2nd Ed., Addison-Wesley Publishing Company, Reading, MA, 1990.

APPENDIX 74

Development of a Surface Intensity Probe for Active Control Applications

P. L. Driesch

G. H. Koopmann

W. Chen

Center for Acoustics and Vibration,
The Pennsylvania State University,
University Park, PA 16802

J. Dosch

PCB Piezotronics, Inc.
3425 Walden Avenue
Depew, NY 14043

H. Iwata

Nagoya R & D Center
Mitsubishi Heavy Industries, LTD.
Nagoya 453, Japan

The type of sensor used in an active noise control system greatly influences the means of control and efficacy of the system. While typical error sensors used in active control, such as accelerometers and microphones, obtain vibration and sound levels, a sensor capable of directly measuring the radiated sound power of a structure would be more advantageous for certain applications.

An intensity probe which is mounted to the surface of a structure has recently been developed. The probe measures both surface acceleration and acoustic pressure in a single compact device and thus provides a measure of the intensity at the mounting position of the structure. An array of these intensity probes then leads to a measure of the structure's radiated sound power. Therefore, to minimize the sound power transmitted through a panel, an array of these intensity probes could be used as error sensors in the active control system.

This paper discusses the design, calibration, and performance of this new sensor. Results from several calibration schemes verify the phase frequency dependency between the accelerometer and microphone. The accuracy of the surface intensity probe is evaluated by a comparison to a two-microphone intensity measurement.

Introduction

The control of noise at low frequencies often proves to be problematic when conventional passive methods are used. Active noise control (ANC) however, offers an attractive alternative since it is ideally suited for applications in this frequency range.

In designing an ANC system, developing a control strategy determines and limits the efficacy of the system. Considerations for which physical quantities to measure and to minimize significantly affect the response of the ANC system. For vibrating structures, some possibilities include minimizing sound power radiation, acoustic particle velocity, or pressure as discussed by Tichy's active control review [1]. The error sensors typically consist of surface mounted accelerometers or field microphones in an attempt to measure acoustic intensity, pressure, or velocity. For applications such as minimizing transmitted sound power through vibrating structures, a surface intensity probe would be a useful error sensor. Its direct means of measuring acoustic intensity by the surface acceleration and the acoustic pressure at the mounting location proposes a useful new error sensor for active control.

The sensor combines local information about a structure's vibration and acoustical response, as opposed to obtaining purely acoustical or purely vibration information. An array of these sensors surface mounted to the vibrating structure could determine the sound power by spatially averaging the individual acoustic intensities. In addition, this sensor could be used for source identification or a transient analysis of acoustic intensity, but only its potential use for active noise control is addressed herein. The main objectives were to design, calibrate, and evaluate its performance.

There are many issues such as surface loading and optimum sensor placement that apply to the surface intensity probe. The advantages and disadvantages to using similar energy-based sensors to other sensors is addressed by Sommerfeldt and Nashif [2]. Generally, critical sources of error in the physical acoustic intensity measurement result from phase inaccuracies in measuring the acoustic pressure and particle velocity. A study by Elliot *et al* [3] concluded that experimental estimates of transmitted power were extremely sensitive to transducer phase errors, causing significant degradation in control performance. Therefore, sound power measurement sensors are very sensitive and limited in accuracy by their ability to measure the phase between the surface velocity and acoustic pressure.

Development of Surface Intensity Probe

Considerations in the design of the surface intensity probe include (1) inexpensive components that effectively measure their physical quantity without significant phase shifts, (2) small in size for less interference with the structure or neighboring components, and (3) lightweight to limit surface loading due to the mass of the probe.

The current probe design consists of an accelerometer and an electret condenser microphone, both within a common titanium housing. The cylindrical housing is 1.46 cm high and 1.10 cm in diameter. The microphone is located beneath the protective titanium grid of the surface intensity probe front face. The probe weighs only 5 grams limiting surface loading. This probe represents the third prototype of surface intensity probes, each reducing in size and weight.

The two components within the surface intensity probe are a highly sensitive piezoelectric ceramic PCB 352B22 accelerometer and an inexpensive Panasonic WM-62A electret condenser microphone. The microphone requires a DC bias of 2-10 V and the accelerometer requires signal conditioning provided by an ICP® voltage amplifier. The probe is surface mounted by standard adhesives used for accelerometers, such as beeswax or Super Glue. Two 5-44 coaxial plug connectors separately transmit the microphone and accelerometer voltage signals from the probe to the amplifiers and conditioners.

To calculate the sound intensity from acoustic pressure and surface acceleration, simple manipulation of the definition for acoustic intensity is sufficient. In the frequency domain, as described by Janzen [4], the sound intensity I is defined in Equation 1 by one-half the real part of the product of acoustic pressure conjugate P* and surface velocity V.

$$I = \tfrac{1}{2}\,Re\left[P^{*}V\right] \tag{1}$$

Velocity is obtained by integrating surface acceleration, A

$$V = j\,\frac{A}{\omega}.$$

where ω is the radian frequency.

After substituting and simplifying, the form of Equation 2 relates the acoustic pressure, surface acceleration, and sound intensity.

$$\begin{aligned} I &= \tfrac{1}{2}\,Re\left[P^{*}j\,\frac{A}{\omega}\right] \\ &= \tfrac{1}{2}\,Im\left[\frac{P^{*}A}{\omega}\right] \\ &= \frac{1}{2\,\omega}\,Im\left[P^{*}A\right] \end{aligned} \tag{2}$$

Recognizing that the imaginary part of the cross-spectrum Q_{12} of two signals is common to many frequency analyzers, Equation 2 simplifies to

$$I = -\frac{1}{\omega}\,Q_{PA}. \tag{3}$$

To compute the sound power W, the sound intensity measured from an array of surface intensity probes is spatially averaged over N equal surface areas S, as

$$W \approx \sum_{i=1}^{N} I \cdot S. \tag{4}$$

This novel design and concept of a surface intensity probe has been analyzed and experimentally verified by Janzen [4] for the first prototype of surface intensity probes. The third prototype discussed in this paper is $\frac{1}{3}$ the weight and consists of different components. New experimental verification was needed for this latest prototype. The first concern and possibly most significant source of error is the calibration of the sensor. The greatest concern in the calibration was determining the frequency dependent phase shifts of the accelerometer and microphone in the probe.

Calibration of Probe

There are standard procedures for calibrating microphones and accelerometers, of which the accelerometer calibration is the simpler method. The magnitude and phase of the accelerometer's sensitivity are experimentally determined by a back-to-back comparison calibration with a PCB 301A03 reference accelerometer. The reference accelerometer provides a standardized 10 mV/g (±0.05°) comparison [5]. The experimental setup for the accelerometer's calibration accelerometer is shown in Figure 1, where Super Glue attaches the probe and the reference accelerometer. A chirp excitation signal to the shaker accelerates both the probe and reference accelerometer. Figure 2 shows the probe accelerometer calibration magnitude and phase for three different probes. A ± 0.5 to 1 degree phase shift for the probes over a 2 kHz frequency range is small and insignificant when considering the potential error in intensity measurements. The variance in magnitude between different probes is resolved by separate sensitivities for the individual probes.

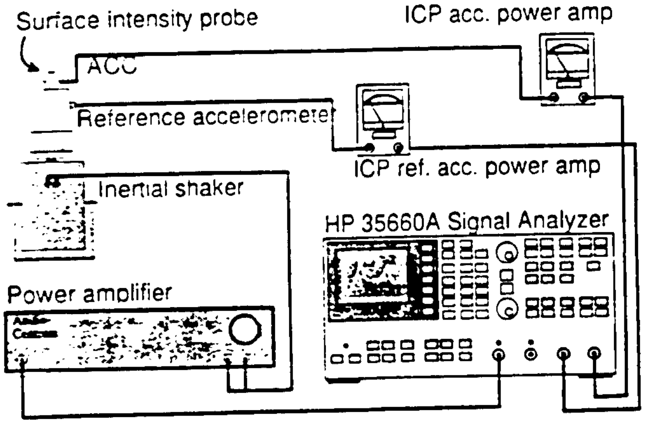

Fig. 1 Experimental setup for the probe accelerometer calibrations

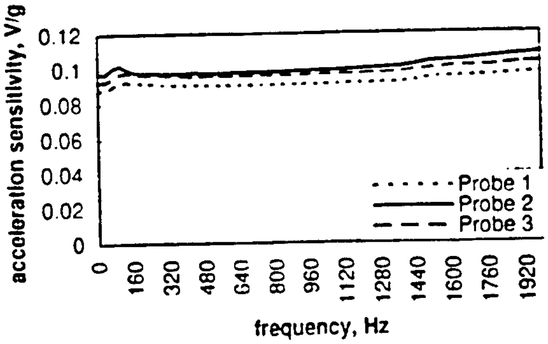

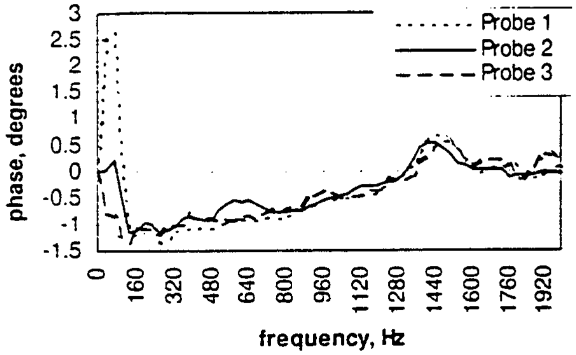

Fig. 2 Magnitude and phase for three different probe accelerometer calibrations

Calibration of the probe's microphone is not as straight forward. Several common techniques lack either the accessibility of easy laboratory experimentation or do not measure the frequency dependency of the microphone's phase shift. To gain confidence in the calibration of the microphone, the common experiments were performed, but a more applicable calibration technique was sought.

The first experiment used a B&K Type 4220 pistonphone, which produces a precision 124 dB SPL (sound pressure level) at 250 Hz [6]. The transfer function between the microphones's output voltage in response to the 124 dB SPL is thecalibrated sensitivity of the microphone. The sensitivities for three probes calibrated by the pistonphone are shown in Table 1. A custom-made adapter was used as a coupler between the probe's microphone and the pistonphone's cavity orifice. This calibration method is valuable for determining the general magnitude of the microphone sensitivity, but gives no indication of the frequency dependency of these results.

Table 1 Probe microphone sensitivities from pistonphone calibration at 250 Hz, 124 dB SPL

	Probe 1	Probe 2	Probe 3
Sensitivity, mV/Pa	13.4	12.2	13.3

The second experiment attempted to calibrate the probe's microphone over a frequency range. Referring to Figure 3, the probe microphone and half-inch B&K Type 4133 condenser microphone with sensitivity 1 mV/µbar [7], are bonded to a square four inch piston loudspeaker. A laser vibrometer measures the surface velocity of the piston, which is divided by radian frequency ω. The speaker is excited by random noise from 50 Hz to 850 Hz. The B&K microphone has a steady response within ±2 dB over a 20 Hz to 40 kHz frequency range [7] and is considered the reference microphone. Shown in Figure 4, the probe microphone sensitivity is the transfer function between the probe microphone and the calibrated B&K microphone. Each microphone was compared to the measured displacement of the piston. The microphones measure a response that closely match the predicted response from a baffled piston radiator.

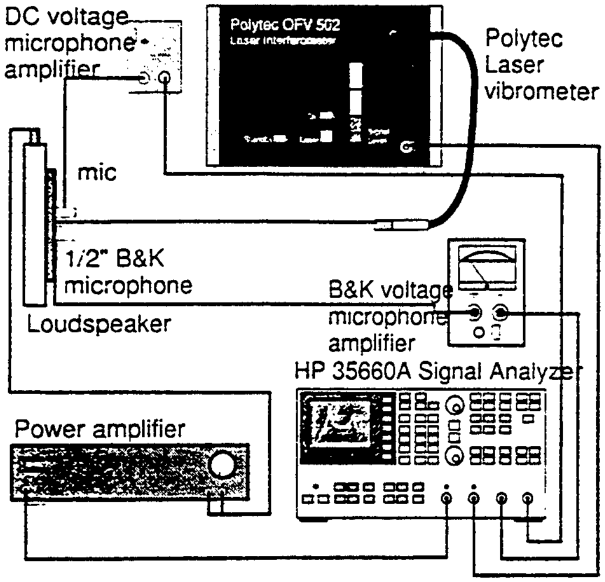

Fig. 3 Experimental setup for microphone loudspeaker calibration

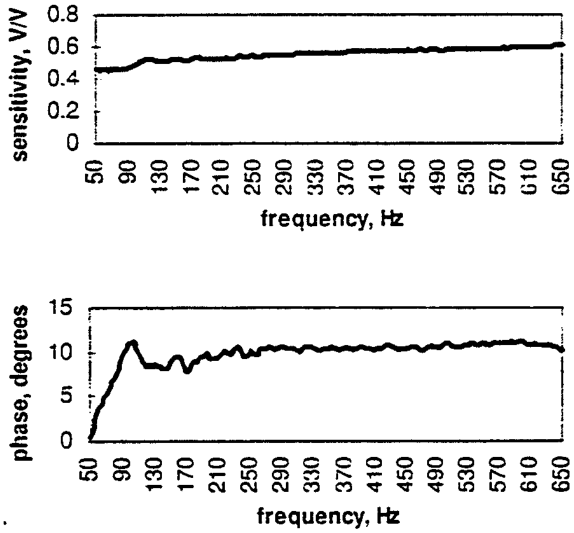

Fig. 4 Magnitude and phase for microphone sensitivities in loudspeaker calibration

New Calibration Scheme

As verified by previous calibration experiments, the phase shift over a 2 kHz frequency range is insignificant for the accelerometer and small for the microphone, but the phase shift could affect highly reactive intensity measurements. Thus, for more accurate intensity measurements, identifying the phase shift inherent in the microphone is needed. A frequency dependent calibration curve would compensate for this phase shift. A new calibration scheme was proposed to verify the microphone calibration for practical applications, such as field testing or when an anechoic room is not accessible.

The calibrator consists of a cylindrical titanium housing enclosing an air cavity 3.81 cm (1.5 inch) tall and 0.76 cm in diameter. The air cavity is sealed by the probe as shown in the exploded cross section view in Figure 4. A thin rubber o-ring compresses so that the probe has a metal-to-metal contact with the air cavity. The calibrator's threaded lid screws on the calibrator body, tightly securing the probe within the calibrator. There are two slots on the calibrator for the 5-44 connector plugs on the probe.

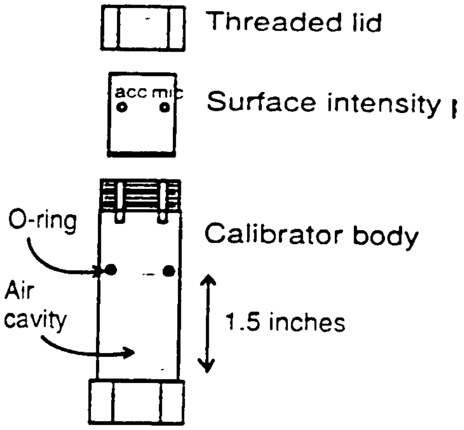

Fig. 5 Exploded cross section view of a probe in the calibrator

When calibrating, the calibrator is attached to a shaker and excited over a 0 to 2 kHz frequency band. The air cavity is not compressed as in the pistonphone calibrations, but rather it is accelerated as a mass of air. The probe's microphone faces the air cavity and measures the resulting force from the accelerated mass, which follows Newton's second law. This simple prediction is that the acceleration, measured by the probe's accelerometer, is in phase with the pressure (force) measured by the probe's microphone. A derivation that relates the pressure measured by the microphone and the acceleration measured by the accelerometer follows.

Newton's second law states

$$F = ma,$$

where F is the force on the microphone's diaphragm and a is the acceleration of the mass of air. Substituting the product of ρ as the air density and the volume of the air cavity as the product of the length L and calibrator's air column surface area S_{cal}

$$F = \rho L S_{cal} a. \qquad (6)$$

The pressure P that correlates with the force on the diaphragm is

$$P = \frac{F}{S_{mic}}.$$

where S_{mic} is the surface area of the microphone's diaphragm. Substituting Equation 6 produces the following relationship between pressure and acceleration,

$$P = \rho L \frac{S_{cal}}{S_{mic}} a. \qquad (7)$$

Recalling that the accelerometer has a flat response, Equation 7 clearly displays that a transfer function of the pressure over acceleration from the probe is constant and will measure any inherent frequency dependent phase shift in the microphone.

The advantages of this calibration scheme are numerous.

- The calibration could be performed in a noisy environment.
- Only a shaker and the new calibrator are needed in addition to the ordinary instrumentation for sound intensity measurements.
- In a field testing situation, a simple impulse to the calibrator could calibrate the microphone.
- It is a simple, inexpensive procedure.

Unfortunately, the initial results from this calibrator were not as expected. Additional phenomena are occurring within the calibrator complicating the results. The pressure to acceleration transfer function magnitude and phase from the probe are shown in Figure 6. These curves are measured by three different probes with precision. The first acoustic resonance of the cavity is measured at 4.5 kHz, and is not the cause of the frequency shift. Currently, we are using lumped parameter modeling to attempt to predict the measured response. Since there is great merit to this calibration scheme, further modeling considerations are being investigated. Although the results were not as expected for this calibration scheme, the previous experiments confirmed a nearly constant phase response over a limited frequency range for the microphone.

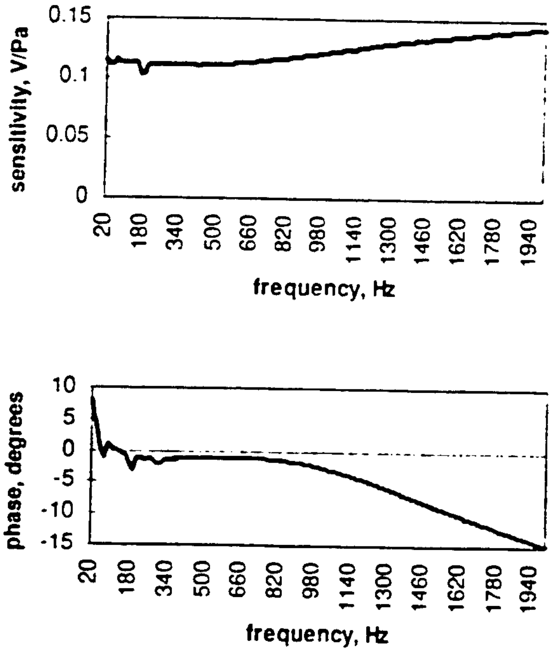

Fig. 6 Calibrator results from the probe pressure to acceleration transfer function in magnitude and phase

Performance Evaluation

To evaluate the performance of the surface intensity probe, an experiment was designed to simply compare the sound power summed from an array of surface intensity probes to the measured sound power from a two-microphone intensity probe. A square 0.29 m by 0.29 m by 1 mm aluminum plate with highly symmetrical mode shapes is excited in its 1-1 structural mode.

Nine probe measurement points, in a symmetrical pattern with center point loading, measure the sound intensity and therefore approximate the sound power radiated from the plate.

These experiments were conducted in a semi-anechoic room. The plate is bonded in a stiff frame simulating clamped boundary conditions. A lightweight loudspeaker is attached by an aluminum push rod to the center of the plate for center point excitation. A schematic of the plate and its surface loading is shown in Figure 7. Making use of symmetry, three probes measure the necessary intensities for a nine element discretization of the plate surface. Dummy masses with the same shape and weight of the surface intensity probes load the plate on the six other elements. The plate was excited with a sine wave excitation at five discrete frequencies, 122.5, 123, 124, 125, and 126 Hz, near or at the 1-1 structural mode at 122.5 Hz. At a discrete frequency, the intensity from three surface intensity probes were measured sequentially, and then the two-microphone intensity experiment was performed. This procedure is repeated for five frequencies.

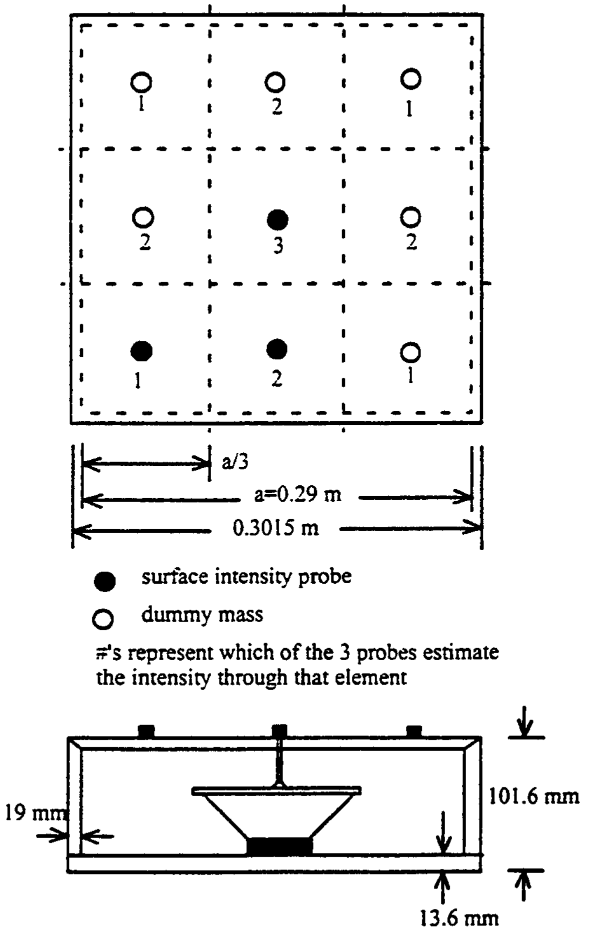

Fig. 7 Schematic of plate and surface loading of plate

The intensity is measured by using Equation 3 programmed in the HP 35660A Signal Analyzer shown in Figure 7. A nine element approximation of the sound power is calculated using Equation 4 for $S = 0.01016\ m^2$, $N = 9$, and using symmetry to estimate the intensities from the six other elements. These results are in Table 2.

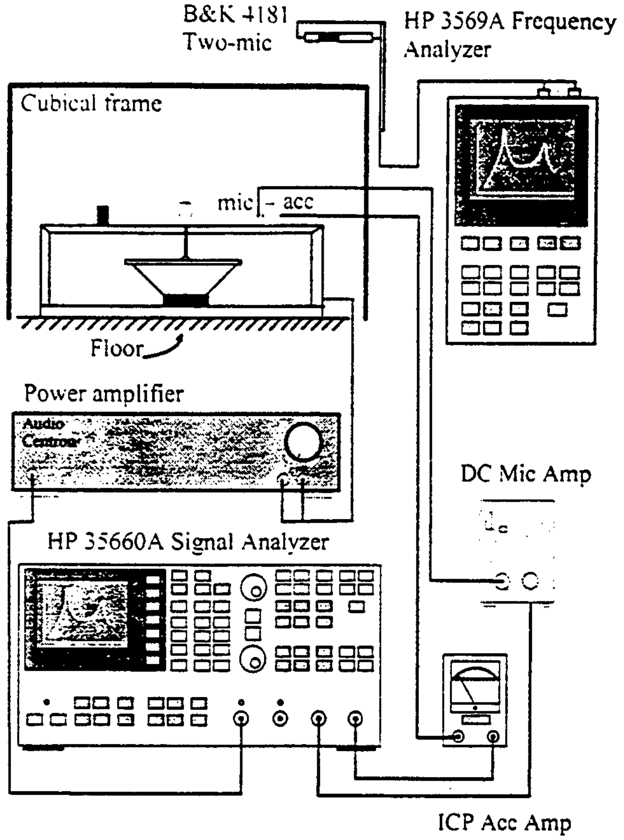

Fig. 8 Experimental setup for plate sound power comparison at discrete frequencies. Setup includes both surface intensity probe and two-microphone experiments.

The two-microphone experiment is a standard procedure for measuring the intensity or sound power. This experiment consisted of setting up a cubical 0.86 m frame around the plate resting on the floor, and then measuring the intensity through each of the 5 faces of the frame enclosing the plate. The sound power is estimated using Equation 4, where $S = 0.7396\ m^2$, $N = 5$, and I is measured by the two- microphone intensity probe. This technique uses two B&K condenser, phase-matched microphones separated 5 cm. to measure an average pressure between the microphones and estimate the velocity by a pressure gradient. As described by Waser and Crocker [8], the intensity is calculated by use of Equation 5.

$$I(\omega) = \frac{Q_{12}}{\omega\rho\Delta r}. \qquad (5)$$

where ρ is the density of air, Δr is the separation between the microphones. Q_{12} is the imaginary part of the cross spectrum between the two microphones, and ω is the angular frequency where Q_{12} is measured. The HP 3569A Frequency Analyzer is specifically designed for this technique, thus Equation 5 is preprogrammed in the analyzer and the sound power is calculated by programming the surface areas in the analyzer. The two-microphone sound power results are in Table 2.

Table 2 Sound power comparison between an array of surface intensity probes and the two-microphone technique at discrete frequencies.

	122.5 Hz	123 Hz	124 Hz	125 Hz	126 Hz
Surface intensity probes, dB	94.2	95.1	95.3	96.7	96.8
Two-microphone, dB	93.5	93.4	94.0	95.5	96.3
Difference, dB	0.7	1.7	1.3	1.2	0.5

Evaluating the sound power calculations from this experimental data indicates that the nine element discretization of the plate and performance of the surface intensity probes closely match the two-microphone technique. A 1 to 2 dB discrepancy is within the possible error of the two-microphone technique. Therefore, these results confirm the surface intensity probe can and does perform accurately under these specified conditions.

Acknowledgments

This material is based upon work supported under a National Science Foundation Graduate Fellowship. The research is supported by an NSF and SBIR contract to PCB. Piezotronics, Inc., Depew, New York. 14043.

Conclusions

The surface intensity probe is a unique design and potentially very useful as an ANC error sensor. An array of these probes can determine sound power by spatially averaging the intensity measured by each probe.

There are three remaining issues to be addressed in the design, calibration, and validation of the surface intensity probe. First, the frequency dependent phase shift response from the probe microphone has been accurately measured, but the noted phase shift effects on sound power have not been determined. This curve differs slightly between different probes, so the error that could result from that variance must be addressed. Therefore, a phase assessment needs to be completed, confirming the sound power error that results from a phase error in calibrating the microphone. The investigation may conclude that narrow band frequency experiments need a microphone sensitivity and phase that apply for the frequency band of interest without significant error in sound power.

Second, the procedure for measuring the frequency dependent sensitivity of the microphone must be practical, suggesting that the new calibrator is a strong candidate. The unexpected and repeatable microphone sensitivity measured in the calibrator suggests it can be useful if there is a theoretical prediction of the results. Then the procedure would require matching the measured response to a predicted response, which aligns with a calibrated microphone. Further investigation is needed to model and predict the measured response when using the calibrator.

Third, the probe will be validated when more experiments test the full range of the surface probe's performance in order to determine the limits of its performance. This would include wide band frequency tests, highly reactive sound intensity measurements, and small vibration levels. Its performance will be evaluated by comparing the two-microphone intensity probe and by comparing theoretical predictions to the sound power measured by the surface intensity probe.

References

1 Tichy, J., 1996, "Applications for Active Control of Sound and Vibration," *Noise/News International*, pp. 73-86.

2 Sommerfeldt, S., and Nashif, P., 1994, "An Adaptive Filtered-x Algorithm for Energy-based Active Control," *J. Acoust. Soc. Am.*, Vol. 96 No. 1, pp. 300-306.

3 Elliott, S., Gardonio, P., Pinnington, R., David, A., Garcia-Bonito, J., Pavic, G., Besombes, M., Ohlrich, M., Laugesen, S., and Henriksen, E., 1997, "The Control of Transmitted Power in an Active Isolation System," Proc. ACTIVE 97, pp. 93-104.

4 Janzen, P., 1995, "Calibration and Validation of an Interfacial Acoustic Surface Intensity Probe," M.S. Thesis, The Pennsylvania State University.

5 PCB Piezotronics, Inc., 1996, "Dynamic Sensing Instrumentation: Vibration and Shock Sensor Selection Guide," Depew, NY, pp. 89

6 Bruel & Kjaer, "Instructions and Applications: Pistonphone 4220," Naerum, Denmark.

7 Bruel & Kjaer, "Instructions and Applications: Half-inch Condenser Microphones 4133/34," Naerum, Denmark, pp. 17.

8 Waser, M. P., and Crocker, M. J., 1984, "Introduction to the Two-microphone Cross-spectral Method of Determining Sound Intensity," *Noise Control Eng. J.*, Vol. 22, Num. 6, pp. 76-85

APPENDIX 75

Design, Modeling, and Performance of a High Force Piezoelectric Inchworm Motor

Timothy Galante[a], Jeremy Frank[b], Julien Bernard[b], Weiching Chen[b], George A. Lesieutre[b], and Gary H. Koopmann[b]

[a]United Technologies Research Center, East Hartford, CT 06108
[b]Center for Acoustics and Vibration, Penn State University, University Park, PA 16802

ABSTRACT

A linear inchworm motor was developed for structural shape control applications. One motivation for this development was the desire for higher speed alternatives to shape memory alloy based devices. Features of the subject device include compactness (60 x 40 x 20 mm), large displacement range (~1 cm), and large holding force capability (~200 N). There are three active piezoelectric elements within the inchworm: two "clamps" and one "pusher." Large displacements are achieved by repetitively advancing and clamping the pushing element. Although each pusher step is small, on the order of 10 microns, if the step rate is high enough, substantial speeds may be obtained (~1 cm/s). In the past, inchworm devices have been used primarily for precision positioning. The development of a robust clamping mechanism is essential to the attainment of high force capability, and considerable design effort focused on improving this mechanism. To guide the design, a lumped parameter model of the inchworm was developed. This model included the dynamics of the moving shaft and the frictional clamping devices, and used a variable friction coefficient. It enabled the simulation of the time response of the actuator under typical loading conditions. The effects of the step drive frequency, the pre-load applied on the clamps, and the phase shifts of the clamp signals to the main pusher signal were investigated. Using this tool, the frequency bandwidth, the optimal pre-load and phase shifts which result in maximum speed were explored. Measured rates of motion agreed well with predictions, but the measured dynamic force was lower than expected.

INTRODUCTION

Solid-state piezoceramic actuators are typically limited to low displacement applications, but may be used at high frequencies. Typical applications include vibration excitation and control actuators and positioning devices. The desire for a smart materials actuator that produces high force and high displacement at relatively high frequencies is not new, but a functional, low-profile, manufacturable actuator has not yet been realized. Developed in pursuit of this goal, the Penn State H3C inchworm is a high authority device that capitalizes on the high forces produced by piezoceramic stacks, while overcoming low displacements using an inchworm actuation scheme. This paper discusses the history of inchworm actuators, design of the subject device, and modeling and experimental results which supported the design.

The research described herein was supported by the DARPA Smart Aircraft and Marine Propulsion System Demonstration (SAMPSON) program. SAMPSON is a system level demonstration of the application of smart materials and structures to submarines and aircraft. One role of the Center for Acoustics and Vibration at Penn State (PSU/CAV) is the development of actuators that will drive adaptively conformable flow control surfaces in annular propulsion units used on aircraft and marine systems, as shown conceptually in Figure 1. The PSU/CAV is assessing the potential of candidate actuators, selecting the best ones, then designing, manufacturing and validating the actuators, their power units and controllers for delivery to the other members of the SAMPSON team.

The successful actuator, which is to be used in shape control applications, will ideally have several features, including: high force, high displacement, high energy density, compact design, ability to be easily integrated and replaced, cost effectiveness, and ease of control. An actuator that uses inchworm type actuation in conjunction with multi-layer piezoceramic stacks was selected for development. Subsequently, a survey of existing inchworm methodology was performed to gain perspective on improvements needed to enable high authority operation.

Further author information -
T.G.: Email: GalantTP@utrc.utc.com. Research Engineer.
J.F.: Email: jef121@kirkof.meche.psu.edu. M.S. candidate.
J.B.: Email: jeb21@kirkof.meche.psu.edu. M.S. candidate.
W.C.: Email: chen@kirkof.meche.psu.edu. Research Associate.
G.A.L. (correspondence): Email: g-lesieutre@psu.edu; Telephone: 814-863-0103. Associate Professor, Associate Director, CAV.
G.H.K.: Email: ghk@kirkof.meche.psu.edu. Professor, Director of the Center for Acoustics and Vibration.

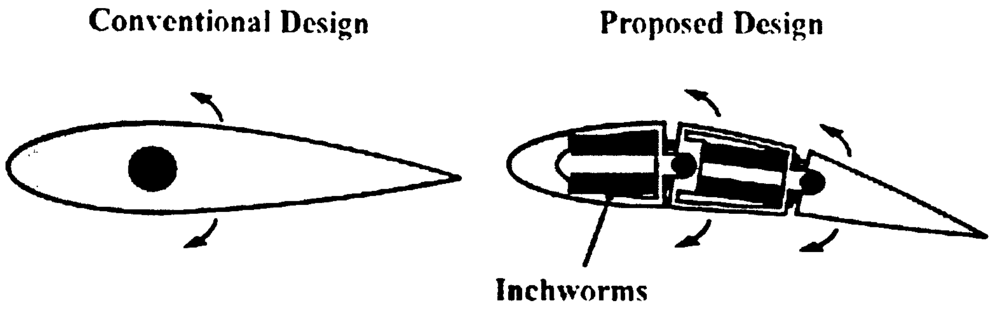

Figure 1: Concept for a deformable flow control surface

LITERATURE SURVEY: INCHWORM STATE-OF-THE-ART

The inchworm devices reviewed generally fell into one of three basic groups. The first group involves a "walker" configuration, in which the induced-strain activation elements (ISA) move with a shaft. The shaft appears to be walking or looping, as it were, along the desired path of actuation. The second basic configuration is the "pusher". In this arrangement the ISA elements are removed from the actuation shaft. The actuator pushes the shaft along using an inchworm technique. The third group is the hybrid walker-pusher. This type mixes the two kinds of actuation, with the ISA elements not completely removed from the actuation shaft.

The first group of actuators represents preliminary designs which paved the way for the inchworm actuators to come. Stibitz & Steele [1] in 1964 were among the first to design an effective inchworm actuation technique. They used magnetostrictive materials to actuate a shaft using a typical "pusher" method. As shown in Figure 2, the Stibitz & Steele actuator was built in three segments which were each used for extending and clamping as a magnetic field was applied. The focus of their design was to create a positioning actuator for use in precision machining and tooling. The second major contribution to inchworm actuators was not itself an inchworm. McNancy [2], in late 1964, developed a method of piezoceramic actuation which used a multi-layer stacked piezoceramic actuator coupled with a motion amplifying structure. As shown in Figure 2, the stacked ISA element drove a combination of ball bearings to produce larger motions in the transverse direction. The use of multi-layer stacked actuators was important in the development of piezoceramic inchworms.

The first patented piezoceramic inchworm was introduced by Hsu [3] in 1966. The design was a complicated walking actuator that used a single hollow cylindrical element to clamp and extend. As shown in Figure 2, the clamping end of the piezoceramic had an annular wedge surface which clamped with an alternating signal. The two-layer piezoceramic disks on each end of the actuator were used to bias the direction in which the wedge would restrict motion. To reverse the direction of travel the polarity of the signal was switched and the disks reversed their direction of bowing. The action switched the direction of motion that would cause the wedges to engage.

The next actuator improved on the previous actuators in several ways. Locher 1967 [4] made several positive improvements in the field of precision linear induced strain actuators. The inchworm was configured in a hybrid structure with the clamping elements engaging a "clam-claw" mechanism as shown in Figure 2. The "clam-claw" allowed motion in one direction, but engaged instantly in the other. This method was the first hybrid inchworm actuator and the first which applied maximum holding force in the un-activated state. This device was designed exclusively for precision actuation and was capable of individual steps of 0.0005 inches.

In 1968, Brisbane [5], designed the simplest actuator to date, as shown in Figure 2. He used a combination of three cylindrical piezoceramic elements, two for clamping and one for extension. This actuator was the first piezoceramic inchworm to use the simple "walking" method. The intent of the design was to have micron range positioning for tooling and claimed actuation speeds of 50 mm/sec.

The inchworm presented by Galutva [6] in 1972 represented a vanguard design of inchworms for its time and the coming decade. This Russian group designed an actuator, as seen in Figure 2, that had micron-range positioning, used stacked piezoceramic elements in a walker configuration, and fit into a slim and compact profile.

The design introduced by Bizzigotti & May [7] in 1975, shown in Figure 2, was the first example of a "pusher" configuration piezoelectric inchworm. The goal of their design was to provide a very precise linear actuator capable of incremental steps of

0.004 micrometers. The piezoelectric elements formed a U shaped actuator which clamped and extended in the now-traditional inchworm manner. An important contribution was the introduction of the term "inchworm" to describe such devices. The next inchworm, patented by Sakitani [8] in 1976, did not advance inchworm technology significantly, but was a fine design in its own right. It was a "walker," as shown in Figure 2, used for precision placement of a electron scanning microscope. The design presented by Ishikawa [9] in 1979 was very similar to the Bizzigotti & May design, except it used two piezoelectric elements for extension, as opposed to one.

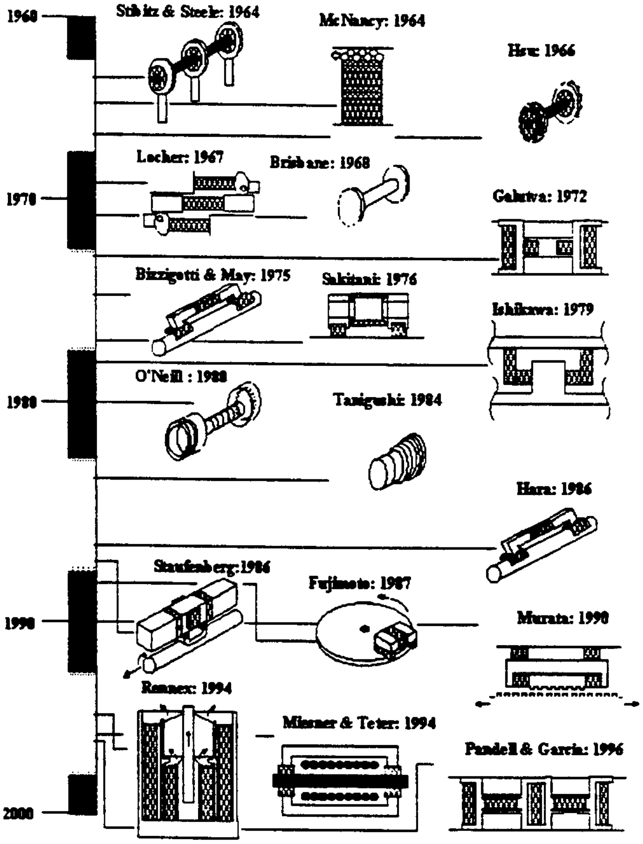

Figure 2: Illustrated Timeline of Inchworm History

The inchworm presented by O'Neill [10] in 1980 was the first to use the stacked piezoelectric actuator to increase the actuation length of the inchworm. The design, shown in Figure 2, used two clamping disks coupled with "cups" that pushed against the outer cylinder when zero charge was applied. When the disks were actuated, the cups retracted from the wall, and the "stacked" piezo-disks extended.

The actuator presented by Taniguchi [11] in 1984 represented a new approach. The actuator, shown in Figure 2, used a multitude of piezoceramic elements stacked upon one another. These elements acted as both clamps and extension actuators. Actuation resembled an earthworm more than an inchworm, in which the elements are driven so that they extend and contract in a wave-like or peristaltic motion. The device presented by Hara [12] in 1986 used a great number of layers in a stacked piezoceramic actuator, by reducing the overall thickness of each layer and bonding them together. This design was a copy of the Bizzigotti & May device and differed mainly in that it made a conscious effort to be compact. This design represented the state of inchworm actuators in the middle of the 1980's, during which time few major improvements were made.

The design by Staufenberg [13] in 1986 was an exception. As shown in Figure 2, the actuator was a pusher-type, capable of translational or rotational motion. Rotational actuation was provided by a method in which a clamping/tangential extension was applied by various actuators to produce torque. The translational method was slightly suspect because it used a rocking method to propel the shaft forward. Fujimoto [14] in 1987 presented an inchworm "pusher" which replaced a stepper motor. The idea was to use a frictional clamp which could be applied to the edge of a disk in order to actuate it in much smaller increments than possible with a stepper motor. In 1990, Murata [15] presented a patent which used a novel "pusher" piezoceramic inchworm configuration to push a shaft using a linear gear rack of extremely small pitch. The idea was to control the x-y position of the gear so that it engaged and disengaged in a method similar to annular gears. This method proved to be highly ineffective and Murata switched to a hybrid inchworm in which magnetic heads applied the clamp.

Rennex [16] presented a novel arrangement of piezoceramics in 1994 in which the actuators were arranged in a parallel. hybrid pusher-walker configuration. This method resembled Locher's design. but removed the use of a "clam-claw" for a flexural clamp. The use of a parallel arrangement slimmed its profile considerably. In 1994. Miesner & Teter [17] presented a paper which gave a detailed description of an inchworm using a hybrid TERFENOL-D and piezoceramic "pusher" system. As shown in Figure 2. the TERFENOL was used for extension and the piezoceramic was used for clamping. This was the first inchworm that was designed for high rate force application. The actuator produced 26 pounds at stall and a rate of 1 inch/sec at no load. The drawback of the design was that it was rather large. spanning almost half a foot. The resonant drive electronics were also of note.

The inchworm proposed by Lee [18] in 1995 (not illustrated) represented a departure from previous designs. This particular design sought to create an inchworm using VLSI manufacturing techniques. The inchworm measured approximately 15 mm in length and produced forces in the mN range and speeds of 13cm/min. These values are unimpressive compared to previous designs, but are very good considering the size of the inchworm.

The final design considered in this review was the piezoceramic caterpillar motor presented by Pandell and Garcia [19] in 1996. Their design was very similar to that of Galutva. twenty years earlier. except (as with Lee) the focus had shifted to larger forces and displacements. A more detailed review of inchworm technology is contained in the thesis by Galante [20].

This new focus. emphasizing increased force capability, is also that of the research described herein. The goal is a device that operates at speeds rivaling those of previous devices. but that also provides forces like those of the range of the Lee inchworm in a much smaller package.

DESIGN AND STRESS MODELING

Piezoceramic inchworms. as described in the previous section. have historically been designed as micron-scale positioners for precision machining or scanning electron microscopes. The H3C inchworm actuator departs from its predecessors in that it is to be a high authority device. capable of large forces and large displacements. Initial shape control applications are anticipated to be relatively low frequency. nearly quasi-static.

Figure 3 illustrates the stepping mechanism employed by the device. The inchworm consists of three parts. two of which are clamping mechanisms. and one called a "pusher". The clamping mechanism consists of a mass-spring system (which applies the frictional clamp to the pusher) and a piezoceramic stack which lifts the clamp from the pusher to allow movement. The pusher consists of a piezoceramic stack embedded in a translating shaft. on which an exterior load may act.

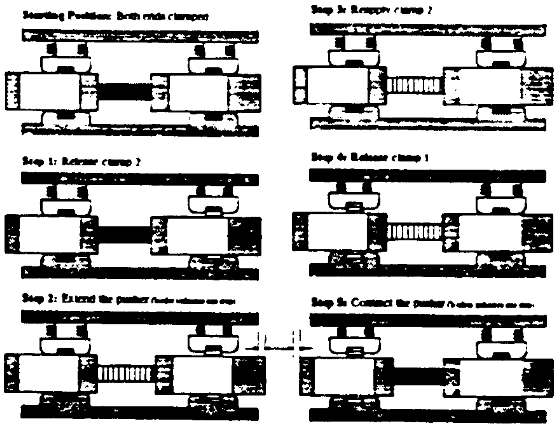

Figure 3: Translational Operation of the H3 Inchworm

Operation begins with both ends clamped. Step 1 shows release of the right clamp. permitting pusher motion to proceed to the right. In step 2. the pusher stack is activated so that front of the pusher extends to a new position. This extension distance is approximately 1-10 μm. depending on the load acting on the shaft. In step 3. the right clamp is reapplied by de-energizing its piezoceramic stack. This position is identical to the original position except for two key points: (1) the right end of the pusher has been slightly displaced: and (2) the center piezoceramic is energized. In step 4. the left clamp is released by energizing its in-line stack. In step 5. the center stack is de-energized. thus contracting components of the pusher. and returning it to its original shape. Once the left clamp is re-applied (not shown) by de-energizing the left piezoceramic stack the inchworm has returned to its clamped state. having completed an incremental displacement of the pusher to the right.

As shown in Figure 3, the H3C inchworm actuator includes two clamping piezoceramic stacks and one transverse piezoceramic stack which extends the pusher. For best performance, the clamping stacks should have several times the blocked force of the pusher stack. For reasons of economy, all the stacks used in the H3C device are identical, and performance is limited by the capability of the clamping stacks. The stacks used are Sumitomo parts PSA-15C45N. They are 5.2 x 4.5 x 20 mm, with individual layer thicknesses of 0.11 mm. The material is a soft PZT-5D.

The clamping stacks are used to disengage an integral flexure which provides the clamping action on the pusher element. The design of this flexure, integral to the upper frame, was crucial to the successful operation of the actuator. The main design goals for this part were to provide maximum clamping force on the pusher when the stack is uncharged, and to completely disengage the clamp when the stack is energized. Several conditions had to be satisfied for the inchworm to operate effectively in this manner: The impedance of the deformed structure needed to closely match the impedance of the piezoceramic stack, to facilitate energy transfer. The Von-Mises stress magnitudes were also required to remain within the yield stress envelope. A standard factor of safety was used to account for anticipated higher transient loads in operation. Further, the stiffness of the structure in the transverse direction was maximized, in order to minimize displacements due to friction applied by the pusher. Another desire was maximization of the resonance frequency of the clamp system, to ensure that it was higher than that of the stack. This would allow the maximum clamping frequency to be limited mainly by the stack. The last condition involved the surface region that defines the interaction of the pusher and the stack: the stress distribution across the stack should be fairly uniform and the structure should clamp onto the pusher in a uniform fashion.

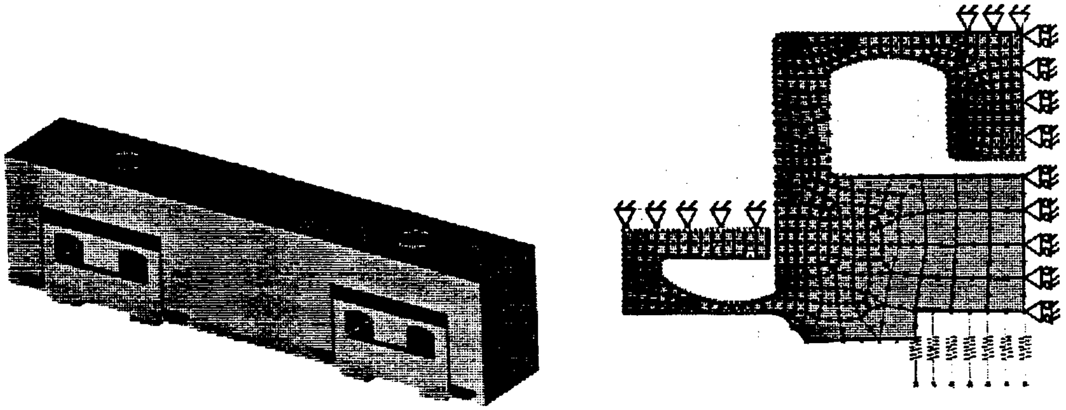

Figure 4: a) Design of the H3C actuator frame and b) a static finite element model of the clamping substructure

The clamping mass/spring sub-structure was modeled, taking advantage of symmetry, using plane stress finite elements and the mesh shown in Figure 4b. The model used spring elements to model the force-displacement characteristics of the piezoceramic stack at low frequency. These spring elements provided a distributed load across the interaction surface with the piezoceramic stack. The value of the combined stiffness was 35 MN/m, which represented the operating point at which the stack would produce a force of 350 N at a displacement of 10 microns. These spring elements were then displaced by 10 microns. Roller boundary conditions were applied to the symmetry line of clamping sub-structure, and clamps were applied at the edge and at the screw interaction point to simulate the relatively high stiffness of the rest of the upper frame. This technique made it unnecessary to model the rest of the upper frame and greatly reduced computation time.

The pusher, lower frame, panels and other small parts were designed with an emphasis on manufacturability and assembly. These parts were made from titanium at PCB Piezotronics, Inc., using wire EDM. The main function of the pusher is to transmits the actuation force and displacement to an exterior load. The design of the pusher was critical to the operation of the inchworm. The pusher has slots for the clamping stacks to pass through, a layout that restricts the total "throw" of the actuator, but acceptably so. The pusher slots allow the stacks to be centrally located in the overall device, without being part of the moving structure. Integral to the design of the pusher is a pre-load feature which allows the extensional stack to be placed under compressive load during assembly.

The area over which the clamping flexural sub-structure of the upper frame interacts with the pusher provides enough surface area for proper frictional force transmission. The material at the interaction surface was lapped to nearly a mirror finish, with rms surface variation on the order of 1-2 microns. This surface precision results in the maximum friction coefficient for the material, while allowing freedom of movement with only a few microns normal displacement of the clamp.

The upper frame dynamic characteristics are very important to the performance of the inchworm. Its modes of vibration should be at frequencies higher than the operating stack frequency range of 0-1000 Hz. It is also important that modes other than the plunging mode be excited only minimally upon impact so as not to disrupt high-rate repetitive operation.

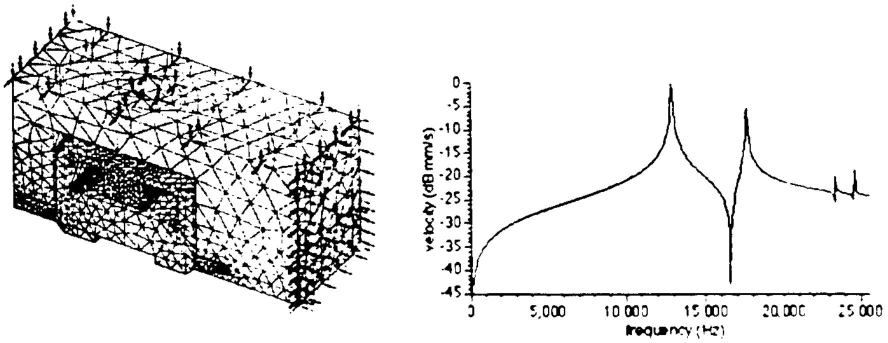

Figure 5: a) Solid finite element model of the upper clamp with boundary conditions, and b) frequency spectrum of the finite element dynamic model

As illustrated in Figure 5, the first mode at 12,660 Hz represents a plunging mode. This mode could be excited by high frequency actuation of the piezoceramic stack and should be avoided. Its excitation would disrupt clamping and likely cause excessive noise due to impact of the clamp on the pusher. The second mode at 17,634 Hz represents rotation of the mass/spring structure about the x axis. Excitation of this tipping motion would cause a stress gradient across the surface of the stack. The third mode at 23,407 Hz involves rotation of the mass/spring structure about the z axis. This rocking mode should have much lower amplitude than the first two modes because it should not be excited by forces applied at the center of the stack interface surface. Were this mode to be excited during operation it would also result in a detrimental stress gradient across the stack. The fourth mode at 24,633 Hz is a rotational mode about the y axis. The response of this mode should also be small compared to that of the first two and should not be excited by any force on the stack interface surface. If excited it would torque the stack and could cause it to shear unnecessarily.

The pusher was modeled in a similar fashion, with results that affect the range of operation significantly. The first mode of the pusher is at about 1,065 Hz and involves bending along the x-y plane. This mode is much lower in frequency than those of the upper clamp and represents an upper bound on the clamping frequency. Also important, the fundamental extensional mode is at about 11,806 Hz and, if excited, would interfere with the extensional motion sequence. This resonance is far beyond the intended operating frequency range, but with additional mass (i.e. loading condition) added to the end of the pusher the resonance frequency could quickly fall into the range of interest.

Easy assembly of the actuator was crucial. As a developmental device, it had to be designed for manufacturability, repairability and integration. The assembly (shown in Figure 6a) allowed ready access to the internal structure.

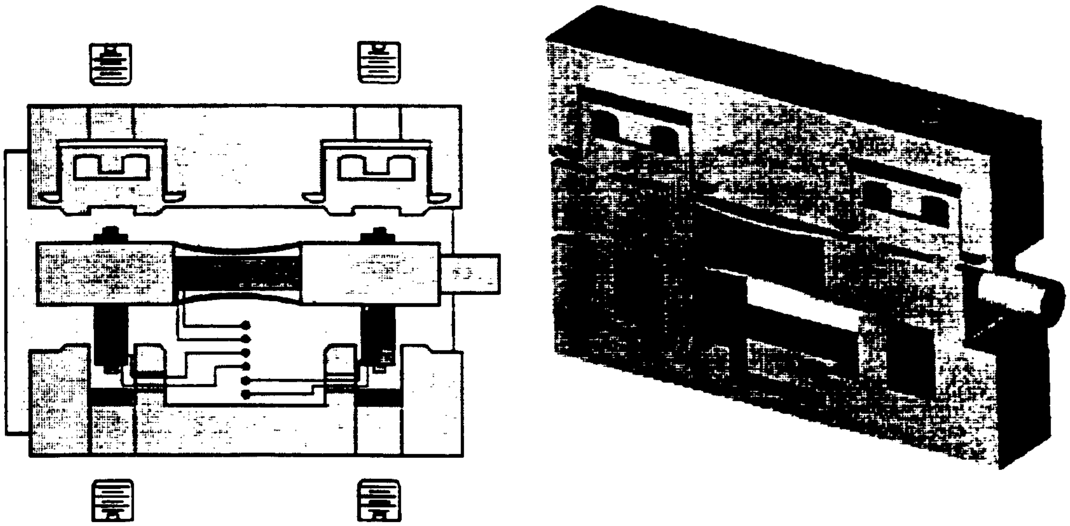

Figure 6: a) Assembly layout of the inchworm actuator and
b) Rendered solid model of the final design of the H3C Inchworm Actuator

DYNAMIC MODELING AND SIMULATION

Dynamic operation of the H3C inchworm was modeled using a 4 DOF lumped parameter system. as shown in Figure 7. The rear and front end of the pusher were modeled as rigid masses. the flexures as mass less springs, and the clamping devices as mass-spring systems. The stacks were represented by spring elements in series with induced displacement elements. The four degrees of freedom corresponded to the displacements of the two ends of the pusher and the two free ends of the clamping elements. The external load consists of a single degree of freedom system and a static force. The connection between the external system and the pusher is assumed to be perfectly rigid, so that any external mass is included in the mass of the front end of the pusher.

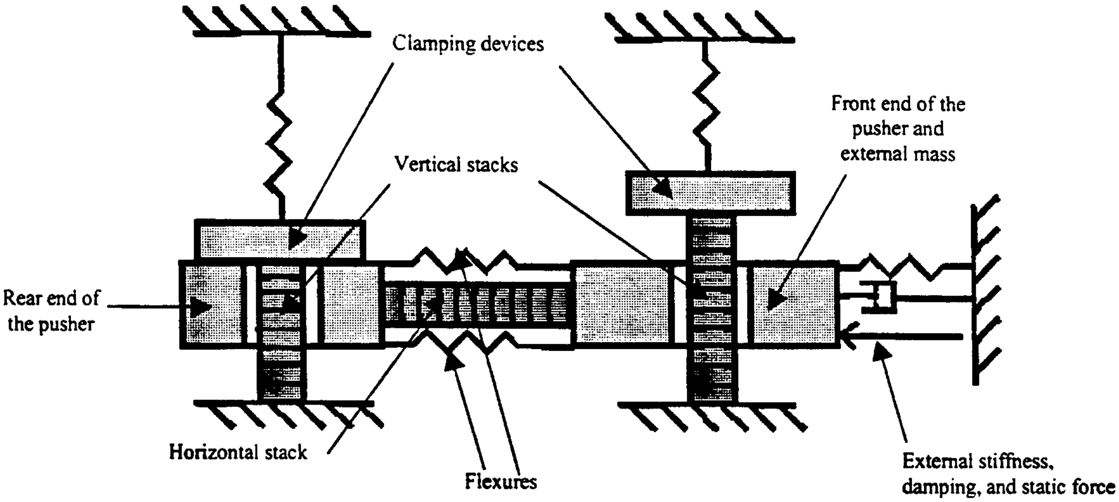

Figure 7: Lumped parameter model of the inchworm H3C

The dynamic response of the system to time-varying drive voltages in the stacks was calculated by the Runge-Kutta-Nystrom method. At step (i), the displacements (i+1) are integrated using the forces of step (i), which include friction forces, induced forces and external forces. The rest of the algorithm evaluates the friction forces for step (i+1). The resultant normal force applied to the pusher by each of the clamping devices is first checked. If it is positive (upward), the friction force is zero and the corresponding end of the pusher is free. If it is negative (downward), the friction force is non-zero and can be either a static or a dynamic friction force. The sum of all the forces of step (i+1) applied to the end of the pusher, including elastic, viscous, and inertial forces, is then computed. If this exceeds the value of the static friction force, the friction force is set to its dynamic value. If it is lower, the displacement (i+1) is set to zero and the friction force is set to the sum of all other forces of step (i+1) acting on the end of the pusher, given the zero displacement.

Figures 8a) and 8b) show the displacements of the rear and front of the pusher, and the friction forces, for the following loading and driving conditions: a mass of 0.5 kg , a spring stiffness of 0.1% of the stiffness of the stack, and a static force equal to the weight of the mass; the clamping stacks were driven with square waves with zero phase shift, 100 Volts peak, and 300 Hz; the pusher stack was driven with a sine wave, 100 Volts peak, and 300 Hz. In this nearly free condition, the numerical model yielded good results, as shown in Figure 9. However, as the external mass increased, the results degraded. The numerical model tended to overestimate the displacements for large external loads, giving results similar to the free case. One flaw in this model is that no friction force is applied to the pusher if the clamping devices bounce on the surface due to oscillations. When attempting to move large external loads, the precompression forces applied to the clamping devices need to be high. The clamping devices are thus more likely to bounce on the surface of the pusher, and to slow it down during the extension phase. Nevertheless, some interesting features can be observed from Figures 8a) and 8b). At each extension, the rear end of the pusher slips back, because of the higher inertia of the front mass. This backward motion is resisted by a positive friction force, but is only stopped after a short time, which creates a delay in the displacement of the front mass as compared to its driving voltage. This suggests that a different clamping signal might be used for the rear of the pusher.

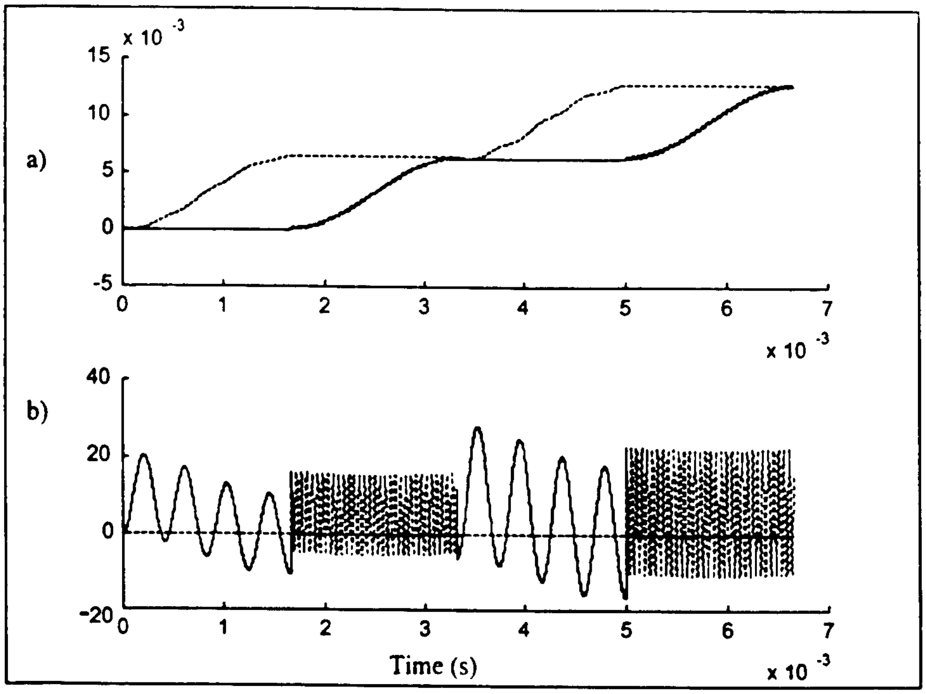

Figure 8: (a) Displacements of the pusher ends (mm); and (b) Friction forces on the pusher ends (N) (dashed : front - solid : rear)

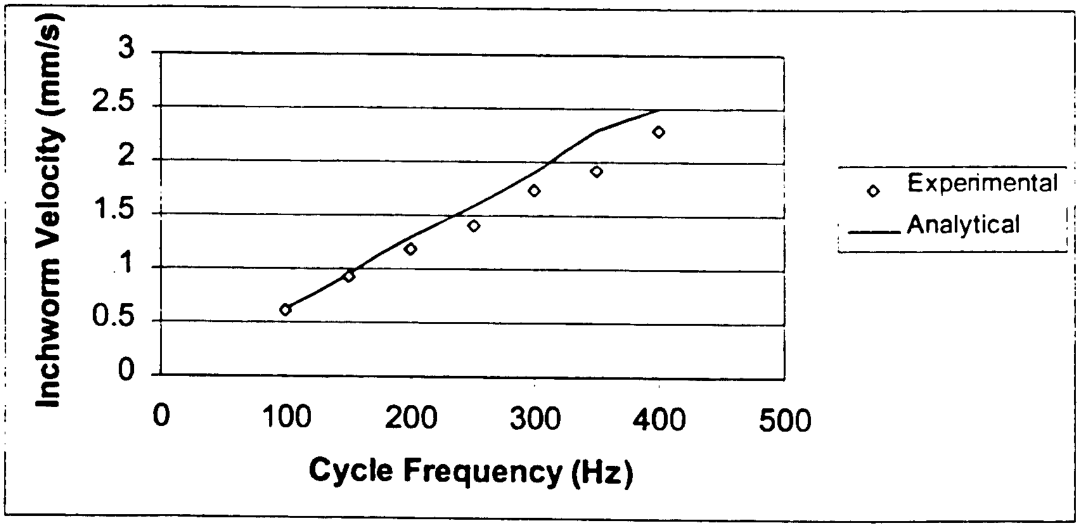

Figure 9. Experimental and computed inchworm speeds under quasi-free loading

Figures 10a) and 10b) show the force applied by the inchworm on the external structure in the following loading and driving conditions: a mass of 0.5 kg, a spring stiffness of 1% of the stiffness of the stack, a static force equal to the weight of the mass; for Figure 10a), the same voltages as in figures 8a) and 8b), and for Figure 10b) an 18 degree phase lag was applied to the front clamp. The purpose of the delay was to ensure that the pusher developed some initial force by the time its front end was released. On the other hand, the delay reduced the time over which the pusher was free to extend. The results show that the front end of the pusher experienced less backlash with delayed voltages. This suggests the existence of an optimal phase shift for the clamp signals.

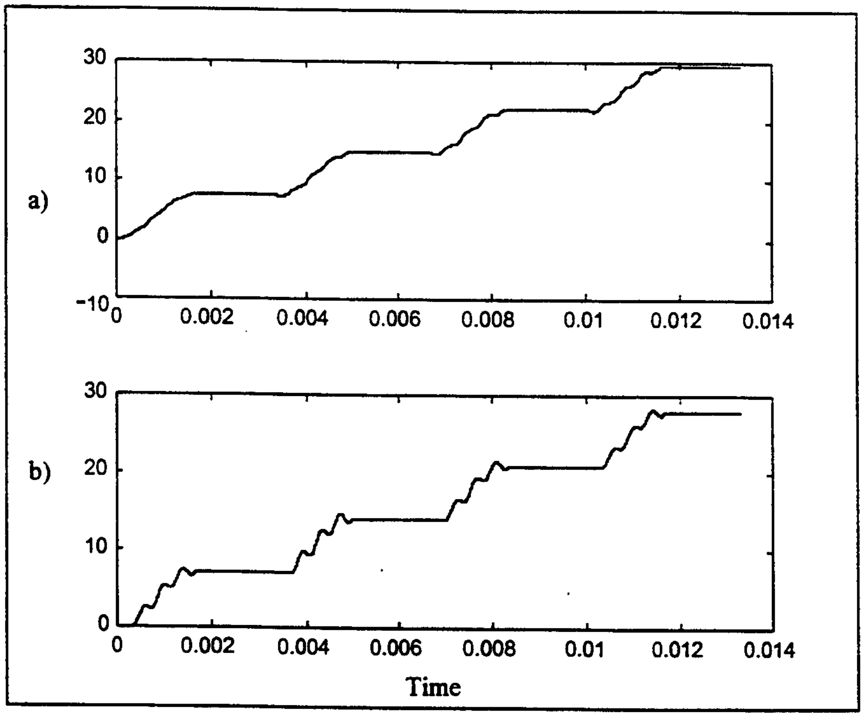

Figure 10: (a) Force output with zero phase lag (N), and (b) Force output with an 18 degree phase lag (N)

TESTING THE PROTOTYPE H3C ACTUATOR

With the actuator designed, manufactured and assembled, it was tested in order to characterize its performance. Many features of the drive signals must be specified, including waveform shape, level, duty cycle and relative phasing. These variables must be simultaneously optimized in order to attain the best possible performance. With this need for flexibility in mind, LABVIEW software was used to generate inchworm drive signals through a PC digital to analog output board. This software was used to create waveforms of virtually any shape, and allowed the frequency, amplitude, duty cycle and phase of the signals to be changed at the touch of a button. Figure 11 shows sample drive signals generated using this software.

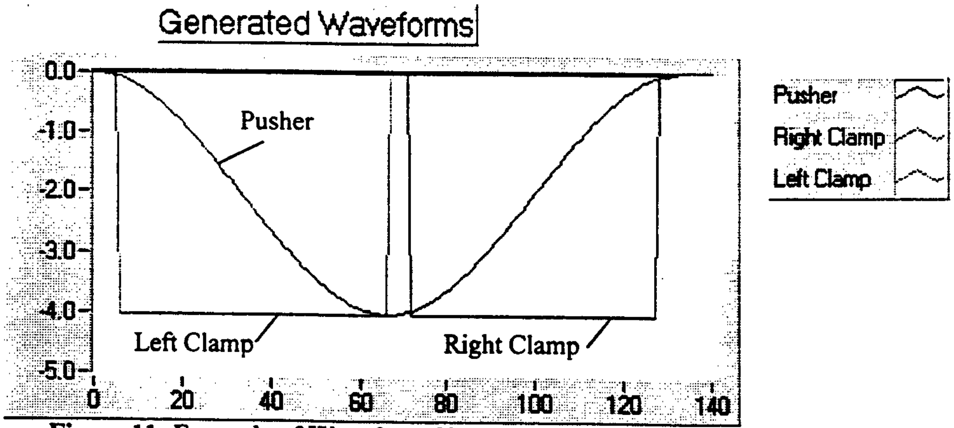

Figure 11: Example of Waveform Signals Generated using LABVIEW Software

A special-purpose calibration fixture was developed for characterization of the inchworm, as shown in Figure 12. Its main feature is a stiff beam pivoted on one end in a precision bearing. An important aspect of this fixture is the ability to selectively drive loads that are primarily inertial in nature, primarily stiffness in nature, or a combination of both. The beam can be driven against a compression spring for a stiffness load, or a mass can be attached to the beam to increase the inertial load. A high-sensitivity strain gauge load cell and an LVDT position transducer were used to measure performance. Further, an analog to digital input board was used to record the output force and velocity in LABVIEW, a feature of the experimental setup that will eventually enable closed-loop operation of the inchworm..

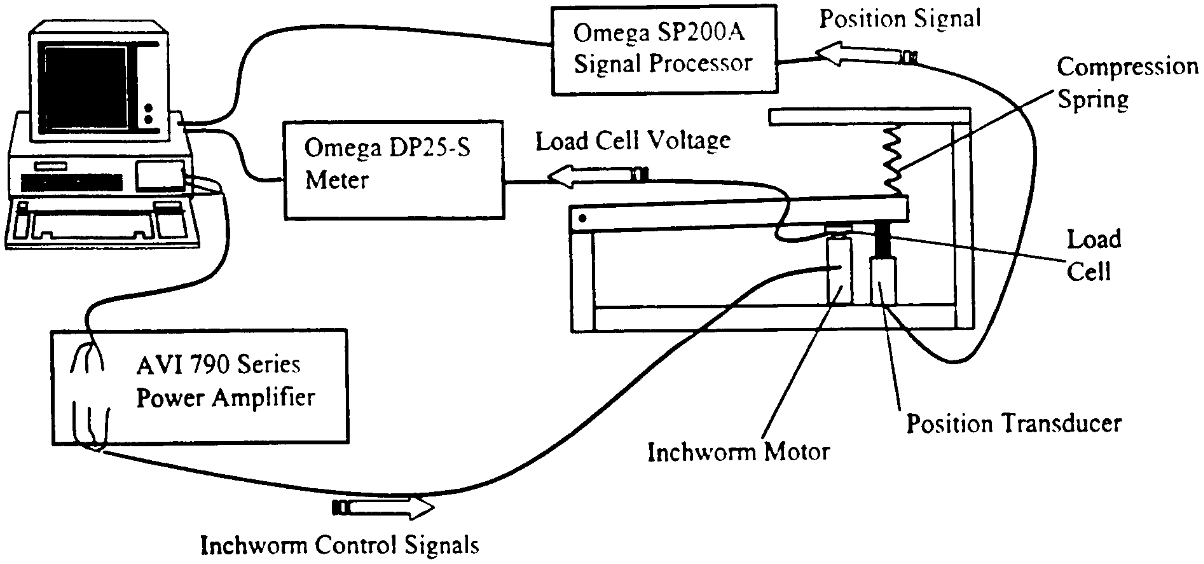

Figure 12: Schematic of the H3C Inchworm Actuator Performance Characterization Experiment

There were two primary objectives of the initial inchworm experiments. The first was to characterize the performance of the inchworm in terms of dynamic force and velocity, and the second was to optimize the clamp and pusher drive signals. Two initial experiments were devised to characterize performance. First, the motor was driven against the compression spring until the maximum dynamic force was reached, and no further displacement was possible. The piezoceramic clamp stacks were driven with square waves, at voltages up to a maximum of 124 V. The signal to the pusher was an offset 0 to 87 V sine wave. As seen in Figure 13, the maximum measured pusher force increased with voltage, due to correspondingly higher clamping forces. The maximum dynamic force measured was 41.5 N, although this is expected to rise as waveform signals and levels are further improved and increased.

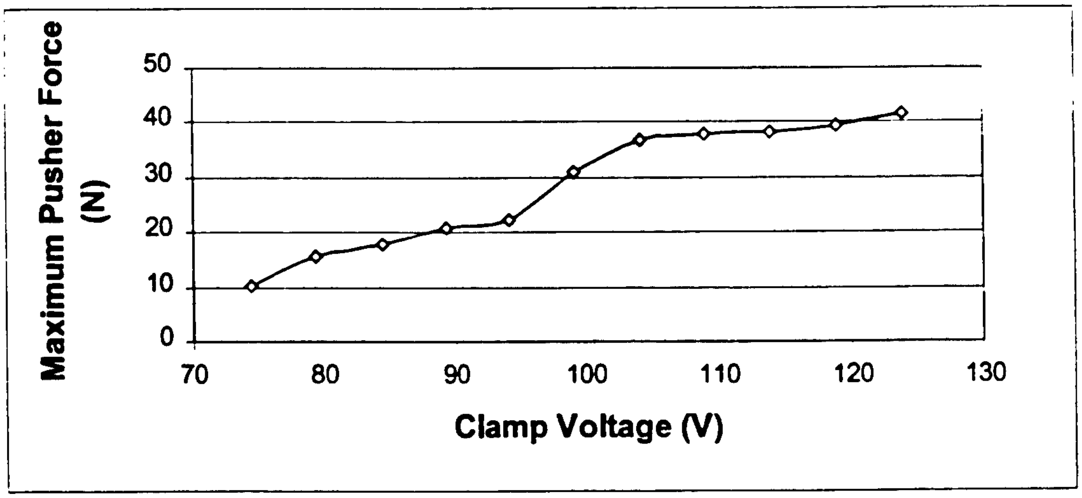

Figure 13: Maximum Dynamic Driving Force Against a Compression Spring

A second experiment devised to characterize performance was to measure the no-load maximum velocity. This time, two different types of signals were used to drive the clamping stacks: a square wave and a sine wave. The amplitude of both kinds of waves was fixed at 97V. As shown in Figure 14, the maximum velocity attained for a square signal was 3.3 mm/s at a drive frequency of 500 Hz: presumably because of dynamic response to impulsive clamp forces, the inchworm would not run at higher frequencies. For a sinusoidal signal, however, a maximum velocity of 5.4 mm/s was attained at a drive

max 0 150V to Sumitomo stack   21. mm
blocked force 700N @ 150V $5^2 \times 4.5$mm

$C^T = 890$ nF

frequency of 900 Hz. Higher driving rates were possible with the sinusoidal signal because the clamp motion was smooth, with less noise and vibration. This is a potentially important observation, since a sinusoidal signal could be easily created using standard AC voltage, perhaps reducing the need for separate complex signal generators and amplifiers. Again, higher velocities are expected as the waveform signals are further improved.

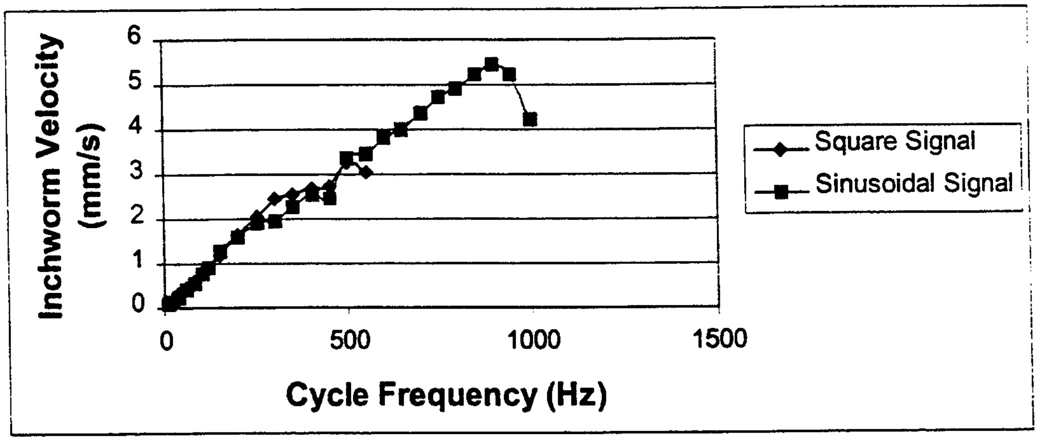

Figure 14: Inchworm Velocity vs. Cycle Frequency, Driven with Square and Sinusoidal Clamp Signals.

The ongoing goal of experimentation is to increase inchworm performance by optimizing clamp signal parameters: waveform shape, voltage, phase, cycle frequency and duty cycle. Because of the large number of signal parameters, each must be independently optimized. With sinusoidal clamp signals, for example, the drive voltage and frequency were held at 90 V and 100 Hz, respectively, while the relative phases of the sine waves were changed. As shown in Figure 15, there was an increase and then a decrease in performance as the phase between the clamp signals was changed. This experiment was carried out for four pusher wave phases (the relative phase between the pusher and the first clamp signals), and demonstrated that the best performance was obtained when the clamp signals were 175 degrees apart, and the pusher signal was 75 degrees after the first clamp signal. A more thorough investigation of this behavior may show that the optimal relative phase settings depend on cycle frequency and waveform, so further experimentation is necessary. In addition, relative phasing optimization experiments will be conducted for each type of waveform shape and voltage, including square waves and more complex signals.

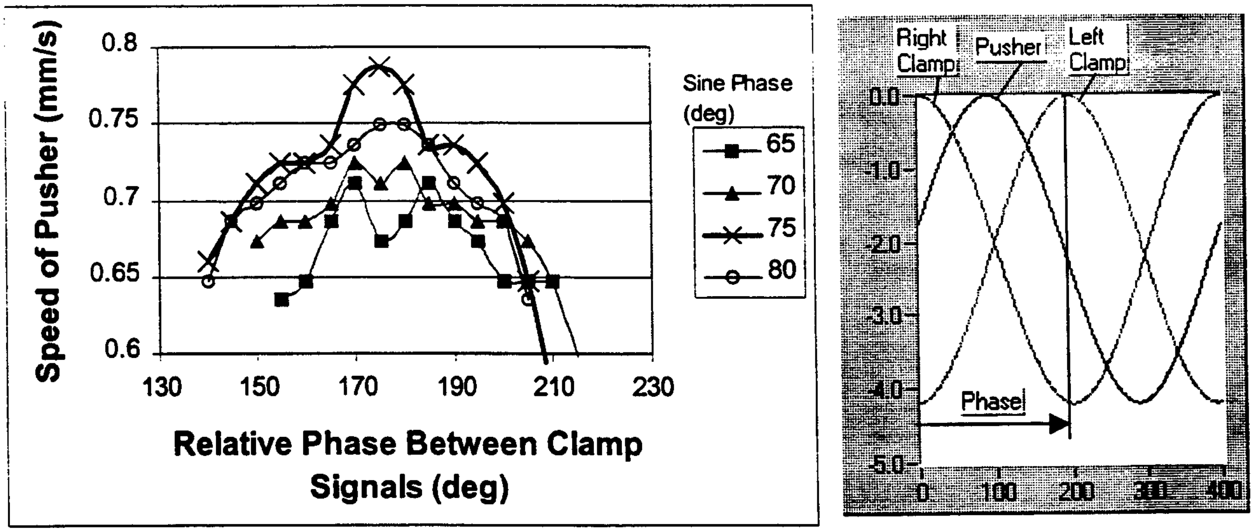

Figure 15: a) Determination of the Optimal Relative Phases between Waveform Signals and b) Sample of Waveform Signals from LABVIEW showing Phase

CONCLUSIONS

A linear inchworm motor was developed for structural shape control applications. Features of the subject device include small size (60 x 40 x 20 mm), strokes of about 1 cm, speeds approaching 1 cm/s, dynamic forces in excess of 50 N, and static holding force capability greater than 200 N. There are three active piezoelectric elements within the inchworm: two "clamps" and one "pusher." Large displacements are achieved by repetitively advancing and clamping the pushing element. The development of a robust clamping mechanism is essential to attain high force capability, and considerable design effort focused on improving this mechanism. To guide the design, a lumped parameter model of the inchworm was developed. This model included the dynamics of the moving shaft and the frictional clamping devices and used a variable friction coefficient. It enabled the simulation of the time response of the actuator under typical loading conditions. The effects of the step drive frequency, the pre-load applied on the clamps, and the phase shifts of the clamp signals relative to that of the main pusher signal were investigated. Using this tool, the frequency bandwidth, the optimal pre-load and phase shifts which result in maximum speed were explored. Measured rates of motion agreed well with predictions, but the measured dynamic force was lower than expected. Although not yet complete, experiments conducted with the H3C inchworm indicate that it has performed as it was designed to, achieving a free velocity of 5.5 mm/s and a dynamic force of 41 N, both at modest drive levels. As a larger matrix of tests to optimize and increase the inchworm drive signals is executed, its performance should improve substantially.

ACKNOWLEDGEMENTS

This work was supported by DARPA under the SAMPSON project, performed in collaboration with engineers at Boeing St. Louis, General Dynamics, Penn State's Applied Research Laboratory, and PCB Piezotronics.

REFERENCES

1. R. Stibitz, "Incremental Feed Mechanisms", *U.S. Patent: 3,138,749*, 1964.
2. J.T. McNancy, "Piezoelectric transducer force to motion converter", *U.S. Patent: 2,154,700* 1964.
3. K. Hsu, and A. Biatter, "Transducer", *U.S. Patent: 3,292,019*, 1966.
4. G.L. Locher, "Micrometric linear actuator", *U.S. Patent:* 3,296,467, 1967.
5. A.D. Brisbane, "Position control device", *U.S. Patent: 3,377,489*, 1968.
6. G.V. Galutva, "Device for precision displacement of a solid body", *U.S. Patent: 3,684,904* 1972.
7. R.A. Bizzigotti, "Electromechanical translational apparatus", *U.S. Patent: 3,902,085*, 1975.
8. Y. Sakitani, "Stepwise fine adjustment", *U.S. Patent: 3,952,215*, 1976..
9. Ishikawa, and Y. Sakitani, "Two-directional piezoelectric driven fine adjustment device", *U.S. Patent: 4,163,168*, 1979.
10. G. O'Neill, "Electromotive actuator", *U.S. Patent: 4,219,755*, 1980.
11. T. Taniguchi, "Piezoelectric driving apparatus", *U.S. Patent: 4,454,441*, 1984.
12. A. Hara, H. Takao, Y. Kunio, T. Sadayuki, and N. Keiji, "Electromechanical translation device comprising an electrostrictive drive of a stacked ceramic capacitor type", *U.S. Patent: 4,570,096*, 1986.
13. C.W. Staufenberg, Jr., and R.J. Hubbell, "Piezoelectric electromechanical translation apparatus", *U.S. Patent: 4,622,483*, 1986.
14. T. Fujimoto, "Piezo-electric actuator and stepping device using same", *U.S. Patent: 4,714,855* 1987.
15. T. Murata, "Drive apparatus and motor unit using the same", *U.S. Patent: 4,974,077*, 1990.
16. G. Rennex, "Inchworm actuator", *U.S. Patent: 5,3323,942*, 1994.
17. J.E. Meisner and J.P. Teter, "Piezoelectric/magnetostrictive resonant inchworm motor", *SPIE*, Vol. 2190, pp. 520-527, 1994.
18. S.K. Lee and M. Esachi, "Design of the electrostatic linear microactuator based on the inchworm motion", *Mechatronics*, Vol. 5, No. 8, pp. 9653-972, 1995.
19. T. Pandell and E. Garcia, "Design of a piezoelectric caterpillar motor", *Proceedings of the ASME aerospace division*, AD-Vol. 52, pp. 627-648, 1996.
20. T. Galante, "Design and fabrication of a high-force linear piezoceramic actuator", M.S. thesis, Penn State University, August 1997.

APPENDIX 76

Galante, T. P. , Design and Fabrication of a High Authority Linear Piezoceramic Actuator,
Master of Science Thesis, August 1997

The Pennsylvania State University

The Graduate School

Department of Mechanical Engineering

DESIGN AND FABRICATION OF A HIGH AUTHORITY LINEAR PIEZOCERAMIC ACTUATOR: THE PSU H3 INCHWORM

A Thesis in

Mechanical Engineering

by

Timothy P Galante

Submitted in Partial Fulfillment
of the Requirements
for the Degree of

Master of Science

August 1997

ABSTRACT

A core technology effort focuses on actuators for high rate shape control. The Center for Acoustics and Vibration at Penn State (PSU/CAV) is developing actuators to drive conformable flow control surfaces for use in marine and aircraft systems. The actuators are selected based on the following characteristics: high displacement, high force, high energy density, high energy conversion efficiency, slender and compact design and cost effectiveness. A down-select process was performed on actuators induce strain actuation (ISA) materials or so-called "smart" materials. A piezoceramic actuator which uses a novel approach of actuation was singled out as the best performer.

The H3 piezoceramic inchworm actuator was designed to emulates the motion of an inchworm, incrementally summing small displacements into large displacements. The design of the actuator was accomplished by using a coupled feature-based solid modeler and finite element solver to design part properties (such as stiffness) to specific values. The actuator was then fabricated and tested to verify the model with which the design was based on. This model proved to be an adequate one in which further design constraints may be tested against. The actuator, no larger than a deck of cards is capable of actuation forces of approximately 30 lbs. (133 N) over a displacement of 0.1-0.2 in. (3-5 mm).

APPENDIX 77

Lesyna, M. W. , Shape Optimization of a Mechanical Amplifier for Use in a Piezoceramic
Actuator, Master of Science Thesis, January 1998

The Pennsylvania State University

The Graduate School

Department of Mechanical Engineering

SHAPE OPTIMIZATION OF A MECHANICAL AMPLIFIER FOR USE IN A PIEZOCERAMIC ACTUATOR

A Thesis in

Mechanical Engineering

by

Mark W. Lesyna

Submitted in Partial Fulfillment
of the Requirements
for the Degree of

Master of Science

May 1998

ABSTRACT

The Penn State Center for Acoustics and Vibrations (PSU/CAV) is developing actuators for shape control of conformable flow control surfaces. In the last year, two versions of high force, high displacement, high energy density linear piezoceramic actuators have been developed using the inchworm concept to transform high frequency small displacements into large displacements at low frequency.

Three piezoceramic inchworm actuators have been designed at the PSU/CAV in the past year. The third design, dubbed the H3-B, is the subject of this research. This actuator is more effective than the previous designs in conformable flow control applications due to a thinner design with larger internal tolerances. The design requires a flexible frame structure having high output stiffness to create large clamping forces, and high coupling with the piezoceramic stack for the unclamping operation. Shape optimization is used in the design process to handle the complex objective function and constraints placed on the flextensional frame. This thesis presents the shape optimization method and includes a study into flextensional design. A prototype of the shape-optimized actuator is verified to meet the design predictions through testing.

The new actuator is about the size of a deck of cards, only half as thick. It is capable of actuation forces of approximately 8 N (1.8 lb.) and velocities of 280 cm/sec (11 in/sec). It is less expensive to produce than the two previous designs because of larger internal tolerances and the elimination of adjustment mechanisms.